Numerical framework for data-driven model-based monitoring of dynamical systems - Application to earthquake engineering

Matthieu Diaz

Numerical framework for data-driven model-based monitoring of dynamical systems

Application to earthquake engineering

Stratégies de simulation et de contrôle de systèmes dynamiques à partir de modèles numériques alimentés par les données

Applications en génie parasismique

Thèse de doctorat de l'Université Paris-Saclay

École doctorale n°579 : Sciences mécaniques et énergétiques, matériaux et géosciences
Spécialité de doctorat: Mécanique des solides
Graduate School : Sciences de l'Ingénierie et des Systèmes - Référent : ENS Paris-Saclay

Thèse préparée au Laboratoire de Mécanique Paris-Saclay (Université Paris-Saclay, CentraleSupélec, ENS Paris-Saclay, CNRS) et au laboratoire d'études en mécanique sismique (Université Paris-Saclay, CEA, Service d'études mécaniques et thermiques), sous la direction de **Ludovic Chamoin**, professeur des universités à l'ENS Paris-Saclay, et le co-encadrement de **Pierre-Étienne Charbonnel**, ingénieur chercheur au CEA Saclay

Thèse soutenue à Gif-sur-Yvette, le 06 juillet 2023, par

MATTHIEU DIAZ

Composition du jury

Membres du jury avec voix délibérative

Pierre FEISSEL Professeur des universités - Université de Technologie de Compiègne, Laboratoire Roberval	Président
Etienne BALMÈS Professeur des universités - Ecole Nationale Supérieure d'Arts et Métiers, Laboratoire de Procédés et Ingénierie en Mécanique et Matériaux	Rapporteur & Examinateur
Stefano MARIANI Associate Professor - Dipartimento di Ingegneria Civile e Ambientale, Politecnico di Milano	Rapporteur & Examinateur
Eleni CHATZI Professor - Chair of Structural Mechanics and Monitoring, Institute of Structural Engineering (IBK), ETH Zürich	Examinatrice
Elías CUETO Professor - Grupo de Mecánica Aplicada y Bioingeniería, Instituto Universitario de Investigación en Ingeniería de Aragón, Universidad de Zaragoza	Examinateur
Mathieu CORUS Ingénieur chercheur expert, EDF R&D	Examinateur

THESE DE DOCTORAT
NNT : 2023UPAST096

Explorer tout cela a été une véritable aventure qui n'a fait qu'attiser toujours davantage notre curiosité. Ce bilan est donc loin d'être définitif, et il se révèle être au final une invitation à continuer l'exploration.

Pablo Servigne & Gauthier Chapelle, *L'entraide, l'autre loi de la jungle*

Remerciements

Quelle dure tâche pour le radoteur que je suis de devoir conclure cette aventure, et en plus par le début ! Si je devais résumer ma thèse aujourd'hui, ce serait avant tout des rencontres... et maintenant que ce manuscrit est déjà trop long, je peux encore profiter de cet avant-propos pour le dédier à toutes celles et à tous ceux qui ont contribué à le façonner. J'espère que ces quelques lignes, probablement les plus peaufinées de ce manuscrit, seront à la hauteur de la reconnaissance et du respect que j'ai envers vous.

Je tiens tout d'abord à présenter ma gratitude aux membres du jury pour l'intérêt qu'ils ont porté à mon travail, et en particulier Etienne Balmès et Stefano Mariani qui ont eu la lourde tâche de relire ce manuscrit, et Pierre Feissel qui m'a fait l'honneur de présider le jury. Egalement merci aux autres membres, Elias Cueto et Eleni Chatzi, dont les riches questions m'ont permis d'imaginer encore de nouvelles pistes de recherche en perspective de mon travail. Un remerciement particulier va enfin à Mathieu Corus, que j'aurai le plaisir de cotôyer en tant que collègue dans quelques semaines chez EDF.

Cette thèse, je la dois avant tout à mes deux encadrants : Ludovic Chamoin et Pierre-Étienne Charbonnel. Je leur suis infiniment reconnaissant de m'avoir fait confiance pour prendre part à ce projet ambitieux et pour avoir instauré un cadre de travail si épanouissant malgré toutes les péripéties que l'on a traversées ces dernières années. Merci à toi Ludo, pour avoir été si inspirant, aussi bien scientifiquement qu'humainement, toujours rigoureux, bienveillant, d'une efficacité redoutable, aussi bien en réunion qu'en blind-test ! Merci à toi PE, pour ta disponibilité au quotidien, pour tous ces échanges animés qui, même s'ils ont souvent fini sans queue ni tête, m'ont appris à aiguiser mon sens critique et ma précision rédactionnelle. D'ailleurs, j'ai même réussi à comprendre au final que te suivre de trop près, surtout à la course le midi, n'était pas toujours une idée judicieuse ! J'espère très sincèrement être amené à retravailler avec vous dans le futur.

Les sept années que j'ai passées à arpenter les couloirs du DGM et du LMT/LMPS, à Cachan et à Saclay, m'ont permis de rencontrer et de tisser des liens avec des gens formidables. Impossible de ne pas commencer par Louis, le collègue de bureau le plus grand que je n'aurai jamais, qui m'a convaincu de me mettre au vélo et qui m'accompagne depuis le tout début de mes années parisiennes. Il y a aussi les irréductibles collègues de promotion, Alexis, Alexandre et Aurélia en tête, avec qui les échanges sont toujours décalés et enrichissants. J'ai surtout une pensée émue pour les collègues du CdS, qui ont eu la lourde tâche de me supporter et de m'entendre râler environ un jour sur deux ces trois dernières années. Malgré cela, les plus jeunes, Floriane, Quentin, Victor, Karim, Louis C., Pierrot, Breno, Sahar, et tous ceux que j'oublie, ont su transmettre leur fougue et leur insouciance, lorsque les plus expérimentés, Ronan, le doyen Willy, Rafael, Yannick, Ahmed, Maxime, Cédric et tous les autres, ont su m'éclairer de leurs conseils les plus avisés, parfois pas toujours les plus studieux. Enfin, merci aussi aux collègues enseignants, enseignants-chercheurs, techniciens, gestionnaires du labo, trop nombreux pour les citer sans en oublier mais qui se reconnaîtront, pour les discussions et moments passés en pause café et en conférence, qui contribuent à l'excellente ambiance du labo.

Egalement, mes remerciements vont à tous les collègues ingénieurs-chercheurs et techniciens du laboratoire EMSI, qui ont très rapidement su m'intégrer parmi eux. En particulier Clément, mathématicien mais mécanicien dans l'âme, Bruno, expert ès tenseurs et envahisseur de tableaux blancs, Antoine, la version 2.0 de Clément, Cyril, toujours à l'écoute avec son tee-shirt à capuche, Giuseppe, la classe à l'italienne, ont toujours été présents lorsqu'il fallait refaire

le monde autour d'un café, ou m'aiguiller dans ma recherche au quotidien. Je n'oublie pas non plus mes anciens co-bureaux sud-américains, Sebastian et Hugo, pour toutes leurs suggestions et mises en garde sur Cast3M.

Et parce que la thèse, ce ne sont pas que des rencontres au travail, je remercie aussi Romain et tous les copaings pour leurs encouragements quand bien même ils ne comprennent pas toujours ce que j'ai pu faire (moi non plus d'ailleurs). Merci aussi à Fred et à tous les coéquipiers de l'Aspique avec qui j'ai pris un grand plaisir à férailler les jeudis après-midi pendant 5 ans, qu'il pleuve, qu'il vente ou qu'il neige. Comme quoi, il n'y a pas qu'à Perpignan que l'on sait jouer au rugby...

Pour terminer, je souhaite remercier mes parents pour leur soutien indéfectible et leurs encouragements quotidiens. Ma détermination et cette volonté que j'ai à me dépasser pour aller au bout des choses, je la tiens de vous deux. Une pensée aussi à ma soeur, qui je l'espère, saura tirer le meilleur de mon exemple dans ses futures escapades en thèse.

Enfin, merci Charlotte pour ta présence, ta patience, ta joie de vivre et ton amour.

université PARIS-SACLAY

ÉCOLE DOCTORALE
Sciences mécaniques et énergétiques, matériaux et géosciences (SMEMAG)

Titre: Stratégies de simulation et de contrôle de systèmes dynamiques à partir de modèles numériques alimentés par les données - Applications en génie parasismique
Mots clés: Recalage de modèle, Assimilation de données, Dynamique des structures, Contrôle de systèmes en temps réel, Génie parasismique, Essais sismiques sur table vibrante.

Résumé: Le laboratoire EMSI du CEA Saclay est équipé de tables vibrantes permettant de reproduire sur des ouvrages de génie civil de taille conséquente des chargements sismiques complexes. Les lois de commande des vérins hydrauliques qui les pilotent n'intègrent pas directement l'évolution de l'état de santé des structures testées, pouvant pourtant soudainement se dégrader et conduire à des essais instables, menaçant l'intégrité de l'installation expérimentale.

L'objectif de cette thèse est de développer une stratégie d'assimilation de données unifiée autour du concept d'erreur en relation de comportement modifiée (ERCm), permettant de recaler un modèle numérique de la structure testée pour régler les lois de contrôle en temps réel. L'ERCm a d'abord été mise en œuvre *a posteriori*, pour traiter les données recoltées d'essais achevés. Une stratégie intégralement automatisée a été proposée pour identifier les paramètres de raideur d'un modèle éléments finis de manière robuste et fiable. Ce cadre a ensuite été étendu à l'assimilation séquentielle de données, en intégrant l'ERCm comme observateur d'un filtre de Kalman (MDKF).

Tous les développements ont été validés avec des mesures simulées issues d'exemples de génie parasismique, puis appliqués avec succès à la campagne expérimentale SMART2013. Avoir pu suivre en temps réel l'évolution de la signature modale d'une structure complexe en béton armé à partir de mesures d'accélération souligne la robustesse et l'efficacité de la stratégie proposée.

Enfin, la question du contrôle adaptatif a été abordée au travers d'une preuve de concept, où une commande par retour d'état adaptée en temps réel par MDKF a pu stabiliser un essai sismique simulé. Ce dialogue essais/calculs ouvre ainsi la voie à des perspectives de contrôle hybride, et à de nouveaux outils pour le suivi de l'état de santé de structures.

Title: Numerical framework for data-driven model-based monitoring of dynamical systems - Application to earthquake engineering problems
Keywords: Model updating, Data assimilation, Structural Dynamics, Real-time control of systems, Earthquake engineering, Shaking table experiments.

Abstract: The EMSI laboratory (CEA Saclay) is equipped with shaking tables that allow to assess the seismic performance of civil engineering constructions. The control laws of the hydraulic actuators that drive them do not directly integrate the health condition of the tested structures, which can suddenly deteriorate and lead to unstable tests. If so, the integrity of the experimental setup is threatened.

This thesis work aims to develop a data assimilation framework unified around the concept of modified Constitutive Relation Error (mCRE), in which a digital twin of the tested specimen is used to adapt control laws on-the-fly. First, a fully-automated mCRE-based finite element model updating strategy is implemented in an offline context in order to perform robust and accurate parameter identification. The methodology has then been extended to online data assimilation by integrating the mCRE within a Kalman filter (MDKF).

All numerical developments have been validated with simulated data from earthquake engineering problems, and successfully applied to the SMART2013 test campaign database. The possibility to monitor in real-time the modal signature of a reinforced concrete specimen from actual acceleration measurements illustrated the relevance and robustness of the proposed strategy.

Eventually, the adaptive control issue has been addressed via a proof-of-concept in which a state-feedback command has been tuned in real-time with MDKF to stabilize simulated shaking table tests. This dynamical data-to-model interaction thus paves the way of future investigations for hybrid control strategies and new physics-guided structural health monitoring techniques.

Contents

List of Figures

List of Tables

List of Algorithms

Notations

Mathematical operators

$\square \cdot \blacksquare$	Inner product
$\square : \blacksquare$	Tensor product
$\square^T / \square^H$	Transpose and Hermitian transpose
$\boldsymbol{tr}\left(\square\right)$	Trace operator
$\square^\dagger$	Moore-Penrose pseudo-inverse
$\nabla_\bullet(\square)$	Gradient of $\square$ with respect to $\bullet$
$\nabla \cdot$	Divergence operator
$\Re, \Im$	Real and imaginary parts extractors
$\mathbb{E}\left(\square\right)$	Mathematical expectation
$\#(\square)$	Cardinal operator
$X(\omega)$	Continuous frequency counterpart of $x(t)$ at angular frequency ω
$\mathcal{S}_{x,y}$	Crossed power spectral density of time signals x and y
$H(\omega)$	Transfer matrix

Finite Element dynamics

$x \in \Omega$	Space variable and domain
$t \in [0; T]$	Time variable and domain
Ω_e	Spatial domain discretized with mesh finite elements
$\boldsymbol{K}, \boldsymbol{D}, \boldsymbol{M}$	FE stiffness, damping and mass matrices
F	Nodal load vector
$\bigoplus$	FE assembly operator
$U, \dot{U}, \ddot{U} \subset \mathbb{R}^{N_x}$	Nodal displacement, velocity and acceleration vectors
$\boldsymbol{\Pi}$	Discretized linear state observation operator (projection matrix)
$\boldsymbol{\Phi}$	Modeshape matrix

Deterministic and stochastic model updating frameworks

$\mathcal{M}$	Model operator
e	Model inputs
u	Model outputs
y	Measurements
$\mathcal{H}$	Observation operator
$\mathcal{J}$	Generic model updating functional
δ	Signal-to-Noise Ratio
$\theta, \theta_0, \hat{\theta}, \theta^\star$	Parameter set, prior guess, estimate and reference
$\Theta \subset \mathbb{R}^{N_\theta}$	Parameter space of dimension N_θ
α	Weighting coefficient associated to the data-to-model distance
$\pi\left(\square\right), \pi_0\left(\square\right)$	Probability density function and prior
$\boldsymbol{\Sigma}_\square$	Covariance error matrix on $\square$

The modified Constitutive Relation Error

D_ω	Frequency range of interest
Δf	Frequency step of discretized D_ω
$z(\omega)$	Frequency weighting function
$\boldsymbol{G}$, $\|\square\|_{\boldsymbol{G}}$	Scaling matrix and associated Euclidean L_2-norm
α	Confidence into measurements coefficient
ζ_ω^2	Constitutive Relation Error (CRE) term at angular frequency ω
e_ω^2	Modified CRE term at angular frequency ω
$\widehat{s}_\omega$	Optimal mechanical fields at angular frequency ω

Optimal sensor placement

$\widehat{\boldsymbol{\Pi}}$	Optimal locations of sensors
N_s	Number of sensors
$\boldsymbol{Q}$	Fisher Information Matrix
$\boldsymbol{Q}_m$	Modified Fisher Information Matrix
h	Information entropy
EI	Effective Independence

Kalman filtering

w_x, w_θ	Model error noises on state and parameters
$\boldsymbol{Q}_x, \boldsymbol{Q}_\theta$	Model error covariance matrix on state and parameters
v	Measurement noise
$\boldsymbol{R}$	Measurement noise covariance matrix
$\widehat{x}_k, \boldsymbol{P}_k^x$	Mean and covariance matrix of x at time step k
$\boldsymbol{K}_k$	Kalman gain at time step k

Control theory

s	Laplace variable
$\boldsymbol{A}, \boldsymbol{B}, \boldsymbol{C}, \boldsymbol{D}$	State-space matrices
$\mathcal{C}, \mathcal{O}$	Controllability and observability matrices
m_δ, m_φ	Gain and phase stability margins
$\boldsymbol{L}$	Luenberger observer
$\boldsymbol{K}$	Regulator gain

Abbreviations

DDDAS	Dynamic Data Driven Application Systems
SHM	Structural Health Monitoring
OMA/EMA	Operational/Experimental Modal Analysis
RC	Reinforced Concrete
FE	Finite Element
BCs	Boundary Conditions
DoF	Degree of freedom
CRE	Constitutive Relation Error
mCRE	Modified Constitutive Relation Error
pdf	Probability density function
PSD	Power Spectral Density
FFT	Fast Fourier Transform
FRF	Frequency Response Function
SNR	Signal-to-Noise Ratio
OSP	Optimal Sensor Placement
FSSP	Forward Sequential Sensor Placement
BSSP	Backward Sequential Sensor Placement
GA	Genetic Algorithm
EI	Effective Independence
MSD	ModeShape Difference
IE	Information Entropy
FIM	Fisher Information Matrix
KF	Kalman Filter
EKF	Extended Kalman Filter
EnKF	Ensemble Kalman Filter
PF	Particle Filter
SPKF	Sigma-Point Kalman Filter
UKF	Unscented Kalman Filter
S3F	Scaled Spherical Simplex Filter
MDKF	Modified Dual Kalman Filter
VCS	Valve-Controlled System
LVDT	Linear Variable Differential Transducer
SS	State-Space
PID	Proportional Integral Derivative
PP	Pole Placement
LQR	Linear Quadratic Regulator
LQG	Linear Quadratic Gaussian
MPC	Model Predictive Control

Introduction

Interaction between models and data...

The design, analysis and prediction of dynamical systems requires the construction of robust numerical models. These models can be directly built from measurements (*black-box modeling*) or derived after in-depth physical description of the involved phenomena (*white-box modeling*). Intermediate hybrid approaches are also conceivable, *e.g.* when a part of the underlying physics is too complex to be properly described (*grey-box modeling*). In each case, ensuring the representativeness of these models is a crucial issue that needs to be addressed for their practical use. On the one hand, one cannot blindly believe in the predictive capabilities of high-fidelity models as an increasing number of internal uncertain parameters must be correctly calibrated to ensure their reliability. On the other hand, one cannot directly generalize a model built on a specific database to a given system in a given environment. Therefore, obtaining a useful virtual model is no longer a question of increasing model complexity, but now conversely consists in **developing trust** by uncertainty quantification and confrontation to experimental data.

As most of modern systems are now equipped with numerous sensors, models are assessed (and even augmented) by comparison with experimental data. The validation, enrichment and exploitation of numerical models from experimental data are part of the *Digital Twin* paradigm, whose applications range from simple post-processing to preliminary design, prognosis, active control, or even decision-making process [Chinesta et al. 2018; Rasheed et al. 2020; Wagg et al. 2020]. These features are also promoted by the Dynamic Data Driven Applications Systems (DDDAS) paradigm [Darema 2004; Chamoin 2021], which formally represents a close (online) dialog established between numerical models and experimental data with a dual objective:

(i) controlling the evolution of the experimental system thanks to model predictions,
(ii) updating the numerical model with measurements acquired in real-time.

To do so, *in situ* measurements have to be sequentially assimilated in order to dynamically update parameters of the model in real-time (see Fig. 1). This challenging framework has many applications[1] and requires the elaboration of fast and robust data assimilation techniques.

Regarding civil engineering applications, earthquake engineering problems are no exception to the need of using experimental data to build, validate and operate robust numerical models. More particularly, the fields of Structural Health Monitoring (SHM) [Chatzi et al. 2020; Ritto and Rochinha 2021] and vibration-based damage detection [Alvandi and Cremona 2006; Avci et al. 2021] have been constant research topics of interest since the safety of structures depends on monitoring the occurrence, formation and propagation of structural damage [J. Brownjohn 2007]. In this framework, measurements are collected in operational conditions to predict the evolution of damage and evaluate the state of the structure. If modal analysis tools based on subspace identification techniques are powerful and popular techniques for *a posteriori* analysis [Overschee and Moor 1996; Reynders 2012] alongside finite element model updating methods [Friswell and Mottershead 1995; Simoen et al. 2015], data assimilation techniques are mandatory to process measurements on-the-fly in real-time (with respect to the time scale of observations).

[1] see http://www.1dddas.org for instance

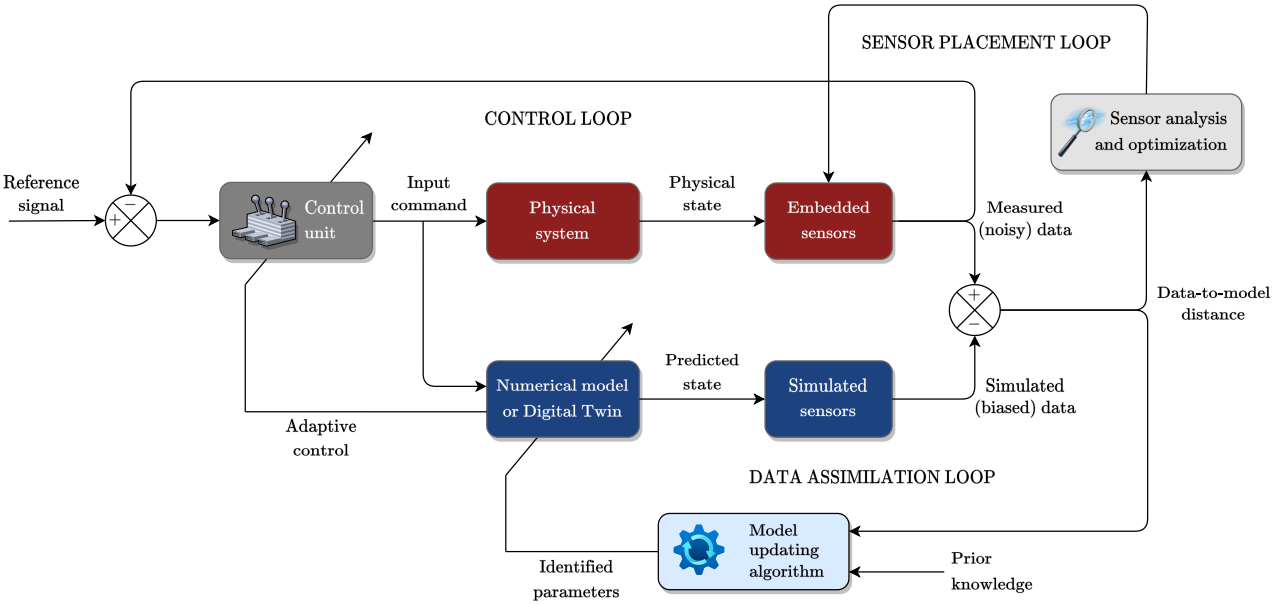

FIGURE 1: Interactions between a physical system and a numerical model in a DDDAS framework.

... for enhanced earthquake engineering experiments

In the industrial nuclear context, power-plant equipments (facility buildings, pipes, tanks, electric closets, overhead cranes, ...) are qualified for their capability to withstand earthquakes according to strict safety norms. To do so, shaking table experiments can be performed to assess the response of structures subjected to ground motion solicitations [McConnell and Varoto 1995; Williams and Blakeborough 2001]. In a research context, shaking table tests on complex structures can also be used to assess the prediction capabilities of nonlinear models [Richard et al. 2016]. The hydraulic actuators that drive the shaking tables can be exploited for hybrid experiments as well [Bursi et al. 2012; Abbiati et al. 2015; 2021].

In this diverse background, the CEA/TAMARIS facility carries out seismic tests using shaking tables moved by high-power hydraulic actuators on complete or partial specimens, at real or reduced scale, to evaluate the capability of civil structures to withstand seismic ground motions.

Controlling the hydraulic actuators of the shaking tables is still a challenging task that emphasizes the need of establishing a close dialogue between model and measurements (see Fig. 2): if the control of shaking tables for seismic replication is a well-identified issue [J. Yao et al. 2016], most of the proposed strategies do not consider the fact that sudden damage occurence may lead to unstable experiments. Actually, because of the strong physical coupling between the actuators, the shaking table and the tested specimen, the controllability of the full device critically depends on the modal signature of the specimen, which is known to be directly conditioned by stiffness changes [Cawley and Adams 1979]. Therefore, during seismic experiments on damaging specimens (such as reinforced-concrete constructions), the modal signature can face sudden changes, which may turn the initial control strategy inadequate with regards to the current state of the tested specimen.

So far, the lack of representativeness of numerical models to predict such phenomena implies to carry out test sequences of increasing level where control laws are iteratively corrected from one test to another to account for the observed frequency drop [Le Maoult et al. 2012]. In spite of these complex protocols, unstable test endings yet may happen, spoil a complete test campaign and put the safety of the facility at risk.

Challenges, objectives and outline

> The ambition of this thesis work consists in developing a novel **data-driven model-based control** strategy that fits within the above-mentioned DDDAS paradigm, in which a **close dialog between the experimental device and a digital twin is performed in real-time**.

From the numerical viewpoint, the integration of a digital twin requires a complex numerical framework including a robust model updating algorithm providing fast and representative solutions of inverse problems. The latter would then be included into an efficient data assimilation scheme to update model predictions from acquired data as frequently as possible, ultimately in near real-time, whereas the computational burden carried by recursive calls to model predictions may be prohibitive. The robustness of the digital twin is essentially conditioned by the properties of the underlying model updating strategy:

- The ill-posedness of the inverse problem in Hadamard's sense [Tikhonov and Arsenin 1977] and ill-conditioning issues [Mottershead and Foster 1991] that are related to the fact that the full state of the structure cannot be measured, and that data acquisition signals include measurement noise. Regularization techniques must then be considered to guarantee uniqueness of the solution and enforce local ellipticity of the problem [Ahmadian et al. 1998; Titurus and Friswell 2008]. For shaking table experiments, this is particularly decisive when performing low-level non-damaging random tests that naturally have a very low signal-to-noise ratio.
- The inverse problem definition itself [Tarantola 2005], including:
  - the sensivity of model parameters to update with respect to the chosen cost-function;
  - the richness of available measurements, *i.e.* the types and densities of sensors;
  - the complexity of the parameter space, and the question of parameter identifiability that may arise;
  - the limited input frequency bandwidth, which is limited by the physics of the system that filters input and output data.
- The robustness with respect to model bias, that always exists as long as the class of involved models does not enable to perfectly replicate the behavior of the experimental device.
- The real-time constraint, that may necessitate the call for reduced order modeling (ROM) techniques [Chinesta et al. 2011; Benner et al. 2020] combined to parallel computing as done for instance in [Pereira Álvarez et al. 2021; Bonney et al. 2022] or [Prudencio et al. 2013].

The construction of such a DDDAS framework implies to fulfill all the previously mentioned difficulties within a single numerical framework. In this thesis, this will be done using the concept of modified Constitutive Relation Error (mCRE) as a cornerstone. Introduced by Ladevèze and co-workers in the late 1990s [Maia et al. 1994; Chouaki et al. 1997; Deraemaeker et al. 2002], the mCRE is particularly attractive as it takes simultaneously model error and measurement noise into account to perform model updating with physics-based regularization. Around this concept, the objectives targeted for this thesis are listed below:

- Establish a robust model updating strategy for correcting finite element models from datasets acquired in low-frequency dynamics, with the aim to detect and quantify structural damage,
- Extend the previous framework to sequential data assimilation for track damage propagation,
- Illustrate the benefits of adaptive data-driven model-based control for shaking table tests,
- Provide a unified numerical framework that can be operated by non-expert users.

In what follows, the preliminary validation of these objectives will systematically be done using synthetic measurements from simulated academic examples representative of earthquake engineering problems. Subsequently, the effectiveness of the proposed strategies will also be illustrated by processing actual measurements recorded during previous test campaigns at the CEA/TAMARIS facility.

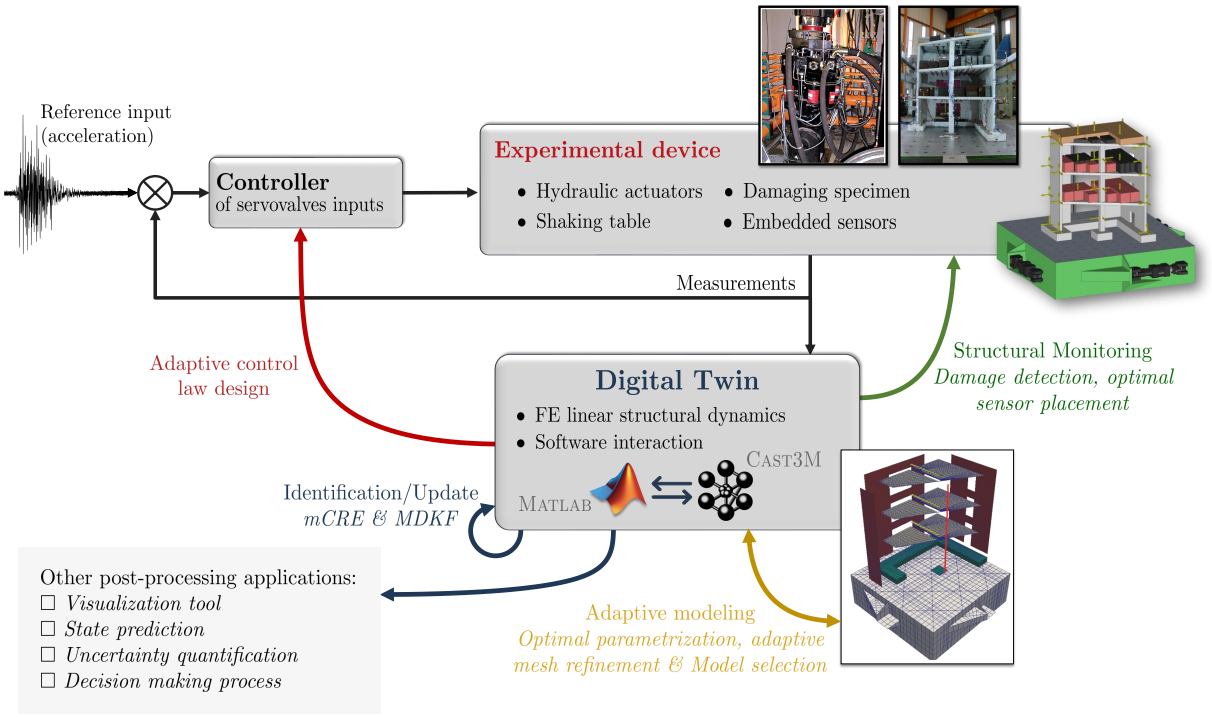

Figure 2: DDDAS framework for enhanced monitoring and control of shaking table experiments.

Letting the introduction and conclusion aside, the research work carried out during the thesis is organized in 3 parts and 5 chapters structured around the perspectives of data-to-model interaction for enhanced shaking table experiments that are illustrated in Fig. 2, as each chapter corresponds to one of the arrows connecting the digital twin to the control loop. The three parts allow to distinguish in which context the presented contributions are applicable. Besides, the state of the art is spread out among all the chapters due to the multidisciplinary dimension of the thesis subject.

The main content of each chapter is detailed in the following.

Chapter 1 proposes a brief review of offline model updating methods for finite element models, with particular attention to damage detection problems. The concept of mCRE is positionned among the state-of-the-art, and the formulation of the mCRE-based model updating problem for damage detection from linear FE models is given. After a first illustration, contributions for robust and enhanced mCRE-based model updating in low-frequency dynamics are presented, with an application to the offline processing of actual measurements from the SMART2013 test campaign.

Chapter 2 focuses on the inherent model updating limitations that have been previously observed, mostly related to parameter identifiability and sensor density. To limit their impact, a fully-automated offline model updating framework is proposed. It does not require any user intervention (once the mCRE formulation is defined). The automated procedure is validated throughout a numerical benchmark in which damage is detected at best from sparse acceleration data.

Chapter 3 is dedicated to optimal sensor placement in order to address the problem of data sparsity when discrete sensors are used for model updating. After a review of classical OSP techniques for SHM with illustrations on an academic example, a new mCRE-based sensor placement technique is proposed, based on a modified formulation of the information entropy and Fisher Information Matrix. The sensor placement results obtained on a frame structure submitted to random ground motion show the efficiency of this new placement technique and the soundness of such an approach in perspective of a DDDAS unified around the mCRE concept for SHM.

Chapter 4 addresses the core problem of extending an offline model updating algorithm to a sequential data assimilation framework. After a review on data assimilation techniques, with special attention paid to Kalman filtering techniques, a novel data assimilation technique called Modified Dual Kalman Filter is presented. The proposed strategy integrates the mCRE within a sequential process as parameters are updated according to the mCRE itself, and not only from a direct data-to-model comparison. The performance of MDKF is first assessed using synthetic measurements from a plane frame subjected to random ground acceleration. Actual measurements from the SMART2013 benchmark are then assimilated in a real-time context to monitor the eigenfrequency drop of a reinforced-concrete structure submitted to a sequence of gradually damaging shaking table tests.

Chapter 5 sets up the DDDAS framework of Fig. 2 by exploring the feasibility of mCRE-based data-driven model-based control. After emphasizing the main difficulties and approaches for the control of electrohydraulic shaking tables, a proof-of-concept on a simulated example shows that MDKF can be advantageously used to improve the quality and the safety of shaking table experiments.

Finally, general concluding remarks of this thesis are drawn, with perspectives of future works of growing complexity also mentioned.

For organizational purposes, several appendices have been included at the end of the manuscript. The recurrent earthquake engineering examples of the thesis are detailed in Appendix A. Appendices B and C provide mathematical details about the mCRE-based model updating framework presented in Chapters 1-2. Appendix D proposes an alternative presentation of Kalman filtering which can be related to Bayesian inference. Finally, Appendix E lists the contributions (publications and communications) that have been made in the context of this work.

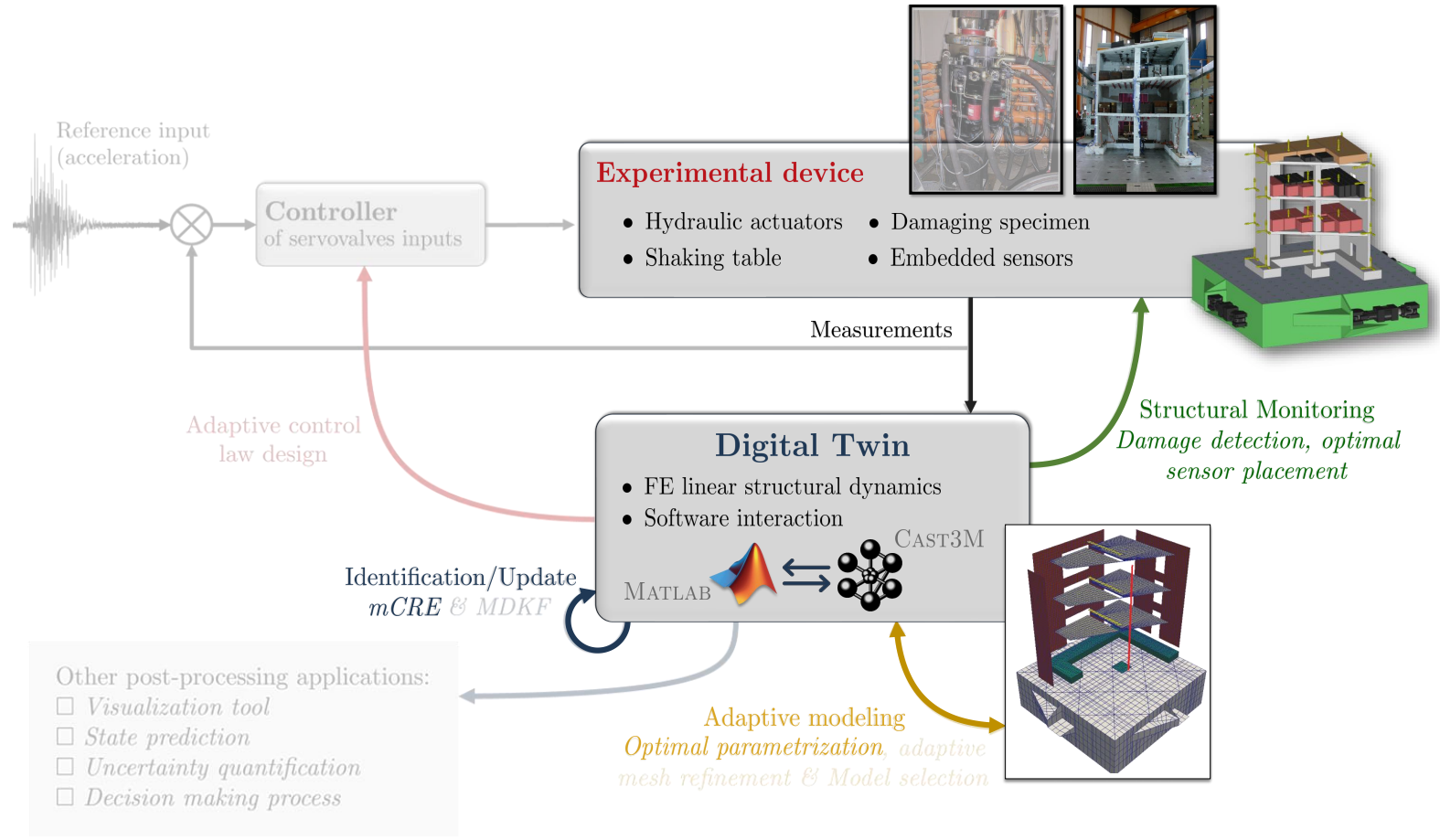

Contributions for a robust and unified model updating framework in low-frequency dynamics

---

Voilà l'homme tout entier, s'en prenant à sa chaussure alors que c'est son pied le coupable.

Samuel Beckett, *En attendant Godot*

Chapter 1

Offline model updating in low-frequency dynamics

State-of-the-art and contributions for an enhanced energy-based formulation

In this chapter, we focus on the offline model updating of finite element models from noisy discrete measurements acquired in low-frequency dynamics. After a preliminary state-of-the-art with particular attention paid to the positioning of the modified Constitutive Relation Error functional among the different standard model updating approaches, we present the associated mathematical framework and minimization algorithm. Several contributions for the enhanced robustness of the mCRE functional are then presented, mostly oriented towards the optimal management of low-SNR measurements. Lastly, the performance of the proposed methodology is shown throughout the processing of acceleration recordings from the SMART2013 test campaign, which represents a first step towards the integration and online update of FE models in shaking table control strategies.

The work presented in this chapter has been the subject of the following contributions:

M. Diaz, P.-É. Charbonnel, and L. Chamoin [2022c]. "Robust energy-based model updating framework for random processes in dynamics: application to shaking-table experiments". *Computers and Structures* 264.106746, p. 40. DOI: https://doi.org/10.1016/j.compstruc.2022.106746

M. Diaz, P.-É. Charbonnel, and L. Chamoin [2023c]. "Fully automated model updating framework for damage detection based on the modified Constitutive Relation Error". *Computational Mechanics*. DOI: 10.1007/s00466-023-02382-z

Contents

1.1 Overview of offline model updating techniques for structural health monitoring

For Structural Health Monitoring (SHM) applications, the calibration of stiffness parameters from experimental data allows to identify (*i.e.* locate and quantify) structural damage. During the last decades, a wide panel of damage detection methods has been proposed [Simoen et al. 2015; Chatzi et al. 2020; Avci et al. 2021]. For the sake of conciseness, we will exclusively focus on damage detection problems from sparse data (obtained from accelerometers, strain gauges, transducers for example) although dedicated approaches operating full-field measurements have also been developed, see [Claire et al. 2004; Helfrick et al. 2009; Curt et al. 2022] to cite a few. When dealing with sparse datasets, the identification of damage in large structures is inherently difficult because of the relatively reduced amount of available measurements, leading to an ill-posed inverse problem [Tarantola 2005].

Because many SHM applications directly exploit modal features, a parametrized model is thus not mandatory as the changes in modal features such as eigenfrequencies, damping ratios or modeshapes can provide direct information about the damage state of a structure. Their evolution with time allows the user to track structural damage [Fan and Qiao 2011]. In particular, classical modal analysis techniques aim to identify modal features through the construction of a (growing-order) state-space model from measurements [Allemang et al. 2010]. One of the most accurate methods are based on stochastic subspace identification [Overschee and Moor 1996], although alternative techniques exist for frequency-domain system identification [Guillaume et al. 2003]. These algorithms have been massively used in *Operational Modal Analysis* (OMA) techniques, that process output-only measurements from (large) structures [Peeters and De Roeck 2001; Deraemaeker et al. 2008; Reynders and Roeck 2008; Reynders et al. 2012] obtained from unknown excitations in an operational environment (*i.e.* wind or road traffic for bridges).

However, Finite Element (FE) models can still be updated according to experimental (possibly modal) data. This will be the case in the following developments as FE models of the specimen that are tested on shaking tables at the CEA/TAMARIS facility are always available (they are developed when designing test campaigns). In such a context, Bayesian/stochastic approaches (whose extended comprehensive review is available in [Simoen et al. 2015]) are classically distinguished from deterministic methods, as explained in the following.

In any case, model updating techniques aim to correct parameters $\theta \in \Theta$ of a mathematical model $\mathcal{M}$ based on a set of observed outputs y obtained under a given set of inputs e. In practice, y may contain any physical measured quantity deriving from a displacement field at sensors location (displacements, velocities, accelerations, strains), whereas the inputs e, if known, are associated to the loading (imposed displacements, forces or accelerations). Optimal parameters $\hat{\theta}$ are searched as minima of a cost-function $\mathcal{J}$ measuring the gap between measurements and associated model predictions :

$$\hat{\theta} = \arg \min_{\theta \in \Theta} \mathcal{J}\left(\mathcal{M}\left(\theta, e\right) \; ; \; y\right) \tag{1.1}$$

As all inverse problems, offline model updating problems are prone to ill-posedness (in the sense of Hadamard) and ill-conditioning issues especially because of measurement noise and model bias [Tarantola 2005]. Regularization techniques must be considered to ensure the uniqueness of the solution, by enforcing local ellipticity of the functional. Extensive literature reviews of validation/model updating approaches can be found [Mottershead and Friswell 1993; F. M. Hemez and Doebling 2001; Bonnet and Constantinescu 2005; Simoen et al. 2015].

> *Remark* 1.1. For the sake of completeness, even though not considered afterwards, let us mention damage detection techniques based on neural networks and machine learning, that are getting more and more popular due to their capability to process large amount of data [Gomes et al. 2019; Avci et al. 2021; García-Macías and Ubertini 2022]. They exploit techniques such as data fusion and statistical pattern recognition that are of growing interest

in SHM [Figueiredo and J. Brownjohn 2022]. However, they still lack of generality in the sense that results obtained by extrapolation outside the learning database may not be relevant. Also, the interpretation of results may also be difficult as data are transformed into non-physical latent spaces.

1.1.1 Deterministic model updating methods

Deterministic methods, extensively reviewed in statics/quasi-statics in [Bonnet and Constantinescu 2005] and for nonlinear transient dynamics in [F. M. Hemez and Doebling 2001] build the cost-function to be minimized as a distance from the response of the model to available measurements and overcome the ill-posedness issue using a so-called Tikhonov regularization term [Tikhonov and Arsenin 1977], containing *a priori* information $\mathcal{G}(\theta, \theta_0)$ on the parameters to identify. The gap between model and data is measured using a (non-necessary Euclidean) norm $|||\bullet|||$ taking the entire amount of available data (y, e) into account. The cost-function reads:

$$\mathcal{J}(\theta) \;=\; \Big|\Big|\Big|\mathcal{H}\left(\mathcal{M}(\theta, e)\right) - y\Big|\Big|\Big| \;+\; \frac{1}{\alpha}\mathcal{G}(\theta, \theta_0) \tag{1.2}$$

where $\mathcal{H}(\bullet)$ is the (possibly nonlinear) observation operator which allows to extract model predictions in order to compare them to the measured quantities, leading to the *data-to-model distance* $\left(\mathcal{H}\left(\mathcal{M}(\theta, e(t))\right) - y(t)\right)$. In the linear case, $\mathcal{H}$ corresponds to a projection matrix operator, whose non-zero terms allow to extract model predictions at sensor locations. The weighting coefficient α associated to the regularization term $\mathcal{G}(\theta, \theta_0)$ is directly related to the degree of confidence the user has into the prediction capability of the model to reproduce the observed data. It can be calibrated using various techniques such as the Morozov discrepancy principle [Morozov 1968] or the L-curve method [Ahmadian et al. 1998].

Modal features can be used as a reference for dynamics problems: the data-to-model distance then directly compares experimental eigenfrequencies, modeshapes and damping ratios to those predicted by the FE model. This is the case of the so-called *mode matching* methods whose cost-function includes an eigenfrequency residual combined with a *modal assurance criterion* (MAC) on modeshapes [J. Brownjohn et al. 2001]. FE model updating techniques can still be involved to correct models based on experimental modal features in dynamics: for example, the sensitivity method is a popular and powerful technique, reviewed in [Farhat and F. M. Hemez 1993; Friswell and Mottershead 1995; Mottershead et al. 2011] and applied in [Teughels and De Roeck 2005; Weber et al. 2007; Moaveni et al. 2009; Batou 2019] among many other works. It is based upon linearization of the generally nonlinear relationship between measurable outputs, such as natural frequencies, mode shapes or displacement responses and the parameters of the model in need of correction. As all deterministic inverse problems, regularization techniques are mandatory to prevent the ill-posedness of the problem [Titurus and Friswell 2008; Weber et al. 2009; C. D. Zhang and Y. L. Xu 2016].

Alternatively, direct data-to-model comparison (1.2) can be performed in the case of having a norm $|||\bullet|||$ that is Euclidean (with measurements processed in the time or frequency domains). This technique is also referred to as the weighted least-squares method [Sorenson 1970]. The interested reader can find a comparative study between modal-based and time-domain updating approaches in [Link and Weiland 2009].

1.1.2 Stochastic model updating methods

Stochastic methods, in turn, use the Bayesian inference framework to describe uncertainties on parameter estimates [Kaipio and Sommersalo 2005; Stuart 2010]. The Bayesian approach aims to improve the *prior* knowledge on the parameters *probability density function* (pdf) denoted $\pi(\theta)$ using both experimental data y and the prediction model $\mathcal{M}$ [Simoen et al. 2015]. The updating strategy is based on the eponymous Bayes theorem, which derives the *posterior* pdf $\pi(\theta|y, \mathcal{M})$ from the *prior* pdf $\pi_0(\theta)$ and the likelihood function $\pi(y|\theta, \mathcal{M})$, such that:

$$\pi(\theta|y, \mathcal{M}) \;\propto\; \pi(y|\theta, \mathcal{M})\, \pi_0(\theta) \tag{1.3}$$

The *prior* $\pi_0(\theta)$ is generally chosen based on engineering judgment and describes an initial guess of the parameters distribution in the absence of observations. If its provides an intrinsic regularization, its choice is crucial when few data are available [Van Biesbroeck et al. 2023]. The likelihood function can be interpreted as a measure of how good the set of parameters θ applied to model $\mathcal{M}$ succeeds in explaining the observations y. Optimal parameters $\hat{\theta}$ can then be recovered based on classical Maximum Likelihood Estimation (MLE) principle, i.e. such as maximizing the log of the likelihood function. The Maximum *a posteriori* principle (MAP), which considers the *posterior* pdf, can also be used. Since no assumption is made on the probability laws, the evaluation of the *posterior* pdf cannot be performed analytically (except for special cases); it is thus necessary to proceed by random selection and propagation. The computation of the likelihood function is the critical issue for stochastic approaches. For example, in a Monte-Carlo sampling framework, the number of calls to the model $\mathcal{M}$ can be too important from the numerical viewpoint, hence the coupling with Reduced Order Modelling (ROM) techniques to gain numerical efficiency. For instance, stochastic model updating methods can be combined to the Proper Generalized Decomposition (PGD) [Rubio et al. 2018] or the Proper Orthogonalized Decomposition (POD) [N.-H. Nguyen et al. 2014].

Remark 1.2. For the particular case where all random variables are assumed to be normally distributed, it can be proved that the Maximum A Posteriori (MAP) estimate defined in the Bayesian framework corresponds to the deterministic minimal solution of a least squares functional weighted by the covariance of the measurement error and enriched with a Tikhonov regularization from the *prior* pdf:

Indeed, let one postulate that the *prior* pdf $\pi(\theta)$ and the likelihood function $\pi(y|\theta)$ are both defined with Gaussian laws such that

$$\pi(\theta) \propto \exp\left[-\frac{1}{2}\left(\theta-\theta_0\right)^T \boldsymbol{\Sigma}_0^{-1}\left(\theta-\theta_0\right)\right] \tag{1.4}$$

$$\pi(y|\theta) \propto \exp\left[-\frac{1}{2}\mathcal{F}(\theta)^T \boldsymbol{\Sigma}_v^{-1}\mathcal{F}(\theta)\right] \tag{1.5}$$

where $\mathcal{F}(\theta) = \mathcal{H}\left(\mathcal{M}(\theta, e)\right) - y$ is seen as a function of θ (model, inputs, and measurements being given), $\boldsymbol{\Sigma}_0$ refers to the *a priori* parameters knowledge covariance matrix, θ_0 to the initial guess of the parameters and $\boldsymbol{\Sigma}_v = \boldsymbol{\Sigma}_m + \boldsymbol{\Sigma}_y$ to the error covariance matrix on model and measurement errors [Tarantola 2005]. Therefore, according to the Bayes theorem and the Maximum *A Posteriori* (MAP) principle, the optimal set of parameters is sought as

$$\begin{aligned}\hat{\theta} &= \arg\max_{\theta\in\Theta} \log\ \pi(\theta|y) = \arg\max_{\theta\in\Theta} \log\ \pi(y|\theta)\pi(\theta) \\ &= \arg\min_{\theta\in\Theta}\Bigg[\underbrace{\frac{1}{2}\mathcal{F}(\theta)^T\left[\boldsymbol{\Sigma}_m+\boldsymbol{\Sigma}_y\right]^{-1}\mathcal{F}(\theta)}_{\text{Weighted least-square term}} + \underbrace{\frac{1}{2}\left(\theta-\theta_0\right)^T\boldsymbol{\Sigma}_0^{-1}\left(\theta-\theta_0\right)}_{\text{Regularization term}}\Bigg]\end{aligned} \tag{1.6}$$

which leads to the typical deterministic minimization problem defined according to the formalism of (1.2) with a weighted least-square functional written as a Mahalanobis distance (the quadratic distance is weighted by the covariance error matrix). The relative weight of $\boldsymbol{\Sigma}_0$ compared to $\boldsymbol{\Sigma}_v$ defines the relative importance of the regularization term, exactly as done by α in (1.2).

Using this approach, the modeling structure is never questioned, as only a parameter set is updated. In the mCRE framework, as described in the next paragraph, an explicit model error term provides more flexibility to choose a suitable model structure from available data.

1.1.3 The modified Constitutive Relation Error in dynamics

An alternative approach consists in using the concept of *modified Constitutive Relation Error* (mCRE) that exploits the concept of reliability of information. This is the main driver behind

its selection as a reference method for model updating in this thesis. Since (i) the model structure may not be able to describe the observed phenomena, (ii) the measurement noise stored in data may significantly disrupt the update of FE models with typical least-squares functionals, and (iii) the computational burden carried by probabilistic models risks to be prohibitive for real-time prospects, a model updating cost-function with enriched physical meaning and strong mechanical content, the so-called mCRE, is preferred. The mCRE is a deterministic energy residual defined as a quadratic model-to-measurements distance enriched with a term based on the concept of *Constitutive Relation Error* (CRE) which allows to relax the unreliable information of the problem. Historically, the CRE was introduced in the 1980s for the purpose of FE verification [Ladevèze and Leguillon 1983], and extensively developed afterwards in [Ladevèze et al. 2006; Louf et al. 2010; Ladevèze and Chamoin 2011; Pled et al. 2011; Ladevèze and Chamoin 2016] among many other references. The CRE concept was later adapted for model validation [Chouaki et al. 1998] in structural dynamics to define a *modified* CRE (mCRE) residual to be minimized with respect to the updated parameters. Without going into much detail for now, the mCRE functional reads:

$$\text{mCRE}(\theta) \;=\; \text{CRE}(\theta) \;+\; \alpha \left|\left|\left| \mathcal{H}\left(\mathcal{M}(\theta, e)\right) - y \right|\right|\right|^2 \tag{1.7}$$

with the scalar α balancing the CRE and the data-to-model distance terms[1]. This energy-based residual offers interesting advantages. In particular, it improves local convexity properties compared to classical least-square functionals [Bonnet and Constantinescu 2005; Feissel and Allix 2007; Aquino and Bonnet 2019]. Besides, the CRE part of the residual, computable over the whole structure, allows to select the most erroneous areas in order to restrain the updating process to a few parameters; this is regularizing (in the Tikhonov sense), particularly when the number of parameters to update becomes important [Bui and Constantinescu 2000; Barthe et al. 2004; Charbonnel et al. 2013]. The mCRE functional has proved robustness and efficiency for model updating throughout a large number of applications involving:

- ▷ Defect detection in linear structural dynamics in beams [Faverjon et al. 2009; Waeytens et al. 2016], composites [Barbarella et al. 2016], or frame structures [Hu et al. 2017; Hu et al. 2019],
- ▷ Very noisy or even corrupted measurements [Allix et al. 2005; Feissel and Allix 2007; H.-M. Nguyen et al. 2008],
- ▷ Modal-based approaches using frequency response functions [T. Silva and Maia 2017] or additional sparse regularization [Guo et al. 2018],
- ▷ Full-field material identification in elastodynamics [Banerjee et al. 2013; Warner et al. 2014; Guchhait and Banerjee 2016; Ghosh et al. 2017; Guchhait and Banerjee 2018],
- ▷ Tolerance to incomplete boundary conditions [Bonnet and Aquino 2015; M. I. Diaz et al. 2015; Aquino and Bonnet 2019],
- ▷ Nonlinear mechanical constitutive behavior identification [Hadj-Sassi 2007; Marchand et al. 2019],
- ▷ Coupling with model order reduction techniques like reduced basis [Deraemaeker et al. 2002] or Proper Generalized Decomposition (PGD) [Bouclier et al. 2013],
- ▷ Coupling to domain-decomposition methods for enhanced flexibility in the updating process [Samir et al. 2022],
- ▷ Real-time data assimilation [Alarcon et al. 2011a; Marchand et al. 2019].

Note that the use of mCRE is not restricted to dynamics: for the sake of completeness, let us mention applications in 3D acoustics [Decouvreur et al. 2007; 2008], statics with digital image correlation measurements [Ben Azzouna et al. 2015; Ferrier et al. 2021; H. N. Nguyen et al. 2022], building thermal problems [Djatouti et al. 2020], and recent advances in multiphysics for wind turbine calibration [Roussel et al. 2022].

[1] In most papers, one will find a weighting scalar α written as $\frac{r}{1-r}$, with $r \in [0; 1[$. This reduces the range of variation of the parameter but has no particular benefit otherwise.

Regarding civil engineering applications, to the authors best knowledge, only [Oliveira et al. 2020; 2021] have used of a CRE-based cost function for the characterization of a RC wall-slab junction from hammer-shock tests, with a dedicated implementation in the FE software Cast3M© [Oliveira et al. 2022].

Eventually, it is worth noticing the closeness between the mCRE and the *Minimal Dynamic Residual Expansion* method (MDRE), developped by Balmès and co-workers in the 2000s [Bobillot and Balmès 2001]: the MDRE functional combines a modeling error and a measurement error as for the mCRE in (1.7). The model error is based on the energy norm of dynamic residual loads of model predictions (using stiffness FE matrix Euclidean norm). To overcome the data sparsity issue, the data-to-model distance of the MDRE is computed using shape expansion methods [Balmès 2000; Corus et al. 2006]. These latter allow to estimate the motion of all DoFs based on a limited set of measurements by interpolation on a well-chosen reduced basis. A similar approach has been presented for the mCRE in [Deraemaeker et al. 2002], except that the reduced basis in the MDRE must not be static and follow the parameter identification process due to the shape expansion requirements. [Balmès et al. 2022; Martin et al. 2022] have recently presented an application of MDRE to a measured brake squeal limit cycle, with 3D scaning laser Doppler vibrometry and use of the SDTools© vibration software. Particular emphasis has been put on the proximity to the mCRE[2] and to the calibration issues of the functional, especially the confidence into measurement weight α, introduced in (1.7): its miscalibration may lead to spurious identification consequences, and an iterative strategy on a wide range of values has been presented as the only sustainable approach to obtain relevant model updating results.

> *Remark* 1.3. Contrary to modal analysis techniques, the mCRE-based model updating algorithm is not restrained to the processing of linear responses of structures. However, the knowledge of the input signal is mandatory for the mCRE-based model updating methodology proposed herein, contrary to operational modal analysis techniques applied to SHM that only take advantage of output-only measurements. Besides, the explicit evaluation of a local model error indicator, namely the CRE part of the residual, provides more insight on the validity of the model itself compared to classical finite element model updating methods.

> *Remark* 1.4. The mCRE and MDRE are not the only model updating frameworks based on the reliability of information. For the sake of completeness, let us also mention the recent work of [M. Bhattacharyya and Feissel 2022] that presents a model updating technique called optimal control based on the reliability of information for Bayesian inference application in quasi-static problems. It considers full-field digital image correlation measurements and unknown boundary conditions. In this framework, the richness of local DIC measurements and the lack of knowledge on boundary conditions is such that the model constitutive law can be fully trusted, leading to a different inverse problem formulation.

1.1.4 Link between mCRE, deterministic and stochastic model updating techniques

In this paragraph, the aim is to shortly discuss the positioning and meaning of mCRE with the above-mentioned deterministic and stochastic model updating techniques.

The mCRE, a deterministic functional

Following the general equations of the previous section, one can notice that (1.7) has a very similar form as the general deterministic residual given in (1.2).

However, if at first sight, the CRE term seems to replace the user *a priori* knowledge, one should not take shortcuts on further comparisons because **the CRE is not a regularization**

[2] It was observed that the mCRE and MDRE functional are almost identical, except for a metric weighting change and a slightly different writting of the model error.

in the sense of Tikhonov! The computation of the CRE is far from being as explicit as that of a Tikhonov regularization. Besides, once the user has identified which equations are considered as "unreliable", there is no need for any additional expert-knowledge, which makes the mCRE model updating approach more independent from some user's expertise, hence its *physics-regularized* feature.

Interpretation of the mCRE from the Bayesian inference viewpoint

Although the proposed mCRE-based model updating strategy is deterministic, one can show that this procedure is equivalent to the Maximum *a posteriori* (MAP) estimation in the Bayesian inference framework with Gaussian distributions, a measurement error norm based on the measurements covariance matrix, and no *a priori* on parameters [Deraemaeker et al. 2004]. Since covariance on the modeling error is usually not known, the idea is to integrate modeling error in a more flexible manner into the Bayesian inference framework.

If one assumes that the *a priori* pdf $\pi(\theta)$ and the likelihood function $\pi(y|\theta)$ are both defined with Gaussian distributions, then it has been shown in (1.6) that optimal parameters are sought as minimizers of a functional in which appears a least-square term weighted by a combination of model and measurement error covariance matrices.

This way, the structure of the constitutive relation is imposed strongly and impacts the least-square term via the model and measurement error covariance matrices, but it is assumed to know the modeling error features, which is not the case in most problems. The value of the CRE functional is thus used to globally quantify the confidence on the less reliable parts of the model (constitutive relations in particular), into a pdf accounting for model error:

$$\pi_{CRE} \propto \exp\left[-\frac{1}{\alpha}\mathrm{CRE}(\theta)\right] \tag{1.8}$$

The confidence on the modeling exponentially decreases when the CRE value increases, with a rate speed specified by the scalar α. Therefore, in a mCRE context with a measurement error norm based on the covariance of the measurements $\mathbf{\Sigma}_y$, one can rewrite the likelihood pdf:

$$\pi(y|\theta) \propto \exp\left[-\frac{1}{2}\left(\mathcal{M}(\theta,e))-y\right)^T \mathbf{\Sigma}_y^{-1}\left(\mathcal{M}(\theta,e))-y\right)\right].\exp\left[\frac{-1}{\alpha}\mathrm{CRE}(\theta)\right] \tag{1.9}$$

Thus, if one no longer assumes any *a priori* assumption on θ (uniform pdf), the application of the MAP principle leads to:

$$\hat{\theta} = \arg\min_{\theta\in\Theta}\left[\alpha\underbrace{\left(\mathcal{M}(\theta,e))-y\right)^T \mathbf{\Sigma}_y^{-1}\left(\mathcal{M}(\theta,e))-y\right)}_{|||\mathcal{H}\left(\mathcal{M}(\theta,e)\right)-y|||} + \mathrm{CRE}(\theta)\right] \tag{1.10}$$

where one easily recognizes the sum of a model error (the CRE) with a data-to-model distance to minimize. It thus illustrates that the mCRE metric can be naturally derived from the Bayesian inference framework.

1.2 FE formulation of the mCRE-based model updating problem in dynamics

This section intends to provide more details on the model updating framework considered in the remainder of the thesis, namely the calibration of FE-based stiffness macromodels using the mCRE written in the frequency domain. For the sake of conciseness, we will directly go through the FE discretized formulation of the model updating problem. The interested reader will find complementary details about the continuous formulation of the presented mCRE-based model updating problem in [Charbonnel et al. 2013; M. Diaz et al. 2022c].

1.2.1 Reference dynamics problem, data and parameter space

Frequency domain dynamical equilibrium

Let us consider the general case of an elastic structure Ω spatially discretized in finite elements such that $\Omega = \cup_{e=1}^{E} \Omega_e$, and subjected to a given dynamical excitation during a given time interval $[0;T]$. $\boldsymbol{K}, \boldsymbol{D}, \boldsymbol{M}$ denote the stiffness, damping and mass FE matrices, respectively, while $F(t)$ and $U(t)$ are the nodal loading conditions and displacement field at a given instant t. With these notations, the dynamical equilibrium reads for all $t \in [0;T]$:

$$\boldsymbol{M}\ddot{U}(t) + \boldsymbol{D}\dot{U}(t) + \boldsymbol{K}U(t) = F(t) \tag{1.11}$$

For a structure submitted to a given ground motion acceleration $\ddot{U}_d$, if one notes F_ω and U_ω the frequency counterparts of F and U, the dynamical equilibrium in the frequency domain for a given angular frequency ω is:

$$\left[-\omega^2\boldsymbol{M} + i\omega\boldsymbol{D} + \boldsymbol{K}\right] U_\omega = \omega^2\boldsymbol{M}\boldsymbol{\Xi}U_{d,\omega} = F_\omega \tag{1.12}$$

where $\boldsymbol{\Xi}$ is a matrix addressing the acceleration ground motion to the associated degrees of freedom (DoF).

Measurements

In addition, a set of sensors is assumed to be scattered over the considered structure. Measurements are often associated to the unknown displacement field U or its time and space derivatives. Excitation forces or actuator state variables may also be available. In practice, the dataset of observed outputs may contain any physical measured quantity deriving from a displacement field at sensors location (displacements, velocities, accelerations, strains, etc.), whereas inputs F, if measured, are associated to the loading (imposed displacements, forces or accelerations).

In the frequency domain, assuming for the moment that measurements are perfect (*i.e.* noise-free), such information can be written without loss of generality as:

$$\boldsymbol{\Pi}U_\omega = Y_\omega \tag{1.13}$$

where Y_ω refers to the frequency counterpart of measurements at angular frequency ω and $\boldsymbol{\Pi}$ denotes an observation matrix that allows to extract the components of U_ω that are measured. It corresponds to the linearization of $\mathcal{H}$ in the frequency domain - see (1.2). For displacement, velocity or acceleration measurements, its non-zero values are integer powers of $(i\omega)$. The matrix of FE shape functions gradient can also be involved in case strain is measured, for instance with strain gauges or optical fibers.

> *Remark* 1.5. It will be assumed that the position of sensors is perfectly known in the following, and that all sensor locations perfectly correspond to a node in the associated FE mesh. It avoids the necessity to interpolate measurements on the mesh closest nodes with FE shape functions.

Stiffness parametrization

As mentioned in the introduction, one can interpret damage as local stiffness loss [Cawley and Adams 1979]. Therefore, a convenient manner to parametrize a linear FE problem for damage detection is to parametrize the FE stiffness matrix. In this work, it is thus chosen to focus correcting actions only on structural stiffness properties. Doing so, the N_θ parameters to update $\theta \in \Theta \subset \mathbb{R}^{N_\theta}$ only affect the stiffness matrix $\boldsymbol{K}$. More precisely, the FE stiffness matrix is decomposed into n_θ non-overlapping subdomains and parametrized as follows:

$$\boldsymbol{K}(\theta) = \sum_{i=1}^{N_\theta} \frac{\theta_i}{\theta_{0,i}} \boldsymbol{K}_{0,i} \quad \text{with} \quad \boldsymbol{K}(\theta_0) = \sum_{i=1}^{N_\theta} \boldsymbol{K}_{0,i} \tag{1.14}$$

This approach is common for model updating problems relying on component mode synthesis [Papadimitriou and Papadioti 2013]. Note that the subdomains can perfectly match with finite elements or gather some of them to reduce the number N_θ of parameters to identify. For example, a typical macro-parametrization for a building model is given in Appendix A, Fig. A.4.

Besides, a current practice for correcting frequency response functions (FRF) in low-frequency dynamics consists in updating stiffness parametrization first to update eigenfrequencies, before updating damping parameters in a second step: this allows to correct eigenfrequencies before the narrowness the resonant peaks. Eventually, mass properties are very often well-identified compared to stiffness and damping properties, even though the original mCRE framework allows to update all properties at once [Chouaki et al. 1998].

1.2.2 The modified CRE: a physics-regularized approach for inverse problems

Reliability of information and CRE

The key idea for the construction of the CRE residual lies into the distinction between reliable and unreliable information on the reference mechanical problem. The mCRE concept extends this distinction to experimental data as well, allowing to build a functional able to simultaneously handle measurement error and model uncertainty.

Practically, the redundant information gathered in (1.12) and (1.13) means all equations cannot be exactly verified: taking the measurements as additionnal boundary conditions overspecifies the mechanical reference problem. Besides, from an experimental point of view, the knowledge of the frequency complex amplitudes of inputs and outputs is subjected to uncertainties because of measurement noise, finite nature of the recordings, sampling process, sensors offset or miscalibration, anti-aliasing filters, etc. Therefore, some equations of the problem must be considered less reliable, and thus relaxed as they will be only verified at best when minimizing the mCRE functional.

In other words, the fundamental idea of the mCRE concept is to compute mechanical fields and material parameters that are a trade-off between all available information without adding any other *a priori* assumption. Although this distinction between reliable and unreliable equations is not unique and deeply relies on the case study and engineering expertise, it is also well-known that, in most applications, constitutive relations are subject to caution. The full separation of equations for the considered damage detection problem is given in Tab. 1.1.

	Reliable	**Unreliable**
Model	▷ Geometry ▷ Boundary conditions ▷ Equilibrium equations ▷ Dissipative and inertial constitutive relations	▷ Elastic constitutive relations
Experiments	▷ Loading frequencies $\omega/2\pi$ ▷ Sensor locations ▷ Measured inputs F_ω	▷ Measured outputs Y_ω

TABLE 1.1: Distinction between reliable and unreliable information for damage detection from stiffness update in dynamics.

> *Remark* 1.6. The distinction made in Tab. 1.1 is the only step involving strong user decision making, contrary to traditional deterministic model updating functionals whose regularization term is fully determined by some user's *a priori* knowledge.

With the above notations, the CRE at a given angular frequency ω reads:

$$\zeta_\omega^2(s_\omega,\theta) = \frac{1}{2}(U_\omega - V_\omega)^H \boldsymbol{K}(\theta)(U_\omega - V_\omega) = \frac{1}{2}\|U_\omega - V_\omega\|^2_{\boldsymbol{K}(\theta)},\ s_\omega = (U_\omega, V_\omega) \tag{1.15}$$

with U_ω a kinematically admissible displacement field ($U_\omega \in \mathcal{U}_{ad}$), which satisfies the reliable kinematic equations of the problem, and V_ω an auxiliary dynamically admissible displacement field ($V_\omega \in \mathcal{D}_{ad}$) derived from the stress field and satisfying the dynamical equilibrium. Mathematically, U_ω and V_ω are related such that:

$$[-\omega^2 \boldsymbol{M} + i\omega \boldsymbol{D}]U_\omega + \boldsymbol{K}(\theta)V_\omega = F_\omega \quad \forall\, \omega \tag{1.16}$$

Integration of measurements: the mCRE

The extension of the CRE concept to unreliable experimental data directly leads to the so-called *modified Constitutive Relation Error* (mCRE). The CRE is completed by a data-to-model distance between the predictions U_ω and the frequency counterpart of measurements Y_ω :

$$e_\omega^2(s_\omega, \theta; Y_\omega) \triangleq \zeta_\omega^2(s_\omega, \theta) + \frac{\alpha}{2}\left\|\Pi U_\omega - Y_\omega\right\|_{\boldsymbol{G}}^2 \tag{1.17}$$

In terms of notations:

- ▷ The CRE $\zeta_\omega^2(s_\omega, \theta)$ measures the closeness of the mechanical displacement fields (U_ω, V_ω) in the sense of the strain energy. U_ω satisfies the reliable kinematic equations of the problem (boundary conditions, closeness to measurements as involved in the data-to-model distance) and V_ω is constrained to satisfy the dynamical equilibrium of the problem. In practice, s_ω is obtained by solving a constrained optimization problem for all ω (for a given parameter set θ):

$$s_\omega(\theta; Y_\omega) = \arg \min_{s_\omega = (U_\omega, V_\omega)} \left[e_\omega^2(s_\omega, \theta; Y_\omega)\right] \text{ s.t. } [-\omega^2 \boldsymbol{M} + i\omega \boldsymbol{D}]U_\omega + \boldsymbol{K}(\theta)V_\omega = F_\omega \tag{1.18}$$

  The minimization of the mCRE with respect to mechanical fields under the dynamical equilibrium constraint is performed using a classical Lagrange multiplier vector Λ_ω and an associated augmented cost function defined for each angular frequency ω:

$$\begin{aligned} \mathcal{L}_\omega(U_\omega, V_\omega, \Lambda_\omega, \theta; Y_\omega) &= e_\omega^2((U_\omega, V_\omega), \theta; Y_\omega) \\ &+ \Re(\Lambda_\omega)^T \Re\left[\left[-\omega^2 \boldsymbol{M} + i\omega \boldsymbol{D}\right] U_\omega + \boldsymbol{K}(\theta)V_\omega - F_\omega\right] \\ &+ \Im(\Lambda_\omega)^T \Im\left[\left[-\omega^2 \boldsymbol{M} + i\omega \boldsymbol{D}\right] U_\omega + \boldsymbol{K}(\theta)V_\omega - F_\omega\right] \end{aligned} \tag{1.19}$$

  The stationarity of $\mathcal{L}_\omega$ with respect to the fields $(U_\omega, V_\omega, \Lambda_\omega)$ leads to the solution of a linear system (the proof is given in Appendix B):

$$AX = b \text{ with } \begin{cases} A &= \begin{bmatrix} \boldsymbol{Z}(\theta)^H & \alpha \boldsymbol{\Pi}^H \boldsymbol{G} \boldsymbol{\Pi} \\ -\boldsymbol{K}^H(\theta) & \boldsymbol{Z}(\theta) \end{bmatrix} \\ X &= \begin{Bmatrix} \Lambda_\omega \\ U_\omega \end{Bmatrix} = \begin{Bmatrix} U_\omega - V_\omega \\ U_\omega \end{Bmatrix} \\ b &= \begin{Bmatrix} \alpha \boldsymbol{\Pi}^H \boldsymbol{G} Y_\omega \\ F_\omega \end{Bmatrix} \end{cases} \tag{1.20}$$

  where $\boldsymbol{Z}(\theta) = \boldsymbol{K}(\theta) + i\omega \boldsymbol{D} - \omega^2 \boldsymbol{M}$ is the dynamical impedance of the structure.

- ▷ The data-to-model distance is a Hermitian norm of the gap between model predictions U_ω with measurements Y_ω. $\boldsymbol{G}$ is a symmetric positive-definite matrix guaranteeing that $\|\square\|_{\boldsymbol{G}}^2$ is homogeneous to ζ_ω^2 and equivalent in level. The choice of $\boldsymbol{G}$ is not critical: a classical choice for $\boldsymbol{G}$ is to use the Guyan reduction of the initial stiffness operator condensed on the sensors locations [Deraemaeker et al. 2002]. Herein, $\boldsymbol{G}$ is chosen proportional to the identity matrix and weighted by the strain energy stored in the first (involved) eigenmodes. Lastly, the tuning factor $\alpha \in \mathbb{R}^+$ enables one to give more or less confidence to the measurements; large values can be specified when measurements are considered reliable whereas close-to-zero values are better suited to corrupted or noisy recordings. The

choice of α is therefore crucial for providing relevant parameter estimates. Its optimal calibration has been deeply studied in [Warner et al. 2014; Balmès et al. 2022], with attention paid to its dependency on the measurement noise level if known. Automated techniques for its optimal tuning will be discussed in the next chapters following the developments initiated in [M. Diaz et al. 2022c; 2023c].

Remark 1.7. Working in the frequency domain with linear FE models allows to solve the adjoint-state problem classically encountered in the time-domain mCRE formulation with a simple matrix system (1.20). As observed in the next sections, the CPU cost for solving such problems is not expensive. In quasi-statics or transient mechanics [Chamoin et al. 2014; Djatouti et al. 2020], the mCRE adjoint-state problem also writes as a matrix system to solve. However, a general time-domain formulation implies the solution of a retrograde time problem to get the adjoint-state vectors [H.-M. Nguyen et al. 2008; Marchand et al. 2019], which is an expensive task from the numerical viewpoint.

Remark 1.8. Note that the damping modeling will not be subject to caution as damping variations are secondary for damage detection. However, note that an analogous formulation can be written when casting doubt on the dissipative part of the constitutive relations, the mCRE being a well-suited functional for updating damping properties [Deraemaeker et al. 2002]. In practice, an additional field (often denoted W_ω) is added and allows to write a dissipation error $\|U_\omega - W_\omega\|^2_{\boldsymbol{D}(\theta)}$ that completes the error on the elastic part of the constitutive relations. As a consequence, the dynamical equilibrium constraint to satisfy writes: $-\omega^2 \boldsymbol{M} U_\omega + i\omega \boldsymbol{D} W_\omega + \boldsymbol{K} V_\omega = F_\omega$. A similar system would be obtained if mass properties were updated as well. Measured forces are not considered herein neither, but can also be integrated, as explained in [Charbonnel et al. 2013].

mCRE in low-frequency dynamics

Eventually, it turns out that the analysis of a single angular frequency is too restrictive in low-frequency dynamics, particularly when several eigenmodes are simultaneously involved in the response of the structure. The model updating procedure must be conducted on a frequency bandwidth D_ω which contains essential information about the response of the structure. The mCRE functional $\mathcal{J}$ to be minimized is thus obtained by direct integration over D_ω:

$$\mathcal{J}(\theta, Y) = \int_{D_\omega} z(\omega) e^2_\omega(\widehat{s}(\theta; Y_\omega), \theta, Y_\omega) \, \mathrm{d}\omega \tag{1.21}$$

where $\widehat{s}(\theta; Y_\omega)$ refers to the optimal mechanical solution for given parameters and measurements in the sense of (1.20). $z(\omega)$ is a frequency weighting normalized function such that $\int_{D_\omega} z(\omega) \, \mathrm{d}\omega = 1$ allowing to modulate the importance of specific frequencies of D_ω. An appropriate manner to define $z(\omega)$ in low-frequency dynamics is discussed in Section 1.4.

For most earthquake engineering problems, the largest part of relevant information is transmitted below 50 Hz. Moreover, as eigenfrequency peaks of frequency response functions are well-separated, one could only compute a mCRE functional as the sum of the contributions associated with the natural frequencies within the interval $[0 \text{ Hz}; 50 \text{ Hz}]$. Although appealing at first sight, this approach reveals to be too restrictive as soon as a significant model bias occurs and that the natural frequencies provided by the FE model do not correctly match with those of the real structure. This is particularly the case for the forthcoming application to the update of the SMART2013 FE model (see Section 1.5). In the following, D_ω will thus correspond to a uniformly discretized frequency range within $[0 \text{ Hz}; 50 \text{ Hz}]$.

The model updating problem

In summary, optimal parameters $\hat{\theta}$ are searched as minima of the mCRE functional

$$\hat{\theta} \;=\; \arg\min_{\theta \,\in\, \Theta} \left[\mathcal{J}(\theta; Y) \;\triangleq\; \int_{D_\omega} z(\omega) e_\omega^2(\widehat{s}(\theta; Y_\omega), \theta, Y_\omega)\, \mathrm{d}\omega \right] \tag{1.22}$$

and the evaluation of the mCRE for a given value of θ requires to solve a matrix system for all $\omega \in D_\omega$ to obtain the optimal mechanical fields $\{\widehat{s}_\omega\}_{\omega \in D_\omega}$. The nested interaction between these minimization problems (resp. on θ and s_ω) can be mathematically emphasized by writting the overall mCRE-based model updating problem as follows:

$$\hat{\theta} \;=\; \arg\min_{\theta \,\in\, \Theta} \left[\int_{D_\omega} z(\omega)\, e_\omega^2\Big(\arg \min_{\substack{[-\omega^2 \boldsymbol{M} + i\omega \boldsymbol{D}] U_\omega + \\ \boldsymbol{K}(\theta) V_\omega = F_\omega}} \left[e_\omega^2(U_\omega, V_\omega, \theta; Y_\omega) \right], \theta, Y_\omega \Big)\, \mathrm{d}\omega \right] \tag{1.23}$$

Remark 1.9. The mCRE-based model updating problem can also be geometrically visualized by manifold representations [H. N. Nguyen et al. 2022], as presented in Fig. 1.1. To do so, two manifolds of full time-space mechanical solutions s must be defined:

- ▷ A manifold (A_d), in which any solution s satisfies the considered reliable equations (s is then said admissible).
- ▷ A manifold (Γ_Y^θ) generated by the parametrized constitutive relations model and noisy observations.

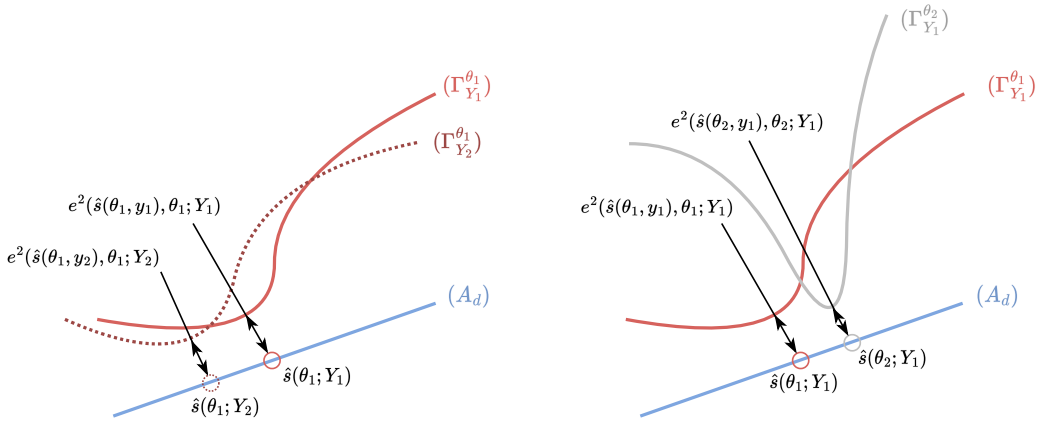

FIGURE 1.1: Geometrical interpretation of the mCRE functional using manifolds, with emphasis on the effects of measurement realization and parameter variations.

Due to the presence of noise in data and modeling bias, nothing guarantees the existence of an intersection between (A_d) and (Γ_Y^θ). In this framework, the mCRE (at fixed θ and Y) represents the minimal distance between these manifolds. As (A_d) in our case is made of linear equations, it has been represented by a blue straight line in Fig. 1.1, contrary to (Γ_Y^θ). The effects of measurement realization and parameter variations on the mCRE are illustrated to recall that (i) the model updating results are always an indirect function of the data, and (ii) when changing parameters value, mechanical fields need to be recomputed accordingly.

1.2.3 mCRE-based model updating algorithm

From the numerical viewpoint, the nonlinear problem (1.23) is solved recursively as the limit of the sequence $\left(\theta^{(k)}\right)_k$ in an iterative localization/correction algorithm for which a detailed pseudo-code is given in Alg. 1.1. Key numerical ingredients for efficient mCRE computation and minimization are detailed below.

Efficient mCRE computation

According to (1.23), the key operation that must be efficiently performed is the solution of system (1.20). Indeed, the only evaluation of the mCRE functional for a given parameter set θ requires to solve $\#D_\omega$ matrix systems whose matrix A is explicitly function of ω and possibly of large size (twice the number of DoFs $2N_u$).

First, parallelization techniques can be used to significantly save CPU time. The solution of system (1.20) for all frequencies in D_ω can be easily parallelized using new in-core page-wise left matrix divide function `pagemldivide` (available since MATLAB© 2022a release).

However, such techniques may still not be efficient enough as the size of the vector X is twice the number of DoF N_u. A manner to drastically reduce the size of the $AX = b$ system consists in projecting the latter in a well-chosen reduced basis [Deraemaeker et al. 2002; Charbonnel et al. 2013; M. Diaz et al. 2022c]. Typically, a projection on a truncated modal basis made of the L first eigenmodes is used to reduce the size and thus the computational cost of the solution of (1.20). An appropriate choice for L can be made such that $\omega_L \gg 2\pi \max(D_\omega)$ and $L \ll N_u$, where ω_L is the eigenfrequency of mode L. To improve the quality of the approximation, a series of so-called Krylov vectors associated with the current excitation or sensor locations might be added to the reduced basis (see [Deraemaeker et al. 2002] for further details). If $\boldsymbol{\Phi}_L$ denotes the reduced basis and $U_{r,\omega}, V_{r,\omega}$ the reduced mechanical fields, then the system (1.20) is simplified as follows:

$$A_r X_r = b_r \text{ with } \begin{cases} A_r &= \begin{bmatrix} \left[\boldsymbol{\Phi}_L^T \boldsymbol{Z}(\theta) \boldsymbol{\Phi}_L\right]^H & \alpha[\boldsymbol{\Pi}\boldsymbol{\Phi}_L]^H \boldsymbol{G} [\boldsymbol{\Pi}\boldsymbol{\Phi}_L] \\ -\left[\boldsymbol{\Phi}_L^T \boldsymbol{K}(\theta) \boldsymbol{\Phi}_L\right]^H (\theta) & \boldsymbol{\Phi}_L^T \boldsymbol{Z}(\theta) \boldsymbol{\Phi}_L \end{bmatrix} \\ X_r &= \begin{Bmatrix} \Lambda_{r,\omega} \\ U_{r,\omega} \end{Bmatrix} = \begin{Bmatrix} U_{r,\omega} - V_{r,\omega} \\ U_{r,\omega} \end{Bmatrix} \\ b_r &= \begin{Bmatrix} \alpha[\boldsymbol{\Pi}\boldsymbol{\Phi}_L]^H \boldsymbol{G} Y_\omega \\ \boldsymbol{\Phi}_L^T F_\omega \end{Bmatrix} \\ U_\omega &= \boldsymbol{\Phi}_L U_{r,\omega} \\ V_\omega &= \boldsymbol{\Phi}_L V_{r,\omega} \end{cases} \tag{1.24}$$

> *Remark* 1.10. The projection of (1.20) using a reduced basis is not the only manner to accelerate mCRE computations. For instance, alternative techniques use a PGD description of the mechanical fields [Marchand et al. 2016], or iterative solvers such as the successive over-relaxation algorithm [Banerjee et al. 2013].

Localization of most erroneous areas

The CRE provides a direct insight regarding the validity of the model itself, making it a relevant tool for identifying erroneous parts of the model due to the possibility to compute all finite element contributions to the CRE independently. In particular, the CRE per subdomain S_i (one subdomain is affected by one parameter θ_i) reads:

$$\forall\, i \in [\![1; N_\theta]\!], \quad \zeta^2_{\omega,i}(s_\omega, \theta) = \sum_{e \subset S_i} \frac{1}{2} \left\| U_\omega - V_\omega \right\|^2_{\boldsymbol{K}_e(\theta)} \tag{1.25}$$

where $\boldsymbol{K}_e(\theta)$ is the contribution of element e to the overall stiffness matrix $\boldsymbol{K}$. This asset can be seen as a Tikhonov regularization in the mCRE framework in the sense that a restrained number of parameters can be updated [Deraemaeker et al. 2002; Charbonnel et al. 2013]. Indeed, defining a threshold $\beta \in [0; 1]$, one can identify subdomains to update such that they satisfy the following inequality:

$$i \in [\![1; N_\theta]\!] \text{ s.t. } \frac{1}{|S_i|} \int_{D_\omega} z(\omega) \zeta^2_{\omega,i}(s_\omega, \theta)\, \mathrm{d}\omega \geqslant \beta \max_{i \in [\![1; N_\theta]\!]} \left\{ \frac{1}{|S_i|} \int_{D_\omega} z(\omega) \zeta^2_{\omega,i}(s_\omega, \theta)\, \mathrm{d}\omega \right\} \tag{1.26}$$

where the normalization by the size of subdomains $|S_i|$ permits to fairly compare subdomains of various sizes. Eventually, if most references consider that $\beta = 0.8$ is a convenient empirical value, no clear parametric study has been performed in order to optimize the choice of β for optimal parameter identification.

Minimization strategy

The nonlinear optimization of the mCRE functional with respect to the parameters is done in practice using a classical BFGS minimization algorithm. Here, the `fminunc` function of the MATLAB© optimization toolbox has been exploited to perform all minimizations. A quasi-Newton algorithm is used, with possibility to specify an objective function gradient. As shown in [Charbonnel et al. 2013], the computational burden associated to the minimization algorithm can be largely improved by suppling an analytical gradient of the functional with respect to the updated parameters. Fortunately, the mCRE gradient with respect to the parameters, the mechanical state, and the mCRE Hessian matrix with respect to parameters have (semi-)analytical expressions.

With the above stiffness parametrization, the mCRE gradient with respect to parameters reads (for a given angular frequency ω):

$$\nabla_{\theta_j} e_\omega^2(s_\omega, \theta; Y_\omega) = \frac{1}{2}\left\|U_\omega - V_\omega\right\|^2_{\boldsymbol{K}_{0,j}} + \Re\left((U_\omega - V_\omega)^H \boldsymbol{K}_{0,j} V_\omega\right) \tag{1.27}$$

where $\Re(\square)$ denote the extraction of real part of $\square$. This result directly derives from the adjoint-state problem written in the frequency domain. The interested reader will find all mathematical developments to obtain such an expression in Appendix B.

Monitoring the convergence with combined stopping criteria

The FE mesh density and the size of the structure strongly depend on the studied problem, and therefore have much incidence on the mCRE numerical value. In order to robustly assess the convergence of the method, a normalization term is defined at the first iteration of the algorithm, leading to a normalized cost-function $\overline{\mathcal{J}}$:

$$\overline{\mathcal{J}}(\theta; Y) = \frac{\mathcal{J}(\theta)}{\mathcal{J}_0(\theta_0; Y)} \tag{1.28}$$

$$\text{with } \mathcal{J}_0(\theta_0; Y) = \int_{D_\omega} \frac{z(\omega)}{2} \|U_\omega^{(0)} + V_\omega^{(0)}\|^2_{\boldsymbol{K}(\theta^{(0)})} \, \mathrm{d}\omega$$

The convergence can be assessed at the k^{th} iteration according to two criteria based on the normalized cost function value and on the stationarity of the optimal parameters:

$$\overline{\mathcal{J}}(\theta^{(k)}; Y) \leqslant \epsilon_1 \tag{1.29}$$

$$\left|\theta^{(k)} - \theta^{(k-1)}\right| \leqslant \epsilon_2 \left|\theta^{(k-1)}\right| \tag{1.30}$$

Appropriate values for the thresholds ϵ_1 and ϵ_2 are between 10^{-6} and 10^{-4}. They must be defined jointly and consistently, depending on (i) the *a priori* assumed accuracy of the model to update and (ii) the noise level in measurements (if known). Once one of the two previous criteria is met, the algorithm is stopped assuming its convergence (see Alg. 1.1).

The algorithm

The mCRE-based standard minimization algorithm is presented in Alg. 1.1. Note that no clue has been given yet for the calibration of internal parameters. Exhaustive details regarding that point will be given in Section 1.4. The idea at this point is to already have a general understanding of the algorithmic structure that is required to perform parameter identification using the mCRE functional.

Algorithm 1.1: Standard mCRE-based model updating strategy.

Data: FE model including mesh and matrices $\boldsymbol{K}, \boldsymbol{D}, \boldsymbol{M}$, subdomain decomposition and associated initial parameter guess $\theta^{(0)} \in \Theta$, measurements y.
Result: Updated set of parameters $\hat{\theta}$.

Preamble & initialization

Computation of the reduced basis $\boldsymbol{\Phi}_L$;
Frequency-domain data preprocessing: $Y_\omega \; \forall \, \omega \in D_\omega$;
Choice of the confidence into measurements weight α and thresholds $\epsilon_1, \epsilon_2, \beta$;
Computation of the frequency weighting function $z(\omega)$;
Evaluation of the initial quality of the model: $\mathcal{J}_0(\theta_0; Y)$;

Model updating algorithm

while $\overline{\mathcal{J}}\left(\theta^{(k)}\right) \leqslant \epsilon_1$ *and* $\left|\theta^{(k)} - \theta^{(k-1)}\right| \leqslant \epsilon_2 \left|\theta^{(k-1)}\right|$ **do**

Step 1: Localization of the most erroneous areas
Solution of the matrix system (1.24) $\forall \, \omega \in D_\omega$;
Computation of $\zeta^2_{\omega,i}\left(s_\omega, \theta^{(k)}\right) \; \forall \left(\omega, i\right) \in \left(D_\omega \times [\![1; N_\theta]\!]\right)$;
Identification of the most erroneous subdomains using (1.25) ;

Step 2: Correction
Minimization of $\mathcal{J}(\theta) : \theta^{(k+1)} \leftarrow \theta^{(k)}$ with respect to the identified parameters from Step 1 (BFGS method with supplied gradient - see (1.27)) ;

Step 3: Convergence assessment
Convergence criteria computation: $\overline{\mathcal{J}}(\theta^{(k+1)})$ and $\left|\frac{\theta^{(k+1)} - \theta^{(k)}}{\theta^{(k)}}\right|$;

end

1.3 Numerical implementation for a two-story plane frame submitted to random ground motion

The objective of this section is to propose a first illustration of the capabilities of mCRE-based model updating on a typical earthquake engineering example. A two-story plane frame that is submitted to a random ground motion is considered (see Fig. 1.2). Complete explanations about FE modeling and measurements simulation are provided in Appendix A.1.

What must be kept in mind is that measurement noise is added to the simulated data (the measurement noise level is denoted δ) obtained with a parameter set $\theta^\star$, that is assumed unknown. The objective is to recover this set of parameters starting from an initial guess θ_0 using the mCRE functional. Six (dimensionless) parameters are updated in this example, one per wall and per slab of the frame structure, all initialized at 1 (see Tab. 1.2).

	Healthy ref.	Damaged modulus in W10	Initial guess
Young's moduli [GPa]	33	20	30
Associated parameters [−]	1.1	0.67	1.0

TABLE 1.2: Material properties of the frame (actual configuration and initial guess).

1.3.1 Reference model updating results

When dealing with ideal noise-free measurements, the model updating procedure converges quickly to the expected parameters as shown in Fig. 1.4-1.3, illustrating the efficiency of the methodology to identify stiffness parameters from sparse measurements and to improve the correlation with reference FRFs (see Fig. 1.3). The analysis has been conducted within the frequency interval $D_\omega = [0 \text{ Hz}; 30 \text{ Hz}]$ with a 0.1 Hz step discretization so as to correctly capture the contribution of the three first eigenmodes of the specimen. A reduced basis involving the first 10 modes was used to compute the mCRE quickly and accurately. The frequency weighting

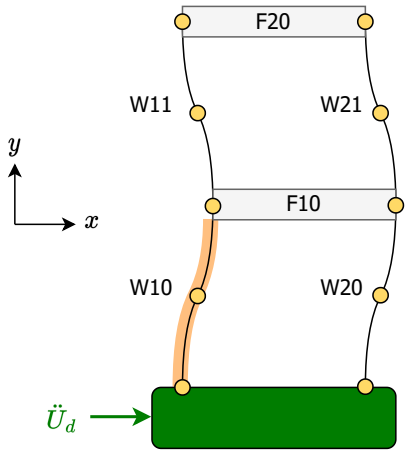

FIGURE 1.2: Plane frame with sensor locations (yellow dots), subdomains labels, and damaged area W10 highlighted in orange.

$z(\omega)$ has been chosen as uniform by default: $z(\omega) = 1/\#D_\omega \; \forall \; \omega \in D_\omega$. If not precised, α is chosen equal to 1 by default.

A last result showing the convexity of the mCRE compared to the measurement error taken alone is proposed in Fig. 1.5 when trying to update the W10 parameter alone assuming all other parameters are already well calibrated. It illustrates how the CRE term drastically improves the convexity of the functional.

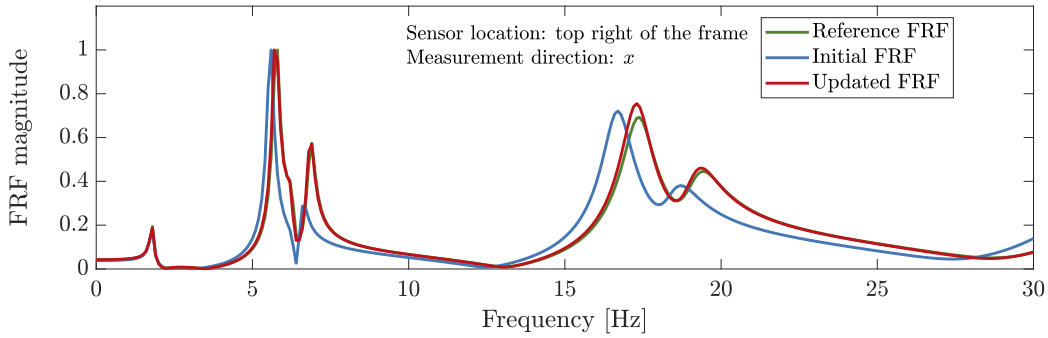

FIGURE 1.3: Experimental, initial and updated frequency response function (FRF) from a sensor located at the top of the frame.

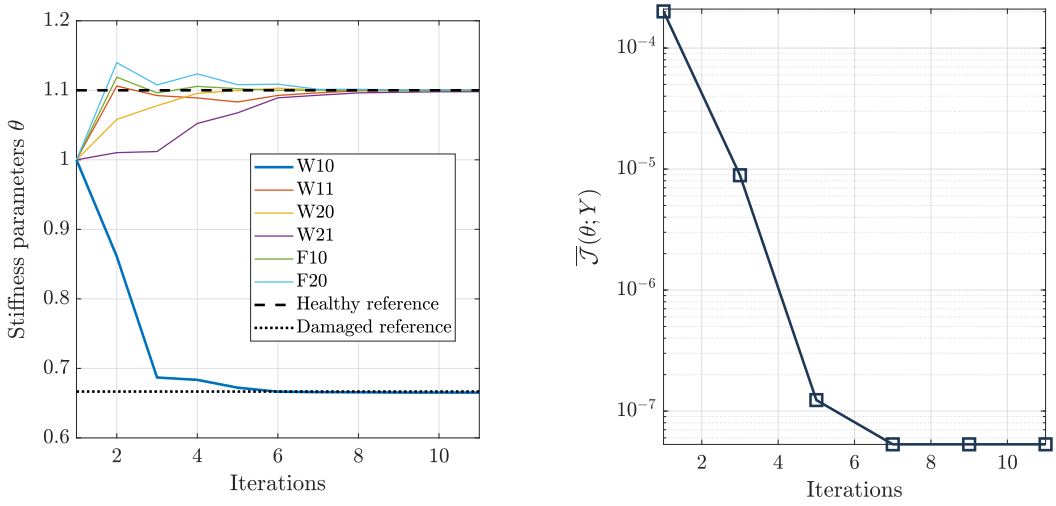

FIGURE 1.4: Plane frame mCRE-based model updating: evolution of the stiffness parameters and associated mCRE-based functional with iterations.

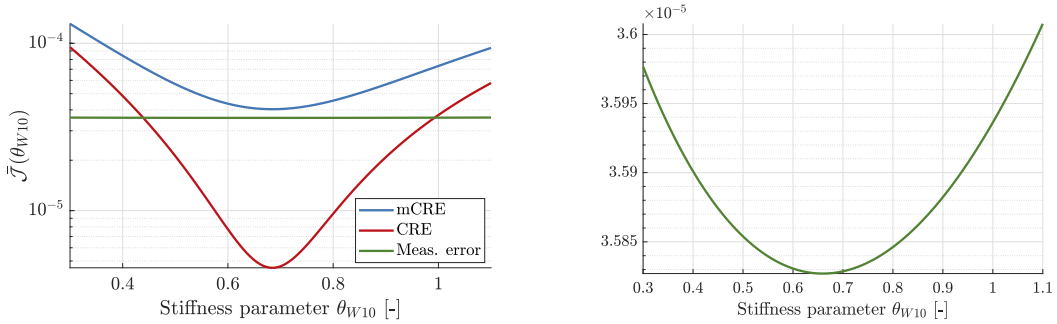

FIGURE 1.5: Plot of the mCRE functional with respect to W10 parameter, illustrating enhanced convexity due to the CRE term. The measurement error term taken alone yet remains convex.

1.3.2 Supplied analytical gradient for enhanced numerical performance

As shown above, the mCRE gradient with respect to the parameters has an analytical expression depending on the current mechanical fields $\{\widehat{s}_\omega(\theta)\}_{\omega\in D_\omega}$ and on the derivatives of the stiffness FE matrix $\boldsymbol{K}$ with respect to updated parameters. Note that these derivatives may not be simple to calculate for structural parameters (thicknesses or geometry parameters for instance). However, in any case, and particularly for the studied parametrization (1.14), the above-written analytical expressions avoid the numerical computation of the gradient (by finite difference approximation) which allows for large CPU time savings, as shown in Tab. 1.3 where CPU times, number of mCRE functional evaluations, and number of iterations are compared for several measurement noise levels. It illustrates the fact that for the same identification accuracy (relative L_2 distance between $\hat{\theta}$ and $\theta^\star$), even for a low-dimensional simple identification problem, significant numerical improvements are observed.

δ [%]	Numerical gradient (finite difference)			Analytical supplied gradient		
	$\mathcal{J}$ eval.	CPU time [s]	Accuracy crit.	$\mathcal{J}$ eval.	CPU time [s]	Accuracy crit.
0	91	4.3405	$1.60.10^{-3}$	13	0.9886	$1.60.10^{-3}$
5	105	4.9903	0.0143	15	1.3121	0.0143
10	105	5.7422	0.077	15	1.2351	0.077
20	147	6.8948	0.1096	21	1.4846	0.1096

TABLE 1.3: Comparison of mCRE-based model updating performances using BFGS minimization algorithm, with finite-difference approximated and supplied analytical gradient.

1.3.3 Robustness with respect to measurement noise

As soon as the noise level δ increases, the mCRE-based model updating algorithm is not able to perfectly recover the expected parameter set $\theta^\star$ (as any inverse problem solver). This is even more significant in that case due to the fact that relative measurements are naturally of low amplitude (which implies low-SNR data to process).

The results collected in Tab. 1.4 illustrate the effect of noise on updated parameters $\hat{\theta}$. The model updating procedure with a default $\alpha = 1$ value does not provide relevant corrections with respect to the reference parameters. However, integrating the knowledge that measurements are noisy by decreasing the value of α to 0.1 provides a parameter estimate closer to the reference one. This simple illustration highlights that dedicated efforts must be done to enhance the robustness of the algorithm, in particular regarding the calibration of the internal mCRE parameters: α, D_ω, and $z(\omega)$ (the effect of the last two has not been highlighted here because less influent compared to α).

Subdomains	Expected parameters	Updated parameters $\alpha = 1$	Updated parameters $\alpha = 0.1$
W10	0.67	0.3550	0.5832
W11	1.1	0.5832	0.9654
W20	1.1	0.9683	1.0630
W21	1.1	0.4586	0.9347
F10	1.1	1.3619	1.1536
F20	1.1	1.5656	1.1901

TABLE 1.4: Comparison of parameter estimation for low-SNR measurements ($\delta = 20\%$).

1.3.4 Choice of the reduced basis for enhanced numerical performance

Following the recommendations given in [Deraemaeker et al. 2002], a truncated modal basis can be used to enhance mCRE computations (1.24). What is also commonly recommended, following traditional modal analysis techniques, consists in adding the static responses associated with different excitations at sensor locations. In practice, a sufficiently rich and constant basis computed in preamble of the model updating algorithm enables to avoid a complex dependency of the solution fields (U_ω, V_ω) in parameters. As long as ω_L is high enough (compared to the input frequency bandwidth) and D_ω well discretized, this is not a critical issue for obtaining accurate results. As illustrated in Fig. 1.6, the amount of eigenmodes stored in $\mathbf{\Phi}_L$ can be significantly reduced using static responses from unit displacement at sensor locations (Krylov vectors). Yet, it does not change the statistical effect of measurement noise.

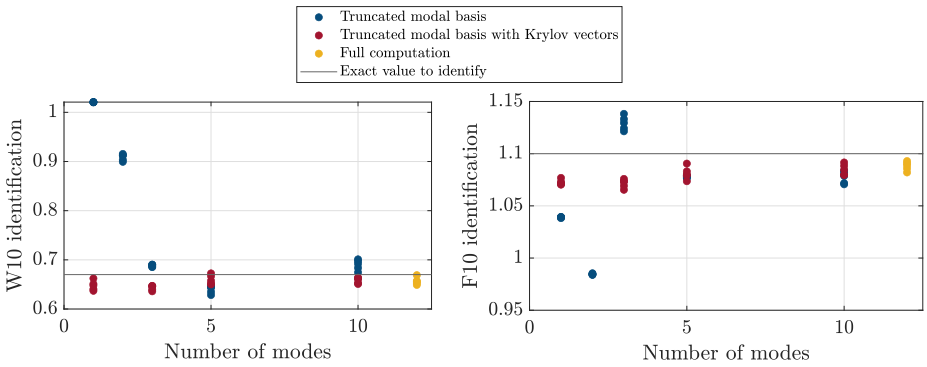

FIGURE 1.6: Effect of the reduced basis on model updating accuracy from 10% noisy data. Adding Krylov vectors allows to reduce the amount of eigenmodes within $\mathbf{\Phi}_L$ for the same accuracy.

If more advanced techniques are available, such as reanalysis or parametric families [Balmès 1996], the direct dependency into the updated set of parameters would turn the overall mini-

mization algorithm more complex as the derative of the reduced basis with respect to θ should be computed in the mCRE gradient.

1.4 Contributions for enhanced robustness to low-SNR random data

The analysis of the previous results motivated the need for automated tuning procedures of mCRE functional to spread the use of the functional in an industrial environment, and to enhance the robustness of the model updating strategy, especially when dealing with low-SNR measurements. The contributions presented herein are devoted to making the mCRE more robust considering the following aspects:

- ▷ **Enhanced robustness with respect to measurement noise** – An automated tuning procedure of the confidence into measurements coefficient α that naturally discriminates low-SNR measurements would be beneficial. As previously illustrated, the choice of α is crucial to obtain relevant parameter estimates. Following the initial studies of [Warner et al. 2014; Balmès et al. 2022], several techniques are proposed to automatically choose the value of α at best. Besides, mostly because of the high values in the very-low-frequency range that occurs due to measurement noise, the mCRE updating procedure may fail at providing relevant identification results. To avoid such issues, the frequency weighting function $z(\omega)$ can be adjusted. In the literature, only [Alarcon et al. 2011a] proposed a non-default frequency weighting function, with a case-by-case procedure to build a piecewise constant function around frequencies having large mCRE values. In [M. Diaz et al. 2022c], a novel tuning of the frequency weighting function $z(\omega)$ is proposed based on the frequency content of the collected data. It allows to automatically favor the vicinity of the experimental modal eigenfrequencies, improving the parameter sensitivities and the accuracy of parameter estimates.

- ▷ **Enhanced robustness with respect to low-magnitude ergodic inputs** – during shaking table experiments, non-damaging broad-band ergodic tests are performed to identify modal signature changes. Similarly to what is classically done for processing periodograms for random processes [Stoica and Moses 2005], a data windowing extension of the mCRE functional is presented and effective for preventing potential divergence of the model updating algorithm and providing more stable estimates even when considering low-SNR measurements from low-PGA random testings.

Complete explanations about these contributions are given in the remainder of this section. The frame example of the previous section will be used to illustrate the proposed improvements, before an application to the processing of actual measurements in Section 1.5.

1.4.1 Averaged formulation for statistical robustness to measurement noise and convergence to measurements in terms of PSDs

When studying systems submitted to *stochastic* inputs, random signals, viewed as discrete-time sequences, do not have finite energy and hence do not possess a discrete-time Fourier transform (see *e.g.* [Stoica and Moses 2005]). However, they usually have a finite average Power Spectral Density (PSD). Under *stationarity* assumption, and introducing a unit window v of length T such that $x_T(t) = v \cdot x(t)$, the PSD matrix of a random signal $x(t)$, denoted $\mathcal{S}_{xx}[\omega]$, can be defined for all ω as:

$$\mathcal{S}_{xx}[\omega] \triangleq \lim_{T\to+\infty} \mathbb{E}\left(\frac{1}{T}\int_{-\infty}^{+\infty} \left[X_{T,\omega}\right]\left[X_{T,\omega}\right]^H \mathrm{d}\omega\right) \tag{1.31}$$

where X_T is the Fourier transform of x_T, and $\mathbb{E}(\bullet)$ denotes the mathematical expectation operator. Defining in practice a correct windowing (number of segments, type and length of the windows for apodization, zeropadding, etc.) might not be an easy task and could add uncertainty to a quantity (the PSD matrix) that, by nature, can only be estimated in a statistical

manner. An example of the windowing used for the SMART2013 application can be seen in Fig. 1.7. Let us simply assume here for the sake of generality that when dealing with random processes, a given set of N_w possibly overlapping windows $\{v_j\}_{j=1}^{N_w}$ is used for the computation of the PSD matrices. Once applied to the input and output time-series, this windowing step provides an ensemble of complex values denoted $(Y_{j,\omega})$.

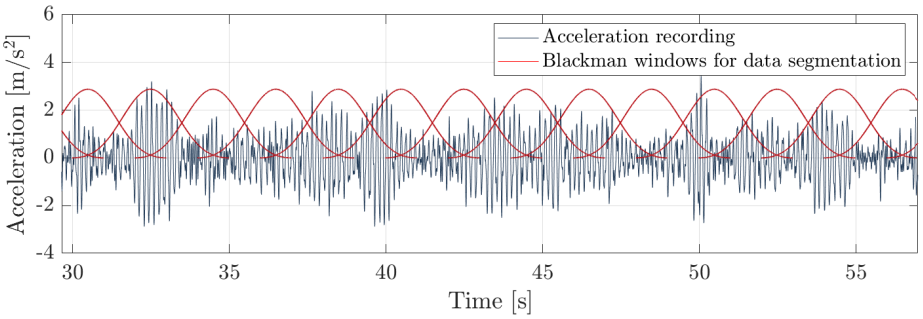

FIGURE 1.7: 60%-overlapped Blackman windows to compute PSDs from acceleration time histories recorded during the run #6 of SMART2013.

Averaged mCRE

Half of shaking table test campaigns consider low-magnitude random as ground motion inputs (see Appendix A.2). The measurements are thus characterized by their low SNR and their stationarity. In order to make the mCRE-based model updating procedure more robust to measurement noise in the statistical sense in such cases, we propose in [M. Diaz et al. 2022c] to integrate within the mCRE functional the same windowing process that is classically involved for PSD computations. To do so, the mCRE is reformulated using windowed frequency-domain preprocessed measurements $(Y_{j,\omega})$. The elementary mCRE term is therefore defined for a given angular frequency $\omega \in D_\omega$ and a given window $v_j, j \in [\![1, N_w]\!]$:

$$\forall\, j \in [\![1, N_w]\!], \forall\, \omega \in D_\omega, \quad e^2_{j,\omega}(s_{j,\omega}, \theta; Y_{j,\omega}) \triangleq \zeta^2_{j,\omega}(s_{j,\omega}, \theta) + \frac{\alpha}{2}\|\mathbf{\Pi} U_{j,\omega} - Y_{j,\omega}\|^2_{\boldsymbol{G}} \tag{1.32}$$

Therefore, on each segment j and each angular frequency, a mechanical solution $\widehat{s}_{j,\omega}$ is searched by solving the matrix system (1.20) whose second member is fed by $Y_{j,\omega}$ and $F_{j,\omega}$. Then, the averaged mCRE can be evaluated with respect to parameters θ as follows:

$$\mathcal{J}_{avg}(\theta; Y) = \mathop{\mathbb{E}}_{j}\left(\int_{D_\omega} z(\omega) e^2_\omega(\widehat{s}_{j,\omega}(\theta; Y_{j,\omega}), \theta; Y_{j,\omega})\, \mathrm{d}\omega\right) \tag{1.33}$$

Note that the integral sign and mathematical expectation can be permuted if the realizations on each segment are statically decorrelated, which is the case if windows are not much overlapped. The main change compared to the standard mCRE functional (1.21) lies in the fact that the matrix system to solve must now be solved for each angular frequency and for each time-window. Therefore, the computational burden of the averaged-mCRE functional is N_w times more important compared to the standard approach. Fortunately, one can easily parallelize the solution of these systems in order to mitigate the additional cost due to data windowing.

Convergence towards measurements in terms of PSDs

In the perspective of dealing with random processes, our claimed objective is to build a cost function that, once minimized with respect to the model parameters θ, would make the model predictions converge to the measurements in terms of PSDs. One could legitimately ask if this

desired requirement is met. To prove this claim, one has to consider the integrated and averaged model-to-measurements term, that reads:

$$\left|\left|\left|\mathcal{H}(\mathcal{M}(\theta,e))-y\right|\right|\right|^2 \;=\; \int_{D_\omega} z(\omega)\,\mathop{\mathbb{E}}_{j}\left(\|\boldsymbol{\Pi}U_{j,\omega}-Y_{j,\omega}\|^2_{\boldsymbol{G}}\right)\,\mathrm{d}\omega \tag{1.34}$$

As previously explained, the involved norm is written using real symmetric positive-definite matrix $\boldsymbol{G}$. Let thus introduce the prediction-error sequence $(\eta)=(\boldsymbol{G}^{1/2}(\boldsymbol{\Pi}U_{j,\omega}-Y_{j,\omega})$ using the square-root of matrix $\boldsymbol{G}$.The distance term reads:

$$\forall\, j,\forall\,\omega,\quad \|\boldsymbol{\Pi}U_{j,\omega}-Y_{j,\omega}\|^2_{\boldsymbol{G}} \;=\; [\boldsymbol{\Pi}U_{j,\omega}-Y_{j,\omega}]^H\,\boldsymbol{G}\,[\boldsymbol{\Pi}U_{j,\omega}-Y_{j,\omega}] \tag{1.35}$$

Now taking the mathematical expectation of this last expression yields:

$$\forall\,\omega,\quad \mathop{\mathbb{E}}_{j}\left(\|\boldsymbol{\Pi}U_{j,\omega}-Y_{j,\omega}\|^2_{\boldsymbol{G}}\right) \;=\; \boldsymbol{tr}\left(\mathcal{S}_{\eta\eta}[\omega]\right)\;\geqslant 0 \tag{1.36}$$

by definition of the PSD sequence, where $\boldsymbol{tr}\,(\bullet)$ refers to the trace operator. Thus, if the matrix $\boldsymbol{G}$ is symmetric, positive and definite, the following distance to measurements term

$$\left|\left|\left|\mathcal{H}(\mathcal{M}(\theta,e))-y\right|\right|\right|^2 \;=\; \int_{D_\omega} z(\omega)\,\boldsymbol{tr}\left(\mathcal{S}_{\eta\eta}[\omega]\right)\,\mathrm{d}\omega \tag{1.37}$$

obviously defines a norm on the PSD sequence $\left(\mathcal{S}_{\eta\eta}[\omega]\right)_{\omega\in D_\omega}$ which is exactly the property that was looked for. Minimizing a weighted norm of the prediction error PSD matrix on the whole frequency domain D_ω with respect to θ thus makes the model predictions converge to the measurements.

Therefore, the preliminary data windowing and the averaged extension of the model updating process enable a better integration of random processes and bring an additional **statistical stability** of the parameters with respect to measurement noise. This makes it worthwhile to extend the convergence of model predictions towards the measurements in terms of PSDs. An illustration using the frame example is given in Fig. 1.8: when running multiple times the model updating algorithm with different measurement noise realizations, one can observe an enhanced stability in the parameter estimate using the averaged mCRE formulation and data windowing. In Fig. 1.8, the width of each plotted interval represents the maximal variability of updated parameters with respect to measurement noise after having repeated 50 times model updating from the same input signal, but with different noise realizations. It is thus clear that the data windowing preprocessing step enables the algorithm to provide more stable estimates: **increasing the amount of windows N_w in the data preprocessing step is beneficial for increasing statistical stability**. However, one shall note that the number of segments cannot be indefinitely increased: statistical independence of data blocks must be guaranteed for the averaging to be meaningful [Stoica and Moses 2005]. Noticing that reducing the time-length of windows does not drastically provide much more accurate results, a compromise must then be sought when designing the shape, number and length of time-windows. In this work, 60%-overlapping Blackman windows lasting up to 2 s have been used and always provided satisfactory results. As a last remark, the comparison of the intervals between subdomains (for a given data windowing configuration) shows the difference in sensitivity of the parameters to the mCRE functional: one can therefore remark that the top walls W11 and W21 are less sensitive due to the fact they do not store much mechanical strain energy compared to the subdomains located at the bottom of the frame.

> *Remark* 1.11. The averaged mCRE formulation can be seen as a generalization of the standard mCRE functional in the sense that $\mathcal{J}(\theta)=\mathcal{J}_{avg}(\theta)$ using a single window segment $N_w=1$ with unitary rectangular shape. However, this generalization remains valid only for random ergodic processes. Therefore, seismic runs should not be processed with the averaged mCRE.

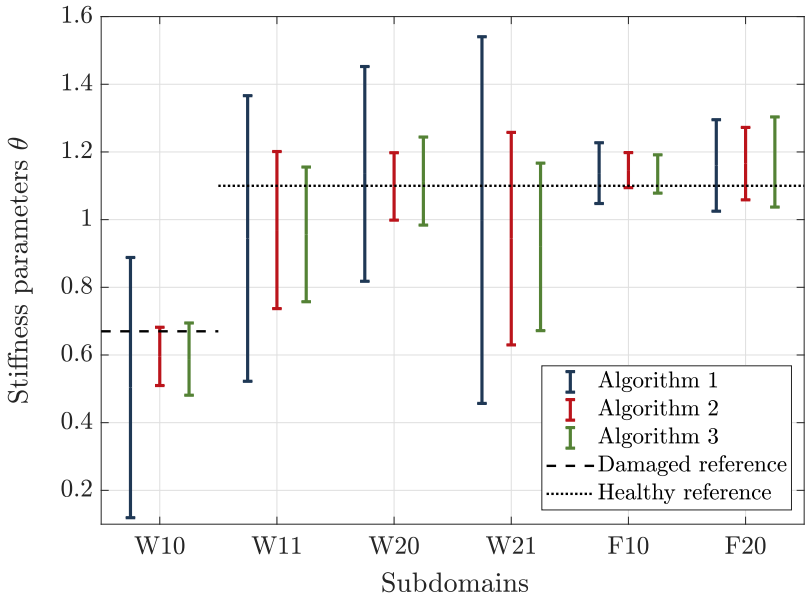

FIGURE 1.8: Statistical variability of parameter estimates with respect to measurement noise. Based on 50 different 60 s-random ground motion inputs and a $\delta = 10\%$ noise level, synthetic acceleration measurements are processed by 3 mCRE-based model updating algorithms having different data windowing: Alg. 1) Single unit rectangular window Alg. 2) Blackman-10 s data windowing, Alg. 3) Blackman-5 s data windowing.

1.4.2 Frequency range and data-based frequency weighting function

The model updating procedure is carried out on a given frequency bandwidth $D_\omega = [\omega_{min}; \omega_{max}]$ which contains the essential part of the mechanical energy of the system. For seismic applications, ground motions usually have a significant frequency content up to 50 Hz, which implies that $D_\omega \subset [0\text{ Hz}; 50\text{ Hz}]$. In practice, the integration over D_ω also requires to introduce a frequency step Δf. The latter must be carefully chosen to correctly capture the frequency content associated to the sollicitated eigenmodes. A common engineering judgment one can recommend is to choose Δf such that the narrowest resonant peak is described by at least three points. Considering the 3 dB cut-off frequency, a simple rule of thumb for the choice of Δf is $3\Delta f \approx \min_i(\xi_i f_i)$ where the couple (ξ_i, f_i) refers to the damping ratio and eigenfrequency of mode i. In the upcoming earthquake engineering-inspired applications, with typical 5% damping ratios and first eigenfrequencies at around $2-5$ Hz, Δf is thus chosen within $[0.1\text{ Hz}; 0.5\text{ Hz}]$.

Then comes the question of the frequency weighting function, often chosen constant by default. One should note that the frequency weighting function $z(\omega)$ can be used as a modulation function to favor frequencies deemed to have the largest influence on the model updating procedure. In this work, an automated data-based computation of $z(\omega)$ is used based on the fact that, for low-frequency dynamics, the essential frequency content of the measurements is gathered around experimental natural frequencies. A normalized version of the *Complex Mode Indicator Function* (CMIF) [Allemang and Brown 2006] on transfer functions is used for frequency weighting as explained in the following lines.

One first needs to compute the transfer matrix $H(\omega)$ from the crossed input/output PSD matrices $\mathcal{S}_{yy}(\omega)$, $\mathcal{S}_{ye}(\omega)$, $\mathcal{S}_{ee}(\omega)$ using one of the three following formulas:

$$H(\omega) = \left[\mathcal{S}_{yy}(\omega)\right]\left[\mathcal{S}_{ey}(\omega)\right]^\dagger \tag{1.38}$$

$$H(\omega) = \left[\mathcal{S}_{ye}(\omega)\right]\left[\mathcal{S}_{ee}(\omega)\right]^\dagger \tag{1.39}$$

$$H(\omega) = \left[\mathcal{S}_{yy}(\omega)\ \mathcal{S}_{ye}(\omega)\right]\left[\mathcal{S}_{ey}(\omega)\ \mathcal{S}_{ee}(\omega)\right]^\dagger \tag{1.40}$$

where $\bullet^\dagger$ refers to the Moore-Penrose pseudo-inverse. The dominant singular value $\Sigma_1(\omega)$ of matrix $H(\omega)$ has the property of peaking in the vicinity of natural frequencies and can be advantageously used to define $z(\omega)$. This indicator based on the transfer matrix is called H-CMIF in what follows (owing to its similarities with classical CMIF). The preliminary smoothing of the PSDs is therefore crucial for allowing the detection of resonant peaks without misinterpretation due to the random nature of the signals when considering random inputs. Finally, to fulfill the condition $\int_{D_\omega} z(\omega)\,\mathrm{d}\omega = 1$, the H-CMIF weighting function $z(\omega)$ is derived as

$$z(\omega) = \frac{\Sigma_1(\omega)}{\int_{D_\omega} \Sigma_1(\omega)\,\mathrm{d}\omega} \tag{1.41}$$

The efficiency of this H-CMIF-based frequency weighting function is highlighted in the next section when the SMART2013 recordings are processed : due to the large gaps in terms of eigenfrequencies, a well-defined $z(\omega)$ that integrates the information from data helps the convergence of the mCRE-based model updating process towards convincing results in terms of eigenfrequency tracking. A H-CMIF example is proposed for the frame example in Fig. 1.9, showing the crucial importance of such weighting when the noise level becomes important: it particularly contributes in preventing spurious increases of the mCRE frequency content below 5 Hz.

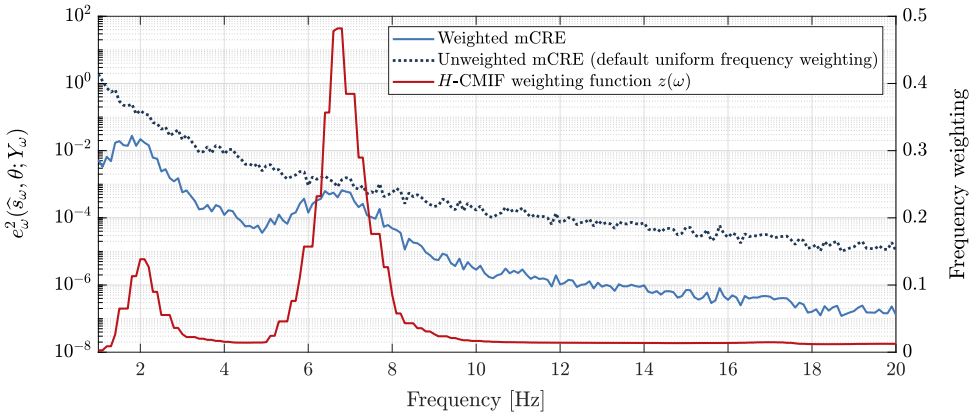

FIGURE 1.9: Data-based frequency weighting function to emphasize the mCRE frequency content on the experimental eigenfrequencies of sollicitated modes.

1.4.3 Automated calibration of the confidence into measurements

Historically, out of the specific continuation scheme proposed in [Banerjee et al. 2013] and the trial-and-error presented in [Balmès et al. 2022], several approaches related to regularization techniques were employed to define an optimal value of α. The influence of α was particularly investigated in [Deraemaeker et al. 2004; Warner et al. 2014; Huang et al. 2016; Ferrier et al. 2021], with empirical conclusions that an equivalent confidence between the CRE and data-to-model distance terms provided relevant model updating results. In other words, one should intend to calibrate α such that the two terms are in the same order of magnitude. This idea is closely related to the L-curve method [Ahmadian et al. 1998].

Alternatively, another technique to choose α lies in Morozov's discrepancy principle [Morozov 1984; Nair et al. 2003]. Therefore, the latter could be used in order to integrate the *a priori* knowledge on measurement noise features appropriately, as it was done in [M. I. Diaz et al. 2015; H. N. Nguyen et al. 2022] to perform mCRE-based identification from imaging databases.

Two tuning strategies based on the previously mentioned principles are discussed in the following. Both require a preliminary parametric study on α that can be done (at low-cost) in preamble of the model updating procedure. Doing so, a full parametric study on α, that would be prohibitive in terms of CPU requirements, is avoided.

A priori balance between modeling and measurement errors

As mentioned above, the (physics-based) CRE term allows to explicitly integrate modeling errors into the updating process. Its relative weight with respect to the modeling error term must be correctly set in order to guarantee relevant identification results. Without any additional *a priori* information, one can choose to calibrate α to ensure a correct *a priori* balance between measurement error and modeling error. This approach, which is close to the L-curve principle in terms of formulation, has been proposed in recent works [Ferrier et al. 2021; M. Diaz et al. 2022c] and provided relevant model updating results.

$$\widehat{\alpha} = \arg \min_{\alpha \in \mathbb{R}^+} \left| \underbrace{\int_{D_\omega} z(\omega) \zeta_\omega^2 \left(\widehat{s}(\theta; Y_\omega), \theta; Y_\omega\right) \, \mathrm{d}\omega}_{\text{Modeling error}} - \underbrace{\int_{D_\omega} \frac{z(\omega)}{2} \left\| \boldsymbol{\Pi} U_\omega - Y_\omega \right\|_{\boldsymbol{G}}^2 \mathrm{d}\omega}_{\text{Measurement error}} \right| \tag{1.42}$$

Note that this approach is non-trivial as the mechanical fields that need to be computed (U_ω, V_ω) are indirectly impacted by the value of α following (1.20).

Morozov's discrepancy principle to integrate the knowledge of measurement noise

In most cases, it seems relevant to take advantage of the knowledge of measurement noise features (if available) to enhance the model updating process. Morozov's discrepancy principle permits to calibrate α so that the measurement error term should not be lower than the noise level δ. We owe to Bonnet and co-workers the only use of Morozov's discrepancy principle from data obtained in the frequency domain within the mCRE framework [Warner et al. 2014], although its implementation remains questionable. Indeed, as expressed in [M. I. Diaz et al. 2015], the measurement noise is assumed to be proportional to the magnitude of measurements, meaning that during the same experiment, sensors measuring low- or high-amplitude data do not have the same noise level. Besides, the implementation of the criterion has only been proposed for harmonic analysis and from synthetic data with low noise levels (up to 5% only).

In this contribution, a Morozov's discrepancy criterion for optimal choice of α dedicated to the considered mCRE-based model updating framework is proposed. If one (legitimately) assumes that the added measurement noise follows a zero-mean Gaussian probability density function, *i.e.* $\eta(t) \sim \mathcal{N}(0, \delta_s^2) \; \forall \, t$, and if $\boldsymbol{G}$ is proportional to the identity matrix, *i.e.* $\boldsymbol{G} = \boldsymbol{G}_0 I$, then one can show that the measurement error term can be statistically approximated by:

$$\mathbb{E}\left(\int_{D_\omega} \frac{z(\omega)}{2} \left\| \boldsymbol{\Pi} U_\omega - Y_\omega \right\|_{\boldsymbol{G}}^2 \mathrm{d}\omega \right) = \frac{1}{2} G_0 \delta^2 N_s \tag{1.43}$$

as the squared modulus of a zero-mean random process follows a non-centered $\chi^2(2)$ probability distribution conditioned by its variance δ^2, whatever the value of ω (see Appendix C for the complete proof starting from Morozov's discrepancy main theorem). One can thus statistically bound the measurement error term, which directly corresponds to the adaptation of Morozov's discrepancy principle to the mCRE written in the frequency domain (when all sensors are supposed uncorrelated, which is legitimate in practice). The statistical upper-bound thus depends simultaneously into the number of sensors N_s, the measurement noise δ and the scaling matrix $\boldsymbol{G}$, which is intuitively consistent.

The practical use of Morozov's discrepancy principle implies to choose the optimal value $\widehat{\alpha}$ *a posteriori* using an iterative scheme, where the value of α is tuned using a bisection method after assessing the quality of the solution once having fully minimized the mCRE functional. Doing so, in a few iterations, one could hope to find a relevant value for $\widehat{\alpha}$. However, one cannot afford to perform several minimization steps to update parameters correctly when performing model updating on-the-fly, as it is the intention of this thesis work. Similarly to the *a priori* balance criterion (1.42), one can also perform a (quick) *a priori* parametric study on α to propose a suboptimal value (that one hopes should be relevant for mCRE convergence):

$$\widehat{\alpha} = \arg \min_{\alpha \in \mathbb{R}^+} \left| \int_{D_\omega} z(\omega) \left\| \boldsymbol{\Pi} U_\omega(\alpha) - Y_\omega \right\|_{\boldsymbol{G}}^2 \mathrm{d}\omega - G_0 \delta^2 N_s \right| \tag{1.44}$$

Remark 1.12. It is important to notice that Morozov's discrepancy criterion works as an *a posteriori* tuning strategy for regularization weighting parameter. It is our choice to freeze α to a value obtained *a priori* on the basis of the initial values of θ (*i.e.* prior to any pamaterer updating). As the perspective of use for the mCRE is on-the-fly model updating, one cannot afford to get a proper value of α by doing multiple times model updating on a fixed dataset whereas brand new data (that may inform on possible damage) is assimilated at the same time.

Despite this choice, the *a posteriori* choice of α is the subject of very-short-term forthcoming investigations, as it is true that a poorly-chosen initialization on θ may lead to an inappropriate calibration of α.

Numerical validation of the criteria for automated *a priori* selection of α

To illustrate the consistency of the proposed criteria, their behaviour with respect to measurement noise on the previous frame example is presented in Fig. 1.10. All mCRE internal parameters (except from α) are identical, and the effect of measurement noise on the calibration of α can be observed. As one could have intuitively expected, the more the measurement noise, the lower "optimal" α. However, there are strong discrepancies between the values provided by these two methods (the x-axis of Fig. 1.10 is in log-scale), which suggests more tests must be done to evaluate the relevance of these two criteria. This will be done in a large benchmark reported in Chapter 2 and concluding remarks will be drawn at this moment regarding the calibration of α.

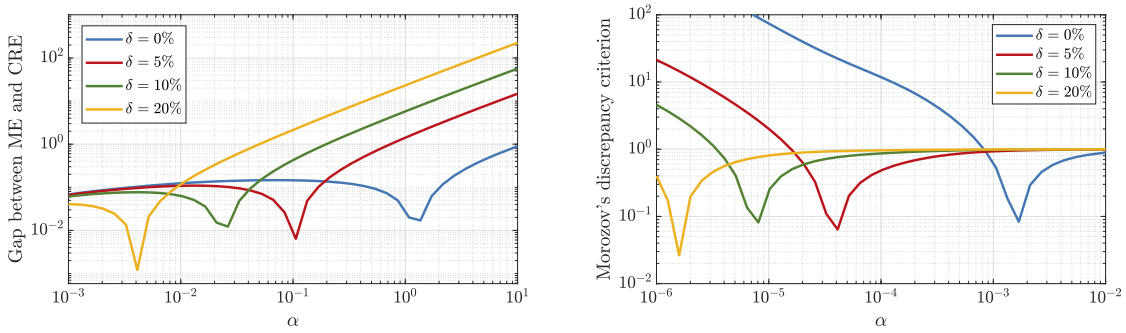

(a) L-curve criterion.

(b) Morozov's discrepancy criterion.

FIGURE 1.10: Automated calibration of the scaling factor α with respect to measurement noise.

1.5 Application to SMART2013: eigenfrequency tracking of a RC specimen using mCRE and acceleration data

In order to assess the vulnerability of RC structures subjected to torsional effects during seismic ground motions, the SMART2013 experimental campaign was conducted in the CEA/-TAMARIS facility. A three-story 1/4 reduced-scale trapezoidal RC specimen clamped on the AZALEE shaking table has been subjected to a sequence of seismic tests. The specimen was instrumented with more than 200 sensors including 64 capacitive accelerometers of ± 10 g range scattered over the RC specimen. 48 out of the 64 accelerometers have been used as experimental reference to correct two FE models that have been produced using the FE software CAST3M©.

Extended details about the campaign and the FE models are given in Appendix A.2 because this application example is also used in Chapter 4.

The purpose of this study is to evaluate, to improve, if possible, and to compare two FE models (developed on the CEA FE simulation software Cast3M©, and fully described in Appendix A.2) using a complete mCRE analysis based on reference data from the experimental campaign. Two objectives are targeted: (i) to determine whether **global stiffness parameters can correct the models to recover the experimental modal signature** and (ii) to **follow the drop of eigenfrequencies** that are directly related to damage occurence during the campaign, which is a crucial information for control law adaptation. Limitations of the method will be highlighted when trying to refine the parameter space for local damage detection purposes.

Figure 1.11: SMART2013 RC specimen anchored to the AZALEE shaking table.

1.5.1 Need for model updating

In spite of the analyses and the work that has been carried out, the SMART2013 database has never been used for model updating purposes. Only [Alarcon et al. 2011b] used it to assess the potential of CRE to identify damage deliberately introduced into a simplified model, even though [Richard et al. 2018] presented a great zoology of models that try to fit with the observed responses of the structure.

The call for model updating is warranted for both models due to the **strong gaps** one can see **between the predicted and the experimental eigenfrequencies** (see Tab. 1.5). As a reminder, each material property of all finite elements will not be updated: an overall stiffness model (1.14) is adjusted in order to propose the best stiffness corrections based on the actual richness of measurements.

Mode number	**Eigenfrequencies [Hz]**				
	Experimental	Model 1	Error [%]	Model 2	Error [%]
1	6.28	9.10	44.8	8.34	32.8
2	9.22	15.72	70.5	14.89	61.5
3	17.6	31.77	80.5	29.47	67.5

Table 1.5: SMART2013 - Comparison of the first eigenfrequencies between FE model initial predictions and modal analysis from experiments.

1.5.2 mCRE settings and first model updating results from initial runs and initial FE models

Model updating settings

Knowing the large gap in terms of natural frequencies between model predictions and available measurements (even at the beginning of the campaign, see Tab. 1.5), a single global stiffness parameter is updated herein. Due to the fact that the seismic loading is bi-axial, only the sensors measuring accelerations along the x and y directions are considered as inputs of the model updating strategy[3].

A preliminary analysis of acceleration time series confirms the low-frequency dynamics of the measurements and therefore justifies the use of the mCRE-based model updating algorithm previously described on the frequency range $D_\omega = [1\text{ Hz}; 30\text{ Hz}]$ with a $\Delta f = 0.1$ Hz frequency step. The averaged formulation can be used for random low-PGA runs.

[3] Acceleration data in the z-direction mostly provide information about measurement noise features.

An important statement to keep in mind is that the signal-to-noise ratio (SNR) for low-PGA inputs of the SMART2013 database is so important (although intrinsic sensors noise level is low) that a uniform frequency weighting function and a default value of $\alpha = 1$ lead to non-physical or divergent results: the variations of the functional $\overline{\mathcal{J}}$ with respect to θ and α are plotted in Fig. 1.12 to illustrate once again the non-neglictible impact of α on the parameter estimate provided by the updating algorithm. In the following, the L-curve based methodology (1.42) has been chosen to adapt α at best[4]. The addition of a normalized H-CMIF frequency weighting function enables to exploit at best all the available information from measurements minimizing spurious noise effects. Fig. 1.13 illustrates that point showing that the frequency content of the mCRE functional is emphasized with the normalized H-CMIF.

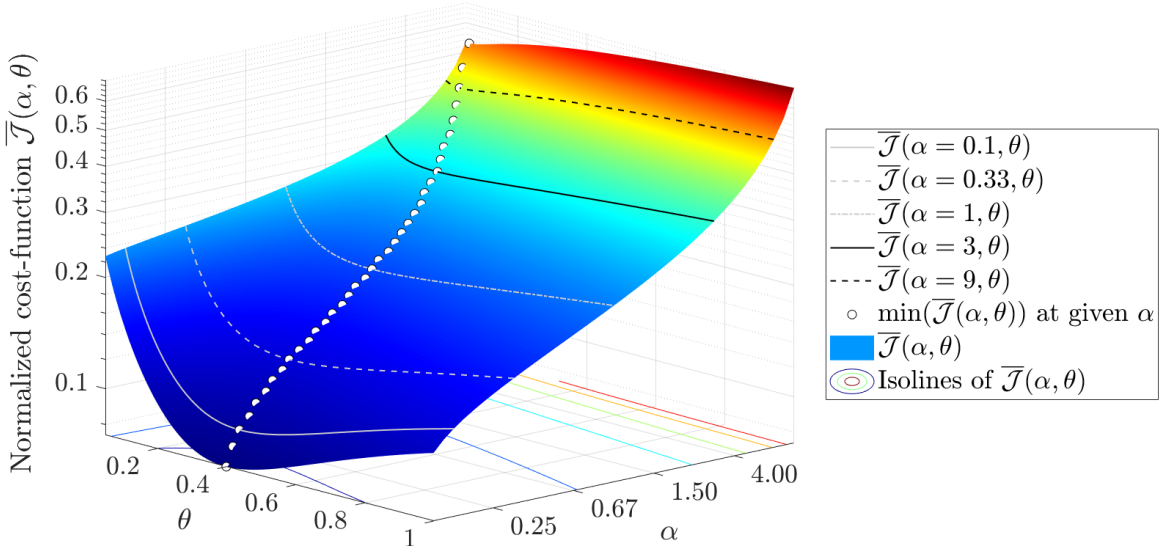

FIGURE 1.12: SMART2013 - run #7 – Influence of α on the model updating procedure. The mCRE functional is always convex but the minimum value is significantly altered with α (the white circles indicate the mCRE minimum location for a given α).

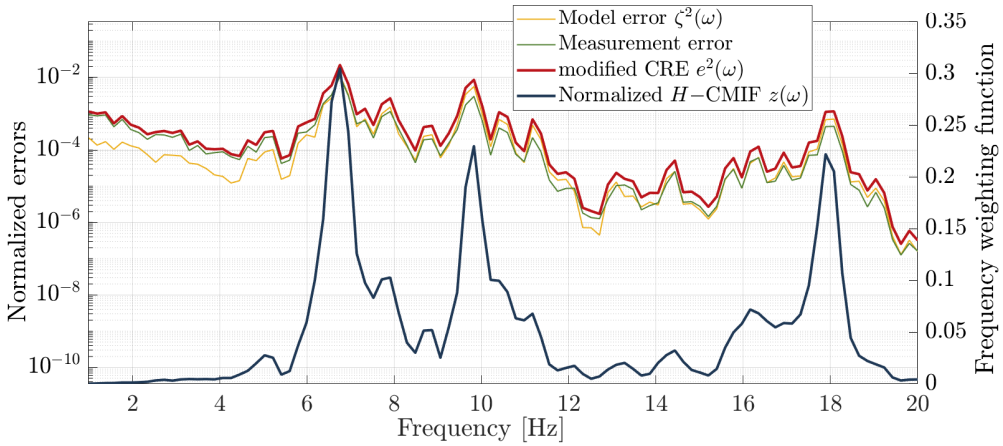

FIGURE 1.13: SMART2013 - run #7 – H-CMIF used as frequency weighting function, leading to sharper peaks of the mCRE profile around the experimental eigenfrequencies.

[4]As already mentioned, exhaustive conclusions on the definition of α are drawn in Chapter 2.

Convexity checking and comparison to total least-squares model updating

One could legitimately wonder about the performance of the mCRE-based proposed methodology when compared to classical Frequency Least-Square (FLS) minimization written in the frequency domain:

$$\widehat{\theta}_{FLS} = \arg\min_{\theta\in\Theta} \left[\mathcal{J}_{FLS}(\theta) \triangleq \int_{D_\omega} \|\mathbf{\Pi} U_\omega(\theta) - Y_\omega\|^2 \, \mathrm{d}\omega \right] \tag{1.45}$$

where $U_\omega(\theta)$ in that case is the direct displacement field obtained from the FE model predictions. Note that it is shown mathematically in [Aquino and Bonnet 2019] that one can see the FLS minimization like a particular limit case of the mCRE-based model updating algorithm with $\alpha \to \infty$. The plot of both mCRE- and FLS-based functionals in Fig. 1.14 illustrates the enhanced convexity properties of the mCRE-based functional, which yields an easier convergence towards the optimal set of parameters.

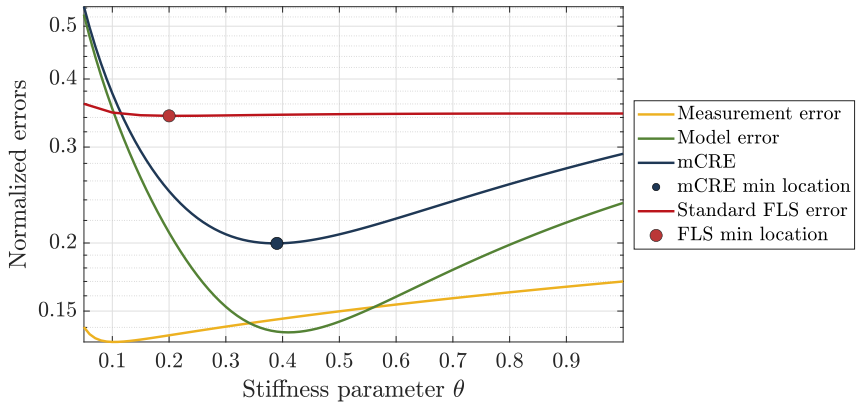

FIGURE 1.14: SMART2013 - run #7 – Identification of a global stiffness parameter using the mCRE-based model updating algorithm (with $\alpha = 0.1$ in that case). An enhanced convexity shows the relevance of the methodology compared to a frequency total least-square error.

Besides, the computation of the updated eigenfrequencies based on the corrected FE model 1 in Tab. 1.6 shows that the mCRE-based algorithm provides much more reliable results (in better match with experimental eigenfrequencies). Similar results has been recovered with model 2 and are not presented here for the sake of conciseness.

Mode number	Experimental frequency	Initial		mCRE updated		FLS updated	
		Frequency	Error	Frequency	Error	Frequency	Error
1	6.28	9.10	44.8	5.68	14.9	4.07	39.1
2	9.22	15.72	70.5	9.82	6.5	7.03	23.7
3	17.6	31.77	80.5	19.84	12.7	14.21	19.3

TABLE 1.6: Model updating results obtained for SMART2013 run #7 – Comparison of the first eigenfrequencies (in [Hz]) and relative errors (in [%]) between experimental reference [Charbonnel 2021], initial model 1 and updated model 1 from the mCRE-based and frequency least-square (FLS) model updating algorithms.

An additional quantitative appreciation of the model updating results on the whole frequency range can be obtained by comparing the experimental reference to model 1 in terms of H-CMIF. Several normalized H-CMIFs are displayed in Fig. 1.15:

(i) Reference experimental H-CMIF computed from accelerometers (see (1.38-1.40)),
(ii) H-CMIF from the initial model ($\theta = 1$),
(iii) H-CMIF from the mCRE-based updated model with default $\alpha = 1$,
(iv) H-CMIF from the mCRE-based updated model with optimal $\widehat{\alpha}$,
(v) H-CMIF from the FLS-updated model.

The numerical H-CMIFs (ii-v) above correspond to the dominant singular value of the transfer function H computed using the FE matrices of model 1. From these plots one can conclude that the parameter estimates provided by the mCRE-based algorithms are more physically relevant with respect to the expected frequency content; the corrected model H-CMIFs get closer to the experimental reference, especially in the vicinity the two first eigenfrequencies. The choice of a single parameter model is obviously too simplistic to perfectly recover the experimental frequency content over D_ω. A better adequacy with higher eigenfrequencies could certainly be obtained by updating several parameters simultaneously, with risks of having convergence issues as shown afterwards. **The choice of an optimal $\widehat{\alpha}$ permits an improved estimation of the two first eigenfrequencies, whose eigenmodes are essential in the low-frequency specimen dynamical response**.

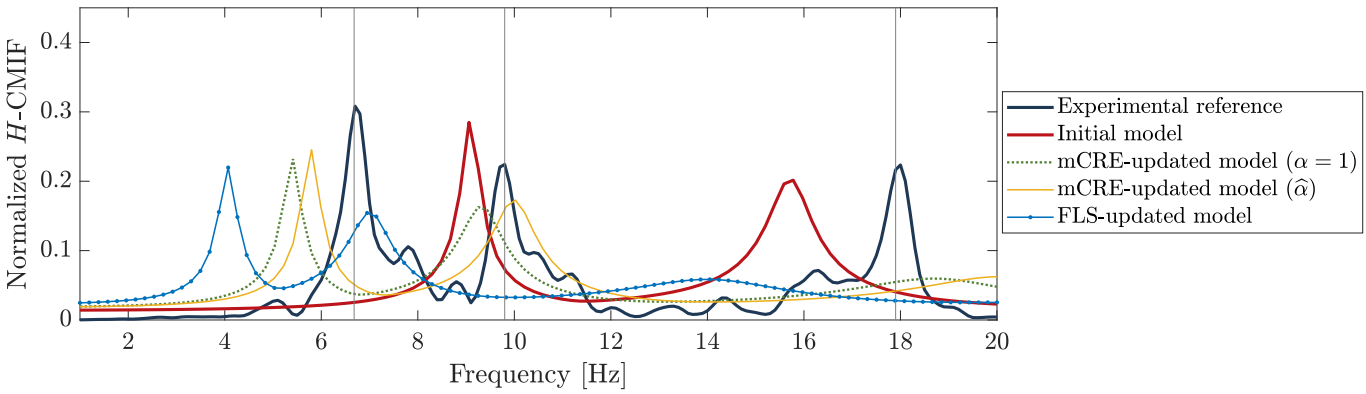

FIGURE 1.15: SMART2013 - run #7 – H-CMIF comparison between experimental reference and model predictions before/after updating. The mCRE-based model updating algorithms provide more accurate results than FLS minimization in terms of H-CMIF. A compromise is made for fitting at best the experimental frequency peaks (marked with grey vertical lines).

> *Remark* 1.13. Note that no data windowing has been performed previously, considering that run #7 time series cannot be assumed ergodic and stationary. The enhanced statistical stability of data windowing will be observed in the next paragraph when considering low-SNR random measurements from even-numbered runs.

1.5.3 Offline correction of the FE model during the full SMART2013 test campaign

In what follows, the mCRE-based model updating procedure will be sequentially used for correcting the FE models along the whole SMART2013 test campaign. As a reminder, a full description of the campaign is available in Appendix A. In practice:

- ▷ the measurements from each run are consecutively processed by the model updating algorithm, meaning that an updated parameter value is obtained per run;
- ▷ when processing run $\#n$, the final result from the previous run $\#(n-1)$ is used as initial guess.

Due to the fact that damaging runs time series inputs cannot be assumed as ergodic and stationary, the averaged mCRE-based model updating algorithm with data windowing (which favors data-model correlation in terms of PSDs) is exclusively assessed on the low-PGA runs. Two variants of the model updating algorithms are thus used:

(a) Model updating using a single unit-rectangular window for data windoing, which is convenient for all testings and does not guarantee optimal stability with respect to measurement noise.
(b) Model updating of the random low-PGA runs (even runs from Tab. A.1) using 60%-overlapping Blackman-5 s windows (illustrated in Fig. 1.7).

Fig. 1.16 presents the evolution of the updated first three eigenfrequencies (squares) compared to the experimental reference from [Charbonnel 2021] (connected circles) using a single parameter stiffness model, whose estimated optimal values are also specified (right subplots). Models 1 and 2 have been equally used for the mCRE-based model updating process, but it seems that model 1 tracking results are more in accordance with experimental data, in particular after run #14. However, in both cases, the model updating procedure provides relevant correcting actions, confirmed by the proximity of the reference eigenfrequencies. The progression of damage can be related to the decreasing values of the updated parameter throughout the different runs.

The study of the frequency drop highlights two stages in the test campaign where parameters remain globally constant: runs #6 to #12 (phase 1: SMART2008 inputs), and #20 to #24 (phase 3: after-shock analysis). One can remark in each of them that the enhanced statistical robustness of data windowing (comparing Fig. 1.16a and 1.16c) confers a better stability of the parameter estimate, as previously observed in the academic two-story frame example. Even though the correcting actions remain global due to the spatial sparsity of accelerometers, one has to notice that **a correctly updated (linear) stiffness FE model is able to follow the state of a structure during the entire test sequence, in which many nonlinear phenomena occur**.

> *Remark* 1.14. Once all mCRE internal parameters have been well calibrated, the algorithms all converged towards physical-meaning values in terms of eigenfrequencies, except for run #13. During the latter, a significant crack propagated at the bottom of the specimen, which lead to an unstable test ending with an emergency stop. As this is typically the problem that this thesis aims to solve, run #13 will be deeply considered in Chapters 4 and 5.

1.5.4 Towards subdomains refinement and underlying identifiability problems

Until now, the updating procedure has only been focusing on one global stiffness parameter, providing relevant tracking of the first eigenfrequencies drop, which is directly related to the evolution of the overall damage state of the specimen. This global damage assessment is **already promising for better control of shaking table actuators**. However, it is certain that the corrections of the FE stiffness matrix proposed herein may lack of relevance for local damage detection purposes as the overall weighting of the stiffness matrix does not give access to any local information. Therefore, the feasibility of the identification of several parameters naturally arises. Indeed, now that the model is globally updated, a next step would consist in defining smaller subdomains in order to evaluate the damage state more locally. It raises new problems, particularly regarding the relative accuracy of the algorithm when identifying several parameters simultaneously and its capability to update accurately all of them.

If one now considers the FE model 1 to be split in four subdomains whose stiffness FE submatrices are obtained by assembling the elementary contributions of the elements belonging to each of them. They are displayed in Fig. 1.17.

To the extent that the CRE distribution per subdomain and mechanical strain energy are intrinsically related, a first preliminary analysis of the modal strain energy contributions per subdomain can be performed remarking that, if among all, certain subdomains have a very low-energy contribution compared to the others, then it will be probably difficult to update the associated parameters properly. For the initial FE model, the modal strain energies per subdomain are displayed in Fig. 1.17 for the first five eigenmodes. One can notice that the contribution of the anchoring and 3rd floor subdomains are of less importance compared to the global mechanical strain of the structure. Therefore, the lack of sensitivity of the associated parameters may lead to an uncertain updated value.

To confirm this statement, a 2D map of the mCRE functional with respect to the 1st and 2nd floor stiffness parameters has been plotted in Fig. 1.18 based on run #6 data. The amount of possible couples of parameters that are relevant in the mCRE sense shows that the algorithm will hardly be able to provide a consistent minimum value. Indeed, the mCRE functional is

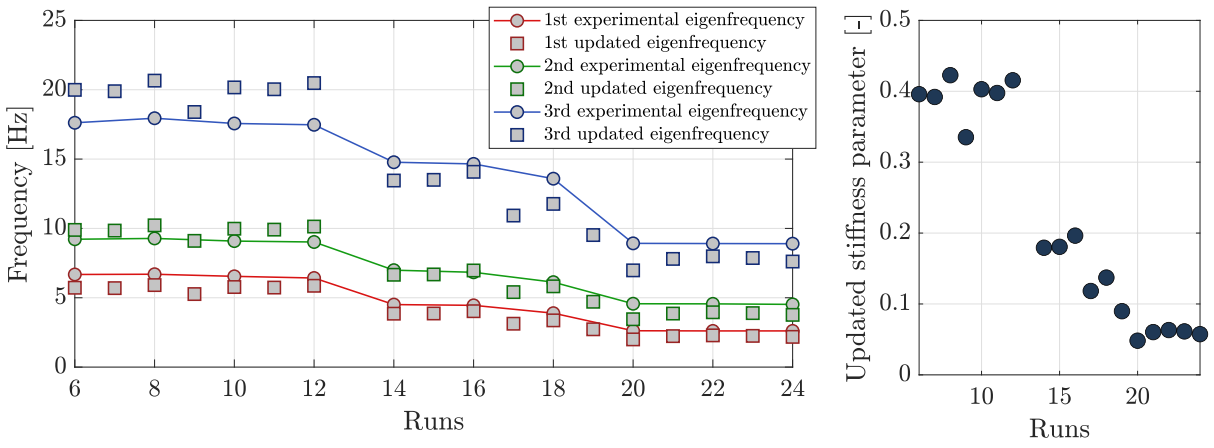

(a) mCRE-based update of model 1 from acceleration measurements in directions (x, y), without data windowing.

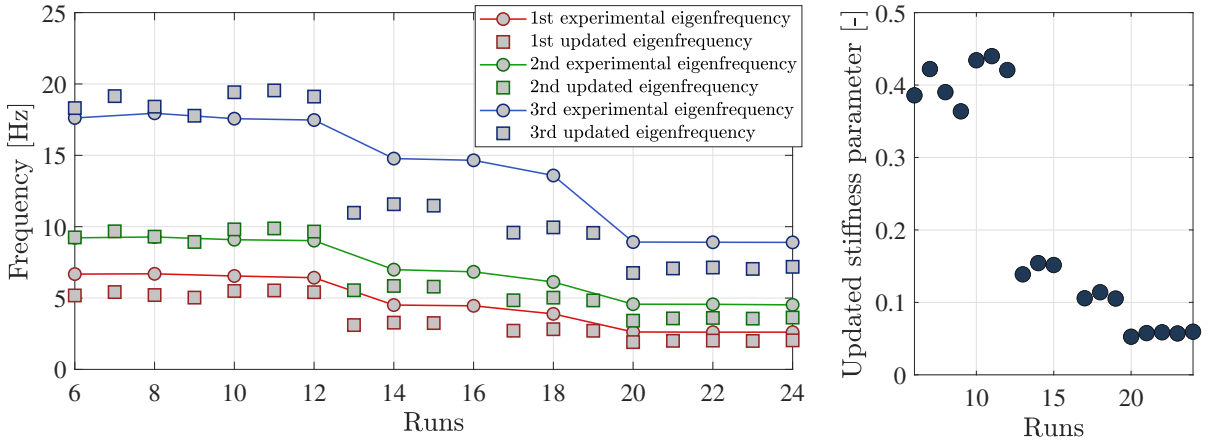

(b) mCRE-based update of model 2 from acceleration measurements in directions (x, y), without data windowing.

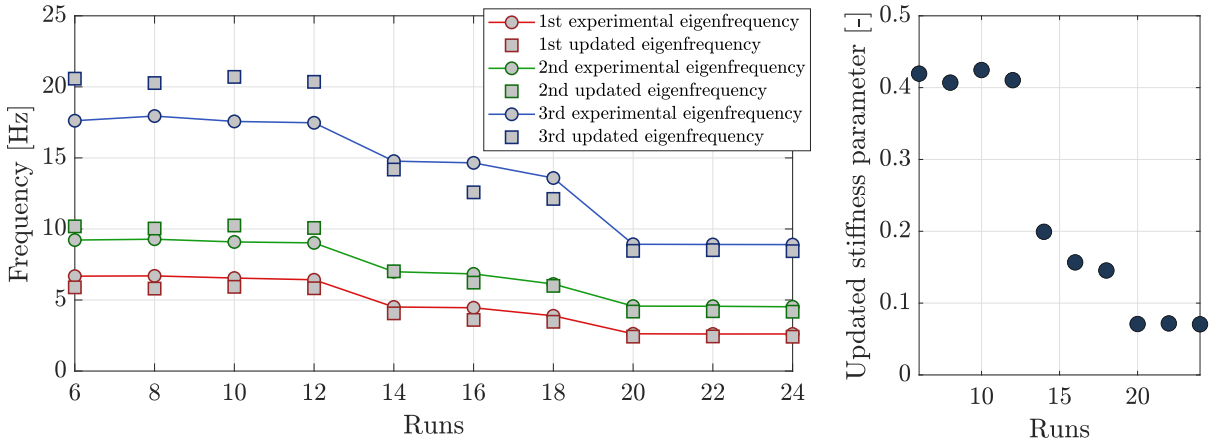

(c) mCRE-based update of model 1 with data windowing for the broad-band low-PGA tests exclusively. 5 s-Blackman windows have been used.

FIGURE 1.16: Correction of SMART2013 FE models using mCRE-based model updating algorithms and acceleration measurements – modal signature tracking and parameter estimate evolution with runs are plotted.

sensitive to both parameters, but the lack of local information (*i.e.* the low spatial density of sensors) limits the capability of mCRE to identify parameters accurately, even if they are selected as most sensitive. **Although a large number of sensors is spread over the specimen, the experimental information they bring is unfortunately not rich enough to locally quantify the damage state of the specimen**, even if the model updating process is restrained to the most

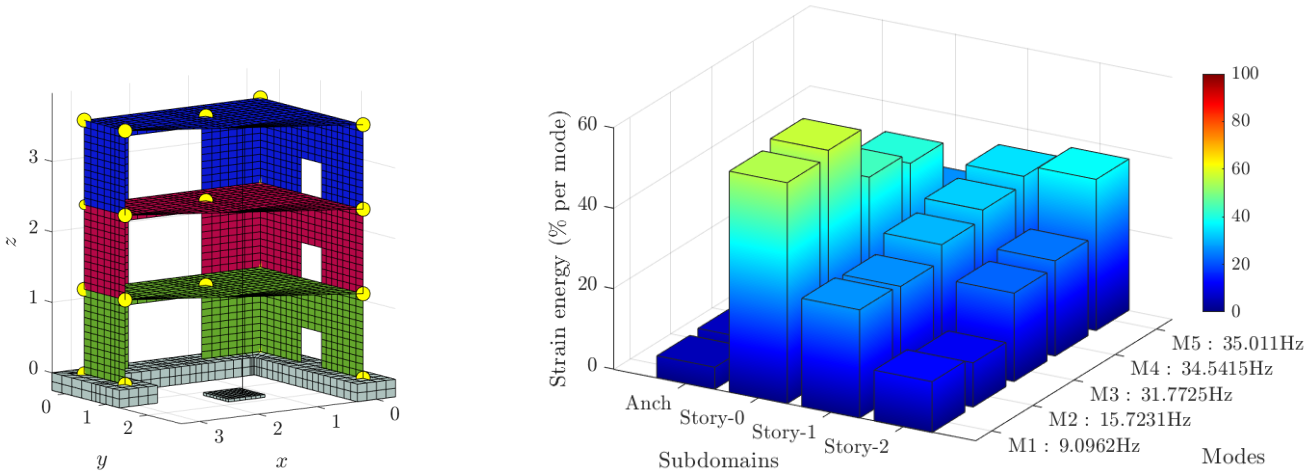

FIGURE 1.17: Four-subdomains decomposition of the SMART2013 specimen FE model and associated mechanical strain energy contributions per subdomain and per mode.

sensitive areas. As a last remark, it is highly likely that the position of sensors is not as accurate as expected: FE nodes may not perfectly correspond to sensor locations, and instrumentalists may have done errors when positioning accelerometers on the specimen as well. This induces additional model bias that may disrupt the model updating process (whatever the chosen functional). The question of sensor location trustworthiness is a short-term perspective of this thesis work.

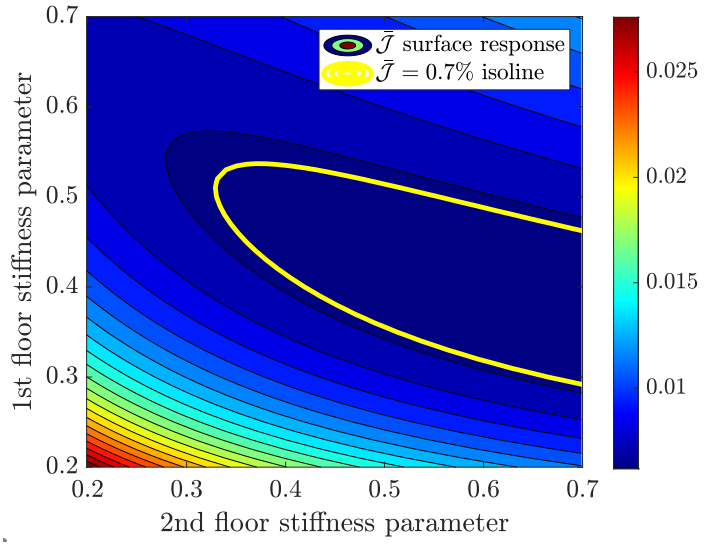

FIGURE 1.18: 2D map of the normalized mCRE $\overline{\mathcal{J}}$ with respect to the 1st and 2nd floor stiffness parameters from run #6 database. An isoline at 0.7% has been emphasized to show the (numerous) relevant set of parameters in the mCRE sense.

1.6 Conclusion & prospects

In this chapter, a robust energy-based model updating framework from data acquired in low-frequency dynamics was proposed. A strategy for correcting FE stiffness models by exploiting at best a set of available measurements *a posteriori* was discussed. The model updating methodology is based on the so-called *modified Constitutive Relation Error*. After a bibliography study and a positioning among other model updating approaches, the mCRE model updating framework has been presented for low-frequency dynamics problems, and (i) extended to random processes with a formulation of the cost function to be minimized in terms of PSDs, and (ii) tuned for an optimal integration of low-SNR measurements in the algorithm. Automated calibration rules for optimal balance between the model and measurement errors have been presented, and the H-CMIF has been exploited as a frequency weighting function to naturally emphasize the experimental eigenfrequencies of the tested structure.

The first application of the implemented algorithm for updating an academic plane frame model subjected to random ground motion validated the robustness of the approach with respect to known noise level. The second application was dedicated to the SMART2013 shaking table test campaign database. Updating a single global stiffness parameter highlighted the possibility to recover the first eigenfrequencies drops of a RC specimen submitted to a sequence of damaging seismic loadings. The nice correlation between subspace-based data-driven identification results and the mCRE-based model updating results suggest the relevance of the approach and its future use as back up to the modal analysis tools currently used at the CEA for eigenfrequency tracking [Charbonnel 2021], that are only limited to the processing of ergodic stationary signals. With the proposed approach, eigenfrequency tracking can be performed even during (stable) seismic runs, and the FE models that are developed in the predesign step of test campaigns can be reused in that sense (which is not the case so far).

In the perspective of more localized damage detection, a finer stiffness parametrization must be introduced. Unfortunately, the algorithm has not been able to provide relevant results with more than one subdomain in the SMART2013 case because of the sparse density of available recordings. The definition of an adaptive model updating strategy that exploits measurements at best to define an optimal (and economous) parametrization is a research topic that very few references have studied, whereas the coupling of adaptive processes with inverse problems may be attractive [R. Becker and Vexler 2005; Bangerth 2008; Bangerth and Joshi 2008; Puel and Aubry 2011]. The strong asset of using mCRE in such a context is the possibility to exploit the CRE as a local refinement indicator, as done for classical verification purposes [Ladevèze and Chamoin 2016]. CRE-based stiffness parametrization in preamble of the model updating process will be one of the main drivers of Chapter 2.

Eventually, the developed tools will be reinvested within a complete data-driven strategy, where coupling with data assimilation techniques and adaptive model-based control theory are the main topics discussed in Chapters 4 and 5.

Chapter 2

Towards a fully-automated mCRE-based model updating framework for damage detection

Adaptive inverse problem for optimal damage detection

The quality of the solution of an inverse problem is conditioned by inherent features of the latter, in particular (*i*) *the richness of available data,* (*ii*) *the a priori experimental and modeling knowledge that allows to regularize the ill-posedness nature of the problem, and* (*iii*) *the complexity of the space in which updated parameters are sought. Motivated by the ambition to understand and overcome the identifiability problems observed when processing the SMART campaign data, we present in this chapter a fully automated robust mCRE-based model updating framework dedicated to the correction of finite element models from low-frequency dynamics measurements. The rules to automatically calibrate mCRE internal parameters are involved, and a clustering strategy based on the CRE term allows to optimize the complexity of the space in which parameters are sought, leading to a fully autonomous algorithm* (*once the mCRE framework has been set*)*. The performance and robustness of the proposed methodology are illustrated using a numerical benchmark in which defects of various shapes are detected on a plate from noisy acceleration datasets, with focus on inherent limitations due to sensors sparsity and identifiability issues.*

The work presented in this chapter has been the subject of the following contribution:

M. Diaz, P.-É. Charbonnel, and L. Chamoin [2023c]. "Fully automated model updating framework for damage detection based on the modified Constitutive Relation Error". *Computational Mechanics*. DOI: 10.1007/s00466-023-02382-z

Contents

2.1 Introduction and motivation

From the numerical viewpoint, the integration of a digital twin requires a complex numerical framework including a robust model updating algorithm able to operate in real-time. In this chapter, we will address the possibilities to perform damage detection from sparse data collected in an offline low-frequency dynamics context, with an emphasis on the trade-off that must be found between:

- ▷ the richness and quantity of available measurements,
- ▷ the richness of excitation inputs,
- ▷ the complexity of the parameter space,
- ▷ the inherent model updating limitations due to the inverse problem itself.

The ambition of this chapter is to propose a mCRE-based fully automated model updating algorithm with the objective of identifying damaged areas optimally, *i.e.*, as accurately as possible at minimal computational cost.

In order to build a fully automated model updating strategy, all mCRE internal tuning parameters must be calibrated with rigorous and robust rules. One must then pay attention to the setting of:

- ▷ the frequency bandwidth D_ω,
- ▷ the frequency weighting function $z(\omega)$,
- ▷ the confidence into measurements coefficient α,
- ▷ the parameter space Θ in which parameters are searched.

As all these parameters have a significant impact on model updating results, a systematic tuning procedure would then be useful to handle potential non-convincing model updating results. The calibration of the 3 first items has been handled in Chapter 1 so as to guarantee relevant model updating results without requiring any user's *a priori* knowledge or experience (once the equations of the problem have been labelled as reliable or unreliable).

The selection of the parameter space and the validation of the tuning strategy for α are extensively discussed in this chapter, as no clear contribution has been found in that sense in the literature, out of empirical studies. More precisely, an automated selection of the parameter space is proposed based on the CRE discrepancies. A clustering strategy is carried out to identify in which areas model updating is more needed, generalizing the above-mentioned concept of localization of most erroneous areas. In the meantime, physics-inherent model updating limitations are highlighted, namely the impact of the sensor placement and the identifiability of defects in problems where the strain energy distribution of the tested structure is too heterogeneous.

2.2 Numerical evidences of mCRE-based model updating ill-posedness and identifiability issues

Identifiability issues have been observed in the study of SMART2013 FE models updating from acceleration data. If experimental errors may have allowed to bring them to light, the limits of identifiability reported when one intends to identify a parameter field from discrete (spatially sparse) measurements are well known, and we propose to present numerical results emphasizing on them in this paragraph.

2.2.1 Toy example: beam subjected to dynamical loading

In this section, we consider a 1D cantilevered beam made of an isotropic material submitted to a dynamical loading (see Fig. 2.1). One unknown damaged area is present, and modelled with a 50%-penalized Young's modulus for $x \in [0.5L; 0.75L]$. Synthetic measurements of known noise level coming from discrete sensors are simulated with a Newmark time integration scheme.

A similar model (without knowing the existence of the damaged area) is updated using the mCRE-based model updating algorithm with the information given by the few available sensors. In this simple example, typical updating situations are considered to draw general conclusions with regards on how to define subdomains in an automated manner.

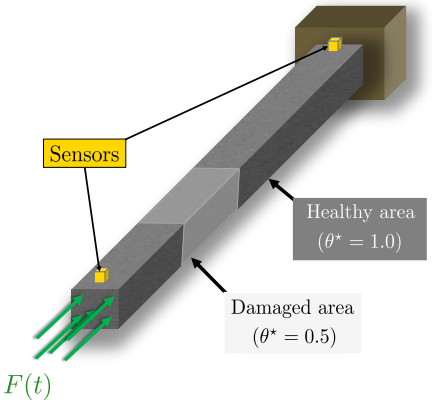

FIGURE 2.1: Cantilevered beam subjected to dynamical loading with damaged area and sensor locations.

Model updating case 1: subdomains are coarser than the defect

Considering only one subdomain (and therefore one single parameter θ) when having only two sensors and no *a priori* information is a reasonable choice. As the subdomain definition is compatible with the sensors locations, the mCRE functional remains convex around a single global minimum $\hat{\theta} \approx 0.8$ (see Fig. 2.2). The identification process is not subjected to local minima issues but the identified value only reflects the overall behavior of the structure, similarly to the SMART2013 problem of Chapter 1.

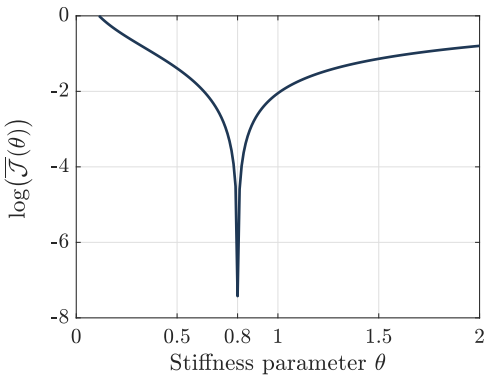

FIGURE 2.2: 1D beam FE model updating – Plot of the mCRE functional with respect to θ when only one overall subdomain is updated.

Model updating case 2: subdomains are finer than the defect

If one hopes the localization of the most erroneous areas is enough to regularize the model updating algorithm, then a finer subdomain decomposition can be chosen and only the parameters associated with erroneous areas are updated. In the considered example, one can postulate a 8-subdomain decomposition with exclusively parameters θ_5 and θ_6 updated (see Fig. 2.3). The lack of local information makes the algorithm unable to identify a global minimum: there exists an infinite number of couples (θ_5, θ_6) that are equivalent in the mCRE sense (even if $(\hat{\theta}_5, \hat{\theta}_6) = (0.5, 0.5)$ is one of them).

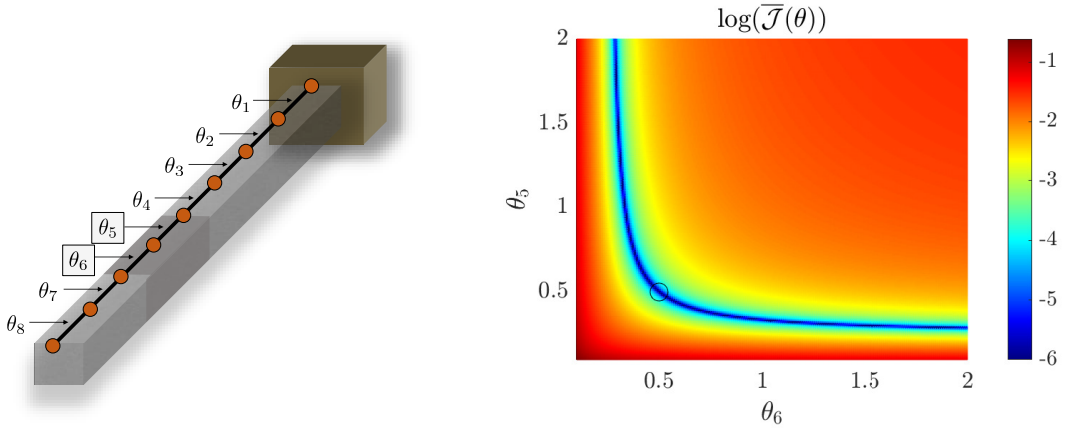

FIGURE 2.3: 1D beam model updating – 8 subdomain decomposition and mCRE map with respect to the two parameters related to the damaged area. The expected parameters (black circle) are located within a valley of local minima, leading irrelevant identification results.

Preliminary conclusions

From the previous results, it should be concluded that **the sparsity of available information is a constraint that is unavoidable and due to the experimental setup**. The mCRE functional is directly impacted by the lack of richness of local information to identify defects accurately. The definition of coarser subdomains regularizes the solution of the minimization problem and helps the convergence towards global minima. Coupled with the localization and correction of the most erroneous areas, it can at least provide good trends to identify damaged areas. In particular, it should be emphasized that:

- ▷ **A low-dimensional parameter space naturally regularizes the model updating process**. The compatibility of subdomains with the available sensors is crucial, even if the localization/correction of the most erroneous areas should help the model updating algorithm to converge.
- ▷ A high-dimensional parameter space is more likely to lead to irrelevant identification results because **several unequal parameter sets (local minima in the parameter space) can have the same overall response if no local information is available**. It confirms that the shape of subdomains should be defined in accordance with the sensors at disposal.

2.2.2 Inherent mCRE identifiability issues and confidence intervals

Cantilevered wall

The sensor placement configuration and the input sollicitation condition the identifiability of parameters and the accuracy of model updating results. These two features may lead to non physical-meaning identification results if they do not allow parameters to be sensitive to mCRE[1].

As the mCRE formulation for stiffness parameters is strongly related to strain energy, one could not expect to identify accurately field parameters in areas where little strain energy is present. This is another reason that may explain the poor identification results obtained when refining subdomains in the SMART2013 problem. To illustrate the identifiability issue on an academic example, let us consider the case of a cantilevered wall having two rectangular defects, submitted to a plane ground motion (see Fig. 2.4). Accelerometers are scattered on the wall and oriented in the outer plane direction, *i.e.* the loading direction. This structure has a highly heterogeneous strain energy distribution: most of it is stored at the bottom of the structure, making the identification of the top defect impossible. In practice, the CRE map is totally insensitive to the top defect even if sensors are located nearby, as shown in the mCRE surface

[1] Actually, this remark has to be made for all inverse problem strategies.

plot of Fig. 2.5 that has been obtained after the (strong) assumption that the two damaged areas were correctly captured. The damage located at the top of the frame is not identifiable as the mCRE totally lacks of sensitivity with respect to the associated parameter.

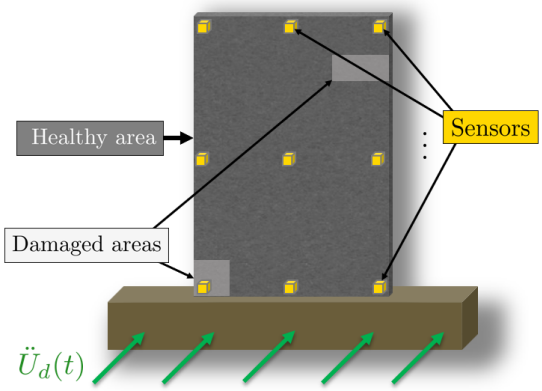

FIGURE 2.4: Cantilevered wall subjected to random ground motion with two damage defects to recover.

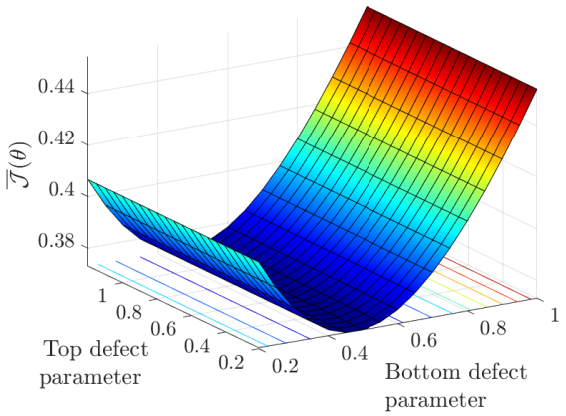

FIGURE 2.5: Evidence of the unidentifiability issue: areas storing few strain energy are less prone to relevant mCRE-based accurate identification.

mCRE-based confidence intervals

What should be recommended to future mCRE users is to plot relative confidence intervals at convergence [Charbonnel et al. 2013]. This low-cost operation will allow to anticipate and assess possible identification difficulties.

Briefly, when identifying several parameters simultaneously, one could wonder what relative precision is reached in the identification process for *Uncertainty Quantification* (UQ). To do so, one can thus consider the computation of confidence intervals. Mathematically, due to the mCRE convexity, there exists a subset $I_\theta \subset \Theta$ such that:

$$\forall\, \theta \in I_\theta, \quad \mathcal{J}(\theta) < \epsilon \mathcal{J}(\theta_0) \tag{2.1}$$

From a UQ point of view, quantifying the measure of I_θ has more sense than the optimal parameters $\widehat{\theta}$ because of the impact of any measurement perturbation on it and the heterogeneous sensitivity of parameters to the model updating problem itself. As explained in [Charbonnel et al. 2013], providing optimal parameters inside confidence intervals is an original and effective way to deal with the *Lack Of Knowledge* associated to the numerical model with a low computational cost, as it is a one-step direct post-processing procedure that is performed easily as mCRE gradient and Hessian matrix have semi-analytical expressions (see Appendix B). The width of the interval I_θ for a given threshold ϵ can be established using a second order Taylor polynomial approximation around the optimal parameters $\widehat{\theta}$:

$$\mathcal{J}(\theta) = J(\theta) + \mathcal{O}\left((\theta - \widehat{\theta})^3\right) \text{ with } J(\theta) = \mathcal{J}(\widehat{\theta}) + \left[\frac{\mathrm{d}\mathcal{J}}{\mathrm{d}\theta}\right]^T (\theta - \widehat{\theta}) + \frac{1}{2}(\theta - \widehat{\theta})^T \left[\frac{\mathrm{d}^2\mathcal{J}}{\mathrm{d}\theta^2}\right] (\theta - \widehat{\theta}) \tag{2.2}$$

Once a threshold ϵ is chosen (its value is a user's choice), the relative width of the confidence intervals allows to identify which parameters are estimated with more doubt than others, which can be relevant for possible focusing model updating actions exclusively on highly sensitive parameters.

> *Remark* 2.1. As explained, the proposed confidence intervals are not rigorously able to quantify the uncertainties on $\widehat{\theta}$. Nonetheless, choosing a consistent value of ϵ after model updating convergence should be enough to draw preliminary conclusions on the identifiability of parameters.

2.3 CRE-based parametrization for fully automated model updating

As explained in Chapter 1, the CRE term provides a direct insight regarding the intrinsic validity of the model. As all finite element contributions to CRE can be computed independently, it is a relevant tool for identifying erroneous parts of the model. This asset can be seen as a Tikhonov regularization because a restrained number of parameters can be updated. However, the efficiency of the localization criterion is constrained by the threshold β of (1.26). If most references consider that $\beta = 0.8$ is a convenient value, no clear parametric study has been performed in order to optimize the choice of β for optimal defect detection based on noisy datasets. Therefore, if the CRE can be a convenient local model indicator, the localization criterion (1.26) alone is limited to provide an automated parametrization (and associated subdomains). The remainder of this section is devoted to present a novel CRE-based clustering technique for automated subdomain definition, which aims to extend the localization criterion traditionally used in the mCRE-based model updating framework.

2.3.1 A brief overview of clustering techniques for automated data analysis and classification

Clustering is one of the most widely used techniques for data analysis and classification [Miyamoto et al. 2008]. The objective of cluster analysis is the classification of objects according to similarities among them, and therefore organizing datasets into groups (the so-called *clusters*). Without going into much details, clustering techniques allow to partition a space in the sense of a given metrics: within a cluster, the distance between objects remains small, whereas the distance between objects of different clusters is larger. There exists many clustering techniques: hard clustering, fuzzy clustering [Bora and Gupta 2014], spectral clustering [Luxburg 2007] to only cite a few of them. Regarding civil engineering applications, clustering algorithms have been mostly used to automatically identify physical modes in modal analysis stabilization diagrams [Carden and J. M. W. Brownjohn 2008; Reynders et al. 2012; Charbonnel 2021].

To recall algorithmic principles in a nutshell, in hard clustering techniques, the data to classify $X \in \mathbb{R}^{d\times N}$ is divided into distinct clusters, where each data point can only belong to exactly one cluster. To do so, the cluster center locations $\{C_j\}_{j=1}^{k}$ are optimized such that:

$$\{C\} = \arg \min_{C_j \in \mathbb{R}^d} \sum_{j=1}^{k}\sum_{i=1}^{N} \|X_i - C_j\|_2^2 \tag{2.3}$$

and the data samples are then directly classified into clusters according to their distance to centers. Although efficient, such algorithms tend to be less effective when dealing with not-well separated, and non-spherical clusters. This motivated the development of *fuzzy clustering* (also referred to as soft clustering) where membership functions are associated to each data point X_i, which somehow relaxes the belonging to a given cluster. The membership function of data point i to cluster j is denoted μ_{ij} and takes values in $[0;1]$. As a consequence, a data point X_i will be more likely to belong to a cluster j if $\mu_{ij} \to 1$. Using a non-necessary Euclidean norm $\|\square\|_A$, the centers and membership functions are sought according to the following constrained minimization problem:

$$\{C,\mu\} = \arg\min_{C,\,\mu} \underbrace{\sum_{j=1}^{k}\sum_{i=1}^{N} \mu_{ij}^m \|X_i - C_j\|_A^2}_{J(C,\mu;X)} \quad \text{with} \quad \sum_{j=1}^{k} \mu_{ij} = 1 \;\forall i \in [\![1;N]\!] \tag{2.4}$$

where the exponent m reflects the degree of fuzziness of the partition: if $m = 1$ corresponds to hard clustering, $m = 2$ is the classical (empirically) chosen value in many applications. The Hermitian norm $\|\square\|_A$ can be defined using a positive definite matrix A, identically chosen for all clusters. Alternatively, the metric can be defined using a k-tuple $\{A_j\}_{j=1}^{k}$, with A_j a positive

definite matrix. The objective function is then extended as $J(C, \mu, A; X)$. This choice allows better identification of elliptic and overlapping clusters. More details on that subtility can be found in [Charbonnel 2021]. In any case, the constrained minimization of these methods is performed numerically using a fixed-point algorithm that iteratively optimizes all the arguments of the functional J (see Alg. 2.1).

Algorithm 2.1: Fuzzy clustering algorithm developed in [Charbonnel 2021]

Data: Data $X \in \mathbb{R}^{E\times d}$, number of clusters to identify k, initial centers $\{C_j^0\}_{j\in[\![1;c]\!]}$ (if known, otherwise random pick), threshold ϵ_0

Result: Updated cluster centers $\{C_j\}_{j\in[\![1;k]\!]}$, ellipticity $\{A_j\}_{j\in[\![1;k]\!]}$ and data points membership functions $\{\mu_{ij}\}_{(i,j)\in([\![1;E]\!]\times[\![1;k]\!])}$

Start with circular cluster shapes $A_j = \boldsymbol{I}\ \forall\ j \in [\![1;k]\!]$;

Assign cluster centers $\{C_j\}_{j\in[\![1;k]\!]}$ with the initial guesses $\{C_j^0\}_{j\in[\![1;c]\!]}$, random pick otherwise ;

Fixed-point algorithm

while $J(C, \mu, A; X) > \epsilon_0$ **do**

Compute membership functions $\mu_{ij} = \left[\sum_{p=1}^{k} \frac{\|X_i - C_j\|^2_{A_k}}{\|X_i - C_p\|^2_{A_p}}\right]^{-1} \quad \forall\ (i,j) \in ([\![1;E]\!]\times[\![1;k]\!])$;

Update centers position $C_j = \frac{\sum_{i=1}^{E} \mu_{ij}^2 X_i}{\sum_{i=1}^{E} \mu_{ij}^2}\ \forall\ j \in [\![1;k]\!]$;

Compute the cost-function $J(C, \mu, A; X) = \sum_{i=1}^{E}\sum_{j=1}^{k} \mu_{ij}^2 \|X_i - C_j\|^2_{A_j}$;

Update the ellipticity of clusters $A_j = (\rho_j|\Sigma_j|)^{1/d}\Sigma_j^{-1}\ \forall\ j \in [\![1;k]\!]$

with $\Sigma_j = \frac{\sum_{i=1}^{E} \mu_{ij}^2 (X_i - C_j)(X_i - C_j)^T}{\sum_{i=1}^{E} \mu_{ij}^2}$, $\rho_j = \frac{k|D_j|^{1/(d-1)}}{\sum_{p=1}^{k}|D_p|^{1/(d-1)}}$ and $D_j = \frac{1}{|\Sigma_j|}\left[\sum_{i=1}^{E}\mu_{ij}^2\right]^d$;

end

However, the damage pattern in a structure may not be convex, particularly when several damaged areas have to be identified. When non-convex clusters are expected, spectral clustering techniques often outperform the above-mentioned traditional approaches by performing clustering on a transformed dataset which hopefully provides better separated and more easily identifiable clusters. The interested reader can find a pedagogical and detailed tutorial in [Luxburg 2007].

Spectral clustering is widely used because of its simplicity to implement and it can be solved efficiently by standard linear algebra methods. The key idea of spectral clustering is to transform the coordinates of the pattern matrix to recover convex subdomains. In practice, a mapping $\mathcal{C}$ is derived from the data X to transform non-convex and possibly overlapping clusters into hopefully better separated clusters of more convex shape Y, through a change of variable:

$$Y = \mathcal{C}(X) \tag{2.5}$$

The mapping $\mathcal{C}$ (more precisely the transformed dataset Y) is constructed from the smallest eigenvalues (0 in the ideal case) of the so-called graph Laplacian L following the steps described hereafter:

- ▷ A similarity matrix S is first assembled. The coefficient S_{ij} estimates how much a given point X_i belongs to the vincinity of X_j. Almost unit values are associated to close points whereas smaller values concern more distant points. The similarity matrix construction is not unique; a common way to do so is to use a Gaussian similarity function and a tuning parameter σ controlling the width of the neighborhood where points are considered closed:

$$S_{ij} = \exp\left(-\frac{1}{2}\frac{\|X_i - X_j\|^2}{\sigma^2}\right) \tag{2.6}$$

Complementary details regarding the definition of the similarity matrix can be found in [Charbonnel 2021].

▷ The graph Laplacian can then be computed. Various weightings have been considered to improve the condition number of L:

$$L = D - S \tag{2.7}$$

$$L_{sym} = D^{-1/2} L D^{-1/2} \text{ (symmetric weighting)} \tag{2.8}$$

$$L_{rw} = D^{-1} L \text{ (random walk weighting)} \tag{2.9}$$

where D is the degree matrix defined as $D_{ij} = \delta_{ij} \sum_{j=1}^{N} S_{ij}$, δ_{ij} denoting the Kroenecker operator.

▷ A set of k eigenvectors $\{\Lambda_c\}_{c\in[\![1;k]\!]}$ corresponding to the k smallest eigenvalues of L (or its weighting variants) are then extracted, yielding to the transformed pattern matrix Y:

$$Y_i = \frac{\Lambda_i}{\left(\sum_{c=1}^{k} \Lambda_c^2\right)^{1/2}} \tag{2.10}$$

Then, hard or fuzzy clustering techniques can be applied to define the clusters on Y, that are built to be more convex in the transformed coordinates space.

An illustration of clustering techniques

The scatter plots presented in Fig. 2.6 and 2.7 illustrate the performance of the above-mentioned clustering techniques and allow to compare them on 2D data classification problems[2]. Fig. 2.6 highlights that fuzzy clustering allows to identify points at the border of clusters (without excessive additional CPU cost). The data points deemed to belong to both clusters are those having membership functions values close to 0.5.

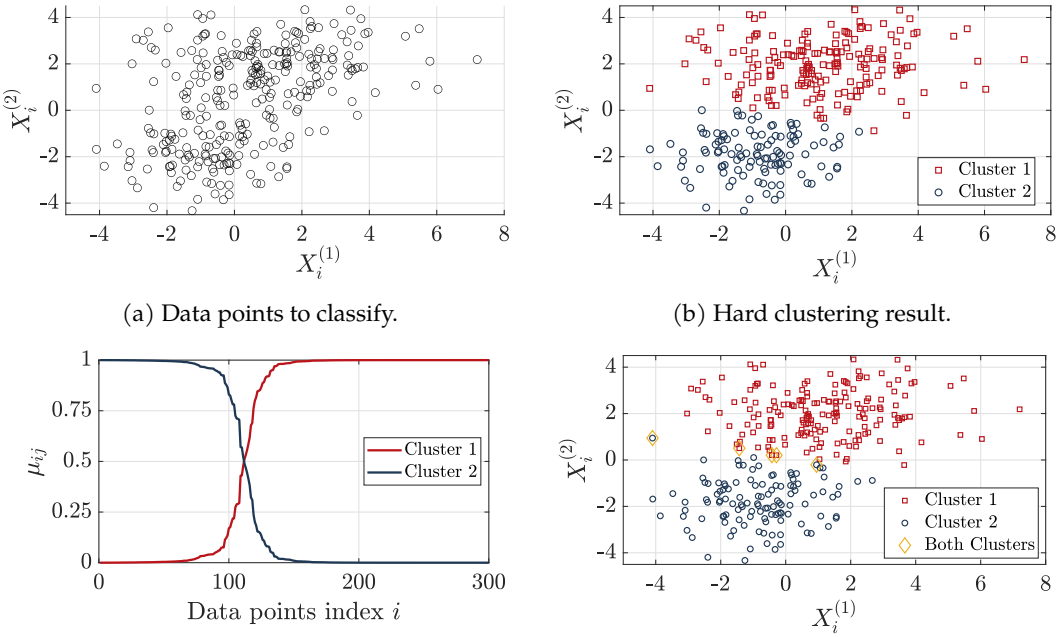

(a) Data points to classify.

(b) Hard clustering result.

(c) Fuzzy clustering membsership functions.

(d) Fuzzy clustering result.

FIGURE 2.6: Hard vs. fuzzy clustering comparison on a 2D database of well-separated non-spherical clusters.

[2]Complementary tutorials are also available online. For instance, MATLAB© users can refer to https://fr.mathworks.com/help/fuzzy/fuzzy-clustering.html.

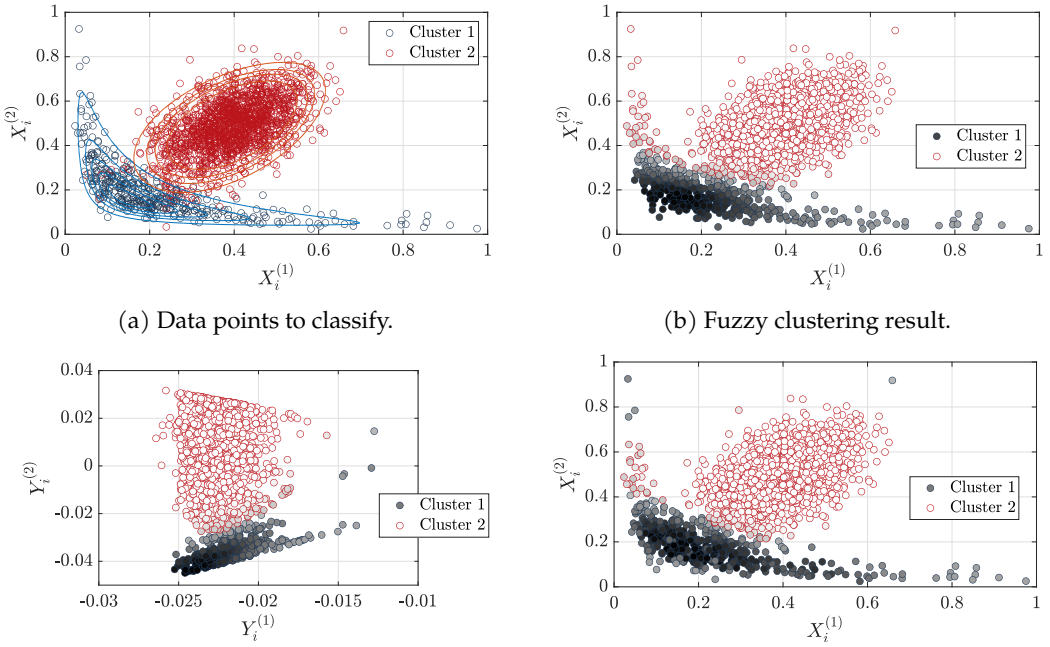

(a) Data points to classify.

(b) Fuzzy clustering result.

(c) Graph Laplacian mapping and fuzzy clustering.

(d) Spectral clustering result.

FIGURE 2.7: Fuzzy vs. spectral clustering comparison on a 2D database of poorly-separated non-convex clusters. Markers gray levels correspond to the membership functions values.

2.3.2 CRE-based clustering for automated parameter space definition

In this work, the fuzzy k-means clustering algorithm developed in [Charbonnel 2021] is reinvested. Originally intended to separate the physical modes from the spurious modes produced by a growing model-order identification algorithm in a modal analysis context, its robustness with respect to non-convex, poorly dissociated, and heterogeneous clusters makes it a relevant tool to define parameter distributions from the CRE map. Starting from the initial model, the key idea is to identify a cluster of most erroneous elements through the computation of the modeling error (CRE) map per element which naturally emphasizes the damaged area. In other words, a two-cluster distinction is performed from the normalized CRE map:

$$X = \frac{\left\{ X_i - \min_{i\in[\![1;E]\!]} \{X_i\} \right\}_{i=1}^{E}}{\max_{i\in[\![1;E]\!]} \left\{ X_i - \min_{i\in[\![1;E]\!]} \{X_i\} \right\}}, \; X_i = \int_{D_\omega} z(\omega)\zeta_{\omega,i}^2 \mathrm{d}\omega \tag{2.11}$$

which allows to label each finite element as "healthy" or "erroneous". Note that this is not a computationally expensive procedure as it is a (vectorizable) post-processing operation once mechanical fields solution of (1.20) has been obtained.

The clustering algorithm technical details (with notations independent from the rest of the manuscript) are given in Alg. 2.1. In the latter, the ellipticity of clusters is updated as well. It is important to notice in this case that the initial position of clusters is specified $(C_1, C_2) = (1, 0)$ so that the first cluster is enforced to be the cluster of erroneous elements. Doing so also avoids the undesired case of equal partitioning when random initial centers are specified.

> *Remark* 2.2. Note that, so far, the number of clusters and center initializations remain unspecified. Before converging towards this clustering framework, several tests were performed: in particular, we tried to cluster a multidimensional dataset X made of the CRE per element, with barycentric coordinates specified. Multiple clustering in this 4D space was interesting in the perspective to assign one parameter per identified defect. However, the absence of finite element barycentric coordinates in X allows to simultaneously identify damaged areas

at different locations. It avoids the complex discussion about the robustness of clustering algorithms when the number of clusters to identify changes from an application to the other [Balasko et al. 2005], and to obtain inaccurate parameter estimates due to a coarse shaping of the damage defect to identify.

The pseudo-code associated to the main steps of the fully automated model updating process is given in Alg. 2.2. At the end of the CRE-based clustering, a new parameter space $\widehat{\Theta}$ is defined in which all erroneous elements are updated independently whereas the healthy elements remain unchanged. This can be interpreted as a generalization of the localization of most erroneous areas principle that was mentioned earlier, but in a more adaptive manner. Numerical illustrations are provided in Section 2.5.

Note that the normalization of the CRE between 0 and 1 before performing clustering allows to automate the initialization of the CRE-based clustering algorithm. Besides, this is efficient in terms of parametrization as long as the overall initial guess is well calibrated, otherwise all elements can be classified as erroneous. Therefore, it is recommended to perform a preliminary model updating procedure with large subdomains (even only one) to properly calibrate the FE model in case of strong *a priori* discrepancies between model predictions and observed data.

Algorithm 2.2: Fully automated mCRE-based model updating algorithm

Data: FE model including mesh and matrices $\boldsymbol{K}, \boldsymbol{D}, \boldsymbol{M}$, subdomain decomposition and associated parameter guess $\theta_0 \in \Theta_0$, measurements $\{y(t)\}$
Result: Updated set of parameters $\hat{\theta} \in \widehat{\Theta}$.

Preamble & initialization:
Computation of the reduced basis $\boldsymbol{\Phi}_L$;
Data frequency domain preprocessing: $Y_\omega \; \forall \, \omega \in D_\omega$;
Data-based computation of $z(\omega)$ using a normalized H-CMIF ;
Confidence into measurements scalar $\widehat{\alpha}$ calibration following (1.42) or (1.44) ;
Evaluation of the initial quality of the model: $\mathcal{J}_0 = \mathcal{J}\left(\theta_0\right)$;
Choice of thresholds ϵ_1, ϵ_2 ;

CRE-based clustering for subdomain definition
Computation of the CRE map per element $\zeta^2_{\omega,e}\left(s_\omega, \theta^{(0)}\right) \; \forall \left(\omega, e\right) \in \left(D_\omega \times \Omega_e\right)$;
CRE-based clustering to identify the subset of most erroneous elements using Alg. 2.1 with 2 clusters of centers initialized at $(1, 0)$;
Definition of the parametrization $\widehat{\Theta}$, as all false elements are independently updated ;

Model updating algorithm
while $\overline{\mathcal{J}}\left(\theta^{(k)}\right) \leqslant \epsilon_1$ *and* $\left|\theta^{(k)} - \theta^{(k-1)}\right| \leqslant \epsilon_2 \left|\theta^{(k-1)}\right|$ **do**

Iterative correction
Minimization of $\mathcal{J}(\theta) : \theta^{(k+1)} \leftarrow \theta^{(k)}$ with respect to the parameters from Step 1 (BFGS method with supplied gradient - see (1.27)) ;

Convergence assessment
Convergence criteria computation: $\overline{\mathcal{J}}(\theta^{(k+1)})$ and $\left|\frac{\theta^{(k+1)} - \theta^{(k)}}{\theta^{(k)}}\right|$;

end

Remark 2.3. A CRE-based subdomain refinement strategy has also been considered to try to catch at best the shape of defects. In this iterative process (not presented in detail as inconclusive), all the elements gathered in the "erroneous" areas were weighted by the same stiffness parameters. Iteratively, following the CRE map, subdomains were refined and the dimension of Θ progressively increased where needed. However, it was empirically noticed that the updating results were corresponding to local minima typical of the toy example of Section 2.2.1.

For instance, following the work of [Bangerth and Joshi 2008; Puel and Aubry 2011], a quadtree subdomain refinement technique was implemented on the case study described in Fig. 2.4. The idea consisted in an iterative quadtree refinement of most erroneous subdomains (in the CRE sense). The algorithm was therefore close to what is presented in Alg. 2.2, except that the parameter space was updated as well (*i.e.* $\theta^{(k)} \in \Theta^{(k)}$). The wall case is optimal for quadtree refinement because the bottom defect one can detect with mCRE has a squared shape as well. Although the model updating process efficiently localizes the damaged area, it has not been able to quantify it properly due to the fall into local minima that is unavoidable in an iterative inverse problem solution (see Fig. 2.8).

Besides, note that this approach was not adapted to the simultaneous detection of several defects, and not compatible with the on-the-fly model updating prospects of this work.

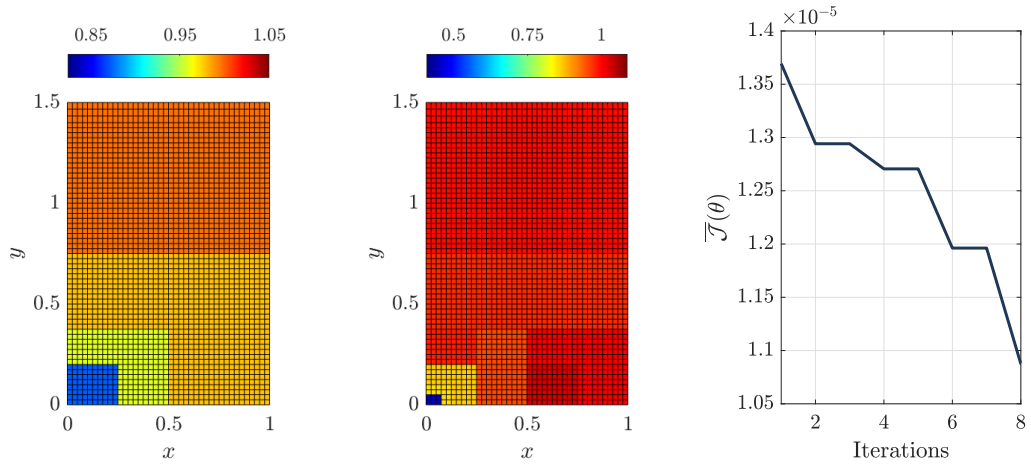

FIGURE 2.8: Quadtree refinement of the parameter space for damage detection. From left to right: parameter estimates at iterations 4 and 8, and mCRE evolution during the whole adaptive process. Localization is correctly performed, but the model updating algorithm converges towards local minima parameter values.

2.4 Alternative approach: sparse-regularized mCRE for localized corrections

Following the developments of [Guo et al. 2018; Ferrier et al. 2021], one could also imagine adding an explicit regularization term to the mCRE so as to favor some *a priori* knowledge on the parameter estimates that are sought. In particular, when it comes to detect localized damage, sparse regularization should allow to focus the model updating process to a reduced amount of parameters [C. D. Zhang and Y. L. Xu 2016; Benning and Burger 2018]. The sparse-regularized mCRE functional $\mathcal{J}_r$ reads as follows:

$$\mathcal{J}_r(\theta; Y, \theta_0) = \int_{D_\omega} z(\omega) e_\omega^2(\widehat{s}(\theta, ; Y_\omega), \theta; Y_\omega) \, \mathrm{d}\omega + \gamma \|\theta - \theta_0\|_1 \tag{2.12}$$

where θ_0 is the *a priori* information one has on the parameters (healthy area stiffness value for example), γ is the weighting parameter allowing to give more or less importance to the regularization, and $\|\square\|_1$ refers to the L_1-norm. The minimization of this functional can be performed using the same algorithmic structure and mathematical developments that have been presented previously, except for the analytical gradient formulation that must be slightly changed to integrate the regularization term. However, the introduction of a new *a priori* information goes against the philosophy of the mCRE which intends to analyze the mechanical equations of the problem in order to exempt the inverse problem of any expert-user's judgment. Another disadvantage of this technique is the arbitrary nature of the choice of a regularizing parameter γ which impacts the smoothness of the solution [Titurus and Friswell 2008].

The impact of sparse regularization and a comparison with CRE-based clustering is proposed in Section 2.5.

> *Remark* 2.4. The purposes of the clustering step and the additive sparse regularization are similar. The use of the CRE to define an optimal parameter space seems to be a more natural approach within the mCRE framework. If one performs model updating without clustering, the effect of the sparse regularization (once well calibrated) should be beneficial on the accuracy of the identified parameters, but it is likely that the clustering alone will be as efficient in terms of accuracy and more robust because less calibration efforts are needed.

2.5 Application to damage detection from sparse data

2.5.1 Description of the problem and objectives of the study

In this section, numerical results are presented and discussed to assess the relevance of the automated mCRE-based model updating strategy for damage detection with typical earthquake engineering applications. To evaluate the performance of the methodology, academic examples are considered in which a simply supported plane rectangular floor is subjected to a vertical low-magnitude ground acceleration input. The reference meshes with the defects one hopes to identify are shown in Fig. 2.9. The optimality criteria for α that have been previously discussed are compared and assessed, as well as the effect of an additional sparse regularization term.

A uniform sensor placement is considered: discrete accelerometers oriented in the outer plane direction are spread over the structure to collect data at the sampling frequency $f_s = 1000$ Hz. The effect of sensor density is illustrated in the following by comparing the sensor placement configurations shown in Fig. 2.10, characterized by the distance between sensors d_s, and more carefully studied in Chapter 3. In order to assess the robustness of the methodology with respect to measurement noise, a white noise of known standard deviation is added to simulated data in order to process noisy synthetic measurements. $\delta \in [0; 1]$ represents in the following the noise level with respect to the input ground acceleration standard deviation $\text{std}(\ddot{U}_d)$.

Two damage detection problems are considered to assess the potentialities of the methodology (see Fig. 2.9):

(a) a Y-shape defect (representative of a propagated crack with bifurcation) that is modeled with a local 50% stiffness loss, and

(b) a double circular inclusion problem, respectively modeled with local 50% and 70% stiffness losses.

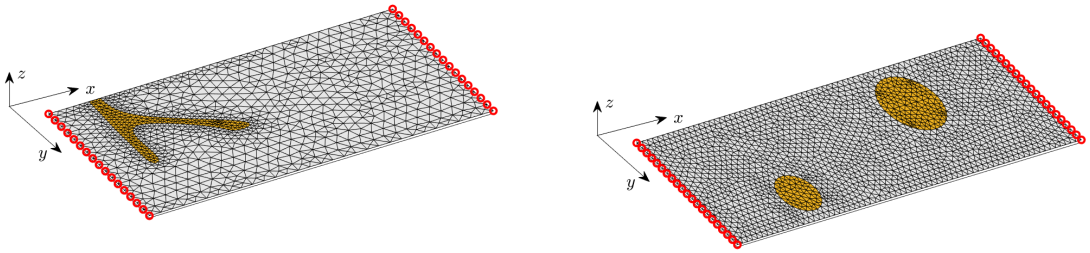

(a) Y-shape defect (propagated crack with bifurcation).

(b) Double circular inclusion defects.

FIGURE 2.9: Reference FE meshes to simulate synthetic data with emphasis on the defect areas Ω_d to identify (orange elements). Locked dofs are specified with red circles.

If the first case is much more representative of what could happen in actual experiments involving crack propagation, the double inclusion case will allow to assess the robustness of the

clustering algorithm to identify several defects while the Y-shape case will permit to assess the possibility to perform relevant clustering of non-convex CRE distributions.

Meshes and FE matrices (reference and initial guess) are built using the CEA simulation sotfware Cast3M© before being uploaded in a MATLAB© environment. In both cases, the initial model guess is made of regular quadrangular shell elements whose homogeneous Young's modulus is equal to the non-damaged reference. Note that, because triangular elements have been used in the reference mesh, a modeling error bias is implicitly introduced as the mesh of the updated model is not compatible with the defects to identify.

The knowledge of the expected parameter estimate $\theta^\star$ enables to assess the model updating accuracy using the following accuracy indicators:

$$\eta(\theta,\theta^\star)=\frac{\displaystyle\int_\Omega \|\theta-\theta^\star\|^2\,\mathrm{d}\Omega}{\displaystyle\int_\Omega \|\theta^\star\|^2\,\mathrm{d}\Omega} \quad ; \quad \eta_d(\theta,\theta^\star)=\frac{\displaystyle\int_{\Omega_d} \|\theta-\theta^\star\|^2\,\mathrm{d}\Omega}{\displaystyle\int_{\Omega_d} \|\theta^\star\|^2\,\mathrm{d}\Omega} \tag{2.13}$$

which indicate the closeness of an estimate θ to the expected parameter set $\theta^\star$, respectively on the full structure Ω or on the restriction to the damaged area Ω_d (see Fig. 2.9).

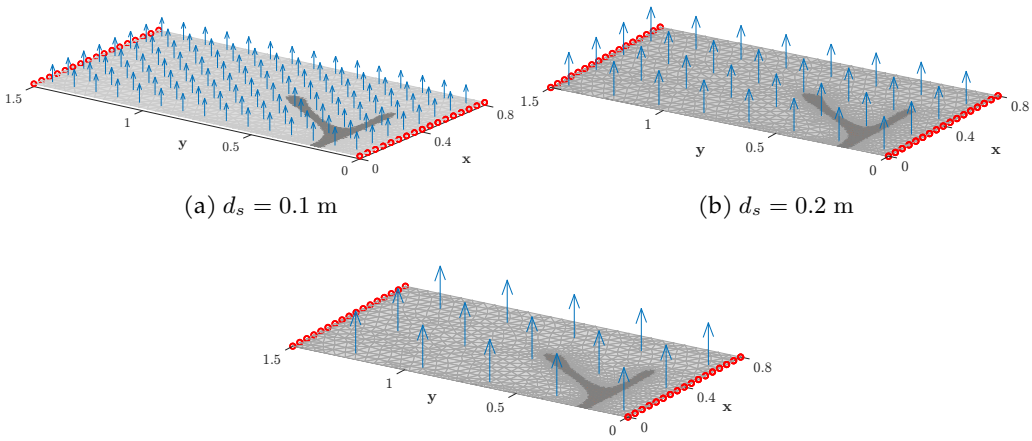

(a) $d_s = 0.1$ m (b) $d_s = 0.2$ m

(c) $d_s = 0.3$ m

FIGURE 2.10: Three uniform sensor placement configurations with different densities (quantified by the distance between sensors d_s). Blue arrows locate the discrete accelerometers and red circles emphasize on boundary conditions.

Performing an accurate model updating from sparse and noisy data in that case is a complex task, particularly for a non-convex defect to recover. From these 2D earthquake engineering-inspired examples, the aim is to emphasize the main underlying issues of model updating from discrete sensors and to validate the automated strategy presented previously. To do so, a complete numerical study is conducted with several objectives:

- ▷ illustrate the limits of the localization criteria for damage detection and emphasize the effectiveness of the CRE-based clustering step for automated parametrization;
- ▷ assess both effectiveness and soundness of the two criteria proposed in Section 1.4.3 for automated calibration of α and evaluate the influence of the confidence into measurements scalar α on parameter estimates;
- ▷ evaluate the robustness of the automated mCRE-based model updating algorithm with respect to measurement noise;
- ▷ illustrate the damage detection expectations from limited sensor density;
- ▷ assess the benefits of the additional sparse regularization to the mCRE functional.

For the sake of conciseness, all similar numerical results will not be shown as most of them are redundant between the two configurations of Fig. 2.9 (in terms of results analysis). As the

Y-shaped defect is the most challenging application, results will mainly be focused on the latter, whereas the inclusion example will be used to drive complementary discussions.

In terms of mCRE calibration, as the first eigenmode (which is the most excited) is at around 20 Hz, a frequency bandwidth $D_\omega = [1\text{ Hz}; 30\text{ Hz}]$ with $\Delta f = 0.1$ Hz has been chosen for the computation of all forthcoming results. The call to a reduced basis made of the first 20 eigenmodes of the structure allowed to achieve convergence in fast CPU times (between 0.5 and 2 minutes per mCRE-minimization with CRE-based clustering) on a personal laptop.

The remainder of this section is structured according to the (above-mentioned) major objectives of this numerical study in order to emphasize the potentialities and limitations of mCRE-based model updating algorithm from discrete noisy data.

2.5.2 Limits of the localization criterion for optimal damage detection

First, a parametric study on the localization parameter β defined in (1.26) has been made in order to assess the capabilities of classical mCRE-based model updating to perform optimal damage detection, *i.e.*, accurate identification at low computational cost. It considers the most convenient model updating setting: large amount of data (sensor placement (a) from Fig. 2.10) and perfect measurements ($\delta = 0\%$) which yields a high confidence into measurements.

The criteria (2.13) are computed for each parameter estimate identified at convergence and stored in Tab. 2.1. Two typical model updating results are plotted in Fig. 2.11 and 2.12. One can observe that mCRE-based model updating with strong localization (Fig. 2.11) is accurate at the full structure scale as it does not correct many parameters (letting most of the undamaged area unchanged). However, the few parameters that are corrected do not permit to obtain an accurate defect shape. On the contrary, with a lower localization value (Fig. 2.12), the defect shape is accurately described, but unexpected corrections occur in the undamaged area, which leads to parameter estimates that are not optimal in the sense of η. Besides, note that the CPU time increases for low values of β as a (too) large amount of parameters is updated at once. Finally, one should notice that iterative model updating approaches with a high value of β do not improve identification results as they take more CPU time and often fall into equivalent solutions (at the specimen scale) that do not describe the defect accurately.

Therefore, the localization of most erroneous areas principle, which regularizes the model updating algorithm in the Tikhonov sense, is not sufficient to perform accurate damage detection from sparse data in reasonable computational times. Comparative results obtained with CRE-based clustering are given in Fig. 2.13 for the same model updating context. As observed, only a restrained group of finite elements is corrected (60 among 480). This group of elements correctly matches with the shape of the damaged area because of its CRE-based construction and permits to obtain an accurate estimate, as shown in Tab. 2.1. Besides, the comparison of modeling error (CRE) map before and after model updating confirms the efficiency of the proposed approach.

Localization parameter β	$\eta(\widehat{\theta}, \theta^\star)$	$\eta_d(\widehat{\theta}, \theta^\star)$	CPU time [s]
0.2	0.00859	1.897	> 5000
0.3	0.00880	1.829	1670
0.4	0.00932	1.794	526.2
0.5	0.01212	1.833	171.9
0.6	0.01041	1.966	192.5
0.7	0.01783	2.168	33.8
0.8	0.04982	2.431	39.6
with CRE-based clustering	0.00955	1.641	100.3

TABLE 2.1: Emphasis on the limitations of the localization of most erroneous areas for accurate and efficient damage detection in the most favorable damage detection case (noisy-free data - high sensor density).

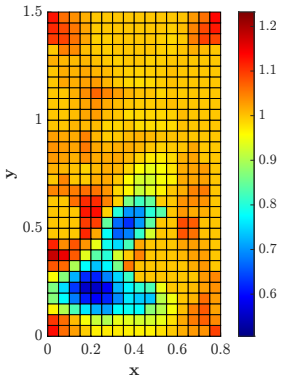

FIGURE 2.11: $\widehat{\theta}$ for $\beta = 0.2$. 92% of elements are individually updated.

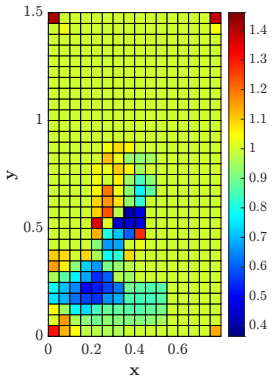

FIGURE 2.12: $\widehat{\theta}$ for $\beta = 0.4$. 25% of elements are individually updated.

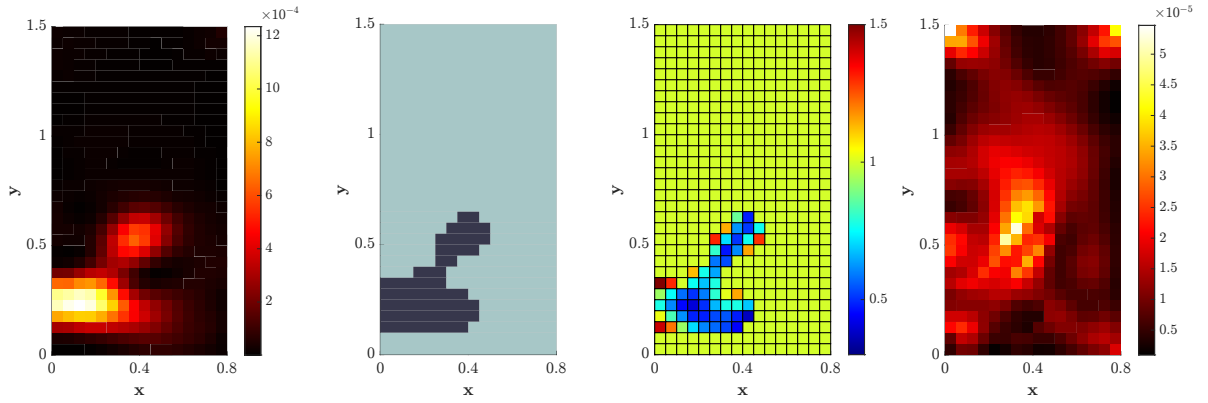

(a) Initial CRE map. (b) Clustering. (c) Parameter estimate. (d) Residual CRE map.

FIGURE 2.13: Fully automated mCRE-based model updating results obtained with the sensor placement of Fig. 2.10a and noise-free data. The CRE-based clustering step allows to restrain correcting actions on the area that surrounds the defect to identify.

2.5.3 Automated confidence into measurements

One of the objectives of this study, already raised in Chapter 1, is to check the validity of the criteria allowing to automatically define an optimal confidence into measurements parameter $\widehat{\alpha}$. As a reminder, a first criterion defines $\widehat{\alpha}_1$ such that the *a priori* balance between model and measurement error is guaranteed (1.42). The second criterion lies on the *a priori* use of Morozov's discrepancy principle and chooses $\widehat{\alpha}_2$ in accordance with the noise level (1.44).

Using the most dense sensor placement and a given random input acceleration signal of $0.1g$ standard deviation, Fig. 2.14 shows the natural decrease of confidence parameters $(\widehat{\alpha}_1, \widehat{\alpha}_2)$ with respect to the measurement noise level δ. Both criteria thus react as expected to measurement noise: the more measurement noise, the less confidence into experimental data.

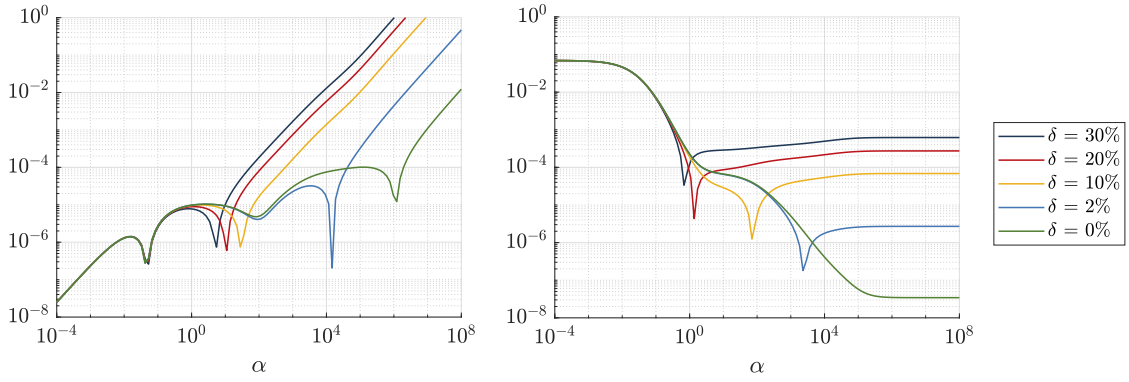

FIGURE 2.14: Automated choice of confidence into measurements coefficient: comparison of L-curve (*a priori* balance - left) and Morozov's discrepancy (right) criteria for several noise levels δ.

δ[%]	Sensor config. (a) $d_s = 0.1$ m		Sensor config. (b) $d_s = 0.2$ m		Sensor config. (c) $d_s = 0.3$ m	
	$\widehat{\alpha}_1$	$\widehat{\alpha}_2$	$\widehat{\alpha}_1$	$\widehat{\alpha}_2$	$\widehat{\alpha}_1$	$\widehat{\alpha}_2$
0	$9.62.10^5$	10^8	284	10^8	570	10^8
5	70.6	452	358	$1.44.10^3$	908	$2.30.10^3$
10	27.9	70.6	112	225	226	452
15	13.9	3.50	70.3	11.0	141	44.3
20	8.70	1.37	44.2	5.49	70.5	13.9

TABLE 2.2: Values $\widehat{\alpha}_1$ (L-curve) and $\widehat{\alpha}_2$ (Morozov) of the confidence into measurements with respect to noise level. The numerical values are implicitly conditionned by the choice for $\boldsymbol{G}$.

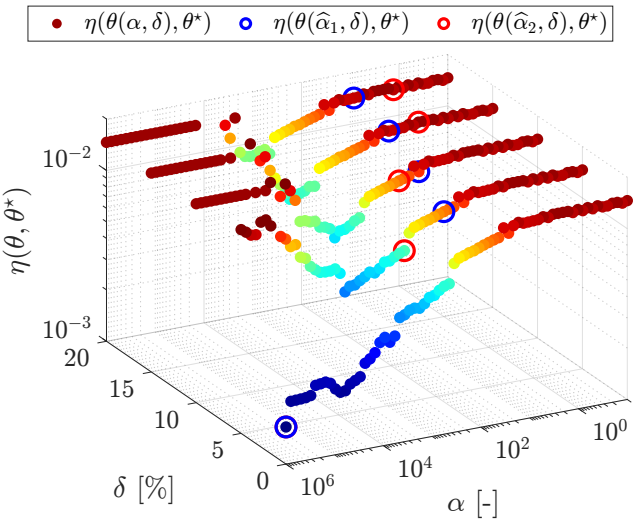

(a) $\eta(\alpha,\delta)$ with the sensor placement $d_s = 0.1$ m

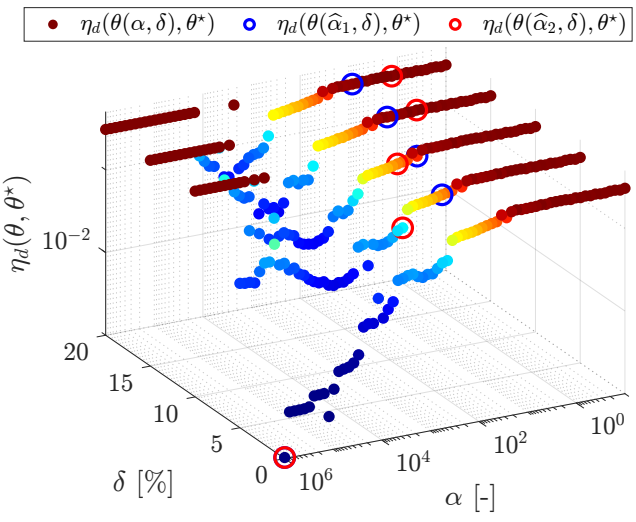

(b) $\eta_d(\alpha,\delta)$ with the sensor placement $d_s = 0.1$ m

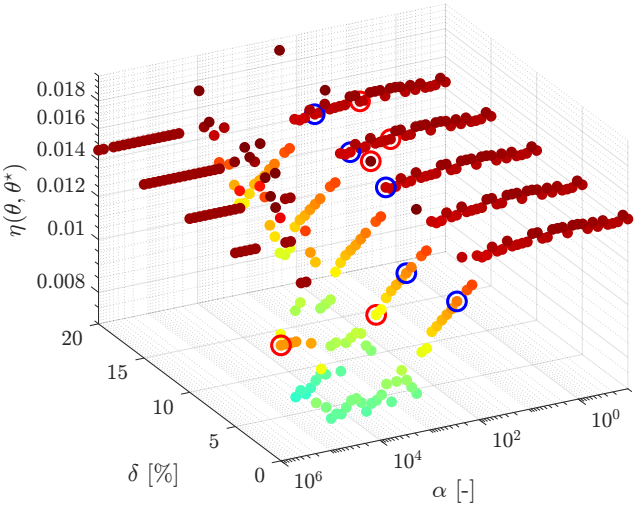

(c) $\eta(\alpha,\delta)$ with the sensor placement $d_s = 0.2$ m

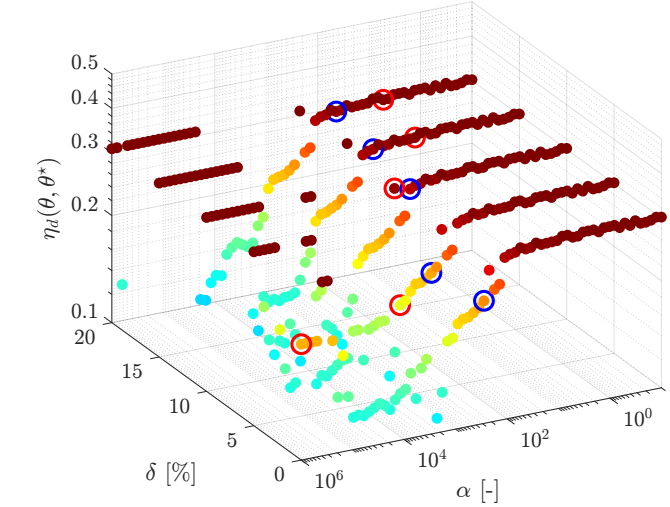

(d) $\eta_d(\alpha,\delta)$ with the sensor placement $d_s = 0.2$ m

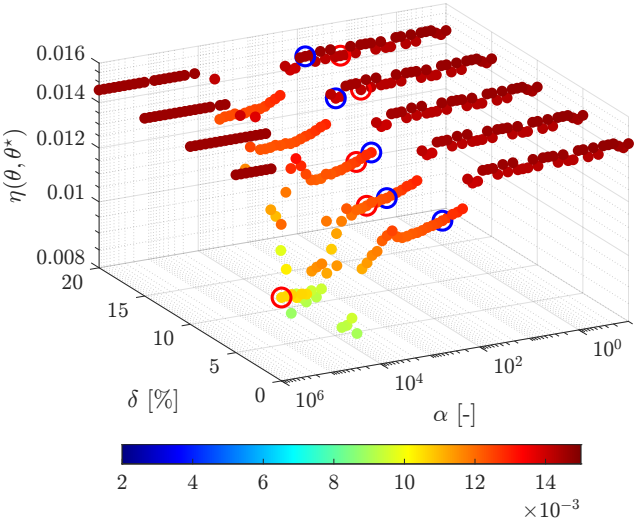

(e) $\eta(\alpha,\delta)$ with the sensor placement $d_s = 0.3$ m

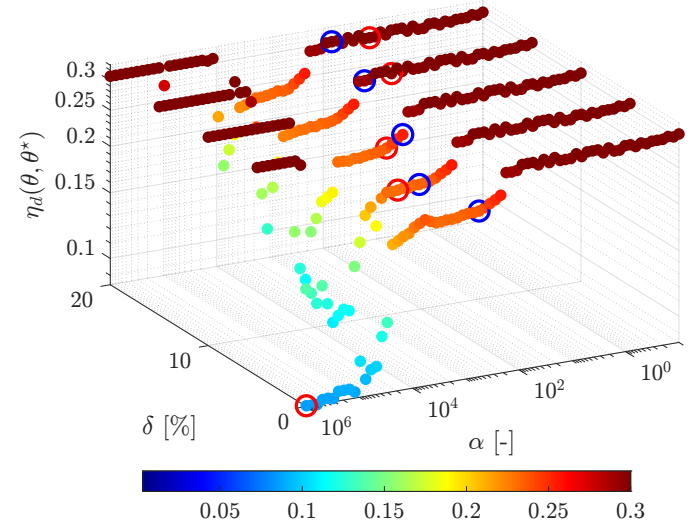

(f) $\eta_d(\alpha,\delta)$ with the sensor placement $d_s = 0.3$ m

FIGURE 2.15: Automated mCRE-based model updating algorithm - Quality assessment of parameter estimates using η (left side) and η_d (right side) according to α, δ and the sensor plans shown in Fig. 2.10. The positions of $\widehat{\alpha}_1$ (L-curve criterion - in blue) and $\widehat{\alpha}_2$ (Morozov's criterion - in red) are also given to evaluate the relevance of the automated methodology. Colormaps are identical in each column to compare the effect of sensors density more easily.

Although similar trends in the evolution of $\widehat{\alpha}$ with respect to measurement noise are observed, the values given by both criteria are quite different, and yet one cannot conclude about their validity so far. To assess which of the criteria is the most appropriate to use, a full parametric study on the joint influence of α and δ on the identified estimates has been conducted. Associated results are given in Fig. 2.15 where criteria η and η_d are plotted as a function of δ and α for the three considered sensor placement configurations previously displayed in Fig. 2.10. The colormaps (that are identical for subfigures a-c-e and b-d-f) allow to appreciate the combined effects of sensor density, noise level and confidence into measurements on the values of η and η_d.

The location of $\widehat{\alpha}_1$ and $\widehat{\alpha}_2$ compared to the optimal α values in the sense of η or η_d suggests that both criteria do not provide the optimal value of α for damage detection in the considered case. They can thus be considered too "conservative" as they **systematically underestimate the optimal confidence one should put into data**. If one has to choose between them, **the criterion based on Morozov's discrepancy principle should be preferred as it integrates additional information about the measurement noise**.

In practice, the "conservative" choice of α should also be seen as a robust feature of the algorithm: excessive confidence into measurements could lead to diverging results (with non-physical negative values of stiffness parameters - see Fig. 2.16). The automated calibration of α using L-curve-type or Morozov's discrepancy criteria allows to avoid such issues, at the cost of suboptimal identification results. Indeed, the "conservative" feature of $\widehat{\alpha}_1$ and $\widehat{\alpha}_2$ directly impacts the quality of identification: the sub-optimal choices in the sense of η and η_d lead to less accurate identification results, with a cluster of false-labeled elements larger than the defect to describe (see Fig. 2.17). However, the obtained results still remain consistent with the location of the defect whatever the sensor placement density.

> *Remark* 2.5. As a last remark, please note that the values of α are indirectly depending on the value given to $\boldsymbol{G}$, showing once again how this scaling matrix is not that crucial if α is afterwards well tuned.

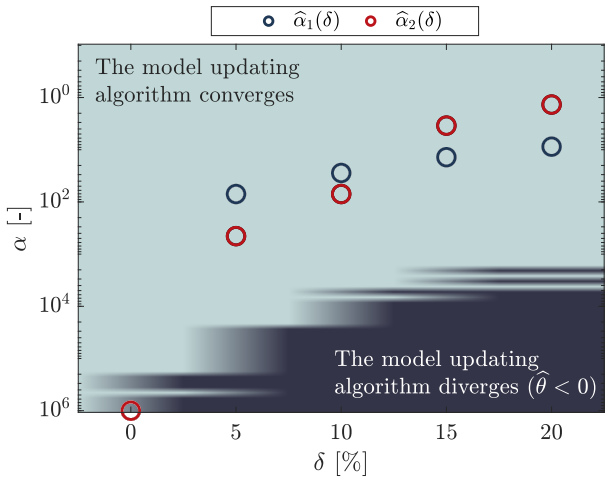

Figure 2.16: Convergence assessment of the automated mCRE-based model updating algorithm. If the algorithm converges most of the time (light area), overexcessive confidence can lead to non-physical results (dark area, where some estimated parameters have negative values). The automated calibrated values of $\widehat{\alpha}_1$ and $\widehat{\alpha}_2$ systematically lead to convergent model updating results.

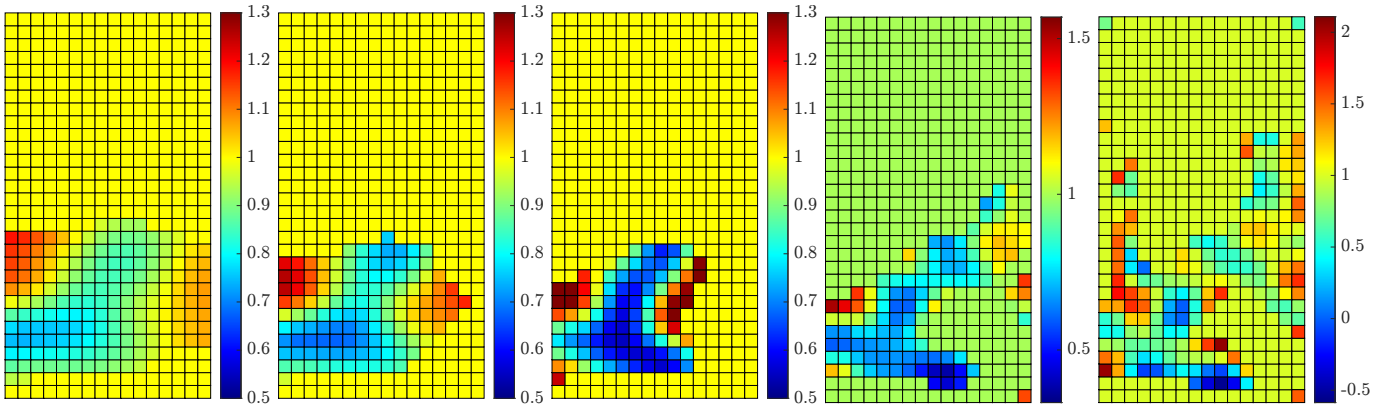

(a) $\alpha \approx 500$ - optimal value $\widehat{\alpha}_2$ (b) $\alpha \approx 1150$ - optimal w.r.t. η (c) $\alpha \approx 1500$ - optimal w.r.t. η_d (d) $\alpha \approx 20000$ - close to divergence (e) $\alpha \approx 30000$ - divergence

FIGURE 2.17: Automated mCRE-based model updating algorithm - Impact of α on clustering and parameter estimates. Results obtained for sensor placement Fig. 2.10.a with $\delta = 10\%$. The identification provided with the Morozov criterion $\widehat{\alpha}_2$ is also provided.

2.5.4 Impact of sensor placement on damage detection performance

As one could have expected, the more scattered sensors, the more accurate identification results. However, for real industrial applications, the amount of available sensors is limited by instrumentation constraints and economic considerations. What is thus interesting to observe from the identification results displayed in Fig. 2.18 is that one can coarsely identify damage locations from a restricted amount of sensors. Here, taking advantage of the knowledge of the defect shape allows to show the effect of the sensor placement while ignoring the one due to the selection of α. It also emphasizes the fact that **inverse problem parametrizations should be made in accordance with the associated sensor placement configuration**, and that optimal sensor placement strategies should be applied in such cases in order to get the most relevant information from a restricted amount of data. This point particularly motivated the optimal sensor placement work presented in Chapter 3.

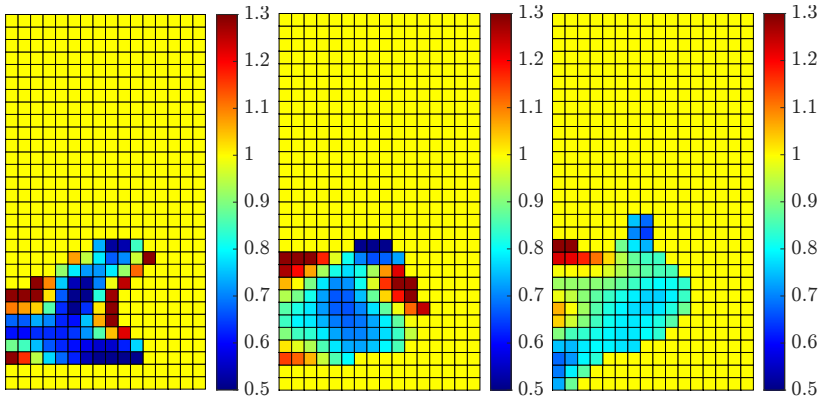

(a) $d_s = 0.1$ m (b) $d_s = 0.2$ m (c) $d_s = 0.3$ m

FIGURE 2.18: Automated mCRE-based model updating algorithm - Impact of the sensor placement configuration on parameter estimates. Results obtained for sensor placement of Fig. 2.10 with $\delta = 10\%$ with the optimal value of α in the sense of η_d.

2.5.5 Multiple defect detection

Although the convex shape of the inclusions makes their identification easier compared to the Y-shape defect, the fact that there are two defects to identify simultaneously is an interesting challenge to face with the parametrization done by CRE-based clustering.

We present in Fig. 2.19 and 2.20 the initial CRE maps and identification results obtained from both noise-free and noisy measurements using the sensor placement of Fig. 2.10.b. The expected parameter value of the small bottom left inclusion and of the larger top right inclusion have been respectively chosen at 0.5 and 0.7. The obtained results illustrate the capability of the methodology to identify multiple defects at once, as attested by the emphasis of the CRE map on the inclusions, even with significant measurement noise level and model bias.

As previously remarked, performing clustering without considering the barycentric coordinates of finite elements allows to avoid the (iterative) process on the optimal number of clusters to distinguish. Note that the value of α had to be divided by 100 between noise-free and 10% noisy data to obtain these results, highlighting once again the crucial role handled by the coefficient of confidence into measurements to get relevant identification results.

2.5.6 Effects of additional sparse regularisation

As written above, the addition of a sparse regularization term to the mCRE should be seen as a backup to the method for identifying localized defects more accurately. Identification results using sparse regularization with variable weighing γ and fixed *a priori* knowledge $\theta_0 = 1$ are shown in Fig. 2.21, where several parameter estimates obtained from the same 10%-noisy measurements are plotted.

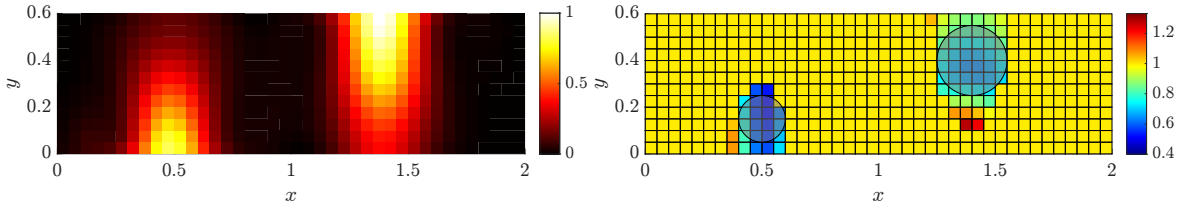

FIGURE 2.19: Identification of the two circular inclusions from noise-free accelerometer data. The initial CRE map used for clustering is plotted on the left. The parameter estimate is plotted on the right with the exact defects shapes on it to qualitatively assess its accuracy.

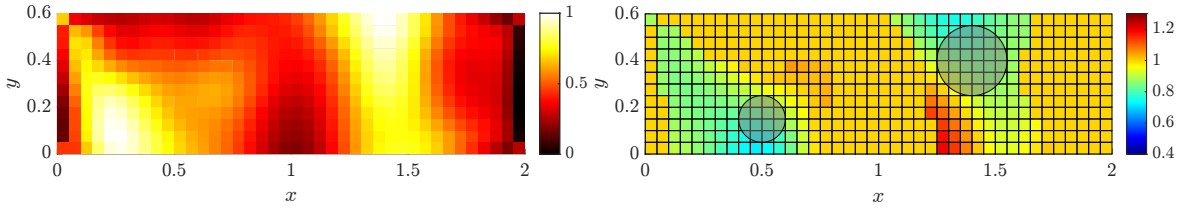

FIGURE 2.20: Identification of the two circular inclusions from 10% noisy sparse accelerometer data. The initial CRE map used for clustering is plotted on the left. The parameter estimate is plotted on the right with the exact defects shapes on it to qualitatively assess its accuracy.

The sparse regularization term permits to provide more accurate results only if the weighting is correctly calibrated. In this example, the weighting $\gamma = 10^{-4}$ has been identified after several tests as a close-to-optimal value. The comparison of parameter estimates obtained with $\gamma = 10^{-3}$ illustrates how the calibration of the sparse regularization term is crucial. Besides, the reader should keep in mind that, in this academic example, the initial guess perfectly matches with the expected parameter value on non-damaged areas, thus making the chosen *a priori* value $\theta_0 = 1$ highly relevant. This may not be the case for industrial applications where the stiffness distribution might not be well-known in advance.

As one can remark from Fig. 2.21 as well, the use of the automated CRE-based clustering step makes the effect of the additional sparse regularization less relevant as corrections are already focused on parameters in need for them. In spite of these limitations, **the additional sparse regularization term, if well calibrated, can be beneficial for getting more accurate parameter estimates**. However, due to the fact it necessitates some *a priori* knowledge, this regularization should be seen as an option that can be considered and calibrated in a case-by-case approach.

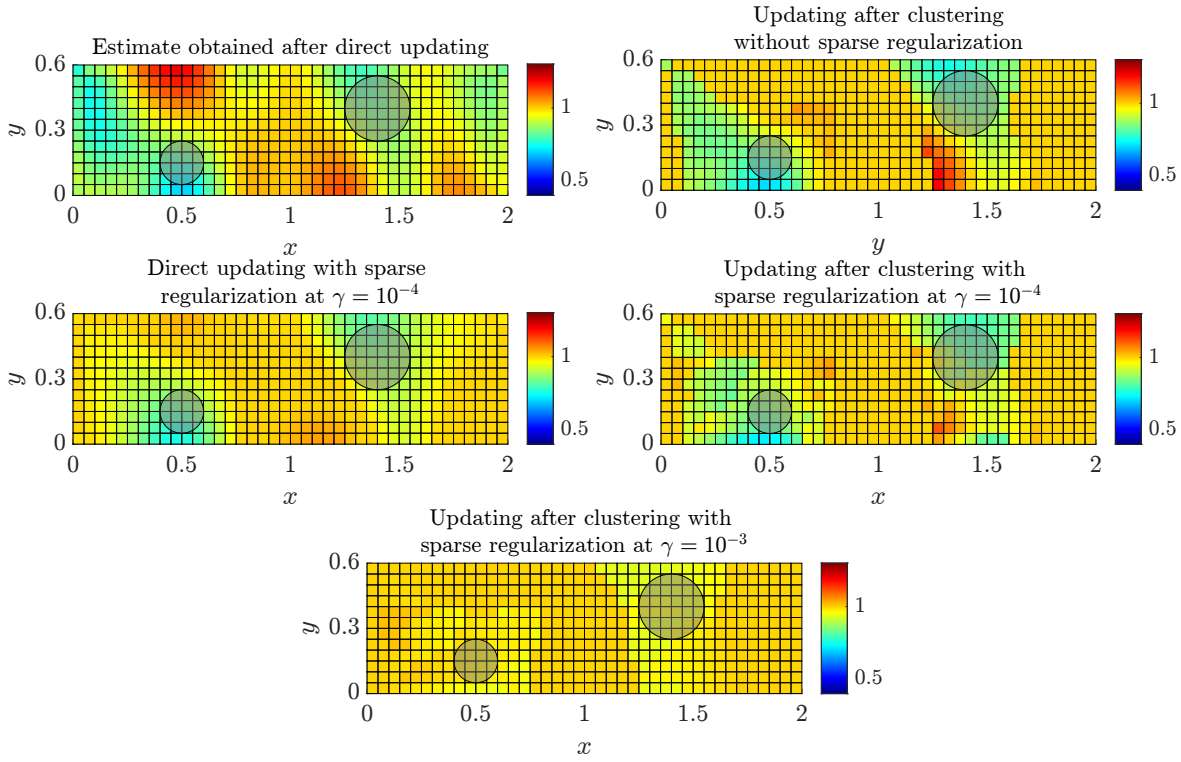

FIGURE 2.21: Effect of the sparse regularization effect over the identification of two inclusions from sparse 10% noisy acceleration datasets, with comparison to CRE-based clustering and direct mCRE-based model updating.

2.6 Conclusion & prospects on the automation of the mCRE-based model updating framework

After having analyzed the results from the numerical benchmark, let us summarize the main advantages (✓) and limitations (✗) of the automated model updating methodology presented in this chapter:

- ✓ CRE-based clustering extends the concept of localization of most erroneous areas. It facilitates damage detection as it strongly restrains the number of parameters to update. This is particularly well suited for damage detection as such defects are supposed to appear locally. Indeed, the simplest (but less computationally efficient) choice would be to update all E finite elements independently. With the proposed strategy, one could legitimately hope for $\dim(\widehat{\Theta}) \ll E$.

- ✓ The proposed model updating strategy is fully autonomous with all the implemented procedures for its automation. As the selection of α, the computation of the CRE map and the clustering steps are fast post-processing operations, significant CPU time savings are made without loosing accuracy.

- ✓ Sparse regularization may be helpful for getting more accurate results in cases where defects are localized, but it requires some *a priori* knowledge and dedicated calibration. Its effect is less significant when combined to CRE-based clustering.

- ✗ The calibration of α becomes even more crucial herein as it also conditions the effectiveness of the CRE-based clustering. The "conservative" feature of the proposed criteria for selecting α provides sub-optimal yet relevant damage detection results. In an offline context, it may be worth trying to update α iteratively in an *a posteriori* manner.

- ✗ The performance of the clustering step and of the model updating process is conditioned by the quantity and quality of available sensors. This limitation has to be kept in mind

when trying to identify damage from sparse datasets. This problem will be addressed in Chapter 3.

✗ Due to the energy-based definition of the mCRE, the identification of defects will be difficult in non-sensitive or heterogeneous areas (in the sense of the strain energy distribution). This problem-dependent issue should not be decisive for the case of damage detection from ground motion testings, but it could be the case when trying to identify inherent defects, *e.g.* due to material uncertainty.

Overall, the automated setting of all the internal tuning parameters without any additional *a priori* engineering judgment and the low computational resources requirements make it an interesting tool for robust model updating problems in dynamics. Although optimal results for damage detection have not been systematically obtained, the methodology has proven robustness through the automated choice of tuning parameters and numerical efficiency as one completed model updating (including data preprocessing) in a couple of minutes on a personal laptop. Those two aspects are essential in the perspective of proposing an efficient model updating toolbox for digital twin applications. Several recommandations on the application of the model updating algorithm according to the context of use can be made:

▷ If real-time constraints exist or if the model updating is exploited for data assimilation, a first precalibration test (with a typical low-magnitude random input) should be made to calibrate all mCRE internal parameters at best. Besides, the initial model guess would be already well calibrated regarding the initial damage state of the specimen under study. This way, the MDKF process (fully detailed in Chapter 4) could integrate all the proposed improvements. The obtained results will not be optimal (as evidenced before), but they should be relevant enough to provide accurate results in real-time.

▷ If there is no particular time constraint, *i.e.* if the algorithm is only exploited as a post-processing tool, then one can afford running several mCRE minimizations around the suboptimal values of $\widehat{\alpha}$ to find optimal results. Indeed, all the minimizations performed in this contribution lasted less than 2 minutes on a personal laptop. To provide a friendly framework in that sense, a MATLAB© visualization tool has been developed, allowing the user to navigate easily through the generated results (see Fig. 2.22).

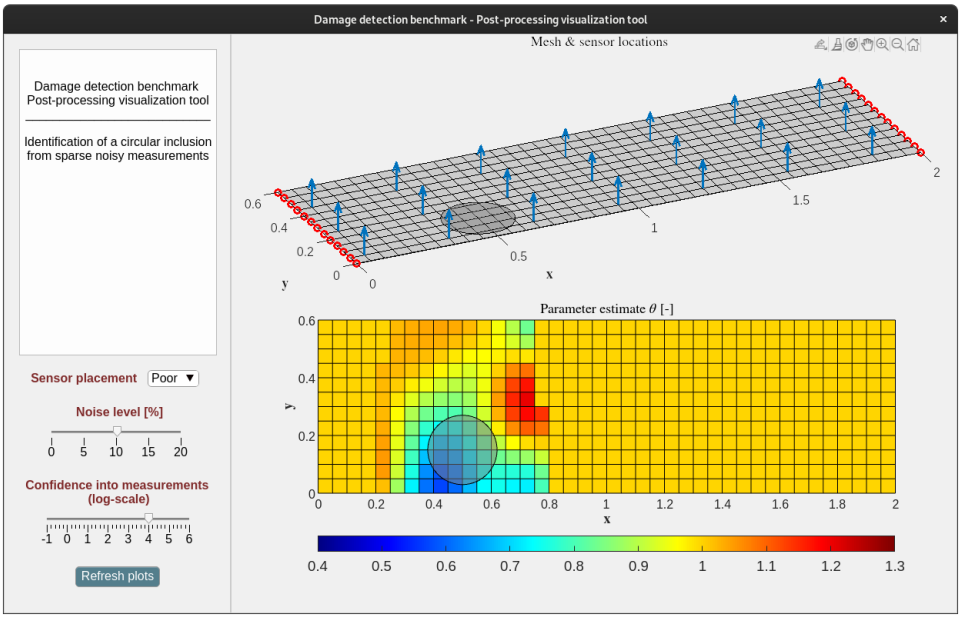

FIGURE 2.22: A visualization tool on Matlab for easy post-processing of model updating results, applied here to the detection of one circular inclusion in a plate.

Eventually, a last perspective lies in using full-field (digital image correlation) or locally highly dense (optic fibers) measurements to perform model updating. In such a context, not all the available data can be processed at once, but the updated model may be progressively enriched to integrate data and refine the parameter space only where needed, whether using model selection or mesh adaptation techniques. Coupling the automated model updating algorithm with mesh adaptation and model selection techniques is a promising idea, that will require dedicated efforts in a long-term perspective of this work.

Chapter 3

Optimal Sensor Placement dedicated to mCRE-based model updating

Unified framework for enhanced structural monitoring

In Structural Health Monitoring (SHM) applications, the data obtained from sensors embedded on large civil engineering structures can valuably be post-processed for digital twin applications. However, as the available data is often spatially sparse and noisy, the identification problem becomes challenging. If the modified Constitutive Relation Error framework has shown to be an interesting alternative to classical model updating approaches in the sense that it is highly robust to measurement noise, the data sparsity problem can only be addressed through optimal sensor placement (OSP). In this chapter, after a brief review of classical OSP techniques for SHM with an illustration on a 1D academic example, a new mCRE-based sensor placement technique is proposed from the definition of a modified Fisher Information Matrix. If this new strategy suffers from the well-known calibration problems of the mCRE, a proof of concept involving an earthquake engineering inspired case study, where accelerometers are positioned on a two-story frame structure subjected to random ground motion, permits to illustrate the soundness and efficiency of the proposed methodology compared to other classical OSP techniques.

The work presented in this chapter has been the subject of the following contribution:

M. Diaz, P.-É. Charbonnel, and L. Chamoin [2023d]. "Merging experimental design and structural identification around the concept of modified Constitutive Relation Error in low-frequency dynamics for enhanced structural monitoring". *Mechanical Systems and Signal Processing (under review) - available in hal (03878634)*

Note from the author: the reading of this chapter is not mandatory for understanding the content of the next chapters. The reader interested in data assimilation problems is invited to directly go to Chapter 4.

Contents

3.1 Introduction

Structural Health Monitoring (SHM) aims to improve the diagnosis of structures in operational conditions in order to prevent potential structural failures. The automated techniques that have been developed in the last four decades, which directly exploit measured data, make it possible to assist and reinforce the health monitoring inspection of structures in order to permit a safe decision-making process. SHM has been particularly studied in the context of localizing, quantifying, and tracking structural damage from ambient dynamic datasets. Throughout the last decades, a broad panel of damage detection methods has been proposed [J. Brownjohn 2007; Gomes et al. 2019; Chatzi et al. 2020] - only to cite a few of them. These techniques all have in common the aim of updating numerical models, and when performing model updating from (possibly spatially sparse) datasets, several difficulties have been identified [Tarantola 2005; Friswell 2007]:

(i) Model bias due to the fact that the chosen class of structural models does not contain the actual behavior of the structure;

(ii) Measurement noise in the test data that implies the addition of *a priori* information for regularization purposes;

(iii) Incomplete observability of the structure due to the limited budget and technologies of available sensing devices, leading to local and incomplete datasets;

(iv) Incomplete number of contributing modes due to limited bandwidth in the input and dynamical response.

As difficulties (i) and (iv) are already addressed via the mCRE-based model updating framework in the previous chapters, we will mainly focus on difficulty (iii) herein as one shall imagine how inappropriate experimental designs can lead to inaccurate identification results.

The will to exploit at best the information provided by a few amount of sensors lead to the development of optimal sensor placement (OSP) techniques to guarantee the relevance of sensor locations for various applications such as modal analysis, structural identification, or damage detection. Indeed, the quality of damage diagnosis from structural vibrations critically depends on the sensor layout, in particular when a small number of sensors is used for large structures under unknown or random excitation. It is especially the case of large-scale civil structures such as bridges or buildings that cannot be fully instrumented in practice. As part of the experimental design, OSP is a challenging problem. Indeed, as sensors are not properly positioned at this stage, actual measurements are not available. The performance of OSP algorithms is thus conditioned by the (assumed good) predictive behavior of the involved numerical models that allow to generate simulated data. Besides, it is also an expensive task from the computational viewpoint due to the numerous calls to data generation simulations. The question of sensor placement is not new [Bensoussan 1972; Yu and Seinfled 1973] and has been massively studied in the last three decades for SHM applications [Yi and H.-N. Li 2012; Mallardo and Aliabadi 2013; Ostachowicz et al. 2019; Barthorpe and Worden 2020] with the introduction of a wide variety of OSP criteria and optimization algorithms.

In this chapter, after having reviewed the most popular sensor placement techniques in the field of SHM, with an application on a 1D multi-DoF spring-mass chain toy example, we will discuss the possibility to integrate the mCRE functional within an OSP strategy. To do so, we will exploit the close links of the latter with Bayesian inference and we will derive the well-known concept of Information Entropy to propose OSP that are dedicated to optimal mCRE-based identification.

3.2 Overview of OSP techniques for SHM

In this section, the most common and popular sensor placement techniques are briefly presented. The interested reader is invited to find complementary explanations in the following

review papers [Yi and H.-N. Li 2012; Mallardo and Aliabadi 2013; Ostachowicz et al. 2019; Barthorpe and Worden 2020].

In most SHM applications, measurements are discrete kinematic quantities (displacement, strain, acceleration) that directly derive from the mechanical state that one tries to predict with a model $\mathcal{M}(\theta, e) \in \mathcal{X}$. The observation operator $\mathcal{H} : \mathcal{X} \mapsto \mathcal{Y}$ thus allows to explicitly compare predictions with the available measurements. Classically, the eponymous observation equation reads [Kalman 1960; Kirkegaard and Brincker 1994; Udwadia 1994]:

$$y = \mathcal{H}(\mathcal{M}(\theta, e)) + v \tag{3.1}$$

where v is an additive noise assumed to be Gaussian of covariance matrix $\mathbf{\Sigma}_y$ allowing to take into account measurement noise and model discrepancies. In what follows attention is paid to the best choice of sensors locations in order to obtain the best identification of $\widehat{\theta}$. The problem is thus to find the best projector $\widehat{\mathcal{H}}$ that minimizes the covariance on the parameter estimate $\boldsymbol{P}^{\theta}$. In the following, the optimal discretized observer operator $\widehat{\mathbf{\Pi}}$ will be sought.

In SHM and structural dynamics applications, OSP problems raised for modal identification purposes, as it has been well-known historically that damage occurence is related to eigenfrequencies loss and mode shapes changes [Cawley and Adams 1979]. It is thus not a surprise to observe that former works have addressed the question of OSP whether for enhanced modal analysis or directly for better system identification. However, the tools that are invested in these approaches are (for the largest part) all related to the information theory, that is presented below.

3.2.1 Information theory, a well suited framework for OSP

Even if the mathematical developments dealing with the information theory date back to the 1920s [Fisher 1925], [Shah and Udwadia 1978] is probably one of the first papers devoted to OSP for parameter estimation of structures subjected to earthquake loading conditions. They exhibit a mathematical expression of the OSP (for a given amount of sensors N_s) that has been after reinvested in many other works [Kammer 1991; Kirkegaard and Brincker 1994; Heredia-Zavoni and Esteva 1998]:

$$\widehat{\mathbf{\Pi}} = \arg\min_{\mathbf{\Pi}} \left[\boldsymbol{P}^{\theta} \triangleq \mathbb{E}\left(\left(\theta^{\star} - \hat{\theta}(\mathbf{\Pi}, y)\right) \left(\theta^{\star} - \hat{\theta}(\mathbf{\Pi}, y)\right)^{T} \right) \right] \tag{3.2}$$

where $\theta^{\star}$ and $\hat{\theta}$ refer to the exact and estimated parameter sets while $\mathbb{E}(\square)$ denotes the mathematical expectation. Note that, because models are numerically discretized (*e.g.* in the finite element sense), then there is no reason to look for the optimal N_s sensors locations in a continuous space. Each sensor position will thus be optimized among a "grid" of all N_d possible sensor locations. Doing so, the OSP problem becomes a combinatorial optimization problem, that is well-known for being exploratory and computationally expensive: if one intends to naively look for a global minimum, $\binom{N_d}{N_s}$ tests are required!

> *Remark* 3.1. The implicit dependency into measurements of the optimal sensor placement is explicitly shown in (3.2) to recall that the OSP is strongly relying on the way data are simulated and sensitive to the considered sensing technology.

If the prediction model is considered as unbiaised, then the Cramér-Rao bound theorem applies. It postulates that the variance of any unbiased estimator is bounded by the inverse of the so-called Fisher Information Matrix (FIM):

$$\mathbb{E}\left(\left(\theta^{\star} - \widehat{\theta}\right) \left(\theta^{\star} - \widehat{\theta}\right)^{T} \right) \geq \boldsymbol{Q}^{-1} \quad \text{with} \quad \boldsymbol{Q} = \int_{\mathcal{Y}} \left. \frac{\partial \mathbf{\Pi}(\mathcal{M}(\theta, e))}{\partial \theta} \right|_{\widehat{\theta}} \mathbf{\Sigma}_y^{-1} \left. \frac{\partial \mathbf{\Pi}(\mathcal{M}(\theta, e))}{\partial \theta} \right|_{\widehat{\theta}}^{T} \tag{3.3}$$

By definition, the FIM is strongly related to the sensitivity of predictions with respect to the parameters. It is a relevant mathematical entity on which the sensor selection can rely as it is a

way of measuring the amount of information carried by a given sensor configuration. Indeed, minimizing the covariance matrix $\boldsymbol{P}^{\theta}$ thus corresponds to maximizing the FIM, in the sense of a certain measure. The latter is often chosen according to the FIM invariants, and therefore its eigenvalues. Traditional optimality criteria are thus based on:

- ▷ the minimization of the condition number of the FIM $\kappa(\boldsymbol{Q})$ - also referred as E-optimality. The condition number is related to the rank of the FIM matrix and to the difficulty in performing its inversion. With this approach, no sensor is redundant with another [Reynier and Abou-kandil 1999].
- ▷ the maximization of the trace of the FIM $\boldsymbol{tr}\,(\boldsymbol{Q})$ - also referred as A-optimality. The trace is a measure of the global sensitivity of data with respect to the parameters and hence has to be maximized. It has been the optimality criterion used in the pioneering works of Udwadia and co-workers [Shah and Udwadia 1978; Udwadia 1994] and reinvested by [Heredia-Zavoni and Esteva 1998; Heredia-Zavoni et al. 1999] to perform OSP for buildings submitted to ground motion from frequency-domain measurements. A-optimality criterion is now combined to sensor sparsity constraints [Nagata et al. 2021].
- ▷ the maximization of the FIM determinant $\det(\boldsymbol{Q})$ - also referred as D-optimality. The inverse of the determinant is a measure of the overall uncertainty on the estimated parameters, which thus needs to be minimized. D-optimality techniques have been widely used as a basis for OSP. For instance, one can mention the Effective Independence method (EI) developed by [Kammer 1991; L. Yao et al. 1993; F. Hemez and Farhat 1994] where attention is paid to the sensitivy of measurements with respect to the modeshape matrix. This measure has also been shown to be strongly correlated to the Bayesian statistical framework in [Beck and Katafygiotis 1998; Katafygiotis and Beck 1998] and to the concept of information entropy introduced by [Papadimitriou et al. 2000].

Remark 3.2. The FIM can also be derived from the probabilistic viewpoint as the variance of the score, *i.e.* the gradient of the log-likelihood function $\pi(y|\theta,\mathcal{M})$:

$$\boldsymbol{Q} = \mathbb{E}\left(\left(\frac{\partial \log \pi(y|\theta,\mathcal{M})}{\partial \theta}\right)\left(\frac{\partial \log \pi(y|\theta,\mathcal{M})}{\partial \theta}\right)^{T}\middle|\,\theta\right) \tag{3.4}$$

OSP for modal analysis: Mode Shape Difference (MSD), Effective Independence (EI) and Modal Kinetic Energy (MKE)

The Effective Independence method (EI) was introduced by Kammer [Kammer 1991] and can be considered as a modal-based OSP technique. Indeed, it exploits the Fisher Information Matrix with the modeshape matrix as quantity of interest due to the fact that the variations of the latter can be directly related to damage. The starting point of this approach is the Mode Shape Difference method (MSD) in which (3.1) is rewritten using a modal basis $\boldsymbol{\Phi}$ and modal coordinates q.

$$y = \boldsymbol{\Pi}\boldsymbol{\Phi}q + v = \boldsymbol{\Phi}_s q + v \tag{3.5}$$

where $\boldsymbol{\Phi}_s$ is the modal basis projected on sensors locations. The key idea is then to consider the modal coordinates of eigenmodes to be the parameters previously designated by θ, which leads in a straighforward manner to the following FIM:

$$\boldsymbol{Q} = \int_{\mathcal{Y}} \boldsymbol{\Phi}_s \boldsymbol{\Sigma}_y^{-1} \boldsymbol{\Phi}_s \tag{3.6}$$

If MSD only considers sensors as relevant if they are sensitive to modeshape changes (when considering several damage scenarios) [Shi et al. 2000; Blachowski 2019], the EI method extends this concept with the independence distribution vector: the contributions of each sensor to each mode of $\boldsymbol{\Phi}$ are quantified within the matrix

$$\boldsymbol{E} = \boldsymbol{\Phi}_s \left[\boldsymbol{\Phi}_s^T \boldsymbol{\Phi}_s\right]^{-1} \boldsymbol{\Phi}_s^T \tag{3.7}$$

which can be interpreted as an orthogonal projector whose rank is equal to the number of targeted modes. $\boldsymbol{E}$ can thus be full rank if the mode partitions resulting from a given SP are linearly independent, which is the objective of EI. The independence distribution vector corresponds to the diagonal terms of $\boldsymbol{E}$. They allow to quantify the potential contribution of sensors to modal analysis. The methodology of EI is given in Alg. 3.1 (for the case of a single damage scenario). Its structure is similar to a Backward Sequential Sensor Placement algorithm, which will be discussed in the following.

The EI method has been widely exploited in the literature: the work has been quickly extended to take into account modeling errors as well as measurement noise effects [Kammer 1992a; Kammer 1992b]. A Genetic Algorithm (GA) based approach has also been proposed in [L. Yao et al. 1993] and the method has been able to successfully position 3D accelerometers for modal vibration tests [Kammer and Tinker 2004]. More recently, it has been coupled with topology optimization-inspired tools [Blachowski et al. 2020]. Besides, EI has been adapted to the particular case of damage detection based on strain measurements in [F. Hemez and Farhat 1994] by considering a strain energy prediction matrix $\boldsymbol{E}$. As a more specific tool, it has outperformed EI for damage detection problems by providing more relevant sensor placements.

Finally, it is also worth mentioning in the Modal Kinetic Energy (MKE) method in parallel of MSD and EI as it intends to locate sensors at points of maximum kinetic energy for the modes of interest [Salama et al. 1987]. The major advantage of MKE compared to EI is that favorable locations are promoted in areas where the SNR should be important, which limits the spurious effects of measurement noise in the identification process. It can be valuably exploited for damage detection [Bach et al. 2023; Le et al. 2023]. [D. S. Li et al. 2007] studied the mathematical connections between MKE and EI and compared them for SHM applications, showing EI can be seen as an iterated version of MKE.

Algorithm 3.1: Effective Independence Sensor Placement Algorithm

Initialization: Grid of all N_d possible sensors locations, targeted number of sensors N_s, eigenmodes matrix $\boldsymbol{\Phi}$

while more than N_s sensors are retained **do**

Compute the current projector $\boldsymbol{\Pi}$ and the modal basis partitioned to sensors $\boldsymbol{\Phi}_s = \boldsymbol{\Pi}\boldsymbol{\Phi}$

Compute the EI vector $E_D = \text{diag}\left(\boldsymbol{\Phi}_s \left[\boldsymbol{\Phi}_s^T \boldsymbol{\Phi}_s\right]^{-1} \boldsymbol{\Phi}_s^T\right)$

Rank E_D terms and eliminate the sensor associated to $\min_i(E_{D,i})$

end

Result: Optimal placement of N_s sensors with respect to the eigenmodes $\boldsymbol{\Phi}$

Information Entropy (IE)

Contrary to MSD, EI and MKE that are based on the sensitivity of modal features, one can formulate the OSP problem from the Bayesian viewpoint. Indeed, the posterior pdf $\pi(\theta|y)$ represents the uncertainty on parameters θ knowing the information stored in measurements y. The concept of *Information Entropy* (IE) has been introduced to provide a unique scalar measure of this uncertainty [Papadimitriou et al. 2000; Papadimitriou 2004]. It benefits from the Bayesian statistical framework proposed by [Beck and Katafygiotis 1998; Katafygiotis and Beck 1998] as it properly handles measurement noise and modeling error features. The IE, denoted $h(\boldsymbol{\Pi}, y)$, reads:

$$h(\boldsymbol{\Pi}, y) = \mathop{\mathbb{E}}_{\theta}\left(-\log \pi(\theta|y)\right) \tag{3.8}$$

OSP is then achieved by minimizing the changes in the IE, that depends on the available data and on the sensor configuration $\boldsymbol{\Pi}$. A rigorous mathematical description of the IE concept for OSP is given in [Papadimitriou et al. 2000; Papadimitriou 2004] for the case of "small" and "large" uncertainties on the parameters to estimate. An important result that has been shown is the asymptotic formulae for a large amount of available data that relates the IE to the determinant of the FIM.

For small uncertainties on θ, one can legitimately choose a relevant value θ_0 that minimizes a classical weighted least-square cost-function defined as

$$\mathcal{J}_{WLS}(\theta) = \sum_{i=1}^{N} \|y_i - \mathbf{\Pi}\mathcal{M}_i(\theta)\|^2_{\mathbf{\Sigma}_w^{-1}} \tag{3.9}$$

where N is the number of measurement samples (in the time or frequency domain) and the i index refers to the i^{th} sample with respect to the discretized time or frequency domain. When $NN_s \to \infty$, it is shown that:

$$\begin{aligned} h(\mathbf{\Pi}, y) \approx H(\mathbf{\Pi}, y; \theta_0) &= \frac{1}{2} N_\theta \log 2\pi - \frac{1}{2} \log \det(\boldsymbol{Q}(\mathbf{\Pi}, \theta_0, y)) \\ \text{with } \boldsymbol{Q}(\mathbf{\Pi}, \theta_0, y) = NN_s \nabla_\theta \nabla_\theta^T \left(\mathcal{J}_{WLS}(\theta)\right) &\approx \sum_{i=1}^{N} \|\mathbf{\Pi}\nabla_\theta \mathcal{M}_i(\theta)\|^2_{(\mathbf{\Pi}\mathbf{\Sigma}_y\mathbf{\Pi}^T)^{-1}} \end{aligned} \tag{3.10}$$

Using (3.10), one can thus look for N_s optimal sensors locations $\widehat{\mathbf{\Pi}}$ solving:

$$\widehat{\mathbf{\Pi}} = \arg\max_{\mathbf{\Pi}} \left[\log \det(\boldsymbol{Q}(\mathbf{\Pi}, \theta_0, y))\right] \tag{3.11}$$

It is important to notice that according to the values of the sought parameters, for complex problems and geometries (considering for example the case of complex damageable structures, one may not straightforwardly guess where damage will appear first), OSP results may strongly differ from one parameter value to the other. In this case, referred to as large model uncertainties in [Papadimitriou et al. 2000], a parameter estimate θ_0 cannot be postulated anymore. This implies that the OSP will be sought as:

$$\widehat{\mathbf{\Pi}} = \arg\max_{\mathbf{\Pi}} \left[\int_\Theta \log \det(\boldsymbol{Q}(\mathbf{\Pi}, \theta, y))\pi_0(\theta)\mathrm{d}\theta\right] \tag{3.12}$$

The parameter space is thus explored (for example with Monte-Carlo sampling) and the contributions of the FIM computed according to each sample are averaged with respect to the prior pdf on parameters $\pi_0(\theta)$.

One of the strong assets of the IE is that it allows to compare sensor configurations of various size [Yuen et al. 2001], as one can guess that adding sensors is always beneficial, or at least equivalent in terms of carried information. In [Papadimitriou 2004], mathematical classification rules are given on the upper and lower bounds of the IE as a function of N_s allowing to perform sequential placements (see Alg. 3.2) that are almost as efficient as genetic algorithms, but obtained with much less computational effort.

There have been much use of the IE for OSP in the last two decades. Without being exhaustive, let us mention some contributions: in [Papadimitriou and Lombaert 2012], the functional has been extended to take into account the effect of sensors spatial correlation in Σ_w. Similarly, a penalty term to enforce the sparsity of the sensor configuration has been added to the IE [Cantero-Chinchilla et al. 2020]. The IE was also used to design optimal characteristics of the excitation e for optimal identification [Metallidis et al. 2003]. In [Papadimitriou 2005; Yang 2022], a multi-objective optimization problem was introduced to design an OSP dedicated to a class of models. IE was reinvested for statistical seismic source inversion in [Long et al. 2015]. IE was also applied to model identification of periodic structures endowed with bolted joints [Yin et al. 2017] and to optimal crack identification on plates from strain measurements in [Argyris et al. 2018]. Very recently, the case of multiple damage scenario with modal shape expansion was considered in [Ercan and Papadimitriou 2021] to handle virtual sensing under output-only vibration measurements.

Eventually, as the next Chapter is dedicated to data assimilation techniques and Kalman Filtering, it is worth mentioning apart [Ercan et al. 2023] and [Taher et al. 2023], that both perform OSP within an augmented Kalman filtering framework. The information gain, *i.e.* the criterion that allows to position sensors, is oriented towards input-state estimation, which enables to perform state reconstruction and monitoring from incomplete datasets.

3.2.2 Optimization methods

The wide variety of OSP strategies do not only differ by the quantity of interest that is optimized, but also by the algorithmic structure that performs sensor placement. In this paragraph, we will briefly review the classical algorithms that are currently used in the literature to perform (sub-) optimal sensor placement in reasonable CPU times, without being exhaustive for the sake of conciseness. We will particularly focus on IE-based OSP applications because these techniques will be illustrated in the following application Section 3.2.3.

Genetic algorithms & metaheuristic algorithms

GAs are algorithmic structures for solving both constrained and unconstrained optimization problems based on a natural selection process that mimics biological evolution. GAs are very popular to solve OSP problems as they are most suitable for solving discrete optimization problems and providing near-optimal solutions of global optimization problems [Goldberg 2002]. GAs are now well known by the scientific community and dedicated toolboxes are available in many numerical environments, for example the MATLAB© global optimization toolbox. [L. Yao et al. 1993] is presented as one of the earliest papers to use GAs to solve EI-based OSP. [Papadimitriou et al. 2000] initially used GAs to solve the IE-based sensor placement problem, using the determinant of the FIM as optimization criterion. The efficiency of GAs with respect to sequential sensor placement strategies has also been illustrated in [Papadimitriou 2004], with emphasis also put on its expensive CPU cost. Finally, let us mention [Zhou et al. 2017] that gathered four OSP techniques within a generic sensor placement framework driven by a GA to facilitate multi-criteria-based OSP.

Neural Networks (NN) are also valuable tools for sensor placement. For instance, [Worden and Burrows 2001] described an approach to fault detection and classification using NN and simulated annealing (SA). A comparison between SA and GA for OSP was recently done in [Nasr et al. 2022]. Among the numerous recent contributions involving NN, it is worth mentioning [Azarbayejani et al. 2008] that trains a NN to predict damage location by observing the damage feature values at all possible sensor locations before maximizing a damage detection probability for a restricted sensor budget, and [Ručevskis et al. 2022] that uses NN to optimally position strain gauges for modal analysis on composite structures.

Of course, the use of metaheuristic/exploratory optimization algorithms does not restrict to GAs and NNs. For example, one can refer to OSP techniques inspired from topological optimization [Bruggi and Mariani 2013; Blachowski et al. 2020], or statistical pattern recognition classifiers [Figueiredo and J. Brownjohn 2022].

Sequential sensor placement techniques

Sequential sensor placement techniques, whether they are Forward (FSSP) or Backward (BSSP) do only provide suboptimal sensors configurations, but they are much less computationally demanding than GAs. The location of the N_s sensors are determined sequentially by placing/removing one sensor at a time. FSSP and BSSP methods proceed with a very similar algorithmic structure, as shown from the IE-oriented algorithms that are given below. Alg. 3.2 and 3.3 are the pseudo-codes for IE-based FSSP and BSSP while Alg. 3.4 is a direct FSSP extension to the case of highly uncertain parameters. This last algorithm allows to appreciate the additional CPU cost required to take multiple scenarios into account, although it remains beneficial and necessary when considering large parameter uncertainties.

As mentioned earlier, the EI method lies on a BSSP strategy [Kammer 1991], but FSSP and BSSP has really been emphasized in the literature with the IE concept because of its intrinsic mathematical properties [Papadimitriou 2004; Papadimitriou and Lombaert 2012]. In fact, it has been shown that FSSP and BSSP provide relevant (yet suboptimal) OSP on many test cases with less computational effort than GAs. For SHM problems where a few amount of sensors must be positioned, it is recommended to use FSSP instead of BSSP or GA. This point will be illustrated in the forthcoming application.

Algorithm 3.2: IE-based Forward Sequential Sensor Placement (FSSP)

Initialization: Grid of all N_d possible sensors locations, targeted number of sensors N_s, set of simulated measurements, $n = 0$ number of selected sensors
while $n < N_s$ **do**
  Consider all possible combinations by adding one new sensor to the previous n: $\{\mathbf{\Pi}_j\}_{j\in[\![1;N_d-n]\!]}$
  for $j \in [\![1; N_d - n]\!]$ **do**
    Evaluate the information entropy IE_j of the sensor configuration given by $\mathbf{\Pi}_j$
  end
  Identify the sensor configuration $J = \arg\min_{j\in[\![1;N_d-n]\!]} \text{IE}_j$
  Store the last sensor of configuration J as the $(n+1)^{th}$ optimal position
  Go to the next iteration: $n \to n+1$
end

Algorithm 3.3: IE-based Backward Sequential Sensor Placement (BSSP)

Initialization: Grid of all N_d possible sensors locations, targeted number of sensors N_s, set of simulated measurements, $n = N_d$ number of selected sensors
while $n \geq N_s$ **do**
  Consider all the combinations from the n sensors by removing one of them $\{\mathbf{\Pi}_j\}_{j\in[\![1;n]\!]}$
  for $j \in [\![1; n]\!]$ **do**
    Evaluate the information entropy IE_j of the sensor configuration given by $\mathbf{\Pi}_j$
  end
  Identify the sensor configuration $J = \arg\min_{j\in[\![1;n]\!]} \text{IE}_j$
  Store the last sensor of configuration J as the $(N_d-n)^{th}$ optimal position
  Go to the next iteration: $n \to n-1$
end

Algorithm 3.4: IE-based FSSP for highly uncertain parameters

Initialization: Grid of all N_d possible sensors locations, targeted number of sensors N_s, N_c number of parameter "scenarios", $n = 0$ number of selected sensors
Sample the parameter space with N_c samples taken randomly (MC, LHS, etc): $\{\theta_c\}, c \in [\![1; N_c]\!]$
Simulate and N_c measurement sets associated to these parameters
while $n < N_s$ **do**
  Consider all possible combinations by adding one new sensor to the previous n: $\{\mathbf{\Pi}_j\}_{j\in[\![1;N_d-n]\!]}$
  for $j \in [\![1; N_d - n]\!]$ **do**
    for $c \in [\![1; N_c]\!]$ **do**
      Evaluate the information entropy $\text{IE}_{j,c}$ of the sensor configuration given by $\mathbf{\Pi}_j$ for parameter θ_c (of occurence probability $\pi_0(\theta_c)$) and associated measurements
    end
  end
  Identify the sensor configuration $J = \arg\min_{j\in[\![1;N_d-n]\!]} \sum_{c=1}^{N_c} \text{IE}_{j,c}\pi(\theta_c)$
  Store the last sensor of configuration J as the n^{th} optimal position
  Go to the next iteration: $n \to n+1$
end

3.2.3 First illustration of OSP in structural dynamics on a toy example

In this section, the main OSP concepts previously mentioned are illustrated in an application to a 1D academic example. Let us consider a 40-DoF spring-mass chain-like model with locked-free boundary conditions as shown in Fig. 3.1. Although not represented, all eigenmodes are uniformly damped at 5%. The last mass is subjected to a random dynamical input $F(t)$. If the masses $\{m_i\}_{i=1}^{40}$ are considered to be identical and well known, the spring stiffness distribution $\{k_i\}_{i=1}^{40}$ is uncertain, which motivates the positioning at best of sensors to identify misfits or possible stiffness changes. For a uniform distribution of $\{k_i(\theta)\}$, the response of the structure to a random input $F(t)$ is given in the frequency domain in Fig. 3.1, showing that the 5 first eigenmodes are significantly involved in the structural response.

The main objective of this study is to illustrate and compare the effectiveness of OSP algorithms (sequential and GAs) for both modal analysis and structural identification using a simple system that allows to understand OSP results with physical-meaningful analysis. Another underlying objective is also to implement a library of OSP strategies that can be exploited in future experimental campaigns at the CEA/TAMARIS facility as an objective decision helping toolbox.

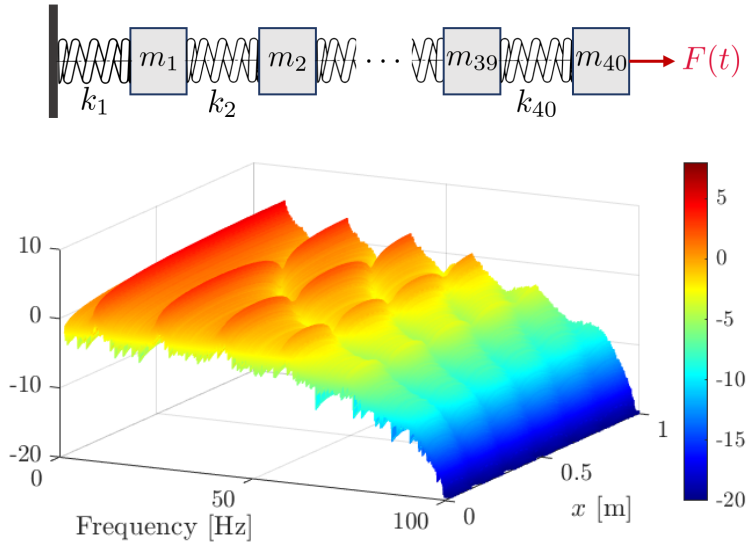

FIGURE 3.1: 40-DoF spring-mass chain-like model and associated frequency-domain response to a random input. Although not represented, 5% uniform modal damping is present.

OSP for modal identification

Let us first consider the case where the objective of OSP is modal identification. Hence, the FIM expression corresponds to the one in (3.6). In that case, the OSP in the sense of its determinant performed using IE or EI will exactly lead to the same results. A-optimality OSP has also been implemented following [Udwadia 1994]. Whatever the chosen criterion, FSSP, BSSP or GA optimization are implemented too. It thus leads to 6 sensor placement strategies whose results are presented in Fig. 3.2 and 3.3.

Each subfigure (a,b,c) respectively presents the OSP obtained with FSSP, BSSP and GA from 1 to 40 sensors. Such figures must be read line per line from top to bottom, with colored squares corresponding to the position of sensors. For example in Fig. 3.2a, the first sensor that has been placed is at the right end of the system, the second at the DoF just nearby on the left, and so on. One can thus properly observe how FSSP and BSSP algorithms behave with iterations. Note that the results from GAs are much different because the OSP at budget N_s does not condition the OSP at budget $N_s + 1$.

Several observations can be made from these results :

- ▷ The optimality criteria (trace or determinant) have a non-neglictible impact on the first positioned sensors, but similar patterns are recovered. It can be noticed that the placement of the first sensors in each case coarsely corresponds to the antinodes of the modes stored in $\boldsymbol{\Phi}$.
- ▷ If FSSP and BSSP do not provide the same OSP for the very first sensors, results are almost equivalent after having placed a very few sensors, as illustrated by the (d)-subfigures. The results obtained by GA are very similar as well.
- ▷ The size of the truncated modal basis $\boldsymbol{\Phi}$ specified to the FIM conditions the sensor placement, as one can see in Fig. 3.4 where IE-based OSP is obtained for reduced basis $\boldsymbol{\Phi}$ made of respectively 5 and 8 modes.
- ▷ The amount of information carried by the first sensors is more important because not redundant: when as many sensors as modes in $\boldsymbol{\Phi}$ have been positioned, the amount of

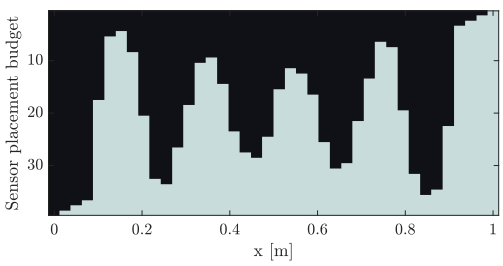

(a) OSP by FSSP.

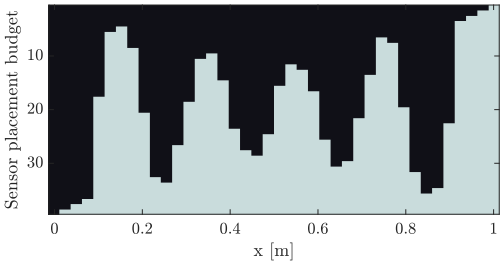

(b) OSP by BSSP.

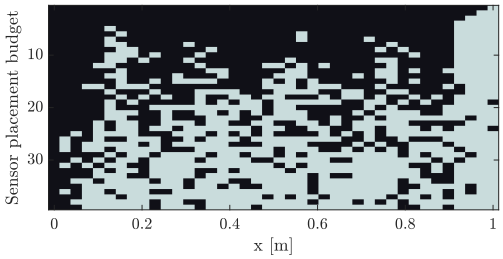

(c) OSP by GA.

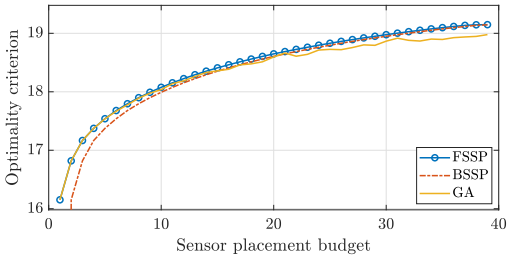

(d) Comparison of algorithms wrt $\boldsymbol{tr}\,(\boldsymbol{Q})$.

FIGURE 3.2: A-optimal sensor placement results (maximization of $\boldsymbol{tr}\,(\boldsymbol{Q})$) for modal analysis of the first 5 eigenmodes. At each line of subfigures a to c (given sensor budget), sensors are located with white squares.

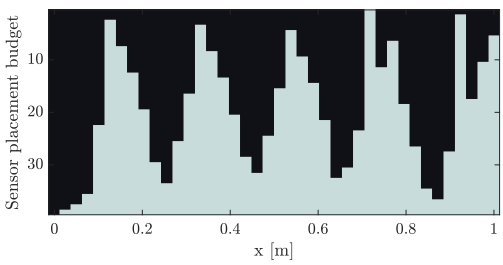

(a) OSP by FSSP.

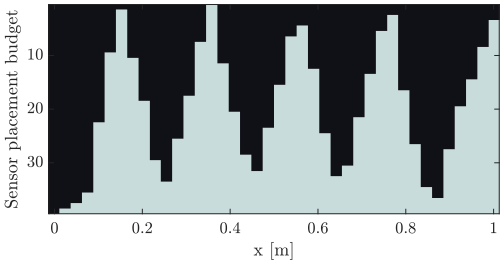

(b) OSP by BSSP.

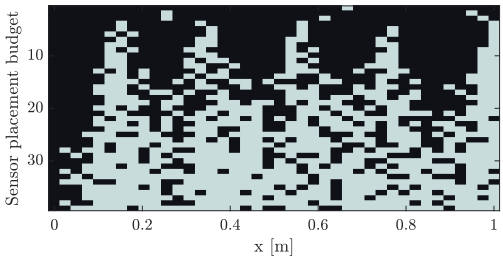

(c) OSP by GA.

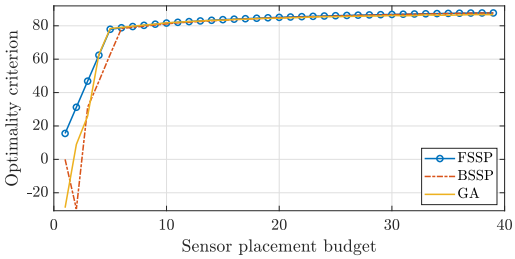

(d) Comparison of algorithms wrt det($\boldsymbol{Q}$).

FIGURE 3.3: D-optimal sensor placement results (maximization of det($\boldsymbol{Q}$)) for modal analysis of the first 5 eigenmodes. At each line of subfigures a to c (given sensor budget), sensors are located with white squares.

information carried by new sensors is less important as it only "conforts" the knowledge carried by the sensors that are already positioned. This is particularly visible with the sudden slope change in Fig. 3.3d.

> *Remark* 3.3. For the sake of reproducibility , it is important to notice that the FIM is singular if there are less sensors than modes in $\boldsymbol{\Phi}$, which is totally normal because there are more modes to identify than sensors. It can create numerical problems when optimizing det($\boldsymbol{Q}$) as the latter is null for all sensor configurations in that context. Following [Papadimitriou and Lombaert 2012], it has been decided to maximize the product of all non-zero eigenvalues

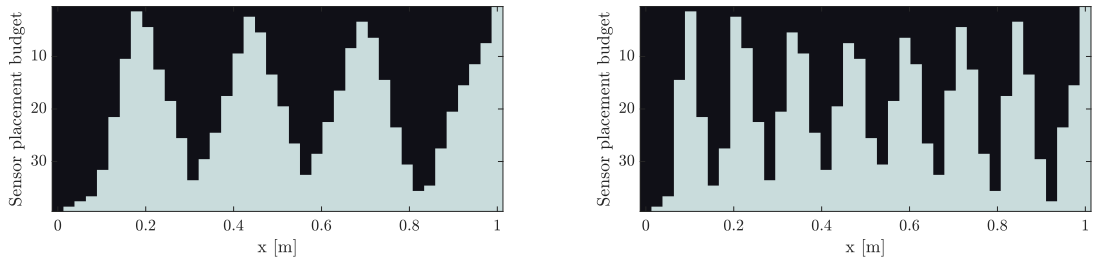

(a) OSP by FSSP with 4 modes in $\mathbf{\Phi}$.

(b) OSP by FSSP with 8 modes in $\mathbf{\Phi}$.

FIGURE 3.4: Effect of the size of $\mathbf{\Phi}$ to D-optimal sensor placement for modal analysis. At each line (given sensor budget), sensors are located with white squares.

of the FIM instead of the full determinant.

OSP for structural identification (with small uncertainties)

Let us now consider the case where the quantity of interest for OSP is directly the set of stiffness properties, and let us assume that they are well known *a priori* (small uncertainties). The FIM can thus be computed as specified in (3.10) with the state x depending on the stiffness distribution $\{k_i\}_{i=1}^{40}$. Because it is obvious that 40 sensors are mandatory to identify 40 parameters accurately, let us gather neighboring springs in subdomains so as to reduce the size of the parameter space. The A-optimal and D-optimal sensor placement results with 5 subdomains are proposed in Fig. 3.5 and 3.6, respectively.

First, the comparison of Fig. 3.5 and 3.6 reveals the soundness of OSP problems driven by the determinant of the FIM rather than its trace. If in both cases, one can recover that sensors are gathered at the subdomains boundaries, it appears that it takes at least 20 sensors with FSSP/BSSP algorithms to position sensors around the two first subdomains when maximizing the trace: A-optimal sensor placements are thus less relevant because of the heterogeneous identification sensitivity of parameters.

Similarly to modal analysis OSP, one can observe that after having positioned 5 sensors, the information carried by new sensors is lower as redundant - see Fig. 3.6d.

To show how the parametrization of the inverse problem to solve infers on the sensor placement results, Fig. 3.7 presents D-optimal sensor placement results for 10 subdomains. Here again, both FSSP and BSSP provide similar OSP, with the 10 first sensors almost located at the boundary between subdomains.

Contrary to the modal analysis case, even if computations are not expensive at all, one can afford a fair comparison of CPU times. In Tab. 3.1 are presented the necessary CPU times to optimally position a given budget of sensors as a function of the chosen OSP algorithm. As previously mentioned in Section 3.2.2, **FSSP should be preferred to BSSP when positioning a few number of sensors**. Although GA appears to be a less effective option, the difference in terms of CPU time with sequential algorithms is much less marked for real industrial applications. It is also important to notice that the tuning of the internal parameters of the algorithm conditions its efficiency[1].

Sensor budget	5	10	20	30
OSP Algorithm	Required CPU time [s]			
FSSP	**0.0243**	**0.0467**	0.0681	0.0746
BSSP	0.0734	0.0709	**0.0612**	**0.0435**
GA	0.6395	1.7274	1.6210	1.9497

TABLE 3.1: CPU time required by FSSP, BSSP and GA to position sensors for structural identification assuming a 5 subdomain parametrization.

[1]The MATLAB© global optimization toolbox in-core GA function ga was used in the present study.

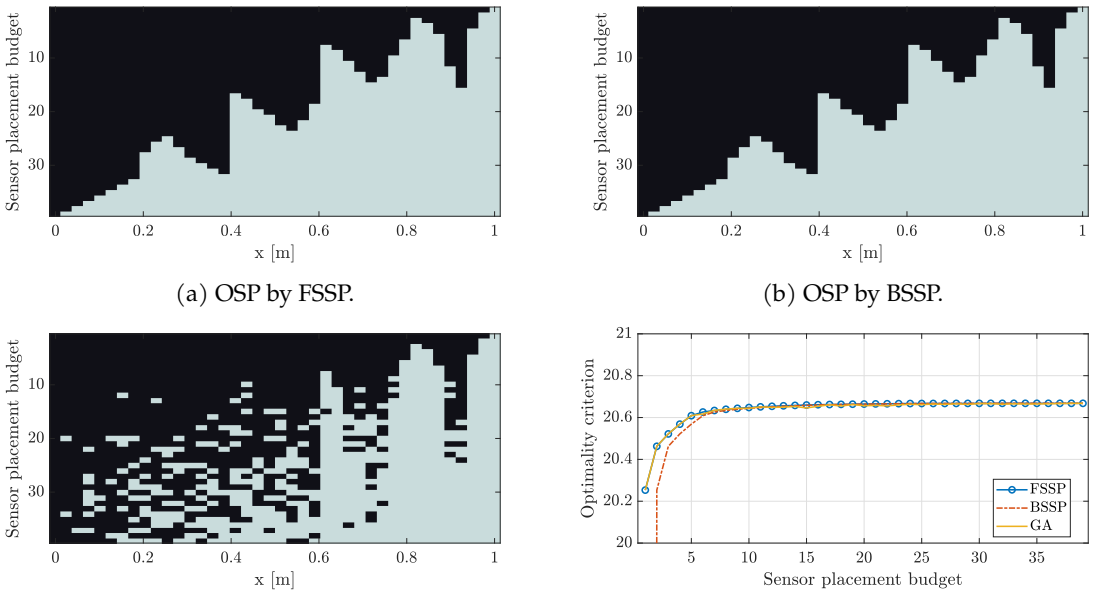

(a) OSP by FSSP.

(b) OSP by BSSP.

(c) OSP by GA.

(d) Comparison of algorithms wrt $\boldsymbol{tr}\,(\boldsymbol{Q})$.

FIGURE 3.5: A-optimal OSP results for structural identification of 5 subdomains.

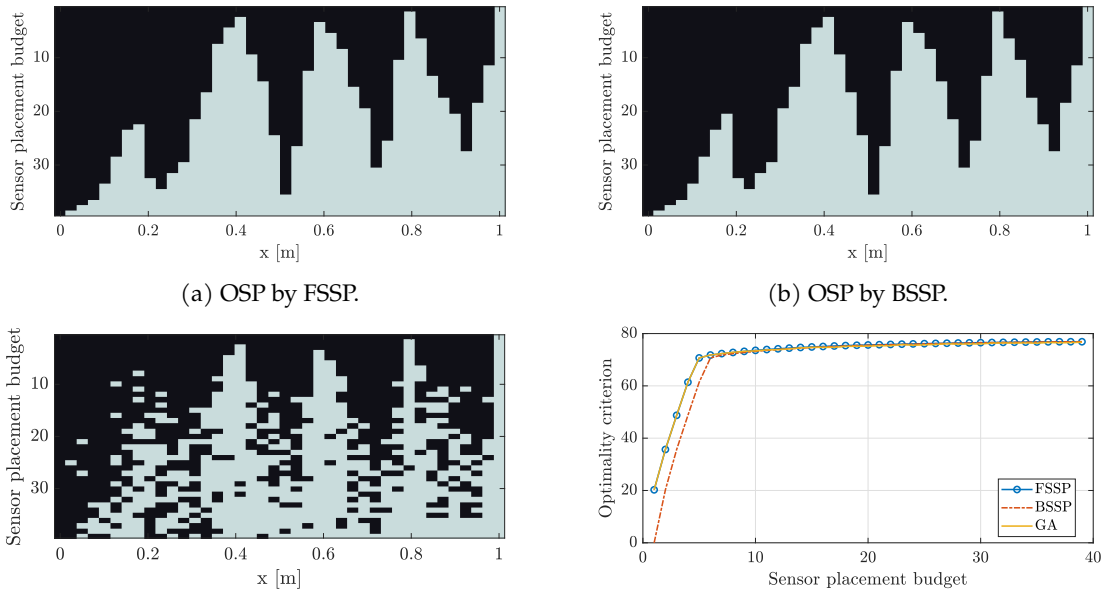

(a) OSP by FSSP.

(b) OSP by BSSP.

(c) OSP by GA.

(d) Comparison of algorithms wrt $\det(\boldsymbol{Q})$.

FIGURE 3.6: D-optimal sensor placement results for structural identification of 5 subdomains.

Eventually, the non-uniqueness (and ill-posedness) nature of the sensor placement problem is emphasized in Fig. 3.8 where one can remark there exist many optimal couples of positions for the two first sensors.

Conclusions from the application of classical OSP techniques

In this section, we illustrated classical OSP techniques on an academic example. It reveals to be a relevant gateway to introduce the main features of OSP, particularly the dependency into the parametrization of the inverse problem that is targeted and the ill-posedness nature of the OSP problem. The soundness of minimizing the determinant of the FIM instead of its trace is also highlighted when performing OSP for structural identification. Unfortunately, because the structural parameters sensitivity is too homogeneous in this 1D example, we have not been able

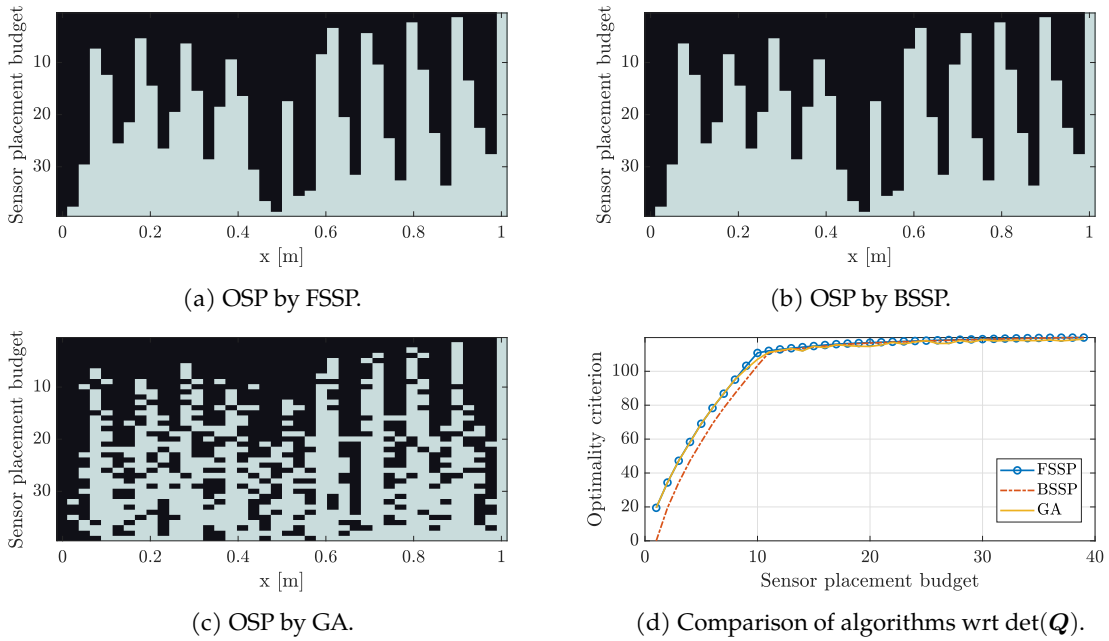

(a) OSP by FSSP.

(b) OSP by BSSP.

(c) OSP by GA.

(d) Comparison of algorithms wrt det($\boldsymbol{Q}$).

FIGURE 3.7: D-optimal sensor placement results (maximization of det($\boldsymbol{Q}$)) for structural identification of 10 subdomains.

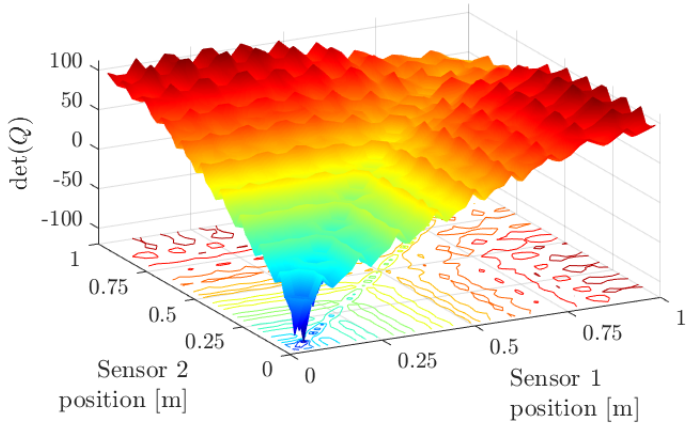

FIGURE 3.8: Illustration of the non-uniqueness and ill-posedness of the optimal placement of 2 sensors in the sense of det($\boldsymbol{Q}$) for structural identification.

to emphasize the case of large uncertainties mentioned in Section 3.2.1.

3.3 A mCRE-oriented OSP strategy

For structures having heterogeneous stiffness sensitivity to model updating, parameter estimates may be quite far from reality when the model updating process is performed using a small amount of sensors, as illustrated in Chapter 2. This is the case for several SHM applications considering one cannot always afford for dense instrumentation on large scale structures. If OSP strategies have been proposed for (standard) structural identification and modal analysis, there is no proper sensor placement strategy dedicated to mCRE-based model updating in the literature whereas it has shown to be an efficient alternative to standard approaches in Chapter 1. In the following, a modified FIM is introduced by integrating the mCRE within the information entropy. This novel approach is legitimate in light of the relationship between the mCRE (though deterministic) and the Bayesian inference framework detailed in Chapter 1.

3.3.1 mCRE-based OSP: modified Fisher Information Matrix

The key idea of this novel OSP technique is to use the mechanical fields $\{U_\omega\}_{\omega\in D_\omega}$ computed for mCRE needs (solution of system (1.20)) within the Information Entropy concept. Mathematically, we thus define a modified Fisher Information Matrix $\boldsymbol{Q}_m$ such that:

$$\boldsymbol{Q}_m = \sum_{\omega\in D_\omega} \left(\boldsymbol{\Pi}\nabla_\theta U_\omega\right)^T \left(\boldsymbol{\Pi}\boldsymbol{\Sigma}_y\boldsymbol{\Pi}^T\right)^{-1} \left(\boldsymbol{\Pi}\nabla_\theta U_\omega\right) \tag{3.13}$$

In other words, the modified FIM analyzes the sensitivity of the mCRE measurement error part with respect to the parameters to identify. The effect of the CRE is implicit in the computation of $\{U_\omega\}$.

Similarly to IE-based OSP techniques, the determinant of the modified FIM is maximized to position sensors (assuming the amount of data is large enough to reuse the asymptotic result mentioned above).

If FSSP has been chosen as reference to test mCRE-based OSP (see Alg. 3.5), all the previously mentioned algorithms are applicable as only the FIM definition is changed. Besides, the access to a semi-analytical expression of the gradient of U_ω with respect to θ is a valuable asset to perform OSP in reasonable CPU times: the modified FIM $\boldsymbol{Q}_m$ can thus be quickly computed without any loss of accuracy. As a reminder, the computation of $\nabla_\theta U_\omega$ is a low-cost post-processing operation once (1.20) has been solved (see Appendix B for the mathematical developments).

Algorithm 3.5: mCRE-based FSSP algorithm

Initialization: Grid of all N_d possible sensors locations, targeted number of sensors N_s, number of selected sensors $n = 0$, initial parameter guess $\theta_0 \in \Theta$, set of simulated measurements y (obtained with θ_0), FE model including mesh and matrices $\boldsymbol{K}, \boldsymbol{D}, \boldsymbol{M}$, mCRE internal parameters (frequency bandwidth D_ω, confidence into measurements α, frequency weighting function $z(\omega)$, reduced basis $\boldsymbol{\Phi}_L$

while $n < N_s$ **do**
- Consider all possible combinations by adding one new sensor: $\{\Pi_j\}_{j\in[\![1;N_d-n]\!]}$
- **for** $j \in [\![1; N_d - n]\!]$ **do**
  - Initialize the modified FIM $\boldsymbol{Q}_{m,j} = 0$
  - **for** $\omega \in D_\omega$ **do**
    - Get mechanical fields (U_ω, V_ω) solving the $AX = b$ system (eq. 1.24)
    - Compute $\nabla_\theta U_\omega$ (eq. 1.27)
    - $\boldsymbol{Q}_{m,j} = \boldsymbol{Q}_{m,j} + \left(\boldsymbol{\Pi}_j\nabla_\theta U_\omega\right)^T \left(\boldsymbol{\Pi}_j\boldsymbol{\Sigma}_y\boldsymbol{\Pi}_j^T\right)^{-1} \left(\boldsymbol{\Pi}_j\nabla_\theta U_\omega\right)$
  - **end**
- **end**
- Identify the sensor configuration $J = \underset{j\in[\![1;N_d-n]\!]}{\arg\min} \{\det\left(\boldsymbol{Q}_{m,j}\right)\}$
- Store the last sensor of configuration J as the n^{th} optimal position
- Go to the next iteration: $n \to n+1$

end

Remark 3.4. Although it is written in [Papadimitriou and Lombaert 2012] that the FIM given in (3.10) is obtained by asymptotical approximation of $N_y N_s \nabla_\theta \nabla_\theta^T \mathcal{J}(\theta, y)$, one should not think that it is possible to directly replace the FIM expression with the semi-analytical Hessian matrix expression of the mCRE functional. Indeed, the analysis of the mathematical proof in [Papadimitriou 2004] confirms that the FIM expression appears by simplifying the second order derivative of $\log \mathcal{J}_{LS}(\theta, y)$ with respect to θ, where $\mathcal{J}_{LS}$ is a classical least square functional between data and model predictions. This does not apply for the mCRE, hence the formulae lying on the gradient.

3.4 Application in structural dynamics on a 3D example

3.4.1 Description of the problem

A realistic (yet academic) earthquake engineering application is considered here with the frame structure of Fig. 3.9 submitted to a 2D random ground acceleration. The problem consists in positioning a set of accelerometers to identify at best the stiffness distribution of the structure. To simulate damage scenarios, inasmuch as it is assumed that very few sensors are available, an intuitive coarse stiffness parametrization of the stiffness is defined. Six subdomains are defined {W10, W11, W20, W21, F10, F20}, one per wall and per slab. The updated stiffness model (1.14) is thus made of $N_\theta = 6$ parameters. The subdomains areas are clearly presented in Fig. 3.9.

In practice, this example is the 3D extension of the plane frame example presented in Appendix A.1. The model is made of shell elements instead of beam elements in CAST3M©, and relative time acceleration measurements in both x and y directions are simulated using fast Fourier transforms and the frequency transfer matrix of the direct dynamical problem formulated in terms of relative displacement.

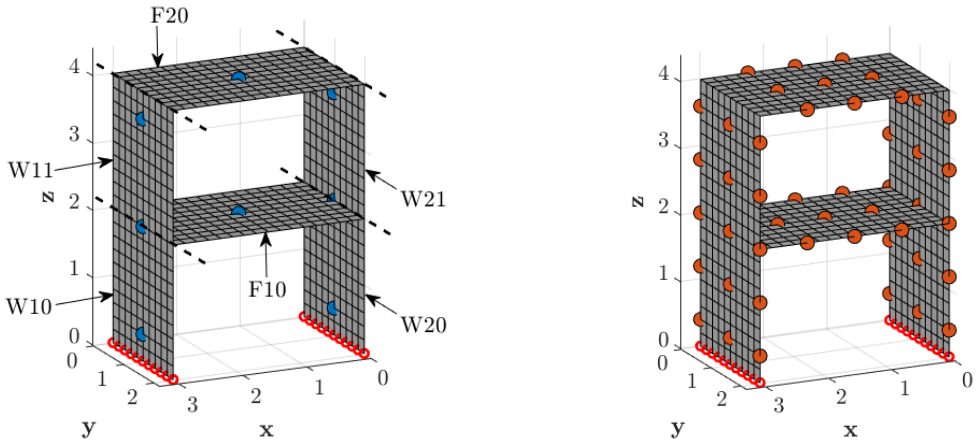

(a) Uniform sensor placement (blue dots).

(b) Grid of possible accelerometer locations.

FIGURE 3.9: Frame structure - uniform default sensor placement and grid of possible locations for OSP. Subdomains areas and denomination are also given.

The objective of this application is to assess the proposed sensor placement strategy for efficient mCRE-based identification. To restrain CPU times and to avoid sensors concentrations, a grid on 48 potential sensor locations is defined: a triaxial accelerometer can be positioned at each orange circle of Fig. 3.9b.

Although several types of sensors could be positioned simultaneously, only accelerometers are considered herein because they are popular, reliable on a large frequency bandwidth, minimally invasive and easily deployable for SHM and earthquake engineering applications. In order to be realistic regarding what could be achieved in practical shaking table tests, a restricted budget of $N_s = 24$ data acquisition channels is fixed. It allows to uniformly spread enough sensors to reproduce typical sensor placement configurations from earthquake engineering applications. Besides, as $N_\theta = 6$ parameters are supposed to be updated, it is theoretically enough to get proper identification results and information redundancy in measurements.

3.4.2 OSP benchmark

In order to assess the relevance of mCRE-based OSP with respect to other strategies, a numerical benchmark has been conducted to compare sensor placements oriented towards different quantities of interest. An overview of the tested strategies is presented in Tab. 3.2.

Description and desingation		Optimality criterion	Accelerometer type
Reference (dense) OSP ($N_s = 48$)	Ref	-	-
Uniform default OSP	Def	-	Triaxial
OSP for modal analysis of the 10 first structural eigenmodes	MA1	$\log(\det Q(\Phi))$	Uniaxial
	MA2		Triaxial
OSP for standard structural identification	SI1	$\log(\det Q(X))$	Uniaxial
	SI2		Triaxial
mCRE-based OSP	mCRE1	$\log(\det Q_m)$	Uniaxial
	mCRE2		Triaxial
mCRE-based OSP for uncertain damage scenarios	mCRE-MS1	$\int_\Theta \log(\det Q_m)\pi_0(\theta)\mathrm{d}\theta$	Uniaxial
	mCRE-MS2		Triaxial

TABLE 3.2: OSP benchmark

OSP algorithms for modal analysis (MA# cases), structural identification (SI# cases) and mCRE-based model updating are compared, for uniaxial and triaxial accelerometers. The case of multiple scenarios is also considered for mCRE-based OSP (mCRE-MS# cases). A FSSP optimization algorithm is used in all cases to fairly compare sensor placement results between methods. Among the proposed sensor placement strategies, it should be highlighted that:

- ▷ In the reference OSP, all the possible locations are covered with triaxial accelerometers. The sensor configuration is thus spatially highly dense. This is not a realistic configuration, neither an economous one, but it provides a reference case when comparing the performance of OSPs in terms of model updating.
- ▷ In the uniform default case, 8 triaxial accelerometers are uniformly spread over the structure. This is typically what should be done naively without considering OSP algorithms.
- ▷ Optimal uniaxial and triaxial accelerometer placement are systematically compared. Positioning triaxial sensors is more practical from the experimental viewpoint and less computationally demanding than uniaxial accelerometer placement because the number of possible sensor configurations is reduced. However, forcing triaxial sensors implies the addition of constraints to OSP strategies, which should thus lead to less performant results.
- ▷ The OSP strategies oriented towards modal analysis aim to identify at best the 10 first structural eigenmodes. As a reminder, the associated Fisher Information Matrix reads:

$$\boldsymbol{Q}(\boldsymbol{\Phi}) = (\boldsymbol{\Pi}\boldsymbol{\Phi})^T \left(\boldsymbol{\Pi}\boldsymbol{\Sigma}_y\boldsymbol{\Pi}^T\right)^{-1} (\boldsymbol{\Pi}\boldsymbol{\Phi}) \tag{3.14}$$

  which is independent of the nominal stiffness parameter values θ_0.
- ▷ The OSP for structural identification directly deals with the identification (in a least-square sense) of the stiffness parameters. In that case, the FIM is directly computed from the sensitivity of the frequency-domain counterpart of the mechanical state U with respect to the parameter set θ:

$$\boldsymbol{Q}(U) = \sum_{\omega\in D_\omega} (\boldsymbol{\Pi}\nabla_\theta U(\theta,\omega))^H \left(\boldsymbol{\Pi}\boldsymbol{\Sigma}_y\boldsymbol{\Pi}^T\right)^{-1} (\boldsymbol{\Pi}\nabla_\theta U(\theta,\omega)) \tag{3.15}$$

  and for the considered stiffness parametrization and dynamical equilibrium (1.12), the gradient formulation is analytical:

$$\nabla_\theta U(\theta,\omega) = -\boldsymbol{Z}(\theta,\omega)^{-H} \frac{\partial \boldsymbol{K}}{\partial \theta} \boldsymbol{Z}(\theta,\omega)^{-1} \left[\omega^2 \boldsymbol{M}\boldsymbol{\Xi}U_{d,\omega}\right] \tag{3.16}$$

  with $\boldsymbol{Z}(\theta,\omega)$ the dynamical impedance of the structure at angular frequency ω. For legitimate comparisons with mCRE-based OSP, the frequency range that is considered to

compute $\boldsymbol{Q}(U)$ is also D_ω. Note that the FIM could also be obtained with time-domain measurements, but the sensitivity matrix would be computed by solving a full-time domain problem [Papadimitriou and Lombaert 2012].

Contrary to the MA cases, the optimal sensor locations depend on the location and type of excitation that is used. Also, the matrix $\boldsymbol{Q}(U)$ may be non-singular even for only one positioned sensor since the structural response obtained from the model may store enough information from all contributing eigenmodes in order to estimate the parameter set θ.

- Regarding the setting of the mCRE, as the first five modes of the structure are below 20 Hz, a frequency bandwidth $D_\omega = [1\text{ Hz}; 30\text{ Hz}]$ with $\Delta f = 0.1$ Hz has been chosen for the computation of all forthcoming results. The call to a reduced basis made of the first 10 eigenmodes (*i.e.*, $\dim(\text{span}(\boldsymbol{\Phi}_L)) = 10$) of the frame allows to achieve fast and accurate mCRE computations as it largely covers the frequency range of interest. The weighting function $z(\omega)$ is computed using the H-CMIF. The value of α is hardly tunable as measurements are not available at the experimental design stage[2]. Its effect will be analyzed via calibration tests, and the tested values will be specified case by case for the sake of reproducibility in the following.

- Because one also intends to provide sensor placements that are still efficient once damage has occurred, the case of multiple scenarios mCRE-based optimal sensor placement has been addressed. Following the subdomain decomposition shown in Fig. 3.9, the 6 parameters have been pseudo-randomly sampled using a Latin Hypercube algorithm (LHS) in order to take into consideration 30 damage scenarios, assuming the parameter set follows a multivariate uniform pdf on $([0.2; 1])^{N_\theta}$. This is the less informative prior pdf in the sense of the statistical maximum entropy. The generated set of samples is denoted Θ_S. Each $\theta_s \in \Theta_S$ is thus used to simulate a dataset y_s, which will be processed to perform OSP. The stiffness parametrization of each scenario is given in Fig. 3.10. The change on stiffness parameters has significant effects on the frequency domain response of the structure as one can observe in Fig. 3.11 where the normalized H-CMIF plot for each considered damage configuration is given, because the frequency shift of the peaks shows how the structural response varies from one scenario to the other.

Following the work initiated in [Papadimitriou et al. 2000] for the case of highly uncertain parameters, the optimality criterion is thus approximated by:

$$\int_\Theta \log\left(\det\left(\boldsymbol{Q}_m(\boldsymbol{\Pi}, \theta, y)\right)\right)\pi_0(\theta)\mathrm{d}\theta \approx \frac{1}{\#\Theta_S}\sum_{\theta_s\in\Theta_S}\log\left(\det(\boldsymbol{Q}_m(\boldsymbol{\Pi}, \theta_s, y_s(\theta_s)))\right) \tag{3.17}$$

leading to an optimal sensor placement that is dedicated to a wider range of damage configurations. In practice, it is true that cases involving damage at the top of the structure are highly unlikely, but the uncertainty on estimated parameters in such cases will naturally discriminate them with regards to more sensitive and realistic damage configurations.

[2] This is also one of the reasons that motivated the proposal of *a priori* calibration rules in Chapter 1.

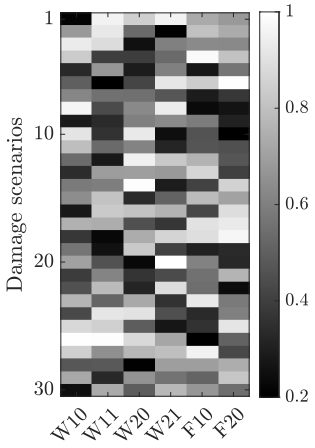

FIGURE 3.10: Stiffness samples Θ_S to simulate multiple damage scenarios.

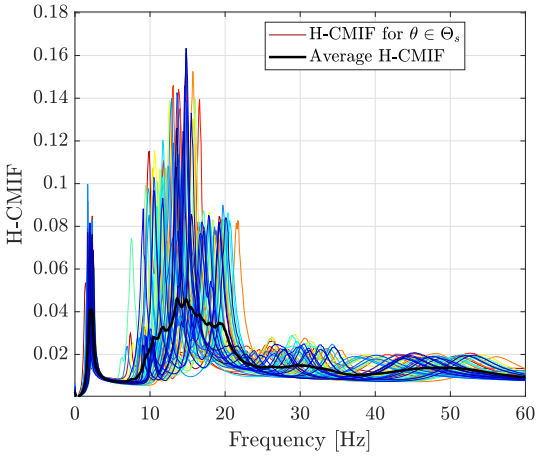

FIGURE 3.11: Impact of damage configuration on the frequency response of the structure. A wide variability of responses is integrated into the OSP framework.

3.4.3 OSP results - first comments

Modal identification

The OSP results obtained for modal analysis using a truncated modal basis made of the first 10 modes of the frame are presented in Fig. 3.12. To confirm the soundness of the results, both $\det(\boldsymbol{Q})$ and the H-CMIF obtained after having positioned accelerometers are plotted, with a comparison to the H-CMIF obtained from the dense OSP configuration.

The amount of information carried by the first sensors is more important as it allows the identification of one supplementary mode. When as many sensors as modes in $\boldsymbol{\Phi}$ have been positioned, the additional information carried by new sensors is less important as it only conforts the modal identification, making it more accurate. Due to the complexity of the structure, no clear visual trend from the sensor position can be easily guessed, except that most sensors are located on the floors. This is legitimate as floor eigenmodes are part of the 10 first ones of the structure.

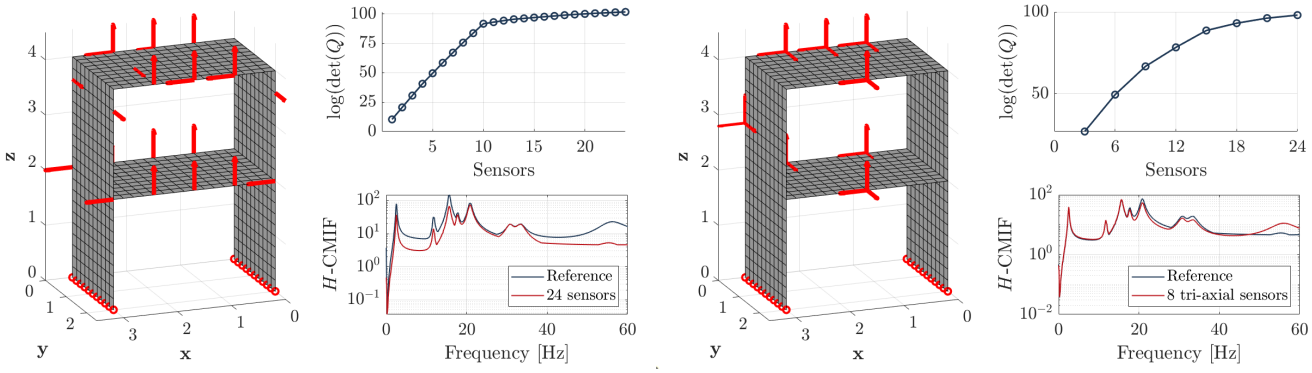

FIGURE 3.12: OSP of uniaxial and triaxial accelerometers for the MA1 (left) and MA2 cases (right). Accelerometers positions are given by the red arrows, while determinant of the FIM (in log scale) and H-CMIF are plotted to confirm the soundness of the approach.

3.4.4 Structural identification OSP results

The OSP results obtained for SI1 and SI2 cases are presented in Fig. 3.13. The evolution of $\det(\boldsymbol{Q}(U))$ is also given to confirm the relevance of the results. Due to the large parameters sensitivity, the sensor placement is not visually intuitive in the sense that not all subdomains

are covered by at least one sensor. One can interpret the fact that sensors are mostly located at the top of the structure because it is the most kinematically responsive part of the latter. However, from the sudden slope change of the determinant of the FIM with positioned sensors, we find that after the placement of 6 sensors, the system is a priori totally identifiable, meaning that new sensors (mostly) bring redundant information.

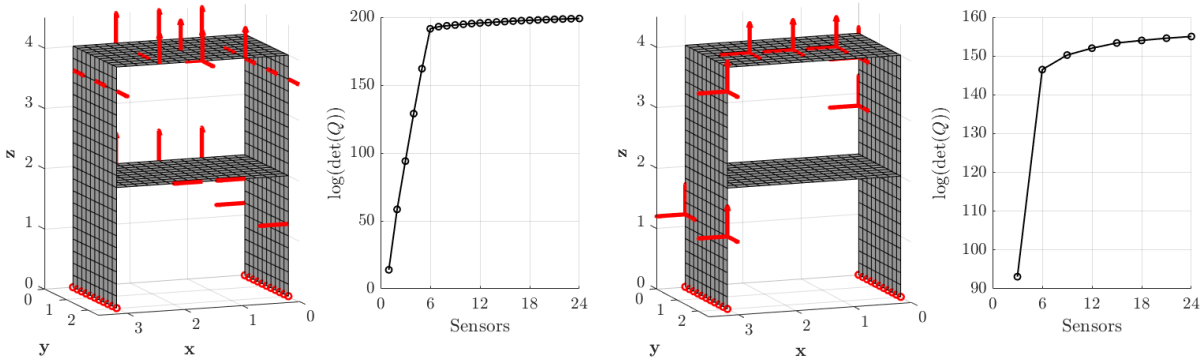

FIGURE 3.13: OSP of uniaxial and triaxial accelerometers for the SI1 (left) and SI2 cases (right). Accelerometers positions are given by the red arrows, and the determinant of the FIM (in log scale) is plotted to confirm the soundness of the approach.

mCRE-based OSP results

The OSP results obtained for mCRE1 and mCRE2 cases are presented in Fig. 3.14. To understand at best the sensor placement process, a particular attention was paid to the sequential positioning of sensors by coloring the sensor position according to its order of appearance in the FSSP algorithm. The value of the $\det(\boldsymbol{Q}_m)$ is also provided. The value of α is well-known to be crucial in the mCRE framework, and as it is not properly tunable at the experimental design stage, its influence on mCRE-based OSP results was explicitely studied. What can be observed at first glance is that the more important the confidence into measurements α, the closer to the bottom of the structure for sensor locations. If the increasing value of $\det(\boldsymbol{Q}_m)$ confirms FSSP behaves correctly, the values plotted in Fig. 3.14 are not comparable as they are function of α (which implicitly modifies the FIM definition). For the following studies, the confidence into measurements coefficient has been chosen at $\alpha = 10^4$ because of the correct dispersion of the sensors on the whole structure (see Fig. 3.14).

Finally, OSP results for mCRE-based sensor placement taking multiple damage scenarios into account are presented in Fig. 3.15. Several remarks can be made from these placements. First, there is no sensor positioned in the x direction for the mCRE-MS1 case, which can explain why mCRE-MS2 is less optimal in the sense of the $\det(\boldsymbol{Q}_m)$. Unsurprisingly, one can notice that the first sensors in both cases are located at the bottom of the structure, where damage is most likely to occur. Similarly, few sensors are located on the top walls as they are less identifiable (in the CRE sense) and less prone to damage. Of course, the numerical resources that are necessary to compute these results are much more important, as $\#\Theta_S$ times more solutions of the mCRE system are required. Hopefully the required CPU time did not exceed more than 12 hours on a personal laptop. This numerical effort should be worthwhile, as the resulting sensor placement will be effective over a wider range of stiffness configurations.

> *Remark* 3.5. The values of $\det(\boldsymbol{Q})$ between the different OSP techniques are not comparable as the FIM definition is different.

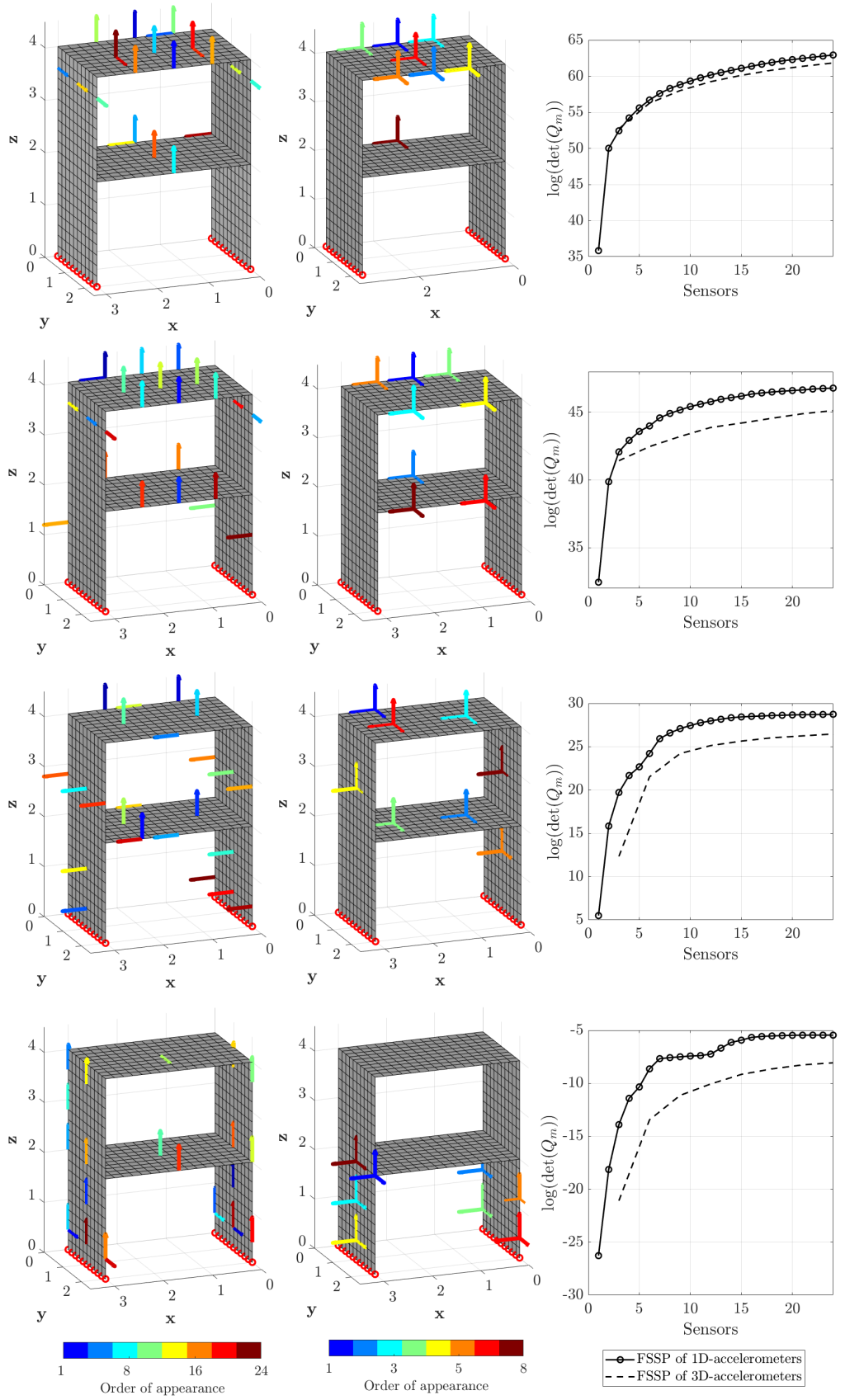

FIGURE 3.14: mCRE-based OSP of uniaxial and triaxial accelerometers for the identification of the 6-subdomain parametrization of the frame. The arrows indicate the sensor position and their color indicates their order of appearance in the FSSP strategy. From top to bottom, results have been obtained with $\alpha = \{1; 10^2; 10^4; 10^6\}$.

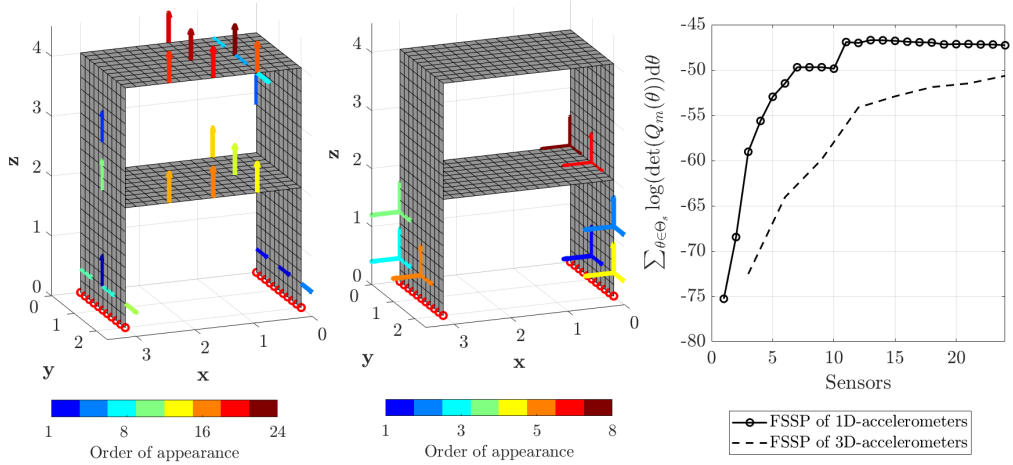

FIGURE 3.15: mCRE-based OSP of uniaxial and triaxial accelerometers taking multiple damage scenarios into account. The arrows indicate the sensor position and their color indicates their order of appearance in the FSSP strategy. A value of $\alpha = 10^4$ was chosen.

3.4.5 Comparisons of OSP methods for mCRE-based model updating

Model updating case study

Because we look for optimal sensor placement in the sense of damage detection, we propose to challenge the different OSP that have been obtained and presented previously for mCRE-based model updating using three datasets that fairly represent the typical situations one can meet in practice:

(i) Updating the model from the same data that has been used to perform OSP. The expected parameter vector is exactly the one that has been used to position sensors.

(ii) Updating the model from data obtained after an overall 10% stiffness underestimation. This is a situation that can be encountered with the presence of modeling bias. In addition, measurements will be polluted with a white noise of 10%-SNR with respect to the input ground acceleration.

(iii) Updating the model from data obtained in a new damage scenario. The expected parameter vector is $\theta^\star = [0.5\ 0.9\ 0.6\ 0.9\ 0.8\ 1]$. Measurements are also polluted with noise (10% in level too). Note that this scenario is not included in Θ_S.

Case (i) is probably the most comfortable model updating situation with ideal measurements; Case (ii) gets more difficult as noise is added to measurements and a uniform model bias must be recovered; Case (iii) is the most challenging problem as a damaged configuration must be identified from noisy measurements using sensors whose location has been optimized from another parameter estimate (except for mCRE-MS1 and mCRE-MS2 cases). Because of the random nature of measurement noise, one cannot expect to properly assess model updating performance exclusively with parameters estimates. Model updating results will thus be assessed using both parameter estimates and relative confidence intervals widths (see Chapter 2 - section 2.2.2), using the highly dense sensor placement as reference.

> *Remark* 3.6. Although not considered here because of the assumed non-damaging nature of the input signals, the variability of loading conditions may also have been exploited if nonlinear damaging models were used, so that the damage scenarios that are generated for OSP are much more realistic.

mCRE-based model updating results

The assessment of OSP for model updating is summarized in Fig. 3.16 with 6 colormaps. For each model updating scenario, we propose two colormaps: the first one indicates the relative gap of parameter estimates with respect to the exact parameter set that should have been recovered $\theta^\star$ (see Fig. 3.16.a). The second map shows the relative width of confidence intervals with respect to the ones given by the reference sensor placement configuration (see Fig. 3.16.b).

For all maps, each line indicates the performance obtained by a given sensor placement (denominations are given in Tab. 3.2) while each column corresponds to a given subdomain (denominations are given in Fig. 3.9).

The understanding of results displayed in Fig. 3.16.b is not direct and is recalled in the following lines: a close-to-zero value means that the convexity of the mCRE functional evaluated around $\hat{\theta}$ with a given OSP is almost the same as the one of the mCRE evaluated with the reference sensor placement case in which twice the number of sensors are present. It suggests that the considered sensor placement is efficient in the sense that there is not much doubt regarding the value of parameter estimate. On the contrary, when the relative gap on confidence intervals width is important, the mCRE functional is less convex around $\hat{\theta}$, meaning that another measurement noise realization may have lead to significantly different model updating results.

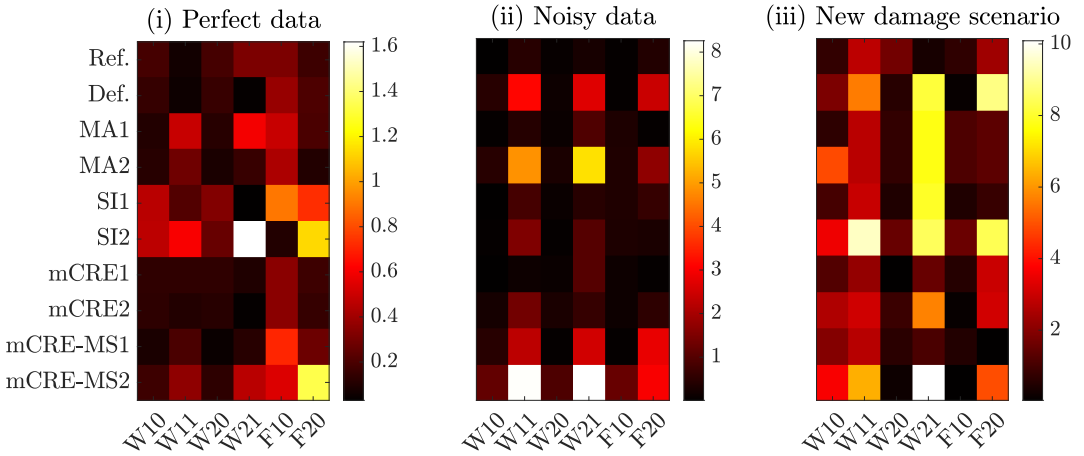

(a) Relative gaps on parameter estimates (in [%]) obtained with the different sensor configurations.

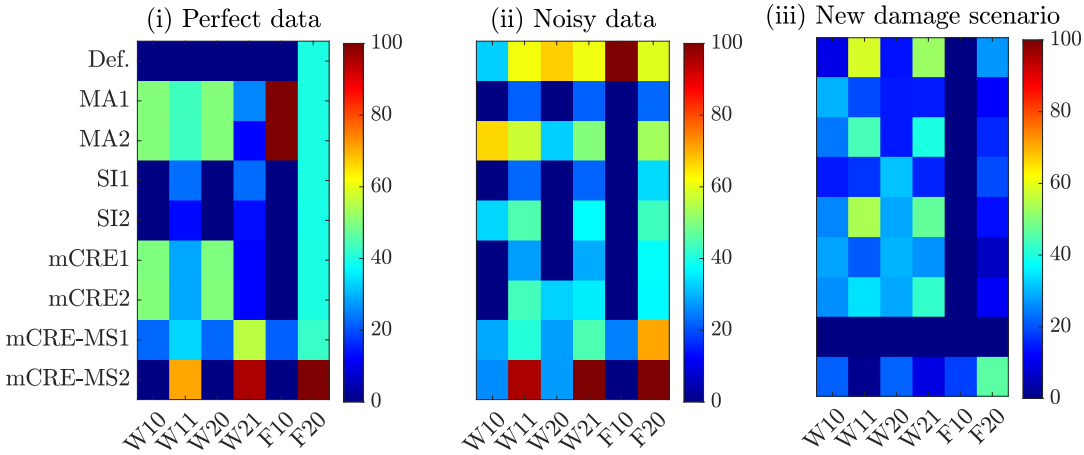

(b) Relative gaps on confidence intervals (in [%]) obtained with the different sensor configurations.

FIGURE 3.16: Assessment of optimal sensor placement algorithms for several model updating scenarios with the mCRE as cost-function.

Discussion on the relevance of the modified FIM

According to the results of Fig. 3.16, one can first conclude that, because the number of sensors ($N_s = 24$) was sufficient with respect to the number of parameters to be identified ($N_\theta = 6$), correct mCRE-based model updating results have been obtained in all cases as parameters have been correctly identified with less than 10% error with respect to the expected values in the most unfavorable case. The comparison of the maps (a.i) and (a.ii) reveals that the presence of noise extends the identification issues on the less sensitive parameters of the problem, namely the top-story ones (W11, W21 and F20). Besides, if one compares the visual positioning of sensors previously shown with the relative confidence intervals widths, it appears that the subdomains of parameters having large intervals are not directly equipped by sensors (associated to poor convexity and low sensitivity). One can also observe that the triaxial accelerometers placement is less accurate, as expected from the values of the determinant of the FIM plotted above.

The overall analysis of Fig. 3.16 confirms the effectiveness of mCRE-based OSP. Indeed, mCRE1 and mCRE2 sensor configurations provide the best parameter estimates, with minimal confidence intervals when data is noisy. This application is thus a **proof of concept showing the benefits of FSSP with the modified FIM that directly yields from the interpretation of mCRE from a Bayesian viewpoint**. Nevertheless, it is important to keep in mind the main limitation of this new OSP approach: the strong dependency in the confidence into measurements coefficient α. As running a mCRE-based OSP algorithm did not last more than 5 minutes for the considered case, the experimental designer can afford to assess mCRE-based OSPs obtained for several values of α. Despite this alternative, in-depth studies must be conducted to clarify this point. In particular, one can legitimately wonder if the optimality criteria for calibrating α that have been proposed in Chapter 1 are convenient to obtain relevant sensor configurations. Additional tests on other damage scenarios can also be done to confirm the observed trends.

Finally, let us point out that **taking into account several damage scenarios allows for a more robust sensor placement with respect to the identification of new parameter configurations**, as shown in Fig. 3.16 - mCRE-MS1 case in scenario (iii), where the identification is almost perfect with small-size confidence intervals. The CPU time spent to "learn" the best trade-off from multiple datasets is thus worth of interest. As one could have expected, taking into account several scenarios makes mCRE-MS1 and mCRE-MS2 model updating results suboptimal (yet efficient) for cases (i) and (ii) compared to mCRE1 and mCRE2. However, the performance achieved in case (iii) by mCRE-MS1 and mCRE-MS2 is remarkable and promising for monitoring the occurrence and evolution of structural defects on structures. This observation goes in the sense of recent contributions [Cantero-Chinchilla et al. 2020; Ercan and Papadimitriou 2021] which emphasize the **need to take both model and measurement uncertainties into consideration to build efficient and robust OSP**.

3.5 Conclusion & prospects on the numerical framework for OSP and model updating unified around the mCRE

Even though the modified Constitutive Relation Error has proved to be a credible alternative to classical model updating approaches, no dedicated sensor placement strategy has been proposed yet, although the literature on this topic in the literature is extensive. The ambition of the work presented in this chapter consisted in proposing a novel sensor placement algorithm dedicated to mCRE-based model updating. Owing to the link between the mCRE and the Bayesian inference framework, and inspired from the Information Entropy concept, a modified Fisher Information Matrix was formulated and its determinant was maximized to optimally position sensors. A proof of concept showing the relevance of this new mCRE-based OSP strategy has been proposed on a 3D academic example where optimal accelerometers locations were searched on a two-story frame structure subjected to random ground motion. This case study permitted to perform deep analysis of this new OSP approach and to compare it with classical techniques in different model updating scenarios, which allowed to illustrate the efficiency and relevance of

the proposed mCRE-based OSP methodology. If this study focuses on accelerometers as they are common and weakly invasive for earthquake engineering applications, all types of sensors can be easily integrated in the proposed framework.

All the OSP techniques that have been implemented in MATLAB© have been capitalized for future use at the CEA/TAMARIS as decision-support tools in forthcoming experimental campaigns.

Therefore, the proposed mCRE-based OSP appears as an interesting additional **asset for the construction of a mCRE-unified framework for SHM or structural dynamics applications** (see Fig. 2). However, there is no doubt that this tool still lacks maturity to be properly exploited, and further research should address the strong influence of the confidence into measurements coefficient and validate the observed trends on more complex case studies. Besides, as OSP are not exclusively intended to perform optimal model updating, future work will focus on finding the best sensor placement trade-off that contributes to multiple objectives simultaneously, for example modal identification and mCRE-based model updating. Pareto front algorithms may be a first tool for this purpose.

Moreover, one of the current on-going investigations of the authors concerns the use of mCRE-based OSP for active sensing purposes in order to improve damage detection in cases where the state of the structure is tracked online via data assimilation techniques (that are presented in the next chapter). Iterative strategies could then be employed to refine the sensing configuration only where needed, *i.e.* where damage occurences are detected.

What may also be interesting to consider is the impact of sensor location errors on the model updating process. Indeed, as most sensors in practical applications are located at vibration nodes and antinodes, the sensitivity of identification results with respect to sensor positioning errors must be estimated for uncertainty quantification purposes. Initial investigations on simple applications (see figure 3.17) have shown that a slight error in sensor position can lead to significant variability in model updating results. Forthcoming studies must be conducted to properly integrate all sources of uncertainty within the model updating process.

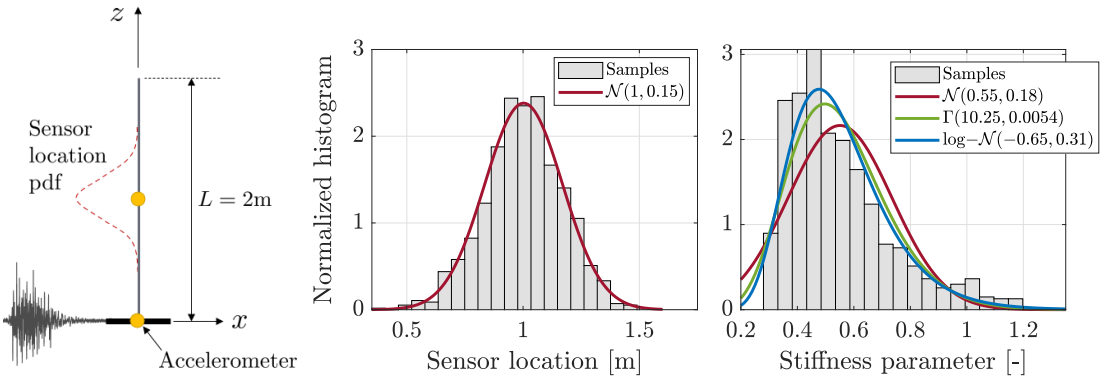

FIGURE 3.17: Highlighting the effect of sensor positioning error on mCRE-based parameter identification. The overall stiffness of a cantilevered beam is estimated with an accelerometer supposed to be located in the middle of the beam. Assuming the sensor location error follows a Gaussian distribution, a Monte-Carlo sampling on the sensor location allowed to quantify the uncertainty on parameter estimates. Based on the parameter distribution, probability densities have been empirically adjusted, showing that a lognormal distribution seems to correspond well to the observed distribution.

Finally, mid-term prospects may concern the extension of the presented OSP method to distributed measurements (*i.e.* optic fibers). At a first glance, one might want to use the presented strategy to identify optimal strain measurement points and then find the best path (with constrained bending radius) through these points to obtain an optimal optic fiber path for mCRE-based damage detection. Another way to do so would be to exploit a parametrized fiber path description, using splines and isogeometric analysis for example.

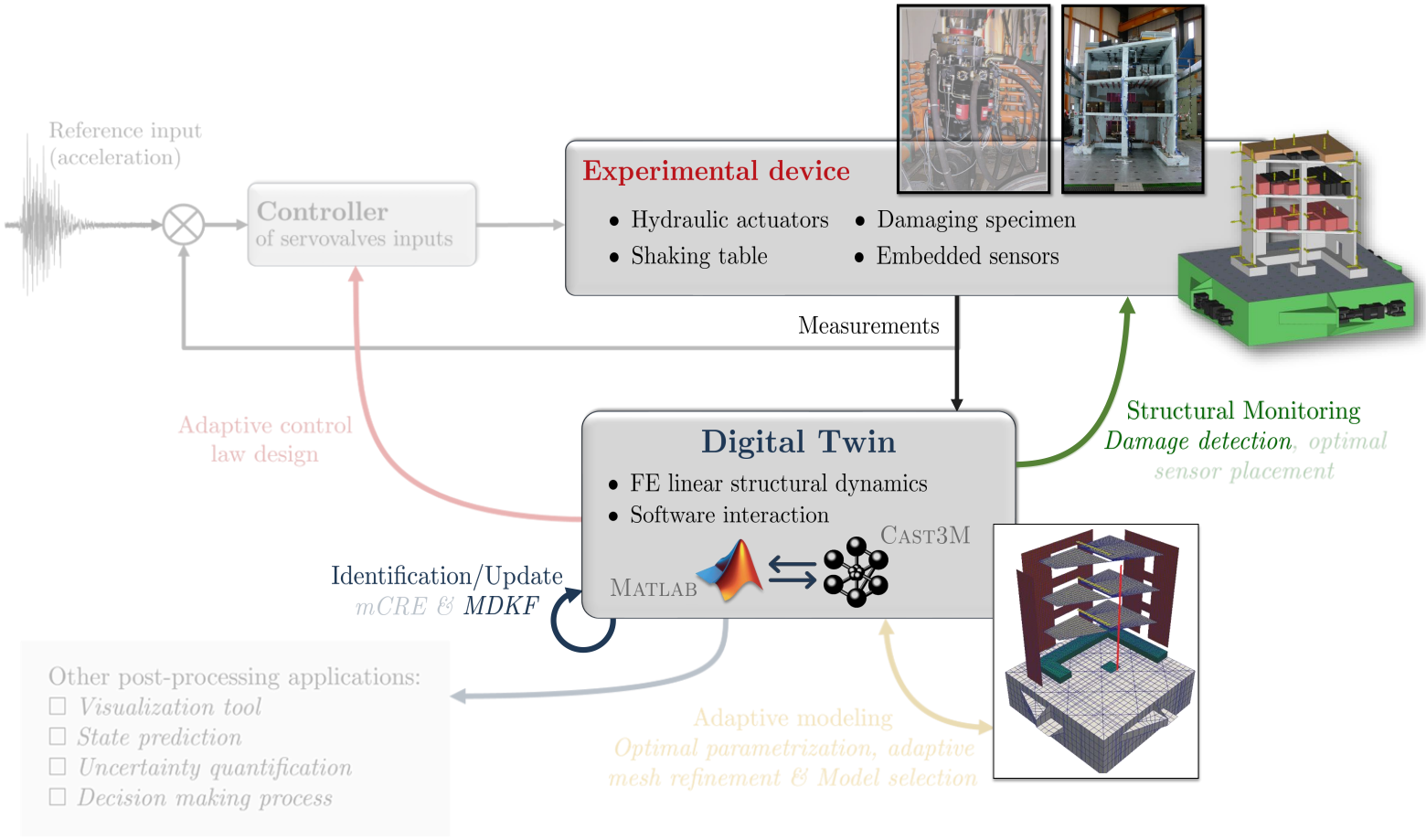

Extension to a data assimilation framework applied to the real-time monitoring of structures undergoing damaging ground motion

Believe nothing you hear, and only one half that you see.

Edgar Allan Poe, *The System of Dr. Tarr and Prof. Fether*

Chapter 4

The MDKF, a physics-guided Kalman filter for real-time model updating in dynamics

Integration of mCRE into a data assimilation framework

The feasibility of DDDAS lies (among others) in efficient data assimilation schemes able to update model predictions from acquired data. Such algorithms must be able to operate in real-time whereas the computational burden carried by recursive calls to model predictions can be prohibitive. So far, a model updating framework based on the modified Constitutive Relation Error has been presented to handle at best sparse noisy dataset in low-frequency dynamics, in an offline context.

In this chapter, attention is paid to the identification/update loop of Fig. 2 and a new Kalman filter-based approach for real-time data assimilation is proposed, where the offline mCRE-based model updating framework is reinvested in order to perform robust on-the fly structural parameter tracking. In practice, this new data assimilation scheme, called Modified Dual Kalman Filter (MDKF), integrates the mCRE through a metric change in the measurement update equation. It thus differs from classical nonlinear Kalman filtering for parameter estimation as the comparison between measurements and model predictions is achieved via the mCRE functional itself.

After a review of classical data assimilation techniques, with particular emphasis on Kalman filtering, the MDKF algorithm is presented in details. The performance of MDKF is assessed using the applications described in Appendix A, i.e., (i) synthetic measurements from a plane frame subjected to random ground motion, and (ii) actual measurements from the SMART2013 benchmark. In this last example, the eigenfrequency drop of a reinforced-concrete structure submitted to a sequence of gradually damaging shaking table tests has been monitored in real-time, which suggests a promising use of MDKF for on-the-fly adaptive control prospects.

The work presented in this chapter has been the subject of the following contributions:

M. Diaz, P.-É. Charbonnel, and L. Chamoin [2023a]. "A new Kalman filter approach for structural parameter tracking: Application to the monitoring of damaging structures tested on shaking-tables". *Mechanical Systems and Signal Processing* 182, p. 109529. DOI: 10.1016/j.ymssp.2022.109529

M. Diaz, P.-É. Charbonnel, and L. Chamoin [2023b]. "A new physics-guided data assimilation framework for online structural monitoring: application to shaking-table tests". *COMPDYN2023 - 9th ECCOMAS Thematic Conference on Computational Methods in Structural Dynamics and Earthquake Engineering*. Athens, Greece

Contents

4.1 Data assimilation for DDDAS - an overview

From the numerical viewpoint, the integration of a digital twin in the control loop of Fig. 2 requires a complex numerical framework including the necessity to adapt classical model updating techniques to an online context where data must be processed on-the-fly. In particular, data assimilation algorithms must be able to operate in real-time even though the computational burden carried by recursive calls to model predictions can be prohibitive [Bonney et al. 2022; Pregnolato et al. 2022]. With the extended availability of data and the difficulties of validating complex nonlinear phenomena modeling, last decades have seen the emergence of hybrid approaches, often referred to as *data-driven* techniques. They systematically involve:

- ▷ Surrogate modeling - model order reduction has been successfully developed for a variety of applications relying on high-fidelity modeling to reduce the CPU burden due to the call to model predictions. This is especially true for data-driven approaches based on projecting a high-fidelity model in low-dimensional subspaces: the so-called Reduced Order Model (ROM) can be obtained using classical techniques such as *Reduced Basis* (RB) [Rozza et al. 2008], *Proper Orthogonal Decomposition* (POD) [Eftekhar Azam and Mariani 2013; Benner et al. 2020], or *Proper Generalized Decomposition* (PGD) [Chinesta et al. 2011];
- ▷ the correction of model predictions (due to mismodeling or unanticipated phenomena) by a data-based enrichment step.

Without necessarily being exhaustive, let us present several classical data assimilation methods whose framework includes the previous statement, before specifically focusing on Kalman filtering (KF) techniques.

4.1.1 The data assimilation problem

The starting point of data assimilation problems is the definition of a dynamical system under space and time discrete form (4.1). This system is made of two equations: a state prediction equation and an observation equation.

$$\begin{cases} x_{k+1} &= \mathcal{M}(x_k, \theta, e_k) + w_{x,k} \\ y_k &= \mathcal{H}(x_k, e_k) + v_k \end{cases} \tag{4.1}$$

In terms of notations, $x_k \in \mathbb{R}^{N_x}$ is the nodal vector describing the state of the system at time point t_k, $y_k \in \mathbb{R}^{N_y}$ is the vector of observed data, and the two vectors $w_{x,k} \in \mathbb{R}^{N_x}$ and $v_k \in \mathbb{R}^{N_y}$ respectively represent model and measurement errors. They are assumed additive in most applications. The dynamical system (4.1) is based on two (possibly nonlinear) operators, namely the model operator $\mathcal{M}$ and the observation operator $\mathcal{H}$. The latter classically extracts local information regarding the predicted state x_k or inputs e_k. Eventually, model predictions also depend on a set of internal parameters $\theta \in \mathbb{R}^{N_\theta}$ (*e.g.* material properties).

> *Remark* 4.1. If one focuses on linear FE dynamics modeling of structures submitted to ground acceleration inputs, the dynamical equilibrium equation (1.12), written in terms of relative displacements, combined to the observation of displacement field derivatives via a (linear) observation matrix $\boldsymbol{\Pi}$ constitute a particular case of (4.1).
> The following matrix system is the so-called *state-space representation canonical form*:
>
> $$\begin{cases} \dot{x} &= \boldsymbol{A}x(t) + \boldsymbol{B}\ddot{U}_d(t) \\ y(t) &= \boldsymbol{C}x(t) + \boldsymbol{D}\ddot{U}_d(t) \end{cases} \text{with } x(t) = \begin{bmatrix} U(t) \\ \dot{U}(t) \end{bmatrix}, \tag{4.2}$$
> $$\boldsymbol{A} = \begin{bmatrix} 0 & \boldsymbol{I} \\ -\boldsymbol{M}^{-1}\boldsymbol{K} & -\boldsymbol{M}^{-1}\boldsymbol{D} \end{bmatrix}, \ \boldsymbol{B} = \begin{bmatrix} 0 \\ -\boldsymbol{\Xi} \end{bmatrix}, \ \boldsymbol{C} = \begin{bmatrix} \boldsymbol{\Pi} \\ 0 \end{bmatrix}, \ \boldsymbol{D} = 0$$
>
> Once discretized in time, this system is given by (4.1):
>
> $$\begin{cases} x_{k+1} = \exp\left(\boldsymbol{A}\Delta t\right) x_k + \boldsymbol{B}\Delta t\ddot{U}_d(t_k) \\ y_k = \boldsymbol{C}x_k + \boldsymbol{D}\ddot{U}_d(t_k) \end{cases} \tag{4.3}$$

> This problem is linear with respect to the state vector, but nonlinear with respect to the parameters θ (whose FE matrices implicitely depend).

4.1.2 Variational data assimilation techniques

Unlike sequential data assimilation (which emanates from estimation theory - see the next paragraph), variational assimilation is based on optimal control theory [Asch et al. 2016]. Variational data assimilation was historically introduced by the meteorological community to solve numerical weather prediction problems [Auroux 2007]. The analyzed state is not defined as the one that maximizes a certain pdf, but as the one that minimizes a cost-function. The minimization process requires numerical optimization techniques, such as gradient descent or BFGS algorithms. These techniques can rely on the gradient of the cost-function, that is obtained in most cases with adjoint state methods.

The most popular variational data assimilation techniques are the 3D-Var and 4D-Var. First, 3D-Var method aims to minimize the following cost-function

$$\mathcal{J}_{3D}(x) = \frac{1}{2}(x - x_0)^T \boldsymbol{P}_0^{-1}(x - x_0) + \frac{1}{2}(y - \mathcal{H}(x))^T \boldsymbol{R}^{-1}(y - \mathcal{H}(x)) \tag{4.4}$$

which measures both the gap between the state x and the prior guess x_0 and the data-to-model distance. $\boldsymbol{P}_0$ and $\boldsymbol{R}$ refer to the covariance error matrices on state prior misfit and measurement error, respectively. One can note that this is a typical regularized weighted least-square functional. Assuming that the observer operator is linear, *e.g.* a projection matrix $\boldsymbol{C}$ like in (4.2), the gradient and the Hessian matrix are explicit:

$$\begin{aligned} \nabla \mathcal{J}_{3D}(x) &= \boldsymbol{P}_0^{-1}(x - x_0) - \boldsymbol{C}^T \boldsymbol{R}^{-1}(y - \boldsymbol{C}x) \\ \nabla^2 \mathcal{J}_{3D}(x) &= \boldsymbol{P}_0^{-1} + \boldsymbol{C}^T \boldsymbol{R}^{-1} \boldsymbol{C}^T \end{aligned} \tag{4.5}$$

The incremental version of the 3D-Var consists in treating the difference between the state of the system and the prior guess as control quantity of interest (QoI), and not the state of the system itself. The main advantage of rewriting the problem in this form is the possible reduction of the control space dimension, and consequently the reduction of the covariance matrices dimension.

The 4D-Var is a generalization of the 3D-Var by adding the time dimension to the minimization problem because the dynamics of the system cannot systematically be neglected. In that case, the 4D-Var cost-function reads:

$$\mathcal{J}_{4D}(x) = \frac{1}{2}(x(0) - x_0)^T \boldsymbol{P}_0^{-1}(x(0) - x_0) + \frac{1}{2}\sum_{k=1}^{n}(y_k - \mathcal{H}(x_k))^T \boldsymbol{R}^{-1}(y_k - \mathcal{H}(x_k)) \tag{4.6}$$

In that case, adjoint state methods are mandatory to compute the gradient of $\mathcal{J}_{4D}(x)$. Similarly to the 3D-Var, an incremental version allows to reduce the dimension of the controlled vector.

Aside from 3D-Var and 4D-Var, a recent variational approach that exploits assimilated data for model enrichment is the *Parametrized Background Data Weak* formulation (PBDW) [Maday et al. 2015a; b]. It is a non-intrusive, reduced-basis, real-time data assimilation method that directly derives from a variational writting of a least-square identification problem. Before recent works [Haik et al. 2023], it has been dedicated to the state estimation of steady-state problems, with extensions regarding the nonlinear case and noisy data [Gong et al. 2019; Cohen et al. 2022]. Its originality lies in the fact it can be seen as a projection-by-data method, contrary to the KF that can be seen as a projection-by-model method. It processes the model *a priori* does not propose any correction directly on the latter, which is limiting parameter identification prospects. In that sense, it is similar to the sparse-PGD data assimilation technique, which aims at enriching a prior PGD basis from sparse data that is progressively assimilated [Ibáñez et al. 2018]. Besides, links have been clearly stated between the PBDW and the *Generalized Empirical Interpolation Method* [Maday and Mula 2013] that has particularly been studied for OSP purposes [Argaud et al. 2017; 2018]. The reader interested in PBDW is referred to the pedagogical review of [Mula 2022] for complementary details.

4.1.3 Sequential data assimilation

Optimal interpolation

One of the first original works regarding sequential data assimilation issues can be attributed to [Aitken 1935] who designed the *Best Linear Unbiased Estimator* (BLUE). Briefly, the principle of optimal interpolation is to look for an optimal combination between model predictions and observed data at the same time steps. The BLUE is the one that achieves minimum error estimate variance. Mathematically, if one starts from the state-space representation of (4.2), and if one denotes $\widehat{x}$ the estimated state obtained from a prior guess x_0, and x the true value of the estimate, then the BLUE must satisfy:

$$\begin{aligned} \widehat{x} &= \boldsymbol{L}x_0 + \boldsymbol{K}y \\ \mathbb{E}\left(\widehat{x}\right) &= x \\ \widehat{x} \text{ s.t. } \mathbb{E}\left((x-\widehat{x})(x-\widehat{x})^T\right) &\text{ is minimized} \end{aligned} \tag{4.7}$$

where $\boldsymbol{L}$ and $\boldsymbol{K}$ are matrices to determine. The unbiased feature directly leads to

$$\boldsymbol{L} = \boldsymbol{I} - \boldsymbol{K}\boldsymbol{C} \tag{4.8}$$

$\boldsymbol{K}$ is computed afterwards as the argument minimizing $\boldsymbol{tr}\left(\mathbb{E}\left((x-\widehat{x})(x-\widehat{x})^T\right)\right)$. With the notations defined in the previous paragraph, it can be shown that:

$$\boldsymbol{K} = \boldsymbol{P}_0\boldsymbol{C}^T\left[\boldsymbol{R} + \boldsymbol{C}\boldsymbol{P}_0\boldsymbol{C}^T\right]^{-1} = \left[\boldsymbol{P}_0^{-1} + \boldsymbol{C}^T\boldsymbol{R}^{-1}\boldsymbol{C}\right]^{-1}\boldsymbol{C}^T\boldsymbol{R}^{-1} \tag{4.9}$$

where $\left[\boldsymbol{P}_0^{-1} + \boldsymbol{C}^T\boldsymbol{R}^{-1}\boldsymbol{C}\right]$ is often referred to as the analysis covariance error matrix. The BLUE thus reads:

$$\widehat{x} = x_0 + \boldsymbol{P}_0\boldsymbol{C}^T\left[\boldsymbol{R} + \boldsymbol{C}\boldsymbol{P}_0\boldsymbol{C}^T\right]^{-1}\left(y - \boldsymbol{C}x_0\right) \tag{4.10}$$

> *Remark* 4.2. The BLUE is the concept that directly relates variational and sequential data assimilation techniques: the state that minimizes the 3D-Var cost-function is directly related to the optimal gain matrix given by the BLUE, and the linear Kalman filter can then be seen as successive calls to the BLUE (at each time step) combined with a linearized model operator.

Statistical estimation theory and Bayesian filtering

Since many physical systems have time-varying properties, and since measurements are regularly acquired, state estimations could be considerably improved by updating the current optimal estimate without having to repeat all model predictions and without having to assimilate all the measurements that have been acquired so far. An appropriate framework for this sequential updating is the Bayesian filtering framework, whose basic principle is to exploit the Bayesian inference framework in a sequential manner [Law et al. 2015]: at each time step measurements are acquired, the prior pdf for the data assimilation process is taken as the posterior pdf obtained at the previous step (see [Kapteyn et al. 2019] for a graphical representation).

However, the most difficult point is to build the likelihood function in order to compute the posterior pdf of the parameters to identify. In the general case without any assumption on the form of uncertainties on model and measurements, the likelihood function needs to be sampled with computationally expensive techniques such as Monte-Carlo. In order to reduce the uncertainty propagation cost, parallel computing techniques may be involved [Prudencio et al. 2013], but a more efficient approach consists in integrating a ROM, for instance using PGD [Rubio et al. 2018; 2021] or POD [Pereira Álvarez et al. 2021].

In the following, we will focus on the Kalman filter (KF) introduced in the 1960s [Kalman 1960; 1964], which can be seen as a Bayesian filter where basically prediction and observation operators are linear and all random variables are Gaussian (see Appendix D for mathematical explanations).

4.2 An extended review on Kalman Filtering

4.2.1 The linear Kalman filter, algorithm and computational origins

The Kalman filter (KF) is a linear optimal recursive state estimator designed for linear time-varying dynamical systems. The KF estimate of the system is statistically optimal with respect to a quadratic function of the estimate error (see [Kalman 1960; 1964; Maybeck 1979; Grewal and Andrews 2008] for a non-exhaustive list of references). At each time point t_k, the algorithm successively alternates between two steps (an illustration is given in Fig. 4.1):

(i) A prediction step, where the future state vector $\widehat{x}_{k+1}^-$ and its covariance error matrix $\boldsymbol{P}_{k+1}^-$ are predicted based on the current model.

(ii) A correction step, where predictions are corrected based on new assimilated measurements y_{k+1}, leading to the updated state vector $\widehat{x}_{k+1}$ and associated covariance error matrix $\boldsymbol{P}_{k+1}$.

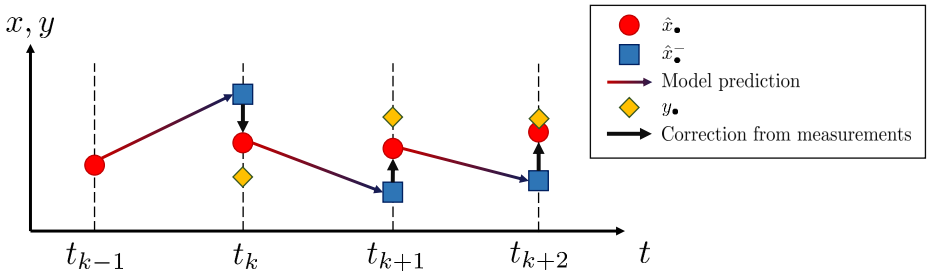

FIGURE 4.1: Illustration of the Kalman filter algorithm.

Fundamental assumptions must be made to recover the linear KF framework:

▷ Both model and observer operators are assumed linear, meaning that (4.1) becomes:

$$\begin{cases} x_{k+1} &= \boldsymbol{A}x_k + \boldsymbol{B}e_k + w_k \\ y_k &= \boldsymbol{C}x_k + v_k \end{cases} \tag{4.11}$$

Note that most of the time, the observer operator does not depend on the loading, which justifies the absence of e_k in the linearized observation equation.

▷ Observation and modeling errors are statistically independent from the state:

$$\mathbb{E}\left(x_k w_k^T\right) = 0 \text{ and } \mathbb{E}\left(x_k v_k^T\right) = 0 \; \forall \; k \geqslant 0 \tag{4.12}$$

▷ Observation and model errors are statistically independent from each other:

$$\mathbb{E}\left(w_k v_k^T\right) = 0 \; \forall \; k \geqslant 0 \tag{4.13}$$

▷ All pdfs are supposed to be Gaussian. The model and measurement noises are assumed to be zero-mean Gaussian random variables:

$$w_k \sim \mathcal{N}(0, \boldsymbol{Q}) \quad ; \quad v_k \sim \mathcal{N}(0, \boldsymbol{R}) \; \forall \; k \geqslant 0 \tag{4.14}$$

where $\boldsymbol{Q}$ and $\boldsymbol{R}$ respectively denote the process and measurement noise covariance matrices. For the sake of simplicity, they will be assumed constant in the following even if they may vary with time.

The remainder of this section intends to recall the fundamentals of KF from computational origins and the algorithm before a first pedagogical illustration so as to understand the influence of noise covariance matrices on the methodology.

Computational origins of the KF

$\widehat{x}_k^-$ is the *a priori* estimate at step k predicted by the model from the KF estimate at step $k-1$. $\widehat{x}_k$ is the *a posteriori* estimate at step k after correction by newly assimilated measurements y_k. As the model is not fully reliable and measurements are noisy, both estimates are not exactly equal to the exact state at step k, denoted x_k. This allows to define *a priori* and *a posteriori* error estimates:

$$\begin{aligned} \epsilon_k^- &= x_k - \widehat{x}_k^- \\ \epsilon_k &= x_k - \widehat{x}_k \end{aligned} \tag{4.15}$$

From these errors are built the *a priori* and *a posteriori* error covariance matrices:

$$\begin{aligned} \boldsymbol{P}_k^- &= \mathbb{E}\left(\epsilon_k^- \epsilon_k^{-T}\right) \\ \boldsymbol{P}_k &= \mathbb{E}\left(\epsilon_k \epsilon_k^T\right) \end{aligned} \tag{4.16}$$

Then, based on the Gauss-Markov theorem[1], the KF objective is to compute the *a posteriori* estimate as a combination of the *a priori* estimate and a weighted difference between the predicted state and measurements:

$$x_k = x_k^- + \boldsymbol{K}_k\left(y_k - \boldsymbol{C}x_k^-\right) \tag{4.17}$$

The so-called Kalman gain matrix $\boldsymbol{K}_k$ must finally be determined. According to the fact that the best estimator minimizes the *a posteriori* error covariance matrix, one gets that

$$\begin{aligned} \boldsymbol{K}_k &= \arg\min_{\boldsymbol{K}_k}\{\boldsymbol{tr}\left(\boldsymbol{P}_k\right)\} = \arg\min_{\boldsymbol{K}_k}\left\{\boldsymbol{tr}\left(\mathbb{E}\left(\epsilon_k \epsilon_k^T\right)\right)\right\} \\ &= \arg\min_{\boldsymbol{K}_k}\left\{\boldsymbol{tr}\left(\mathbb{E}\left(\left(x_k - \widehat{x}_k^- - \boldsymbol{K}_k\left(y_k - \boldsymbol{C}\widehat{x}_k^-\right)\right)\left(x_k - \widehat{x}_k^- - \boldsymbol{K}_k\left(y_k - \boldsymbol{C}\widehat{x}_k^-\right)\right)^T\right)\right)\right\} \\ &= \boldsymbol{P}_k^- \boldsymbol{C}^T\left(\boldsymbol{C}\boldsymbol{P}_k^- \boldsymbol{C}^T + \boldsymbol{R}\right)^{-1} \end{aligned} \tag{4.18}$$

The presence of the measurement noise covariance matrix $\boldsymbol{R}$ in the definition of $\boldsymbol{K}_k$ naturally allows to consider measurement uncertainty when correcting model-based predictions. However, the process noise covariance matrix $\boldsymbol{Q}$ only appears at the prediction stage and it is a quantity which is very difficult to estimate as it should be somehow representative of model bias.

> *Remark* 4.3. The comparison between (4.10) and (4.18) illustrates the proximity between optimal interpolation and KF. Actually, the KF can be seen as a succession of calls to the BLUE (at each time step) on a linearized model operator.

The linear KF algorithm

The prediction/correction algorithm of the linear KF (in the case model and observation operators remain constant with time) is detailed in Alg. 4.1.

4.2.2 Academic example: tracking of a ballistic shot

To illustrate the linear KF concept, a simple academic problem is considered, namely the estimation of the trajectory of a ballistic shot. The reference model used to simulate noisy data takes into account the viscous friction of the projectile in the air, whereas the model used for the data assimilation process is built without taking into account this phenomenon. Doing so, it is possible to illustrate the impact of the process noise on the quality of the state predictions.

We assume that the projectile is modeled by a point of mass m, initially launched at the speed $\dot{u}_0$ from the origin of a 2D Galilean reference frame. It is subjected to viscous friction of

[1] For a linear model in which the model and observation errors are uncorellated and have null expected values, the best linear unbiased estimator is the least squares estimator.

Algorithm 4.1: Linear Kalman Filter.

Data: Model and observation matrices: $\boldsymbol{A}, \boldsymbol{B}, \boldsymbol{C}$, loading conditions $e_{0:\infty}$, noise covariance matrices: $\boldsymbol{Q}, \boldsymbol{R}$, initial state vector $\widehat{x}_0$ and associated covariance matrix $\boldsymbol{P}_0$

Result: Successive predictions of the state vector and associated covariance matrix

Loop on data assimilation time steps

for $k = 1 : \infty$ **do**

1) **Prediction step**

$$\widehat{x}_k^- = \boldsymbol{A}x_{k-1} + \boldsymbol{B}e_{k-1} \; ;$$
$$\boldsymbol{P}_k^- = \boldsymbol{A}\boldsymbol{P}_{k-1}\boldsymbol{A}^T + \boldsymbol{Q} \; ;$$

2) **Data assimilation and correction step**

$$\boldsymbol{K}_k = \boldsymbol{P}_k^-\boldsymbol{C}\left(\boldsymbol{C}\boldsymbol{P}_k^-\boldsymbol{C}^T + \boldsymbol{R}\right)^{-1} \; ;$$
$$\widehat{x}_k = \widehat{x}_k^- + \boldsymbol{K}_k(y_k - \boldsymbol{C}\widehat{x}_k^-) \; ;$$
$$\boldsymbol{P}_k = (\boldsymbol{I} - \boldsymbol{K}_k\boldsymbol{C})\boldsymbol{P}_k^- \; ;$$

end

coefficient η and to gravity of acceleration g. Then, the trajectory of the projectile in the (e_x, e_y) plane is theoretically perfectly known:

$$u(t) = \left\{ \begin{array}{c} \dot{u}_0.e_x\tau\left(1 - e^{-t/\tau}\right) \\ \left(\dot{u}_0.e_y + \tau g\right)\tau\left(1 - e^{-t/\tau}\right) - \tau g t \end{array} \right\}_{(e_x,e_y)} \tag{4.19}$$

with $\tau = m/\eta$. The position $(X(t), Y(t))$ and velocity $(\dot{X}, \dot{Y})$ of the projectile are the state variables. The (linear) dynamical system (4.11) then reads:

$$\left\{ \begin{array}{rcl} x_{k+1} & = & \begin{bmatrix} X_{k+1} \\ Y_{k+1} \\ \dot{X}_{k+1} \\ \dot{Y}_{k+1} \end{bmatrix} = \begin{bmatrix} 1 & 0 & \Delta t & 0 \\ 0 & 1 & 0 & \Delta t \\ 0 & 0 & 1 & 0 \\ 0 & 0 & 0 & 1 \end{bmatrix} x_k + \begin{bmatrix} 0 \\ 0 \\ 0 \\ -\Delta t g \end{bmatrix} + w_k \\ y_k & = & \begin{bmatrix} 1 & 0 & 0 & 0 \\ 0 & 1 & 0 & 0 \end{bmatrix} x_k + v_k \end{array} \right. \tag{4.20}$$

with process and observation noises of covariance matrices $\boldsymbol{Q}$ and $\boldsymbol{R}$. Several KF estimates depending on the process noise covariance $\boldsymbol{Q}$ are displayed in Fig. 4.2. One can remark that, when considering small values of $\boldsymbol{Q}$ coefficients, the assimilation process fails to compensate the fact that model predictions are incomplete. However, the obtained state is smooth with time. On the contrary, for important process noise covariance coefficients, the KF tends towards the real (measured) state but with disturbed predictions due to the excessive confidence into measurements, that are incomplete (in the sense that velocity is not measured in this example). A crucial **compromise must then be made to carefully choose the process noise covariance matrix**. A user-defined $\boldsymbol{Q}$ is often not well justified in the literature although it is critical in the quality of the assimilation process. Eventually, it is worth noticing that **the measurement noise covariance matrix $\boldsymbol{R}$ can be quantified based on the knowledge of measurement noise features** (particularly from the standard deviation of the latter).

Necessity for nonlinear extensions of the Kalman filter

As most physical systems are nonlinear, the main limitation of the linear KF lies in the fact that linear models and observers are required, which is problematic in most applications. Several extensions of the KF to handle nonlinear models and observers have been proposed over the last decades. One can classically divide them in two families:

- Methods based on **model and observer linearizations** – probably the most intuitive, but not the most efficient way to handle nonlinearities. The *Extended Kalman Filter* (EKF) is

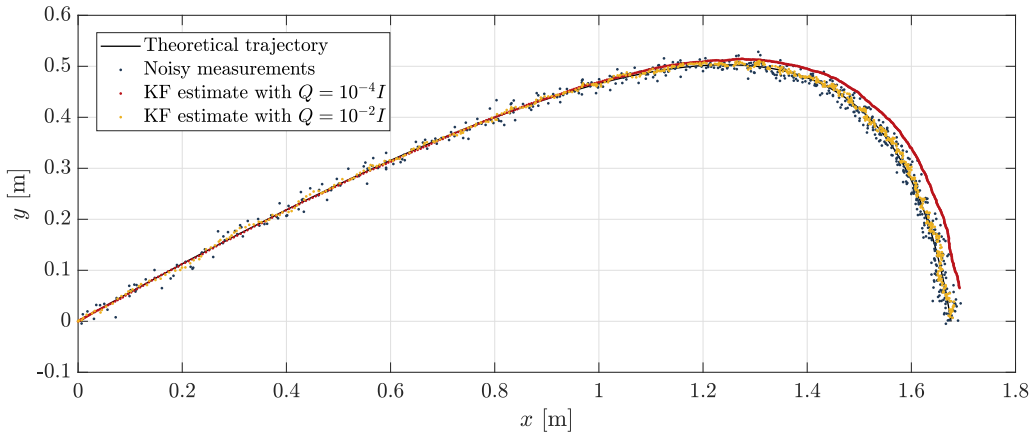

FIGURE 4.2: Ballistic shot – $m = 1$ kg, $\eta = 5$ kg.s^{-1}, $dt = 10^{-4}$ s, $v_0 = 10$ m.s^{-1} – Estimated trajectories from linear KF predictions. The choice of the process noise covariance $\boldsymbol{Q}$ is crucial in the quality of the predictions.

based on this principle and it is probably one of the most popular in the literature, both for state and parameter estimation [Hoshiya and Saito 1984; Welch and Bishop 2006; Terejanu 2008; X. Liu et al. 2009];

- ▷ Methods based on **statistical regularization** – these techniques are based on the fact that sampling points transformed by nonlinear operators enable to approximate state statistics correctly. Particular reference is made here to the *Particle Filter* (PF) [Orlande et al. 2011] or *Ensemble Kalman Filter* (EnKF) [Evensen 1994; 2003], where a set of sampling points generated by the Monte-Carlo algorithm are propagated through the nonlinear operators. On the contrary, the *Unscented Kalman Filter* (UKF) paradigm consists in carefully selecting a small-size set of sampling points (in a deterministic manner) that allows to compute state mean and covariance accurately [Mariani and Ghisi 2007; Terejanu 2011]. This deterministic sampling point generation is called the *Unscented Transform* – UT [S. Julier et al. 2000; S. Julier 2002; Van Der Merwe and Wan 2004; Kandepu et al. 2008]. An alternative to the UKF has been recently proposed with the *Scaled Spherical Simplex Filter* (S3F) [Papakonstantinou et al. 2022a], that almost divides by two the amount of sampling points to propagate for the exact same accuracy as UKF.

In the following, recall the concepts associated to the above-mentioned KF extensions for nonlinear systems ae briefly recalled, with illustrations on the plane frame example presented in Appendix A.1.

4.2.3 Extended Kalman filter (EKF)

A Taylor series expansion to recover the linear Kalman filter

As previously mentioned, the key idea of the *Extended Kalman Filter* (EKF) is to linearize both model and observer operators around the current mean and covariance in order to directly reuse the linear KF detailed in Alg. 4.1. The interested reader can find comprehensive reviews of EKF in many references [Sorenson 1970; Hoshiya and Saito 1984; Terejanu 2008] (to cite a few) and several programming softwares already include in-core EKF implementations[2].

Starting from the nonlinear dynamical representation (4.1), and ignoring model parameters for the moment, one can approximate state and measurements without taking into account the process and measurement noises. This introduces $\tilde{x}_k$ and $\tilde{y}_k$ defined such that

$$\begin{cases} \tilde{x}_{k+1} = \mathcal{M}(\widehat{x}_k, e_k) \\ \tilde{y}_k = \mathcal{H}(\tilde{x}_k, e_k) \end{cases} \tag{4.21}$$

[2]For instance, the MATLAB© EKF block in the Simulink control system toolbox.

From these approximations and from the nonlinear operators, one can rewrite a linearized set of governing equations, using Jacobian matrices and first-order Taylor series approximation:

$$\begin{cases} x_{k+1} \approx \tilde{x}_{k+1} + [\nabla_x \mathcal{M}(\widehat{x}_k, e_k)]\,(x_k - \widehat{x}_k) + w_k \\ y_k \approx \tilde{y}_k + [\nabla_x \mathcal{H}(\tilde{x}_k, e_k)]\,(x_k - \widehat{x}_k) + v_k \end{cases} \tag{4.22}$$

From the last equation, new prediction and measurement errors can be introduced:

$$\tilde{\epsilon}_{x,k} = x_k - \tilde{x}_k \tag{4.23}$$

$$\tilde{\epsilon}_{y,k} = y_k - \tilde{y}_k \tag{4.24}$$

As the actual state x_k is not available (because it is the quantity to estimate), the set of governing equations (4.22) can be rewritten as:

$$\begin{cases} \tilde{\epsilon}_{x,k+1} \approx \nabla_x \mathcal{M}(\widehat{x}_k, e_k)(x_k - \widehat{x}_k) + \varepsilon_k \\ \tilde{\epsilon}_{y,k} \approx \nabla_x \mathcal{H}(\tilde{x}_k, e_k)\tilde{\epsilon}_{x,k} + \eta_k \end{cases} \tag{4.25}$$

where ε_k and η_k are random variables such that $\varepsilon_k \sim \mathcal{N}(0, \boldsymbol{Q})$ and $\eta_k \sim \mathcal{N}(0, \boldsymbol{R})\ \forall\ k$.

Note that system (4.25) is presently linear, and in a close form to the linear KF discrete equations (4.11). This motivates us to introduce another error between the approximation $\tilde{x}_k$ and the final state prediction $\widehat{x}_k$:

$$\widehat{\epsilon}_k = \widehat{x}_k - \tilde{x}_k \tag{4.26}$$

Given all the previous assumptions and letting the prediction value of $\widehat{\epsilon}_k$ be 0, the Kalman filter correcting action from (4.25) to estimate $\widehat{\epsilon}_k$ is:

$$\widehat{\epsilon}_k = \boldsymbol{K}_k \tilde{\epsilon}_{y,k} \tag{4.27}$$

The substitution of (4.27) into (4.26) then leads to

$$\widehat{x}_k = \tilde{x}_k + \boldsymbol{K}_k \tilde{\epsilon}_{y,k} = \tilde{x}_k + \boldsymbol{K}_k (y_k - \tilde{y}_k) \tag{4.28}$$

where $\boldsymbol{K}_k$ is the Extended Kalman gain obtained from (4.25). The EKF algorithm is given below in Alg. 4.2 to emphasize on the similar algorithmic structure compared to linear KF, as the main consequence of the linearization process remains the substitution of $\widehat{x_k^-}$ by $\tilde{x}_k$.

> *Remark* 4.4. It has been fairly assumed that process and measurement noises are additive to model and observer operators. In a very general framework where one cannot dissociate these noises from model and observer operators, then
>
> $$\varepsilon_k \sim \mathcal{N}\left(0, \left[\nabla_w \mathcal{M}(\widehat{x}_k, e_k, w_k)\boldsymbol{Q}\nabla_w \mathcal{M}(\widehat{x}_k, e_k, w_k)^T\right]\right)$$
> $$\eta_k \sim \mathcal{N}\left(0, \left[\nabla_v \mathcal{H}(\widehat{x}_k, e_k, v_k)\boldsymbol{R}\nabla_v \mathcal{H}(\widehat{x}_k, e_k, v_k)^T\right]\right)$$

Limitations of the Extended Kalman filter algorithm

Although EKF is a common tool for sequential data assimilation, let us mention several well-identified limitations:

- ▷ The computation of the Jacobian matrices is necessary at each time step. It is a consuming operation from the computational viewpoint but recent advances tried to limit that nasty effect with the use of model reduction techniques such as reduced basis [X. Liu et al. 2009] or PGD [González et al. 2017].
- ▷ The Jacobian matrix $\nabla_x \mathcal{H}(\tilde{x}_k, e_k)$ propagates the relevant components of measured data, which makes the filter quite sensitive to measurement noise. In other words, important measurement noise can lead to divergent estimates because of the operators linearization.

▷ The EKF is most of the time effective enough but its results may be of poor quality compared to other nonlinear KF extensions in cases where nonlinearities are too strong to be correctly approximated with a first-order Taylor expansion. This limitation has been classicaly highlighted in former research works [Wan and Van Der Merwe 2000; Lefebvre et al. 2004; Mariani and Ghisi 2007; Hommels 2008; Eftekhar Azam 2014].

Algorithm 4.2: Extended Kalman Filter (for additive model and measurement errors).

Data: Nonlinear model and observation operators: $\mathcal{M}, \mathcal{H}$, loading conditions: $e_{0:\infty}$, error covariance matrices: $\boldsymbol{Q}, \boldsymbol{R}$, initial state vector $\widehat{x}_0$ and associated covariance matrix $\boldsymbol{P}_0$
Result: Successive predictions of the state vector mean and associated covariance matrix

Loop on data assimilation time steps

for $k = 1:\infty$ **do**

1) **Prediction step**

$$\tilde{x}_k = \mathcal{M}(\widehat{x}_{k-1}, e_{k-1}) ;$$
$$\boldsymbol{P}_k^- = \nabla_x \mathcal{M}(\widehat{x}_{k-1}, e_{k-1}) \boldsymbol{P}_{k-1} \nabla_x \mathcal{M}(\widehat{x}_{k-1}, e_{k-1})^T + \boldsymbol{Q} ;$$

2) **Data assimilation and correction step**

$$\boldsymbol{K}_k = \boldsymbol{P}_k^- \nabla_x \mathcal{H}(\tilde{x}_k, e_k) \left[\nabla_x \mathcal{H}(\tilde{x}_k, e_k) \boldsymbol{P}_k^- \nabla_x \mathcal{H}(\tilde{x}_k, e_k)^T + \boldsymbol{R}\right]^{-1} ;$$
$$\widehat{x}_k = \tilde{x}_k + \boldsymbol{K}_k (y_k - \mathcal{H}(\tilde{x}_k, e_k)) ;$$
$$\boldsymbol{P}_k = (\boldsymbol{I} - \boldsymbol{K}_k \nabla_x \mathcal{H}(\tilde{x}_k, e_k)) \boldsymbol{P}_k^- ;$$

end

4.2.4 Ensemble Kalman filter (EnKF)

Contrary to EKF, Sigma-Point Kalman Filters (SPKF) use the statistical linearization technique [Gelb 1974; Lefebvre et al. 2004]: a nonlinear function of a random variable is linearized through a linear regression between n sampling points drawn from the prior distribution of the random variable. This approach tends to be more accurate than Taylor series linearization, in particular when nonlinearities cannot be properly linearized, as illustrated in Fig. 4.3.

The EnKF originated as an alternative KF for large problems [Evensen 1994] (essentially, the covariance matrix is replaced by the sampled covariance), and it is now a major data assimilation technique for weather forecasting [Evensen 2003; Hommels 2008; Lakshmivarahan and Stensrud 2009; Mandel 2009] (to cite a few). EnKF is related to the PF but the EnKF makes the assumption that all involved probability distributions are Gaussian. The EnKF takes its name from the ensemble of n possible state vectors that are sampled at each iteration, which avoids representing the covariance matrix. Each ensemble member is then propagated through the nonlinear model. The weighting terms associated with the σ-points $\{w_k^i\}_{i=1,\dots,n}$ are often defined uniformly by default, *i.e.* $w_k^i = 1/n$ for all $i \in [\![1; n]\!]$. Key equations of EnKF are summarized in Alg. 4.3 for a linear observer[3].

With the generation of ensemble matrices, there is no need (and no interest) in computing covariance matrices, as the information carried by the propagation of the ensemble of samples is richer. Besides, the generation of random state vectors may lead to non-physical meaning states. Resampling techniques can be implemented to avoid such spurious effects.

The main limitation of EnKF is the need to propagate a large number of samples $n \gg N_x$ through the nonlinear function to ensure sufficient accuracy (see Fig. 4.3), which limits the prospects of using EnKF for on-the-fly data assimilation processes [Eftekhar Azam et al. 2012a].

[3] The nonlinearity tends to be more present in the model operator rather than in the observer operator. The latter is very often a projection matrix at sensor locations. In the literature, there has not been any EnKF application involving nonlinear observer so far, to the author's best knowledge.

Algorithm 4.3: Ensemble Kalman Filter.

Data: Nonlinear model $\mathcal{M}$, observation operator $\boldsymbol{C}$, loading conditions: $u_{0:\infty}$, error covariance matrices $\boldsymbol{Q}, \boldsymbol{R}$, initial state vector $\widehat{x}_0$ and associated covariance matrix $\boldsymbol{P}_0$
Result: Successive predictions of the ensemble state (whose statistics can be post-processed)
Generate the ensemble matrices from the prior statistics of x: $X_0 = \left[x_0^1 \dots x_0^n\right]$;

Loop on data assimilation time steps

for $k = 1 : \infty$ **do**

1) **Prediction step**

Propagation of the ensemble matrix:
$X_k^- = \left[\mathcal{M}(x_{k-1}^1, e_k) + w_{x,k}^1 \dots \mathcal{M}(x_{k-1}^n, e_k) + w_{x,k}^n\right]$
where $\{w_{x,k}^i\}$ are random realizations of model error following the covariance $\boldsymbol{Q}$;

Predicted observation ensemble: $Y_k = \left[\boldsymbol{C}([X_k^-]^1, e_k) + v_k^1 \dots \boldsymbol{C}([X_k^-]^n, e_k) + v_k^n\right]$
where $\{v_{k+1}^i\}$ are random realizations of measurement noise following the covariance $\boldsymbol{R}$;

2) **Data assimilation and correction step**
Kalman gain: $K_k = X_k^- Y_k^T [Y_k Y_k^T]^{-1}$;
Assimilate a new data point y_k and update the ensemble: $X_k = X_k^- + K_k(y_k - Y_k)$;
Option: compute mean and covariance of ensemble state by discrete sum.

end

Remark 4.5. The *Particle Filter* (PF) is a method close to EnKF, except that particles are generated by Sequential Monte Carlo sampling [Arulampalam et al. 2002; Kaipio and Sommersalo 2005; Orlande et al. 2011]. The idea is to represent the posterior pdf by a set of random samples (the so-called particles) with associated weights, and to compute the estimates based on these weighted samples. As the number of samples is often large, this Monte-Carlo characterization becomes an equivalent representation of the posterior pdf, and the solution tends to sequential Bayesian filtering. Similarly to EnKF, the computational burden associated to the propagation of particles may be prohibitive for real-time model updating purposes.

4.2.5 Unscented Kalman filter (UKF)

The Unscented Transform in a nutshell

To overcome the EnKF curse of dimensionality, [S. Julier et al. 2000] developed an automated deterministic sampling selection algorithm to approximate the statistics of a random variable which undergoes a nonlinear mapping: the so-called *Unscented Transform* (UT). The UT guarantees a second-order accuracy (mean and covariance) with a minimal $(2N_x + 1)$ amount of well-chosen σ-points (see Fig. 4.3).

To illustrate the UT, let us consider the stochastic equation $y = h(x)$, with $h(\bullet)$ a nonlinear function and $x \in \mathbb{R}^{N_x}$. To compute the mean and covariance $(\widehat{y}, \boldsymbol{P}_y)$ of y from the mean and covariance of x $(\widehat{x}, \boldsymbol{P}_x)$, the matrix of the $2N_x + 1$ σ-points (denoted $\mathcal{X}$) is built according to the set of equations given in the left column of Tab. 4.1. The triplet (α, β, κ) controls the statistical behavior of the UT process as it conditions the weighting of each σ-point and their distance to $\widehat{x}$. It has been shown that $\beta = 2$ is optimal for Gaussian distributions. κ is a secondary parameter, often set to zero in the literature and $\alpha \in [0; 1]$ has a direct influence on the spread of the σ-points. The performance of the algorithm is directly related to their choice (even though the calibration of noise covariance parameters is more critical). Once computed, the σ-points are propagated through the nonlinear function h and the statistical linearization technique yields:

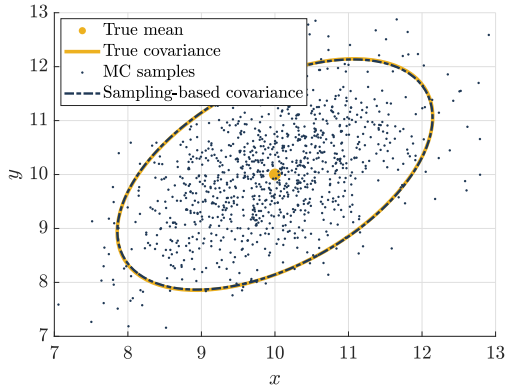

(a) Prior pdf and MC sampling for EnKF.

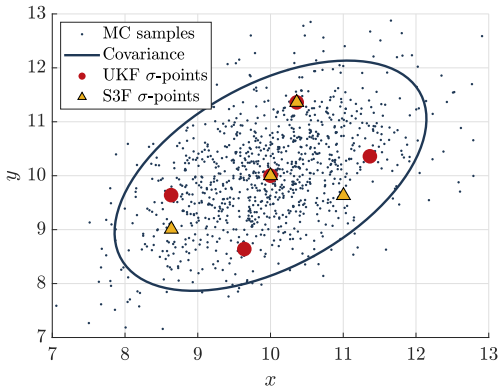

(b) Computation of σ-points for UT.

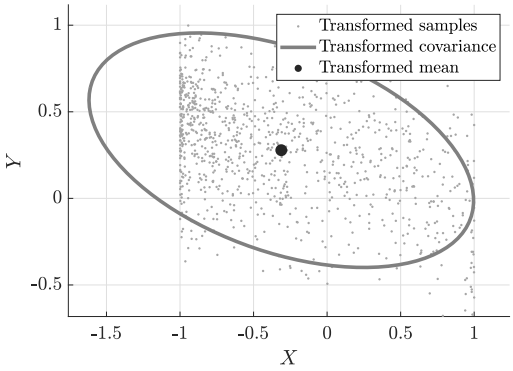

(c) Transformed MC samples and EnKF estimate mean and covariance estimate (reference).

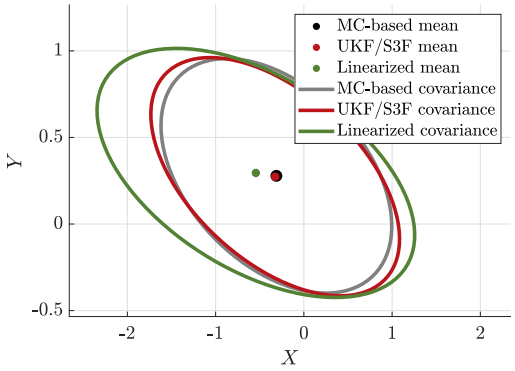

(d) Comparison of estimated mean and covariance between EnKF (reference), UT and linearization.

FIGURE 4.3: Illustrative 2D comparison of EnKF, EKF, UKF and S3F for predicting mean and covariance after a nonlinear transformation $(X, Y) = f(x, y) = \left[\sin|x|; \cos y^{0.7}\right]$.

$$\widehat{y} = \sum_{i=0}^{2N_x} \mathcal{W}_i^m h(\mathcal{X}_i) \tag{4.29}$$

$$\boldsymbol{P}_y = \sum_{i=0}^{2N_x} \mathcal{W}_i^c \left(h(\mathcal{X}_i) - \widehat{y}\right)\left(h(\mathcal{X}_i) - \widehat{y}\right)^T \tag{4.30}$$

Remark 4.6. Sometimes, the space in which lies the state may be strongly constrained (*e.g.*, bounded coordinates for physical reasons, or positive material properties). To avoid the propagation of physical-meaningless samples, [Kandepu et al. 2008] proposed a projection technique allowing to take such constraints into account.

The UKF algorithm

The UKF is a straighforward extension of the UT to the recursive KF estimation framework where the state random variables are redefined as the concatenation of the original state and noise variables:

$$x_k^a = [x_k^T \; w_k^T \; v_k^T]^T \tag{4.31}$$

The UT is then applied to this augmented state to calculate the corresponding σ-points, denoted $\mathcal{X}_k^a$. Then, the classical KF equations are applied (see Alg. 4.4).

Some technical points about the UKF algorithm should be mentioned:

- ▷ Contrary to EKF, no explicit Jacobian computation is required and, contrary to EnKF, only a restrained number of calls to the nonlinear function is required.
- ▷ For high-dimensional state vector, the computation and propagation of the σ-points can be time consuming. Parallelizing their propagation can limit this issue, as illustrated in [Eftekhar Azam et al. 2012b].
- ▷ The performance comparison of EKF, EnKF and UKF has been extensively studied in the literature [Wan and Van Der Merwe 2000; Bolzon et al. 2002; Lefebvre et al. 2004; Mariani and Ghisi 2007; Eftekhar Azam et al. 2012a; Astroza et al. 2019b] (to cite a few), always showing that UKF and EnKF are more accurate but less intuitive to implement than EKF.
- ▷ A similar version of UKF has also been proposed without requiring an augmented state vector in [Wan and Van Der Merwe 2000] for the case of additive noise (which is the case in many applications). The covariance of process and measurement noise are then incorporated using a simple additive procedure when computing $\boldsymbol{P}_k^-$ and $\boldsymbol{P}_{yy}$.

Algorithm 4.4: Unscented Kalman Filter.

Data: Nonlinear model and observation operators: $\mathcal{M}, \mathcal{H}$, loading conditions: $e_{0:\infty}$, noise process and measurements covariance matrices: $\boldsymbol{Q}, \boldsymbol{R}$, UT parameters: $\alpha, \beta, \kappa = 0$, initial state vector $\widehat{x}_0$ and associated covariance matrix $\boldsymbol{P}_0$.
Result: Successive predictions of the state vector and associated covariance matrix
Initialization: Augmented state and covariance computation:
$\widehat{x}_0^a = [\widehat{x}_0^T \; 0 \; 0]^T$; $\boldsymbol{P}_0^a = \text{diag}(\boldsymbol{P}_0, \boldsymbol{Q}, \boldsymbol{R})$;

Loop on data assimilation time steps

for $k = 0 : \infty$ **do**

1) **Compute σ-points and associated weights**

$\mathcal{X}_{k,0} = \widehat{x}_{k-1}$;
$\mathcal{X}_{k,i} = \widehat{x}_{k-1} + \alpha\sqrt{N_x}\left[\sqrt{\boldsymbol{P}_{k-1}}\right]_i, \quad \forall i \in [\![1; N_x]\!]$;
$\mathcal{X}_{k,i} = \widehat{x}_{k-1} - \alpha\sqrt{N_x}\left[\sqrt{\boldsymbol{P}_{k-1}}\right]_i, \quad \forall i \in [\![N_x+1; 2N_x]\!]$;
$\mathcal{W}_0^m = 1 - \frac{1}{\alpha^2}$; $\mathcal{W}_0^c = W_0^m + 1 - \alpha^2 + \beta$;
$\mathcal{W}_i^m = \mathcal{W}_i^c = \frac{1}{2\alpha^2 N_x} \; \forall \, i \in [\![1; 2N_x]\!]$;

2) **Prediction step**

State prediction:
$\widehat{\mathcal{X}}_k^- = \mathcal{M}(\mathcal{X}_k^x, e_k, \mathcal{X}_k^w)$;
$\widehat{x}_k^- = \sum_{i=0}^{2N_x} \mathcal{W}_i^m \mathcal{X}_{k,i}^x$;
$\boldsymbol{P}_k^- = \sum_{i=0}^{2N_x} \mathcal{W}_i^c (\widehat{\mathcal{X}}_{k,i}^- - \widehat{x}_k^-)(\widehat{\mathcal{X}}_{k,i}^- - \widehat{x}_k^-)^T$;

Observation prediction:
$\mathcal{Y}_k = \mathcal{H}(\mathcal{X}_k^x, e_k, \mathcal{X}_k^v)$;
$\widehat{y}_k^- = \sum_{i=0}^{2N_x} \mathcal{W}_i^m \mathcal{Y}_{k,i}$;
$\boldsymbol{P}_{yy} = \sum_{i=0}^{2N_x} \mathcal{W}_i^c \left(\mathcal{Y}_{k,i} - \widehat{y}_k^-\right)\left(\mathcal{Y}_{k,i} - \widehat{y}_k^-\right)^T$;

Cross-covariance matrix:
$\boldsymbol{P}_{xy}^- = \sum_{i=0}^{2N_x} \mathcal{W}_i^c (\widehat{\mathcal{X}}_{k,i}^- - \widehat{x}_k^-)(\mathcal{Y}_{k,i} - \widehat{y}_k^-)^T$;

3) **Data assimilation and correction step**

Kalman gain matrix: $\boldsymbol{K}_k = \boldsymbol{P}_{xy}^- \boldsymbol{P}_{yy}^{-1}$;
State and covariance update:
$\widehat{x}_k = \widehat{x}_k^- + \boldsymbol{K}_k(y_k - \widehat{y}_k^-)$;
$\boldsymbol{P}_k = \boldsymbol{P}_k^- - \boldsymbol{K}_k \boldsymbol{P}_{yy} \boldsymbol{K}_k^T$;

end

4.2.6 Scaled Spherical Simplex Filter (S3F)

Very recently, another SPKF algorithm, called *Scaled Spherical Simplex Filter* (S3F), has been developed in [Amir et al. 2022; Papakonstantinou et al. 2022a; Papakonstantinou et al. 2022b]. S3F can be used in all applications where UKF can be involved, achieving the exact same numerical performance in terms of accuracy, with about 50% CPU time savings. By sampling $N_x + 2$ σ-points instead of $2N_x + 1$, S3F preserves all the important features of UKF with the minimal amount of sampling points to propagate (see Fig. 4.3 for a 2D and Fig. 4.4 for a 3D conceptualization). Fundamentally, the S3F and UKF algorithms do only differ in the way σ-points (and associated weights) are declared. The overall structure from Alg. 4.4 remains the same, except from the definition of σ-points that is recalled in the right column of Tab. 4.1 taken from [Papakonstantinou et al. 2022a].

UT (of parameters $\alpha, \beta, \kappa = 0$)	S3F
Sigma-points definition	
$\forall\, i \in [\![0; 2N_x]\!], \mathcal{X}_i = \widehat{x} + \left[\sqrt{\boldsymbol{P}_x} C\right]_i,\ C \in \mathbb{R}^{N_x \times (2N_x+1)}$ with $C = \begin{bmatrix} 0 & q & & & -q & & \\ 0 & & q & & & -q & \\ \vdots & & & \ddots & & & \ddots \\ 0 & & & & q & & -q \end{bmatrix}$ with $q = \alpha\sqrt{N_x}$	$\forall\, i \in [\![0; N_x+1]\!], \mathcal{X}_i = \widehat{x} + \left[\sqrt{\boldsymbol{P}_x} C\right]_i,\ C \in \mathbb{R}^{N_x \times (N_x+2)}$ with $C = \begin{bmatrix} 0 & -q_1 & q_1 & 0 & \dots & 0 \\ 0 & -q_2/2 & -q_2/2 & q_2 & \dots & 0 \\ \vdots & \vdots & \vdots & \vdots & \ddots & \vdots \\ 0 & -q_n/N_x & -q_n/N_x & -q_n/N_x & \dots & q_n \end{bmatrix}$ and $q_i = i/\sqrt{i(i+1)\mathcal{W}_i^m}\ \forall\, i \in [\![1; N_x+1]\!]$
Sigma-points weights	
$\mathcal{W}_0^m = 1 - \frac{1}{\alpha^2}$; $\mathcal{W}_0^c = W_0^m + 1 - \alpha^2 + \beta$ $\mathcal{W}_i^m = \mathcal{W}_i^c = \frac{1}{2\alpha^2 N_x}\ \forall\, i \in [\![1; 2N_x]\!]$	$\mathcal{W}_0^m = 1 - \frac{1}{\alpha^2}$; $\mathcal{W}_0^c = W_0^m + 1 - \alpha^2 + \beta$ $\mathcal{W}_i^m = \mathcal{W}_i^c = \frac{1}{\alpha^2(N_x+1)}\ \forall\, i \in [\![1; N_x+1]\!]$

TABLE 4.1: Sigma-points sampling for UKF and S3F from a N_x-dimensional estimate $(\widehat{x}, \boldsymbol{P}_x)$.

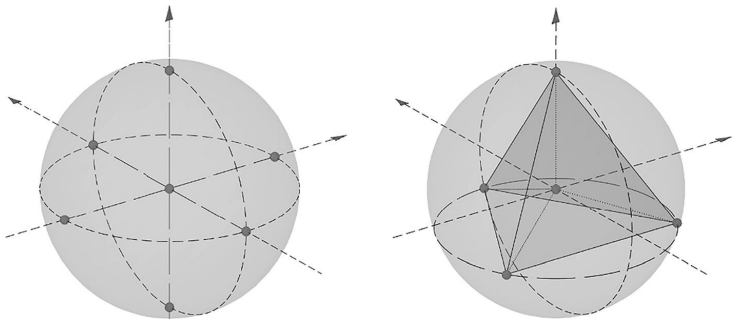

FIGURE 4.4: σ-points locations around the current mean state estimate for UKF (equally spread over a hypersphere - left) and S3F (corners of a simplex - right). Figure from [Papakonstantinou et al. 2022a].

4.2.7 Joint and Dual nonlinear KFs for parameter estimation

The above-mentioned extensions of the linear KF permit to update physical state vectors in sequential data assimilation processes involving nonlinear dynamical systems. However, in many applications, internal model parameters θ are uncertain QoI that need to be tracked. More specifically, in the last decades, research work was dedicated to damage detection and parameter identification based on KF algorithms.

[Hoshiya and Saito 1984] was the first (to the author's best knowledge) that used EKF for structural dynamics model identification. Let us also cite [Corigliano and Mariani 2001] that identified composite interface models using EKF, and [Bolzon et al. 2002] that updated a cohesive crack model with EKF. More recently, the EKF was coupled with model order reduction techniques such as POD to identify damage in civil engineering structures [Eftekhar Azam 2014; Eftekhar Azam and Mariani 2018] or PGD for real-time applications [González et al. 2017].

UKF was also largely used for similar applications, see [Wan and Van Der Merwe 2000; Gove and Hollinger 2006] for pedagogical tutorials about the use of UKF for nonlinear state and parameter identification. [Mariani and Corigliano 2005; Eftekhar Azam et al. 2012a; Eftekhar Azam et al. 2012b] compared UKF and EKF for characterizing composite delamination. A dedicated comparison between EKF and UKF in nonlinear structural dynamics was proposed in [Mariani and Ghisi 2007], and real-time data assimilation prospects were investigated in [Wu and Smyth 2007]. Several modifications of UKF, especially to save CPU time, were also discussed in [Moireau and Chapelle 2011; Onat 2019]. More recent works intend to apply EKF and UKF to update classical nonlinear reinforced concrete models based on earthquake engineering experiments [Astroza et al. 2019a; b; Song et al. 2020; Cheng and T. C. Becker 2021].

Finally, let us mention apart the works of [Alarcon et al. 2011a; Alarcon et al. 2011b; Marchand et al. 2016; 2019] who successfully coupled UKF and mCRE for model updating purposes (these contributions will be discussed in more detail at the beginning of Section 4.3).

Formulation of an evolution law on model parameters

Parameters must be explicitely integrated to the dynamical system (4.1) if one wants them to be identified in a KF framework. Let us consider that the model operator relies on a set of unknown structural parameters $\theta_k \in \mathbb{R}^{N_\theta}$. Without any *a priori* knowledge, one can formulate a simple stationary evolution law:

$$\frac{\partial \theta}{\partial t} = 0 \tag{4.32}$$

Of course, all parameters are not constant with time (damage is a relevant example). The stationarity assumption is thus relaxed with the addition of a zero-mean Gaussian white-noise w_θ so as to model uncertainty on parameters and enable their evolution during the data assimilation process. Therefore, the full dynamical system (4.1) now reads

$$\begin{cases} \theta_{k+1} &= \theta_k + w_{\theta,k} \\ x_{k+1} &= \mathcal{M}(x_k, \theta_k, e_k) + w_{x,k} \\ y_k &= \mathcal{H}(x_k, \theta_k, e_k) + v_k \end{cases} \tag{4.33}$$

In the above-mentioned works, two formulations are used to apply nonlinear KF to the system (4.33): the so-called *Dual* and *Joint* nonlinear KFs, that are equally applicable to any nonlinear KF (EKF, UKF, S3F, ...). Their principles are schematically presented in Fig. 4.5.

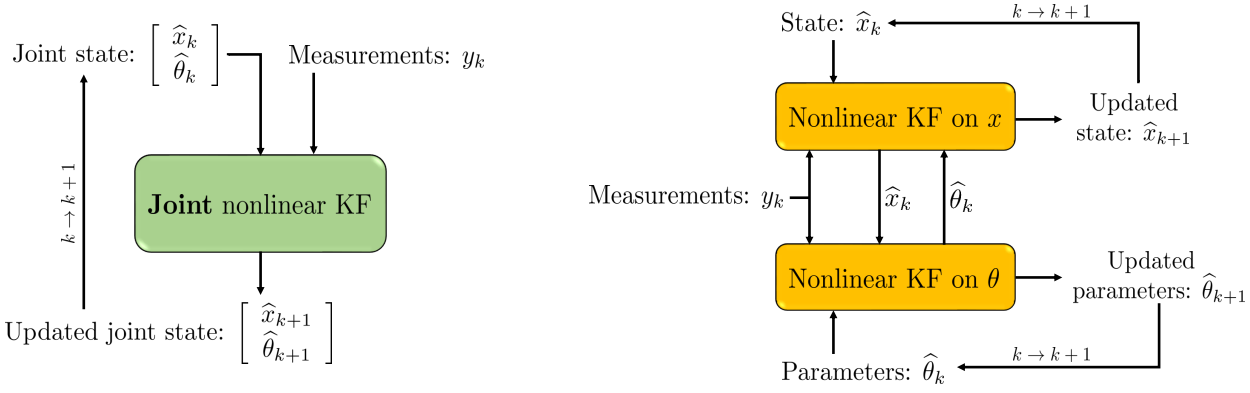

FIGURE 4.5: Joint and dual Kalman filters schemes.

Remark 4.7. The stationarity assumption is not critical for the identification of time-evolutive parameters. First, the covariance of parameters that defines the pdf of $w_{\theta,k}$ allows them to vary between consecutive steps. Besides, if data assimilation time steps are small enough

compared to the characteristic time that is required to assess a significant parameter evolution, then the stationarity assumption is worthwhile. For strongly discontinuous dynamical problems, a dedicated formulation has been recently proposed in [Chatzis et al. 2017].

Joint Kalman filter

The joint Kalman filter consists in a simple concatenation of state and parameters into a joint state vector $x_k^\star = [x_k^T \ \theta_k^T]^T$ (see Fig. 4.5). The associated dynamical state/observation system reads:

$$\begin{cases} x_{k+1}^\star &= \begin{bmatrix} \mathcal{M}(x_k, \theta_k, e_k) + w_{x,k}) \\ \theta_k + w_{\theta,k} \end{bmatrix} \\ y_k &= \mathcal{H}(x_k^\star, e_k) + v_k \end{cases} \tag{4.34}$$

Dual Kalman filter

The dual Kalman filter principle is to keep the parameters as state vector alone. This implies to turn the observer (often a linear projector when considering classical KF) into a state evaluation operator $\mathcal{H}_{dual}$:

$$\begin{cases} \theta_{k+1} &= \theta_k + w_{\theta,k} \\ y_k &= \mathcal{H}_{dual}(x_k, \theta_k, e_k, w_{x,k}, v_k) \end{cases} \tag{4.35}$$

This new observer is itself based on a second Kalman filter (which is at the origin of the "dual" denomination):

$$\begin{cases} x_{k+1} &= \mathcal{M}(x_k, e_k, \theta_k) + w_{x,k} \\ y_k &= \mathcal{H}(x_k, \theta_k, e_k) + v_k \end{cases} \tag{4.36}$$

Comparison of both approaches

Even though they do not seem that much different, from the computational viewpoint, DKF appears to be more complicated and time demanding than JKF. Both methods have been implemented in former studies, even compared in structural dynamics by [Mariani and Ghisi 2007]. Even if DKF may provide slightly better estimates, the combined use of two KFs also introduces more user-defined parameters (especially process and observation noise) that are difficult to calibrate. Besides, the risk of divergence in case of corrupted measurements is higher.

Remark 4.8. Beyond JKF and DKF, the estimation of state and parameters can also be separated with other schemes, for example via marginalization - see the Rao-Blackwellisation of PF [Olivier and Smyth 2017]. This approach enables to marginalize out all the states/parameters which do not contribute to any high nonlinearity in the system equations. Hierarchical separations are also applicable, as proposed in [Tatsis et al. 2022].

Remark 4.9. Although it is not our main concern, *Augmented Kalman Filters* (AKF) enable to estimate both state and input forces. The principle is close to the joint KF: unknown input forces are included in the state vector and estimated alongside during the data assimilation process. AKF have been studied as a stochastic force identification technique in structural dynamics applications [Lourens et al. 2012; Naets et al. 2015b], with extensions to state-input-parameter identification [Naets et al. 2015a; Capalbo et al. 2023]. Eventually, it has also been used for OSP in [Ercan et al. 2023; Taher et al. 2023].

4.2.8 Application of nonlinear KFs to structural dynamics

In this section, the aim is to compare the performance of UKF and EKF for parameter estimation from sparse measurements in a typical earthquake engineering academic problem. Let us consider the plane frame example already exploited in the previous chapters, that is fully detailed in Appendix A.1.
The frame is clamped to a rigid moving support (shaking table) and submitted to a 30 s random low-PGA ($0.1g$) ground motion input. The stiffness properties are assumed uncertain. The reference stiffness reference field $\theta^\star$ presents a defect in wall W10 whereas the initial guess is uniformly underestimating the healthy properties of the structure by 10% (see Tab. 1.2). The vector θ is then made of 6 parameters, one associated to each of the subdomain depicted in Fig. 4.6.

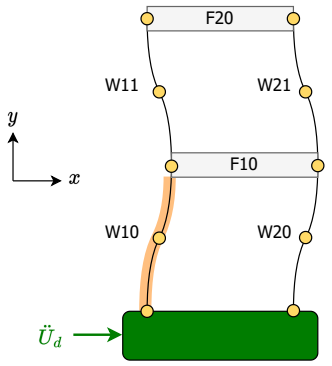

FIGURE 4.6: Frame submitted to ground motion, with subdomains and sensor locations.

The numerical objective is to recover $\theta^\star$ using nonlinear KFs and simulated acceleration measurements with noise of known level coming from discrete sensors scattered over the structure (yellow dots in Fig. 4.6). Simulations are performed using a Newmark time integration scheme. Note that to ensure that a residual model bias remains, the updated FE model is based on a coarser mesh (4 times less elements) than the model used for simulating data. JEKF and JUKF have been successfully implemented from scratch in MATLAB© so as to identify key difficulties and limitations of the algorithms. All drawn remarks are listed below with related figures.

- The process and measurement covariance matrices must be well calibrated in order to obtain relevant results. On the one hand, the measurement noise covariance can be estimated quite accurately assuming that all measurements are statistically independent and disturbed by a noise modelled as a zero-mean Gaussian random variable of covariance δ:

$$\boldsymbol{R} = \delta \boldsymbol{I} \tag{4.37}$$

  On the other hand, providing an "optimal" value of the process covariance is not an easy task. Considering that covariance of state and parameters must be defined in accordance to their order of magnitude, Q is defined as a block diagonal matrix:

$$\boldsymbol{Q} = \begin{bmatrix} q_X \boldsymbol{I} & 0 \\ 0 & q_\theta \boldsymbol{I} \end{bmatrix} \tag{4.38}$$

  where $q_X \in [10^{-8}; 10^{-6}]$ and $q_\theta \in [10^{-4}; 10^{-2}]$ are convenient values for this problem.
- Both **JEKF and JUKF are able to quickly and accurately update both state and parameters** when considering non-noisy measurements (see Fig. 4.7-4.8), as both the gap between state predictions and measurements (*i.e.*, $\|y_k - \boldsymbol{C}\widehat{x}_k\|_{L^2}$) and the gap between estimated parameters and their expected values (*i.e.*, $\|\widehat{\theta}_k - \theta^\star\|_{L^2}$) converge towards 0.
- As one could have expected, **EKF and UKF performances are altered by measurement noise**, even if $\boldsymbol{R}$ is calibrated in accordance. As observed in Fig. 4.9-4.10, the presence of low-level noise makes the algorithm converge slowly to the expected parameter values. As one could have guessed, once the noise level becomes too important compared to the magnitude of the measurements, KF algorithms may diverge. Note that **the calibration of the covariance matrix $\boldsymbol{Q}$ is a painful task for non-expert users**, and may necessitate several trials before obtaining a relevant result.
- In the JUKF, most of the CPU time is spent for propagating information through the nonlinear model which needs to call many times the Newmark time integration scheme. In the JEKF, the computation of the gradient of the model operator also requires recurrent calls to the model operator if Jacobian matrices are obtained using a finite difference method.

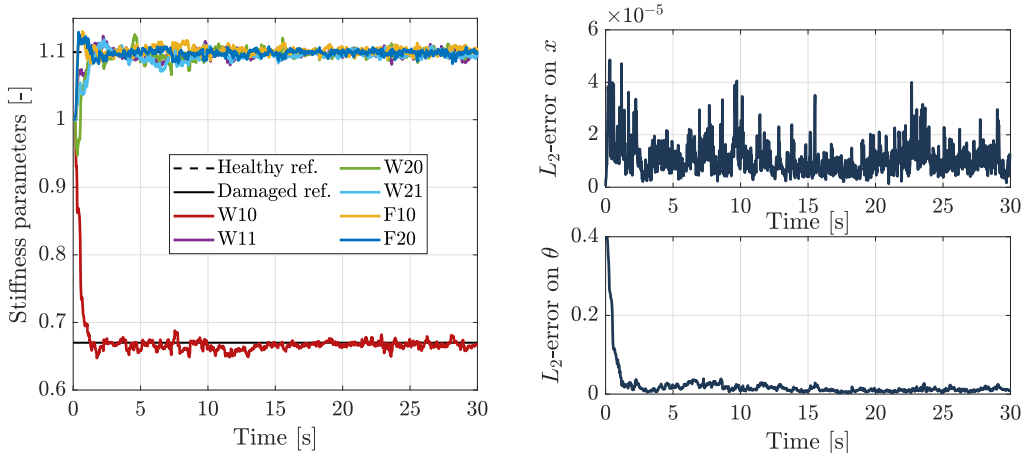

FIGURE 4.7: Sequential data assimilation results for the truss problem using JEKF. Parameter means are getting closer to expected values while state gets well predicted with time. Credible intervals have not been plotted for the sake of clarity.

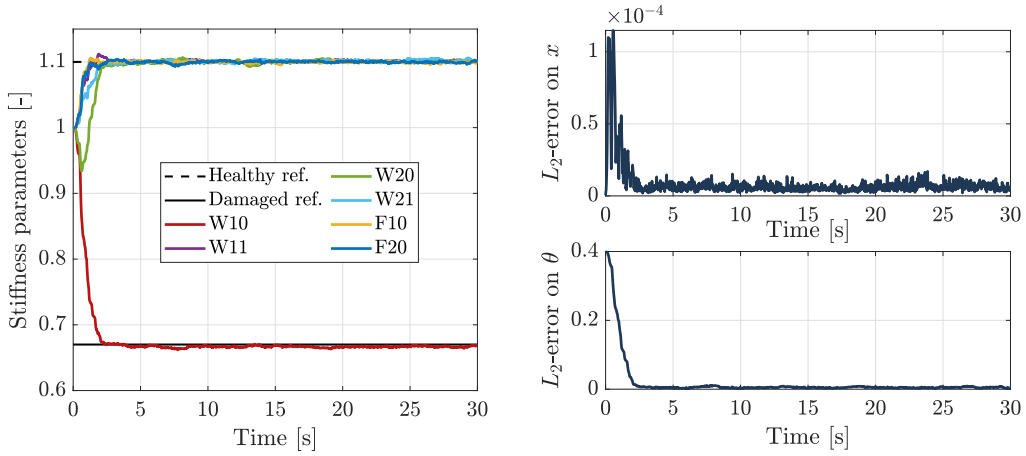

FIGURE 4.8: Sequential data assimilation results for the frame problem using JUKF. Parameter means are getting closer to expected values and state gets well predicted with time. Credible intervals have not been plotted for the sake of clarity.

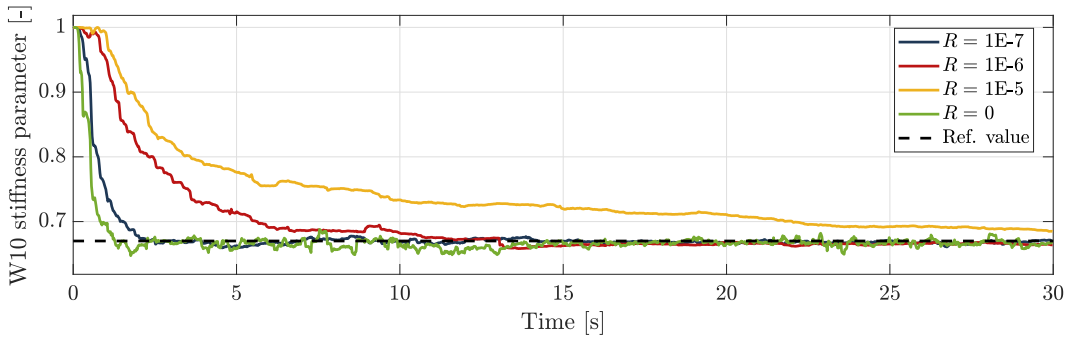

FIGURE 4.9: Noise influence on JEKF parameter predictions. The W10 parameter (damaged area) is harder to recover when noise level increases.

4.2.9 Conclusions on the use of nonlinear KF for model updating

This brief bibliography review emphasized that nonlinear KFs are relevant tools to update on-the-fly FE models of dynamical (and evolutive) systems. They allow to track and identify accurately structural parameters from sparse and noisy measurements, as illustrated for EKF and UKF in the previous example. This last example was the opportunity to implement classical KF from scratch and to understand their inherent limitations. In particular, the calibration of the co-

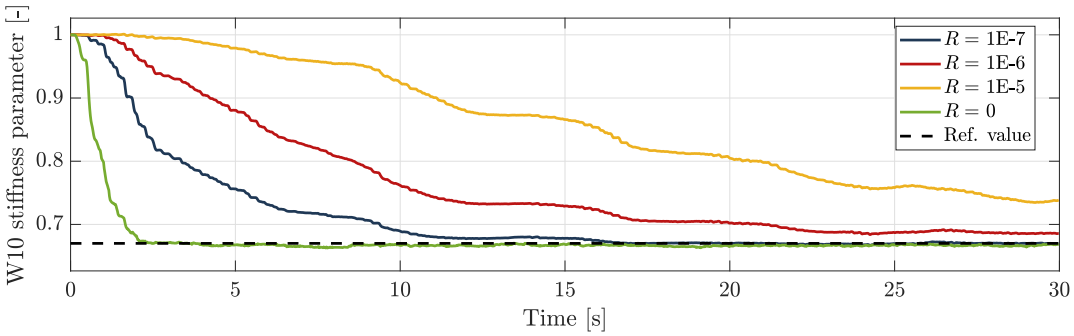

FIGURE 4.10: Noise influence on JUKF parameter predictions. The W10 parameter (damaged area) is harder to recover when noise level increases.

variance error matrices still remains a difficult task as the miscalibration of matrices $\boldsymbol{Q}_x, \boldsymbol{Q}_\theta, \boldsymbol{R}$ may lead to irrelevant results, although recent works have presented adaptive techniques for automating their choice [W. Li et al. 2016; Astroza et al. 2019a; Song et al. 2020]. Besides, the computational effort associated with state predictions makes the real-time constraint not affordable if no reduced order modeling technique is involved. Finally, typical increase of convergence time towards expected values has been observed when increasing measurement noise; this means the lack of robustness of KFs with respect to measurement noise can limit their performance.

These aspects motivate the integration of the mCRE within a KF framework, so as to benefit from the capabilities of the mCRE to perform robust and reliable parameter identification from highly noisy data within a sequential data assimilation framework. Inspired from the previous works of [Alarcon et al. 2011a] and [Marchand et al. 2016], a novel data assimilation concept called the *Modified Dual Kalman Filter* (MDKF) is proposed in the following.

4.3 mCRE-based KF for robust data assimilation

In this section is introduced a new Kalman filter-based data assimilation strategy that extends the offline mCRE-based model updating algorithm presented in Chapters 1 and 2. The mCRE is integrated within a nonlinear dual Kalman Filter for stiffness parameter tracking, leading to the so-called *Modified Dual Kalman Filter* algorithm (MDKF).

Note that this coupling has already been the subject of extensive research work by [Marchand et al. 2016] who developed a Modified Kalman filter approach dedicated to quasi-statics model updating where the mCRE written in the time domain was integrated to an UKF and combined with PGD. However, this formulation is not well suited in our context, the frequency domain formulation of the mCRE being more adequate and practical in the context of low-frequency dynamics. To our best knowledge, there is no previously published work presenting a data assimilation strategy coupling mCRE written in the frequency domain and KF, except for the proof of concept addressed by [Alarcon et al. 2011a] in which a FE model of the SMART2013 specimen was used, but in an artificial manner: large-size defaults were introduced in the model to simulate measurements, and localized afterwards using the CRE map.

4.3.1 MDKF formulation: change of observation metrics

Although the common definition of a projection matrix as observer seems rather intuitive since sensors directly collect measurements to be compared to model predictions, the choice of the observation metrics (and thus the way measurements are processed) can be reconsidered for enhanced robustness with respect to measurement noise. In that sense, the developments initiated in [Marchand et al. 2016] differ from the classical nonlinear KF framework for parameter estimation as the metric space of the observer is no longer the typical L^2-norm guaranteeing the convergence of state estimates towards measurements.

From the dual KF, one can choose to replace the dual observation operator (classically being a state prediction Kalman filter) with another functional able to quantify the closeness between model predictions and assimilated measurements. In this work, relying on advances that have been performed in the tailoring of mCRE to low-frequency dynamics, the *Modified Dual Kalman Filter* (MDKF) derives the mCRE as new observer operator in a dual Kalman filtering framework. Practically, in a similar manner as one would compute optimal parameters minimizing the functional $\mathcal{J}$ from (1.21), the observation equation of the MDKF will reinvest the mCRE gradient $\nabla_\theta \mathcal{J}$ in order to guarantee the stationarity of the cost-function. Please note that no additional numerical error is made with the call to the mCRE gradient as its analytical expression can be explicitly derived from the constrained minimization problem (1.24) (see Appendix B). The MDKF dynamical system thus reads:

$$\begin{cases} \theta_{k+1} &= \theta_k + w_{\theta,k} \\ 0 &= \nabla_\theta \mathcal{J}(\theta_k, y_k) + v_k \end{cases} \tag{4.39}$$

This new framework thus differs from classical KFs as measurements are indirectly compared with model predictions through the mCRE functional. Parameter estimates are then sought as minimizers of the mCRE (according to current measurements). The doubt put on the mCRE gradient (with the classical observation noise v) then quantifies the authorized proximity of estimates to the optimal set of parameters that minimizes the mCRE at each time step.

> *Remark* 4.10. Inspired by [Marchand 2017], an initial attempt was made to directly minimize the value of the mCRE in the observation equation of the KF rather than its gradient. This approach remains less efficient since the normalization of the mCRE depends on the initial parameter guess, and since the mCRE does reach exactly 0 due to the existence of measurement noise.

4.3.2 Technical details about MDKF - Calibration guidelines

The coupling between mCRE and dual Kalman filtering avoids the calibration of process and measurement covariance matrices for state estimation as the mechanical state is directly built and processed within the mCRE framework. However, some influent (and tunable) parameters still need to be defined, either following engineering judgement or using automated procedures. These parameters are gathered in Tab. 4.2. Besides, several issues have to be addressed:

- ▷ the time-frequency domains nested interaction when mixing sequential data assimilation (in time) and mCRE (written in the frequency domain) properly;
- ▷ the robustness of the methodology and the calibration of internal parameters. General guidelines must be given on how to adapt the enhanced tools from Chapters 1-2 to a data assimilation framework (namely how to tune α and $z(\omega)$) and how to choose process and measurement noise covariance matrices ($\boldsymbol{Q}_\theta, \boldsymbol{R}$);
- ▷ the KF variant that should be used for optimal trade-off between numerical performance and accuracy. So far, EKF, UKF, and S3F are viable alternatives.
- ▷ the capability to perform data assimilation in real-time for online adaptive control prospects.

These issues will be discussed in the remainder of this section.

Data assimilation	mCRE functional
▷ Parameter covariance error matrix $\boldsymbol{Q}_\theta$	▷ Confidence into measurements coefficient α
▷ Observer covariance error matrix $\boldsymbol{R}$	▷ Frequency weighting function z
▷ Data assimilation time steps $\{t_k\}$	▷ Frequency bandwidth D_ω and its sampling

TABLE 4.2: Listing of the influential parameters related to the MDKF algorithm.

Sliding window technique

The fact that the mCRE operates in the frequency domain implies that a dedicated effort must be made to define how measurements are assimilated by the mCRE functional. Indeed, compared to classical KF approaches, **updating parameters for all new data points does not seem relevant as the observer operates on data in the frequency domain**. A sliding window technique, whose principle is illustrated in Fig. 4.11, is thus proposed for handling the time-frequency nested interaction.

The key idea of the sliding window technique is to process the most recent data block that (partially) includes new assimilated data in order to characterize changes in the measurements frequency content. The design of the sliding window is crucial as **it determines the tracking capabilities of MDKF and how fast the changes in structural parameters can be captured**. This is especially decisive in cases where abrupt stiffness degrations due to damage may occur.

The design of the sliding window must be done in accordance with the measurements acquisition sampling frequency f_s and the mCRE frequency bandwidth D_ω discretized with a frequency step Δf. The latter must be carefully chosen to correctly capture the frequency content associated to the participating eigenmodes. As mentioned in Chapter 1, common engineering judgment can recommend to choose Δf such that the narrowest resonant peak is described by a least three points. In the upcoming earthquake-engineering applications, with typical 5% damping ratio values and 2-5 Hz first eigenfrequency values, Δf is then chosen within $[0.1\ \text{Hz}; 0.5\ \text{Hz}]$. Therefore, in order to process accurate Fourier transforms in the mCRE framework, the number of data points N in the projection window must verify:

$$N \geqslant \frac{f_s}{\Delta f} \tag{4.40}$$

In order to react efficiently to abrupt changes, one should avoid to average the information provided by the newly assimilated data with former measurements. N is thus chosen as the smallest integer satisfying the above inequation. Note that zeropadding can permit to reduce N without decreasing much the Fourier transforms accuracy, but it should not be used abusively. Besides, the shape of the window must be carefully chosen due to Fourier transforms apodization issues. In the following, Blackman windows are used, as illustrated in Fig. 4.11.

To track at best sudden structural changes, some overlapping between windows can also be authorized as the Markov process assumption from the KF remains valid. The overlapping rate between two consecutive windows α_o defines the amount of new assimilated data at each time step. Using α_o-overlapped windows thus implies that the last $(1-\alpha_o)N$ data points are new.

> *Remark* 4.11. In practice, non-overlapping sliding windows may limit the tracking capabilities of MDKF: if one imagines that $\Delta f = 0.5$ Hz and $f_s = 1000$ Hz, then $N = 2000$ data points are required per window. In other words, time-windows must be at least 2 s-long. As seismic experiments on shaking tables commonly last up to 60 s, overlapping should be authorized to prevent from an insufficient number of data assimilation time steps.

Finally, please note that **the sliding window also fully conditions the real-time prospects of the MDKF algorithm** to the extent that one considers data is assimilated in real-time if the necessary CPU time per iteration is lower than the time between two consecutive data assimilation time steps. Therefore, a compromise has to be found on the overlapping rate α_o to allow MDKF to perform in real-time and to react fast enough to damage occurrences. A dedicated study below shows the paramount effect of α_o for accurate real-time identification and confirms that it must be chosen as high as possible, considering real-time computational constraints.

Calibration of MDKF tuning parameters

Contrary to offline model updating algorithms, the mCRE tuning parameters $(\alpha, z(\omega))$ cannot be computed using all the available data since the latter is progressively assimilated. However,

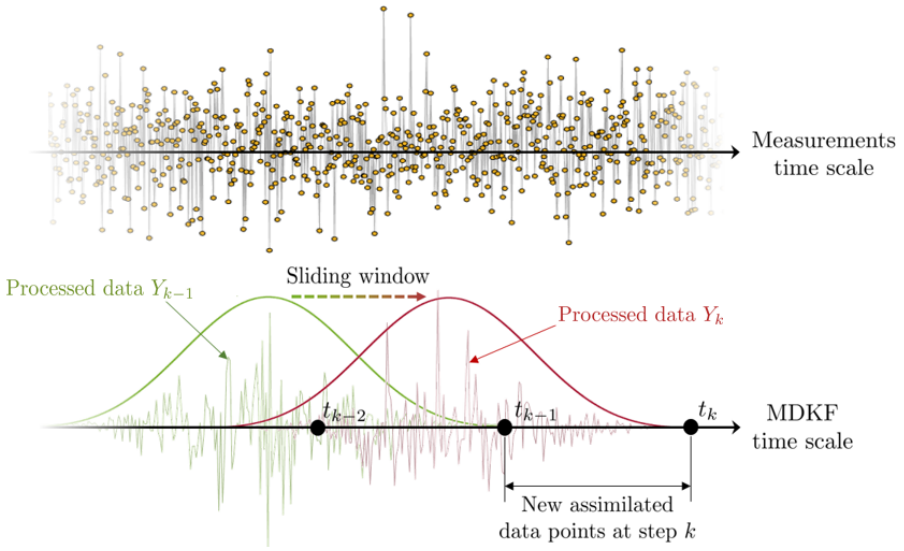

FIGURE 4.11: Illustration of the sliding window technique for progressive assimilation of data to be processed in the frequency domain by mCRE. A coarse MDKF time scale is defined according to the overlapping rate α_o and the window slides from t_{k-1} to t_k to assimilate new available data and to identify changes in the frequency content.

after a first training stage, it can be realistically assumed that α and $z(\omega)$ have already been computed from a low-level non-damaging random input using the automated procedures given in Chapter 1 before performing data assimilation. Nevertheless, if the value of α is not supposed to be tuned during experiments (as it is essentially driven by the measurements SNR), the initial frequency weighting function can become irrelevant if the modal signature of the damaging specimen significantly changes. $z(\omega)$ can be ponctually updated if strong changes in the frequency content are observed, as noticed in Alg. 4.5-4.6.

Regarding the crucial selection of filtering parameters, some guidelines are given for choosing matrices $\boldsymbol{Q}_\theta$ and $\boldsymbol{R}$ (assumed time-invariant). Using a discretized form of (4.39), one can directly relate the value of $\boldsymbol{Q}_\theta$ with the expected possible variation of parameters with time:

$$\boldsymbol{Q}_\theta = \mathbb{E}\left[w_{\theta,k} w_{\theta,k}^T\right] \approx \Delta t^2\, \mathbb{E}\left[\left(\frac{\partial \theta}{\partial t}\right)\left(\frac{\partial \theta}{\partial t}\right)^T\right] \tag{4.41}$$

Therefore, assuming the data assimilation time step $\Delta t = (1-\alpha_o)N/f_s$ to be given by the sliding window design, an engineering judgement regarding the possible variability of parameters allows to give a relevant estimation of $\boldsymbol{Q}_\theta$. Regarding the calibration of $\boldsymbol{R}$, as mentioned above, the observation noise v_k quantifies the tolerance one can have on the expected stationarity of the mCRE gradient: it tempers the fact that the mCRE may not be exactly minimized by θ_k considering the current measurements y_k. Even if one should pick $\boldsymbol{R} = 0$ idealistically, a small non-zero value of $\boldsymbol{R}$ is used so as to limit the spurious influence of time steps where data does not store much relevant information for model updating. Typical convenient values of $\boldsymbol{R}$ are given in the following applications.

4.3.3 Computational considerations for real-time prospects

To prove the relevance of MDKF to perform data assimilation efficiently, the last point to address concerns the numerical performance, in particular when the parameter set θ and/or the number of degrees-of-freedom of the FE problem become important.

The analysis of Alg. 4.5-4.6 emphasizes the most time-consuming steps of the algorithm (colored in gray), namely the frequency domain data preprocessing and the computation of the mCRE for each frequency of D_ω (and each σ-point in a SPKF context). Even if the call to Fast Fourier Transforms is unavoidable, the computation of the mCRE can be drastically shortened

using all the numerical tools previously mentioned in Chapter 1: reduced basis, parallelization of frequency samples of D_ω, analytical expression of the gradient with respect to parameters.

It should be noticed that (4.39) is not constrained to be used in an UKF framework as originally presented in [Marchand et al. 2016] and [Alarcon et al. 2011a]. As mentioned earlier, the S3F is an alternative σ-point Kalman Filter that has proved to have the same numerical performance than UKF with almost 50% CPU time reduction. Besides, UKF was preferred to EKF due to its better accuracy in higher order statistical moments. However, from the computational viewpoint, EKF avoids the (costly) propagation of σ-points, which implies that it should be quicker without being less accurate as the analytical expression of the mCRE gradient and the semi-analytical expression of the mCRE Hessian are available (see Appendix B).

MDKF based on dual EKF, dual UKF and dual S3F structures will be compared in terms of accuracy and CPU time in the following application, in the next section of this chapter.

4.3.4 CRE-based clustering for partial state-update

The CPU performance of sampling-based KFs remains directly proportional to N_θ. Therefore, the processing of data in real-time may not be possible in cases where $N_\theta \gg 1$, which can be the case in realistic monitoring applications on large-scale structures. A possible way to improve numerical performance without loss of accuracy is to use the full potential of the mCRE within the MDKF.

We have presented in Chapter 2 a CRE-based clustering low-cost preprocessing step allowing to focus model updating actions on parameters in need for correction. The clustered extension of MDKF is presented in Alg. 4.7 for a MDKF with SPKF basis. In a very similar manner that the parameter space is optimized in the CRE sense when automating offline mCRE-based model updating, clustering can be exploited in MDKF to restrict the update to a well-chosen subset of parameters. They are gathered at each data assimilation time step in the subset $R \subset [\![1; N_\theta]\!]$. The subset R corresponds exactly to the cluster of erroneous parameters, to which correcting actions will be focused in order to **update optimally at minimal cost**. Non-updated parameters are then not considered from one data assimilation time step to the other, which **allows for large CPU time savings and may avoid the MDKF to fall into physical-meaningless parameter configurations**. The relevance of the clustered MDKF is illustrated in Section 4.4.

4.3.5 The algorithms

Algorithm 4.5: Modified Dual Kalman Filter with SPKF basis.

Data: Sliding window, data assimilation time steps $\{t_k\}$, loading conditions $e_{0:\infty}$, mCRE tuning parameters: $D_\omega, \alpha, z(\omega)$ and reduced basis $\boldsymbol{\Phi}_L$, initial statistics on parameters: mean $\widehat{\theta}_0$ and covariance $\boldsymbol{P}_0^\theta$, process and measurements noise covariance matrices: $\boldsymbol{Q}_\theta, \boldsymbol{R}$

Result: Successive estimates of the parameter vector statistics $(\widehat{\theta}_k, \boldsymbol{P}_k^\theta)$

Loop on data assimilation time steps

for $k = 1 : \infty$ **do**

1) **Compute σ-points and associated weights**

Use Tab. 4.1 to compute σ-points $\{\mathcal{X}_{k,i}\}_i$ and associated weights $\{\mathcal{W}_i^m, \mathcal{W}_i^c\}_i$;

2) **Prediction step**

Direct propagation of the σ-points: $\mathcal{X}_{k,i}^- = \mathcal{X}_{k-1}^i \; \forall \, i$;
Computation of *a priori* mean and covariance:
$\widehat{\theta}_k^- = \sum_i \mathcal{W}_i^m \mathcal{X}_{k,i}^-$;
$\boldsymbol{P}_k^{\theta-} = \sum_i \mathcal{W}_i^c \left(\mathcal{X}_{k,i}^- - \widehat{\theta}_k^-\right)\left(\mathcal{X}_{k,i}^- - \widehat{\theta}_k^-\right)^T + \boldsymbol{Q}_\theta$;

3) **Processing new data in the frequency domain**

Extraction of the new data block with the sliding window: $y_k(t)$
Fast Fourier Transform for mCRE analysis: $Y_k(\omega) \; \forall \, \omega \in D_\omega$
Possible option: update the frequency weighting function $z(\omega)$

4) **Correction step**

Propagation of the σ-points through the mCRE functional:
$\mathcal{Y}_{k,i} = \nabla_\theta \mathcal{J}(\mathcal{X}_{k,i}^-; Y_k) \; \forall \, i$;

Compute propagated mean and covariance matrices
$\widehat{y} = \sum_i \mathcal{W}_{k,i}^m \mathcal{Y}_{k,i}$;
$\boldsymbol{P}_{yy} = \sum_i \mathcal{W}_{k,i}^c \left(\mathcal{Y}_{k,i} - \widehat{y}\right)\left(\mathcal{Y}_{k,i} - \widehat{y}\right)^T$;
$\boldsymbol{P}_{\theta y} = \sum_i \mathcal{W}_{k,i}^c \left(\mathcal{X}_{k,i}^- - \widehat{\theta}_k^-\right)\left(\mathcal{Y}_{k,i} - \widehat{y}\right)^T$;

Correct predictions to compute *a posteriori* statistics:
$\boldsymbol{K}_k = \boldsymbol{P}_{\theta y}\left(\boldsymbol{P}_{yy}\right)^{-1}$;
$\widehat{\theta}_k = \widehat{\theta}_k^- - \boldsymbol{K}_k \widehat{y}$;
$\boldsymbol{P}_k^\theta = \boldsymbol{P}_k^{\theta-} - \boldsymbol{K}_k \boldsymbol{P}_{yy} \boldsymbol{K}_k^T$;

end

Algorithm 4.6: Modified Dual Kalman Filter with EKF basis.

Data: Nonlinear model and observation operators: $\mathcal{M}, \mathcal{H}$, loading conditions: $e_{0:\infty}$, error covariance matrices: $\boldsymbol{Q}, \boldsymbol{R}$, initial state vector $\widehat{x}_0$ and associated covariance matrix $\boldsymbol{P}_0$
Result: Successive estimates of the parameter vector statistics $(\widehat{\theta}_k, \boldsymbol{P}_k^\theta)$

Loop on data assimilation time steps
for $k = 1 : \infty$ **do**

1) **Prediction step**
$\tilde{\theta}_k = \widehat{\theta}_{k-1}$;
$\boldsymbol{P}_k^{\theta-} = \boldsymbol{P}_{k-1}^\theta + \boldsymbol{Q}_\theta$;

2) **Processing new data in the frequency domain**
Extraction of the new data block with the sliding window: $y_k(t)$
Fast Fourier Transform for mCRE analysis: $Y_k(\omega) \; \forall \, \omega \in D_\omega$
Possible option: update the frequency weighting function $z(\omega)$

3) **Correction step**
Compute mCRE value $\mathcal{J}(\tilde{\theta}_k; Y_k)$ and derivatives (see Appendix B)

Compute Kalman gain: $\boldsymbol{K}_k = \boldsymbol{P}_k^{\theta-} \nabla_\theta^2 \mathcal{J}(\tilde{\theta}_k; Y_k) \left(\nabla_\theta^2 \mathcal{J}(\tilde{\theta}_k; Y_k) \boldsymbol{P}_k^{\theta-} \nabla_\theta^2 \mathcal{J}(\tilde{\theta}_k; Y_k) + \boldsymbol{R} \right)^{-1}$;
Correction of parameter estimate mean and covariance:
$\widehat{\theta}_k = \tilde{\theta}_k - \boldsymbol{K}_k \mathcal{J}(\tilde{\theta}_k, Y_k)$;
$\boldsymbol{P}_k^\theta = (\boldsymbol{I} - \boldsymbol{K}_k \nabla_\theta^2 \mathcal{J}(\tilde{\theta}_k; Y_k)) \boldsymbol{P}_k^{\theta-}$;

end

Algorithm 4.7: Clustered Modified Dual Kalman Filter (with SPKF basis)

Data: Sliding window, data assimilation time steps $\{t_k\}$, loading conditions $e_{0:\infty}$, mCRE tuning parameters: $D_\omega, \alpha, z(\omega)$ and reduced basis, initial statistics on parameters: mean $\widehat{\theta}_0$ and covariance $\boldsymbol{P}_0^\theta$, error covariance matrices: $\boldsymbol{Q}_\theta, \boldsymbol{R}$
Result: Successive estimates of the parameter vector statistics $(\widehat{\theta}_k, \boldsymbol{P}_k^\theta)$

Loop on data assimilation time steps
for $k = 1 : \infty$ **do**

0) **CRE-based clustering**
Computation of the CRE map at the current estimate: $\zeta_i^2(\widehat{\theta}_{k-1}) \; \forall \, i \in [\![1; N_\theta]\!]$
Identification of a restricted subset in need of correction $\theta_{R,k-1}$, $R \subset [\![1; N_\theta]\!]$ using Alg. 2.1

1) **Generation of σ-points**
Computation of σ-points for the restricted parameter set $\theta_{R,k}$ using Tab. 4.1

2) **Prediction step**
Direct propagation of the σ-points through the state-update equation
Computation of *a priori* mean and covariance for $\theta_{R,k}$

3) **Processing new data in the frequency domain**
Extraction of the new data block with the sliding window: $y_k(t)$
Fast Fourier Transform for mCRE analysis: $Y_k(\omega) \; \forall \, \omega \in D_\omega$

4) **Correction step**
Propagation of the σ-points through the mCRE functional
Correction of predictions to compute *a posteriori* statistics of θ_R
The statistics of the non updated parameters remain unchanged from the previous time step.

end

4.4 Illustrations on a two-story plane frame submitted to random ground motion

In this Section, the intention is first to validate MDKF for parameter estimation from sparse measurements with a typical earthquake engineering academic example, before comparing MDKF structures (EKF, UKF, S3F) and the benefits of the CRE-based clustering approach for partial state-update. The frame example described in Appendix A.1 will be reinvested here again. Contrary to the first KF illustrations of Section 4.2.8, the frame structure is submitted to a 120 s random bi-axial ground motion input, and the reference stiffness field presents a defect that appears during the test in wall W10 (see Fig. 4.12) while the initial guess underestimates by 10% the healthy reference configuration.

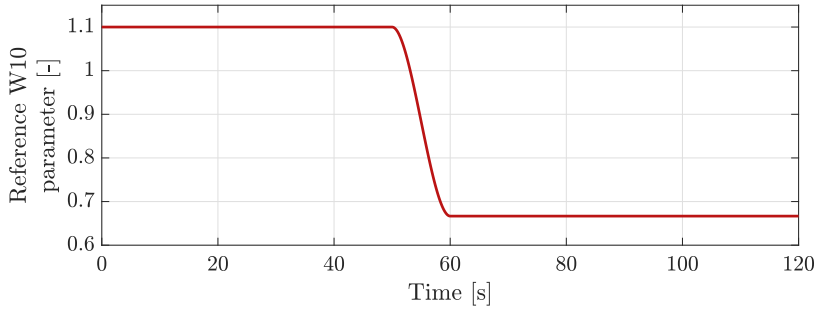

FIGURE 4.12: MDKF application to a plane frame submitted to ground motion - W10 reference stiffness parameter evolution.

The intuitive wall/slab decomposition of Fig. 4.6 is still chosen: 6 subdomains are defined {W10, W11, W20, W21, F10, F20}. The stiffness model to update on-the-fly is then made of $N_\theta = 6$ parameters. Note that the case of $N_\theta = 12$ subdomains will be considered to evaluate the clustered MDKF extension.

The objective of this academic example is to **assess the MDKF ability to recover the expected parameters from simulated acceleration measurements acquired by discrete sensors scattered over the structure** (yellow dots in Fig. 4.6), with particular attention paid to the capability of identifying evolutive parameters.

The list of reference MDKF tuning parameters used to obtain the forthcoming results is stored in Tab. 4.3. These values are implicitly used in the following if not specified.

MDKF framework	Reference value		
Data sampling frequency	f_s	$=$	1000 Hz
Overlapping rate for Blackman windows	α_o	$=$	90%
mCRE frequency interval	D_ω	$=$	[1 Hz; 20 Hz]
mCRE frequency sampling step	Δf	$=$	0.1 Hz
Amount of new data per window	$(1-\alpha_o)/\Delta f$	$=$	0.1 s
Covariance on parameter state	$\boldsymbol{Q}_\theta$	$=$	$10^{-4}\boldsymbol{I}$
Covariance on mCRE gradient	$\boldsymbol{R}$	$=$	10^{-8}
Initial covariance on parameters	$\boldsymbol{P}_0^\theta$	$=$	$0.05\boldsymbol{I}$

TABLE 4.3: Reference MDKF setting parameters for the considered applications. $\boldsymbol{I}$ denotes the identity matrix of appropriate dimension.

4.4.1 MDKF reference data assimilation results

Numerical results are presented below to assess the overall data assimilation algorithm and the effect of its internal parameters. Before considering the effect of the underlying nonlinear KF basis of MDKF and the potentialities of its clustered extension, we will exclusively focus on the

MDKF algorithm based on UKF as default choice from previous literature works. The latter is described in Alg. 4.5, with σ-points definition explicitly written in Tab. 4.1.

Assimilation of perfect measurements

The MDKF algorithm is first assessed using (idealistic) non-noisy acceleration measurements (*i.e.*, $\delta = 0$). Stiffness parameters are correctly updated, as shown in Fig. 4.13 where the Gaussian pdfs $\pi(\widehat{\theta}_k|y_{0:k})$ of the parameters are plotted at each data assimilation time step. The close correlation of pdfs with the reference parameter values as well as the tightness of credible intervals illustrate the relevance of MDKF for on-the-fly model updating.

Even though the first time step is longer as not enough data has been assimilated to perform accurate FFTs (10 s-long sliding window), the short time response in the first iterations emphasizes that all parameters are quickly and correctly identified. Moreover, **the decay of the W10 parameter is well monitored**, with an unavoidable slight delay due to the use of the sliding window. This is certainly the main drawback of the proposed approach. Note also that the update of the time-evolutive W10 parameter does not lead the algorithm to erroneous local minima.

Eventually, one can note that the relative confidence in parameter estimates can be observed throughout the relative width of the plotted pdfs. It highlights how MDKF can indirectly provide information regarding (relative) uncertainties of estimates, similarly to the confidence intervals evoked in Chapter 2.

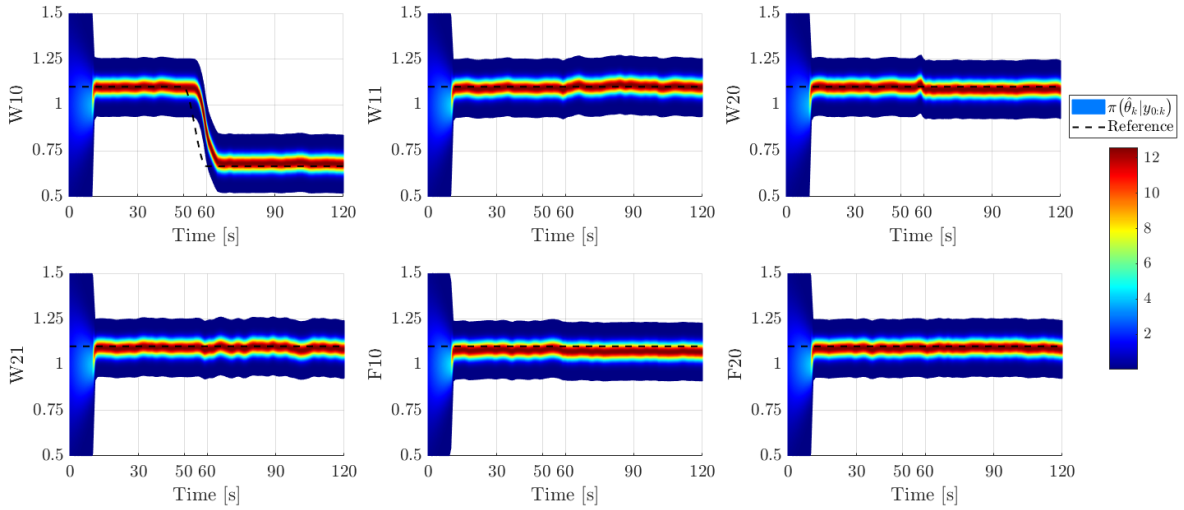

FIGURE 4.13: MDKF data assimilation results of the frame FE model from non-noisy measurements ($\delta = 0\%, \alpha = 0.1$). Probability density functions are plotted for each stiffness parameter with expected values to identify.

To confirm the fact that MDKF parameter estimates are corrected so as to sequentially minimize the mCRE, we compare in Fig. 4.14 the W10 parameter estimate given by MDKF and the full mCRE evolution with respect to W10 parameter computed after each data asssimilation time step in an offline manner (with the same data blocks Y_k that are used in the MDKF process). The strong concordance between mCRE minima and MDKF predictions confirms that the data assimilation process behaves as planned.

> *Remark* 4.12. Actually, any KF with a prediction equation defined from a model can be referred to as *physics-informed*. We claim the MDKF to be *physics-guided* in the sense that the physics knowledge is no longer hidden within the prediction stage, but in the observation metrics.

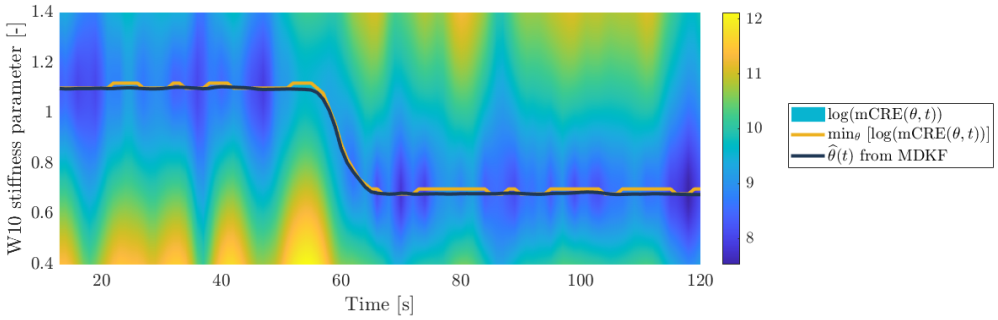

FIGURE 4.14: Emphasis on MDKF being driven by sequential minimization of mCRE during the data assimilation process. The mCRE map has been plot in an offline manner after each data assimilation time step using current measurements, and the mCRE minima are compared to the W10 mean estimate provided by MDKF.

Enhanced robustness with respect to measurement noise

For real-life realistic applications, the stability and robustness of the MDKF with respect to measurement noise must be addressed. In Fig. 4.15, low-SNR measurements (with $\delta = 20\%$) are successfully assimilated. As measurement noise disturbs the data assimilation process, the credible interval identified for all parameters becomes larger. The mean estimate $\widehat{\theta}_k$ is also oscillating around the expected value due to the fact that noise directly impacts the convexity of the mCRE functional. The difference in terms of sensitivity between subdomains (W10, W20, F10) and (W11, W21, F20) is even more significant.

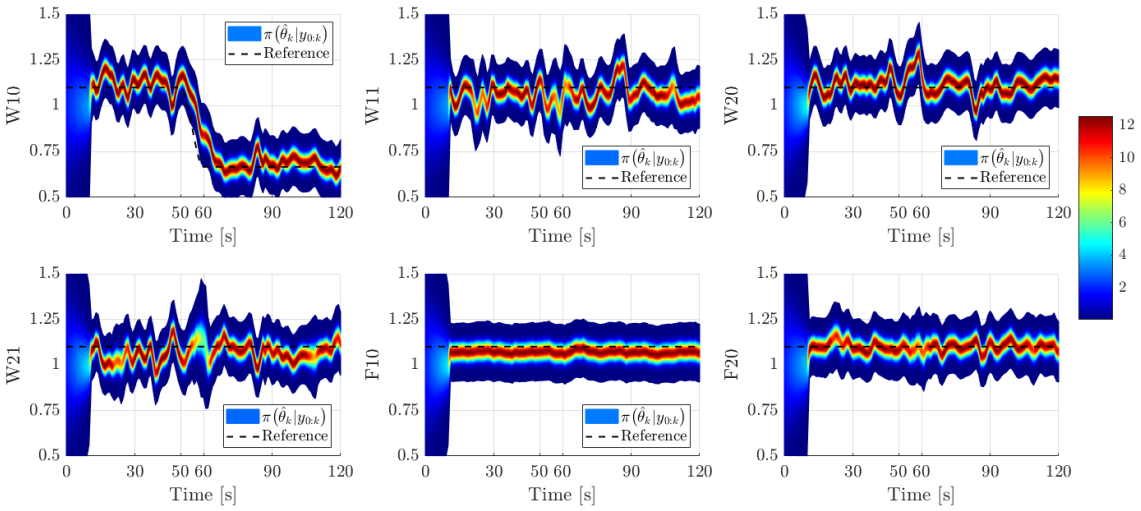

FIGURE 4.15: MDKF data assimilation results of the frame FE model from noisy measurements ($\delta = 20\%, \alpha = 10^{-2}$). Probability density functions are plotted for each stiffness parameter with expected values to identify.

Due to the fact that MDKF benefits from mCRE properties, the data assimilation algorithm shows a different behaviour compared to classical nonlinear KFs with respect to measurement noise. Indeed, as mCRE tuning parameters are automatically adapted to measurement SNR, **the MDKF algorithm directly integrates the reliability of available data through the mCRE observer, which leads to an enhanced robustness with respect to measurement noise**. In particular, the estimated means of parameters tend to (slowly) oscillate around the target values rather than being systematically biased, and increasing the noise level does not affect the reactivity of MDKF (observed by comparison of Fig. 4.13 and 4.15).

Design of the sliding window

As mentioned in Section 4.3.2, the design of the sliding window must be made with caution so as to guarantee a compromise between real-time computational constraints and reactivity to detect defects accurately. Fig. 4.16 allows to show the necessity to correctly calibrate the overlapping rate between consecutive windows α_o when trying to track a local sudden stiffness change appearing in W10 subdomain. Low values let a lot of remaining CPU time available between iterations (to perform post-processing operations) but are not reactive enough to follow sudden stiffness changes whereas high values do not enable MDKF to perform in real-time. The $\alpha_o = 90\%$ value defined in Tab. 4.3 appears to be a good compromise between accurate parameter tracking and real-time CPU constraints.

Here again, one can observe the slight delay due to the use of the sliding window, which is unavoidable and due to the time-frequency domains nested interaction through the mCRE functional. Although this is probably the main limit of the method, one expects it not to impact much the additional post-processing operations.

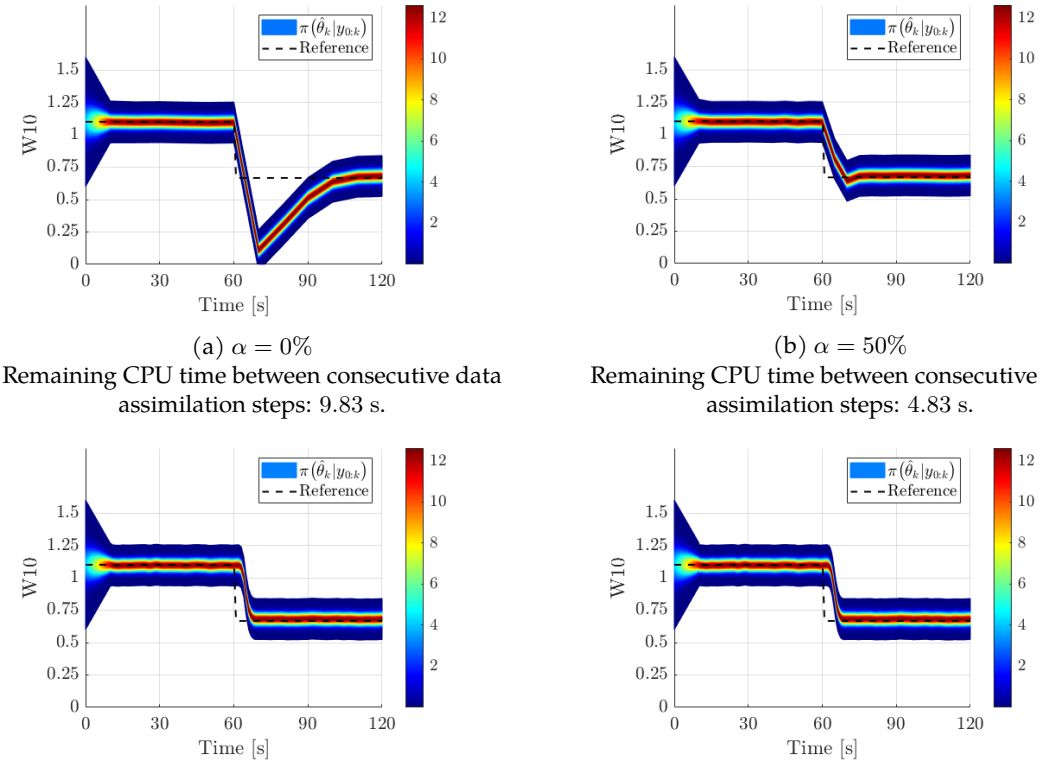

(a) $\alpha = 0\%$
Remaining CPU time between consecutive data assimilation steps: 9.83 s.

(b) $\alpha = 50\%$
Remaining CPU time between consecutive data assimilation steps: 4.83 s.

(c) $\alpha = 90\%$
Remaining CPU time between consecutive data assimilation steps: 0.83 s.

(d) $\alpha = 99\%$
CPU time to assimilate data is too long by 0.08 s for real-time prospects.

FIGURE 4.16: Impact of the overlapping rate between consecutive sliding windows to accurately track sudden stiffness changes in real-time.

Calibration of MDKF error covariance matrices

As the calibration of classical KFs covariance error matrices strongly impacts parameter estimates, a complete study regarding the influence of internal parameters of MDKF that may affect its performance must be done. As the reference parameters $\theta^\star(t)$ are known in this academic example, an overall performance indicator, denoted ϵ, can be defined:

$$\epsilon = \frac{\|\theta^\star(t) - \widehat{\theta}(t)\|^2_{L^2}}{\|\theta^\star(t)\|^2_{L^2}} \quad \text{with} \quad \|\square\|^2_{L^2} \triangleq \int_0^T \square^2 \, \mathrm{d}t \tag{4.42}$$

where T is the duration of the test. The computation of this performance indicator allows to carry out a sensitivity analysis on the key parameters of the MDKF algorithm, namely $\boldsymbol{Q}_\theta, \boldsymbol{R}$ and α, whose results are presented in Fig. 4.17.

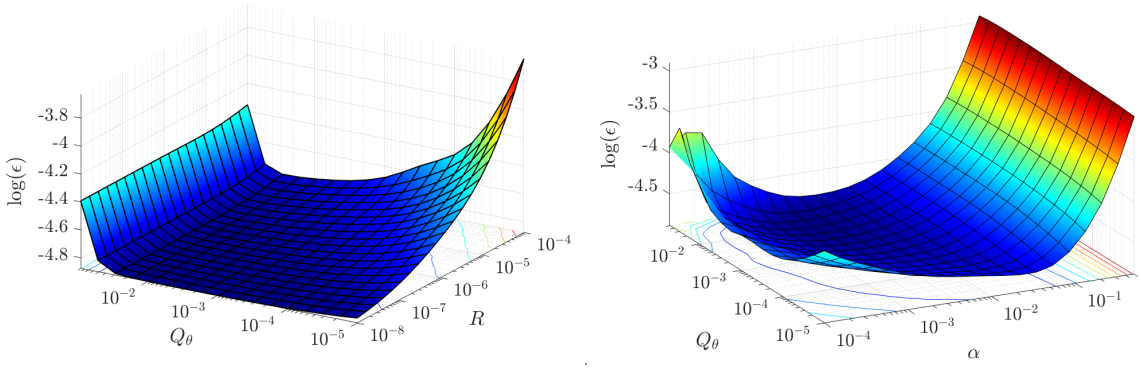

(a) $\log(\epsilon)$ as function of $\boldsymbol{Q}_\theta$ and $\boldsymbol{R}$

(b) $\log(\epsilon)$ as function of $\boldsymbol{Q}_\theta$ and α

FIGURE 4.17: Impact of tuning parameters $\boldsymbol{Q}_\theta, \boldsymbol{R}$ and α on the performance of MDKF from noisy measurements ($\delta = 10\%$).

Even if this analysis is computationally expensive and not possible in realistic applications (only because reference parameters are not always known), several remarks can be made:

(i) there exists a set of optimal parameters that minimize the error between the estimated mean and reference parameters (for a given dataset);

(ii) sub-optimal choices for $\boldsymbol{Q}_\theta, \boldsymbol{R}, \alpha$ (*i.e.* values close to the optimum) are yet leading to correct and acceptable results. Indeed, there is no need to select the optimum value among $\boldsymbol{Q}_\theta, \boldsymbol{R}, \alpha$ to get satisfying results. For instance, observing Fig. 4.17.a, $\boldsymbol{Q}_\theta$ can be merely adjusted between 10^{-4} and 10^{-2} and MDKF will still provide accurate results. Actually for this example, any triplet $(\boldsymbol{Q}_\theta, \boldsymbol{R}, \alpha)$ that satisfies $\log \epsilon < -4.6$ is satisfying. These results suggest that the general guidelines provided in Section 4.3.2 are sufficient to calibrate tuning parameters correctly;

(iii) the optimal values provided by the plots of Fig. 4.17 do not take into account the width of credible intervals, which is of major importance if the complete parameter statistics are post-processed.

> *Remark* 4.13. The MDKF results presented above have been obtained processing measurements faster than they were assimilated. With an overlapping rate $\alpha_o = 90\%$, 1 s-overlapped windows were assimilated in less than 0.2 s using a personal laptop (8Go RAM - Intel i5 1.70 GHz processor). The computational burden carried by the numerous calls to mCRE is considerably reduced using all parallelization techniques that have been mentioned previously. Considering realistic industrial applications, the remaining available CPU time could be exploited to update mCRE tuning parameters (in particular $z(\omega)$) or to communicate with the experimental system in order to adapt control laws in a DDDAS context.

4.4.2 MDKF vs. classical joint UKF

One could legitimately question the interest of MDKF in comparison with the classical data assimilation methods mentioned in Section 4.2. Although it is well known that nonlinear KFs can lose accuracy with high noise levels, a dedicated comparison in the current case study with joint UKF (implemented according to Alg. 4.4) has been performed. Key results are shown in Fig. 4.18 for the tracking of the W10 (evolutive) stiffness parameter. One can first observe that JUKF does not suffer from the slight delay due to the MDKF sliding window process as it integrates every single new data point independently, which (i) necessitates much more calls

to the model and limits real-time prospects from complex models, and (ii) creates spurious oscillations around the mean value due to measurement noise. Besides, JUKF estimates hardly correspond to the expected value after $t = 60$ s, showing here the limitations of classical approaches to recover damage parameters from acceleration measurements using explicit time integration schemes for model predictions. On the contrary, **MDKF parameter estimates are much more stable in time, whatever the noise level**.

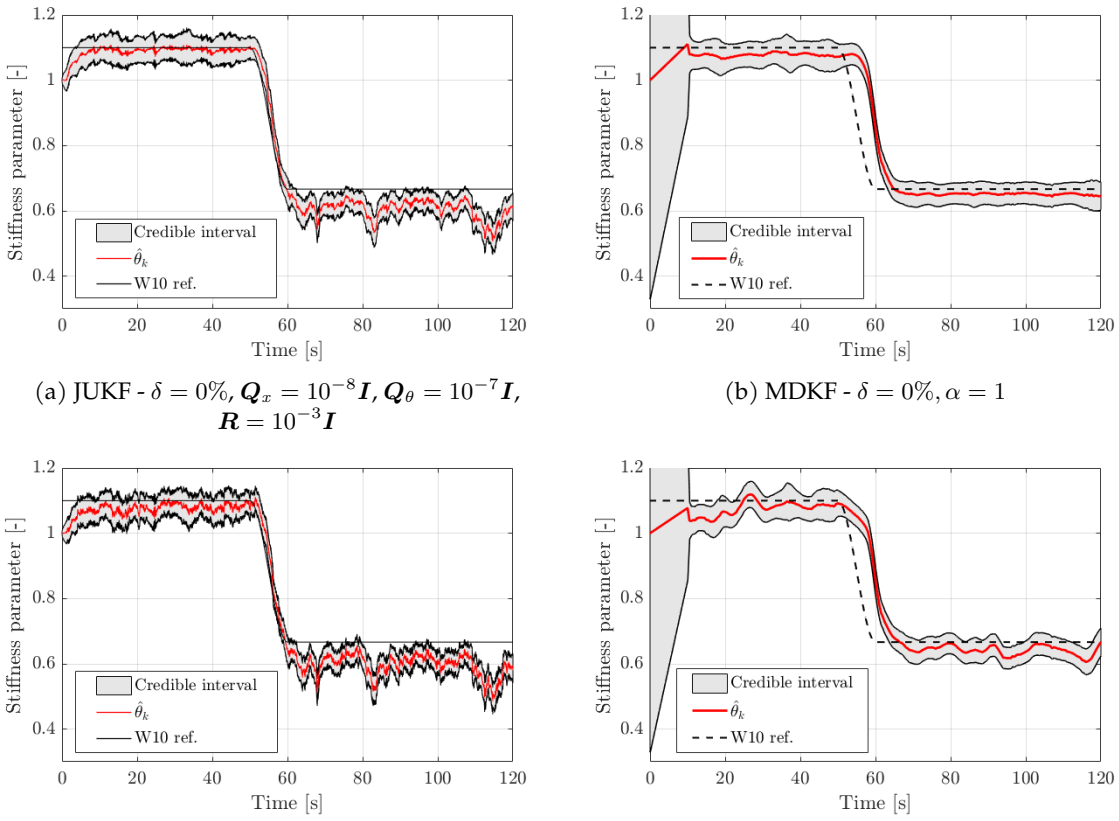

(a) JUKF - $\delta = 0\%$, $\boldsymbol{Q}_x = 10^{-8}\boldsymbol{I}$, $\boldsymbol{Q}_\theta = 10^{-7}\boldsymbol{I}$, $\boldsymbol{R} = 10^{-3}\boldsymbol{I}$

(b) MDKF - $\delta = 0\%, \alpha = 1$

(c) JUKF - $\delta = 20\%$, $\boldsymbol{Q}_x = 10^{-8}\boldsymbol{I}$, $\boldsymbol{Q}_\theta = 10^{-7}\boldsymbol{I}$, $\boldsymbol{R} = 10^{-1}\boldsymbol{I}$

(d) MDKF - $\delta = 20\%, \alpha = 10^{-3}$

FIGURE 4.18: Comparison of JUKF and MDKF for the identification of the W10 stiffness parameter from acceleration measurements. Credible intervals are defined at $\pm 3\sigma_\theta$. For the sake of conciseness, only the pdf of W10 parameter is plotted.

Another important remark relates to the calibration of the JUKF tuning parameters, which is a complex task without any *a priori* idea about the intrinsic relevance of both model and measurements. In particular, the compromise between $\boldsymbol{Q}_x, \boldsymbol{Q}_\theta$ and $\boldsymbol{R}$ is a sensitive user-dependent manipulation that strongly conditions the quality of JUKF results.

Finally, whether for joint or dual UKF, the amount of σ-points to be propagated at each data assimilation time step is a major limitation considering real-time applications prospects (justifying among other reasons why recent works focus on ROM techniques).

4.4.3 Comparative study between mCRE-based Kalman filters

So far, a UKF has been used as MDKF algorithmic structure, but the formulation given in (4.39) does not restrain to UKF. In this paragraph, the aim is to assess which nonlinear KF structure (UKF, EKF, S3F) is the most appropriate to perform stiffness parameter tracking with MDKF in real-time from discrete acceleration measurements. Various noise levels are considered $\delta = \{0; 5; 15\}\%$ to assess the robustness to measurement noise. Accuracy is quantified via the L^2-norm misfit error on parameters defined in (4.42). Results of this comparative study are stored in Tab. 4.4, and illustrated in Fig. 4.19.

Dataset	$\delta = 0\%$ (perfect data)			$\delta = 5\%$ (noisy)			$\delta = 15\%$ (highly-noisy)		
KF basis	UKF	S3F	EKF	UKF	S3F	EKF	UKF	S3F	EKF
ϵ_{W10}	0.0052	0.0052	0.0083	0.0054	0.0054	0.0111	0.0069	0.0070	0.0198
ϵ_{W11}	0.0001	0.0001	0.0001	0.0005	0.0005	0.0004	0.0017	0.0017	0.0011
ϵ_{W20}	0.0002	0.0002	0.0002	0.0004	0.0004	0.0005	0.0004	0.0004	0.0005
ϵ_{W21}	0.0001	0.0001	0.0001	0.0009	0.0009	0.0015	0.0009	0.0009	0.0015
ϵ_{F10}	0.0004	0.0004	0.0003	0.0007	0.0007	0.0006	0.0007	0.0007	0.0006
ϵ_{F20}	0.0001	0.0001	0.0000	0.0003	0.0003	0.0004	0.0003	0.0003	0.0004
Average CPU time per step [s]	0.22303	0.16379	0.13590	0.21300	0.16154	0.13137	0.21424	0.16375	0.12753

TABLE 4.4: Comparison of mCRE-based KFs accuracy for stiffness parameter tracking.

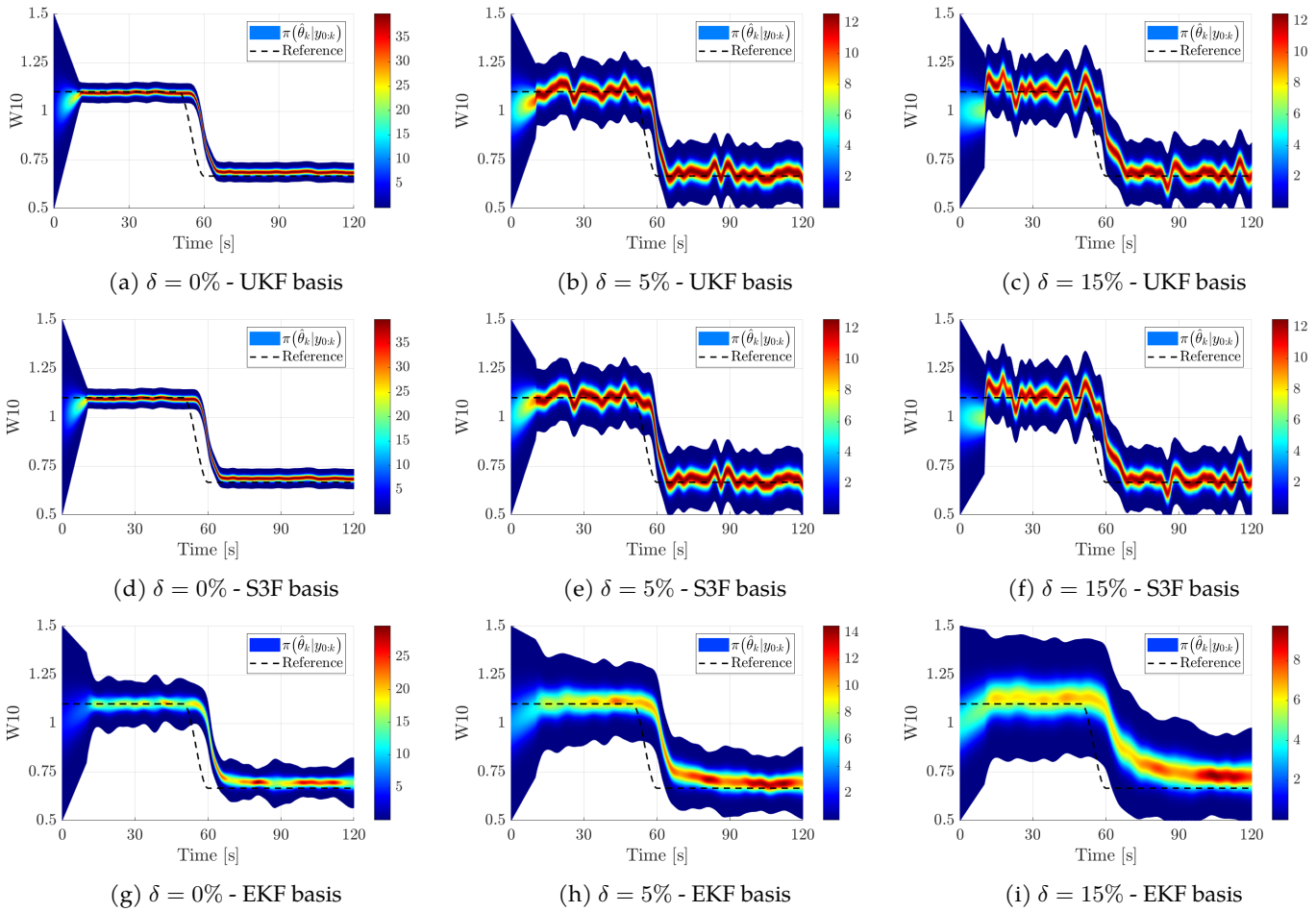

(a) $\delta = 0\%$ - UKF basis (b) $\delta = 5\%$ - UKF basis (c) $\delta = 15\%$ - UKF basis

(d) $\delta = 0\%$ - S3F basis (e) $\delta = 5\%$ - S3F basis (f) $\delta = 15\%$ - S3F basis

(g) $\delta = 0\%$ - EKF basis (h) $\delta = 5\%$ - EKF basis (i) $\delta = 15\%$ - EKF basis

FIGURE 4.19: Online update of W10 stiffness parameter using several mCRE-based KFs.

Several remarks can be made from these results:

- ▷ Whatever the KF in which the mCRE is integrated, the tracking of parameters is successfully performed in real-time, with always more than 50% of remaining time to perform other operations online. Even for highly-noisy measurements, the stiffness drop of W10 parameter is well captured by mCRE-based data assimilation algorithms.
- ▷ From the error indicator values $\epsilon_\bullet$ displayed in Tab. 4.4, one can consider the identification of correct quality. The fact that ϵ_{W10} is one order of magnitude higher is due to the slight delay at the identification of the sudden change in W10, which is a direct consequence of the sliding window technique.
- ▷ Owing to the fact that UKF and S3F produce the exact same estimates [Papakonstantinou et al. 2022a], Fig. 4.19a-4.19c and Fig. 4.19d-4.19f are identical. The analysis of CPU times in Tab. 4.4 confirms that using S3F σ-points enables a significant gain on this academic

example (30% faster, 8 σ-points instead of 13 in that case). There is no doubt that this CPU gain will be higher in problems where the parameter space dimension N_θ is larger. **The systematic use of S3F instead of UKF is thus strongly recommended, as it is as accurate for a lower computational cost**.

- ▷ EKF-based MDKF benefits from the simplicity of EKF and the parallel computation of mCRE computations to process data faster than σ-points-based MDKF. However, it also naturally carries the limitations of EKF in terms of accuracy, with the loss of tracking reactivity that appears at high measurement noise levels. Therefore, **if EKF-based MDKF is faster, it is also less accurate than SPKF-based MDKF**.

In the end, it appears that S3F-based MDKF is the best compromise between computational cost and accurate estimates. It will thus be chosen as reference mCRE-based KF algorithm.

4.4.4 Towards an optimal use of CPU resources: a proof-of-concept for the clustered MDKF

Finally, we intend to validate the clustered MDKF when trying to update the frame parametrization described by $N_\theta = 12$ non-overlapping subdomains. Having "too numerous" subdomains compared to the defect to identify will allow to assess the relevance of the clustered MDKF for high-dimensional identification problems. More specifically, emphasis is put on the compromise between estimate accuracy and CPU time savings compared to standard MDKF.

In order to avoid falling into local minima as the initial guess does not match correctly with the expected parameters (10% gaps), the first 10 iterations (over 110) are forced to update the full set of parameters. Afterwards, the CRE-based clustering automatically drives which parameters have to be updated (see Alg. 4.7).

The clustered MDKF is applied to assimilate the same data that is processed to obtain the results displayed in Fig. 4.20, that will be used as reference. Parameter identification results are shown in Fig. 4.21 and the comparison between CPU times is summarized in Tab. 4.5.

Algorithm	N_θ	Average CPU time per iteration
UKF-based MDKF	6	0.33 s
S3F-based MDKF	6	0.16 s
UKF-based MDKF	12	0.76 s
S3F-based MDKF	12	0.44 s
Clustered UKF-based MDKF	12	0.48 s (including 0.02 s for the clustering step)
Clustered S3F-based MDKF	12	0.35 s (including 0.02 s for the clustering step)

TABLE 4.5: Comparison of CPU time per iteration between MDKF and clustered MDKF to assimilate the same amount of data.

It can be observed that the clustered MDKF does not impact the accuracy of parameter estimates by respectively comparing Fig. 4.20 and 4.21. Indeed, the noise level and MDKF internal parameters still condition accuracy results, whether the clustering step is present or not. In terms of CPU times, it is undeniable that the clustering step is not a time-consuming procedure: only 0.02 s of the 0.5 s allowed to process data in real-time. It provides a significant speed-up according to the results given in Tab. 4.5: in most time steps only half of the parameters stored in θ are updated. The remaining saved time can therefore be spent for DDDAS purposes instead of trying to update low-sensitive or already well-identified parameters (in the mCRE sense). Besides, although only 12 parameters were updated here, the speed-up one can expect when $N_\theta \gg 1$ may thus be even larger in practice as the ratio between false and healthy elements may be smaller.

Lastly, CPU time comparisons between UKF-based MDKF and S3F-based MDKF have also been reported in Tab. 4.5, and show that **when combining (i) a KF in which the number of σ-points is optimized and (ii) an adaptive parametrization of the problem, considerable gains can be made for substantially equivalent accuracy**.

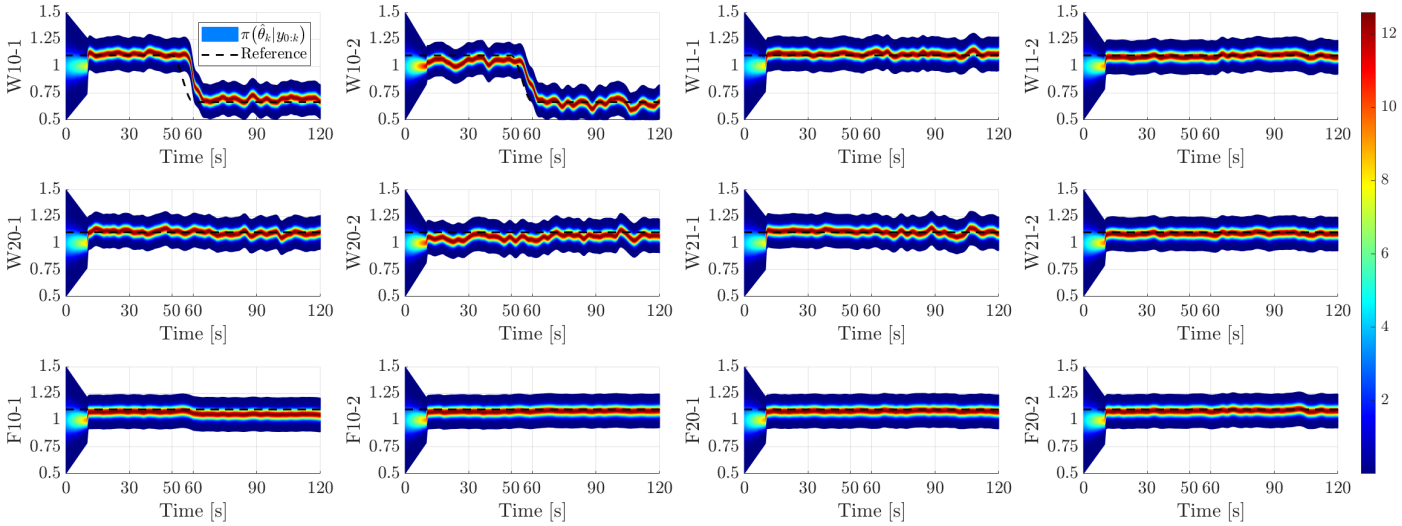

FIGURE 4.20: MDKF results of the frame model from noisy measurements ($\delta = 2\%$). Pdfs are plotted for each of the $N_\theta = 12$ parameters with expected values.

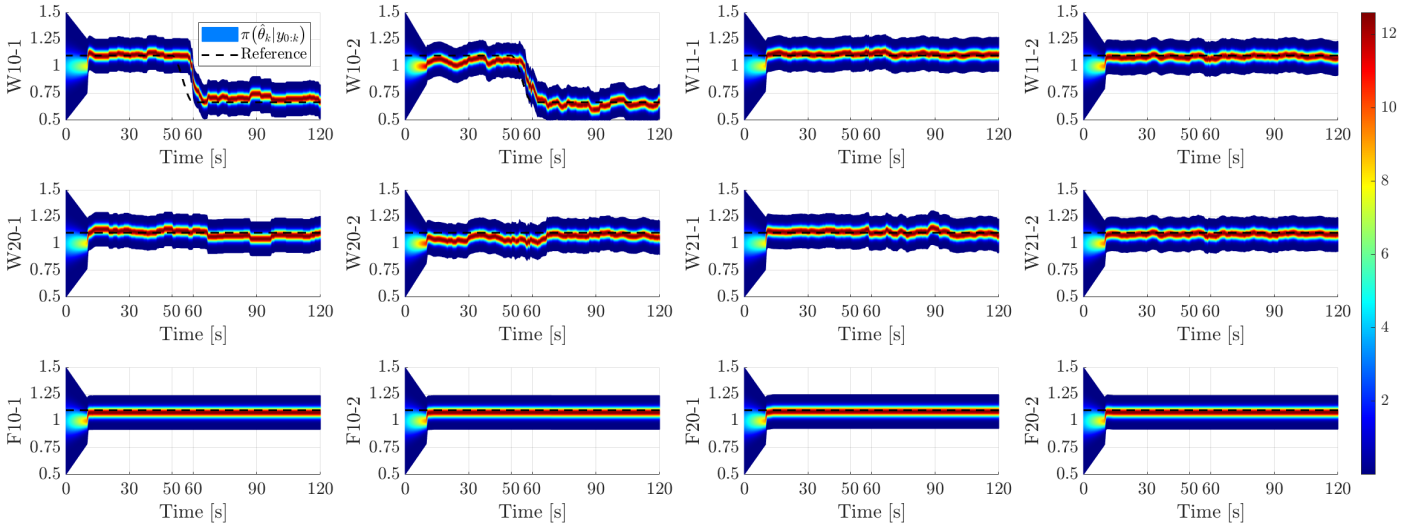

FIGURE 4.21: Clustered MDKF results of the frame model from noisy measurements ($\delta = 2\%$). Pdfs are plotted for each of the $N_\theta = 12$ parameters with expected values.

4.5 Online modal signature monitoring of the SMART2013 specimen from acceleration measurements

4.5.1 Procedure for the online correction of SMART2013 FE model

To assess the applicability of MDKF to process actual measurements, we propose in this second application to process the SMART2013 acceleration database to update a FE model of the tested specimen. Complete information about the SMART2013 test campaign is given in Appendix A.2. As a reminder, a trapezoidal three-story RC specimen was subjected to a test sequence built as an alternation of bi-axial gradually damaging seismic inputs and of random ground motions with low acceleration level chosen such that the first eigenmodes of the experimental system are excited but without adding further damage to the RC specimen.

The non-damaging low-PGA tests allow to iteratively adapt the linear control laws according to the observed eigenfrequency drop. However, when the specimen response becomes strongly nonlinear (due to damage) within a seismic test, the control strategy fails to keep the input

stable: it has been the case for run #13 where the test end became unstable after important damage occured at the bottom of the specimen (see Fig. 5.1). To avoid such issues, the control strategy must integrate a tool allowing for online modal signature monitoring.

In Chapter 1, the SMART2013 database has already been considered to successfully perform offline mCRE-based model updating for eigenfrequency tracking. The objective herein is to extend these results so as to **perform online modal signature tracking in real-time from actual acceleration measurements**.

If two FE models have been developed to reproduce the SMART2013 specimen response, attention will be exclusively given to the model 1 of Fig. A.4 developed by S. Cherubini in [Richard et al. 2016] because it has shown slightly better results for offline model updating in Chapter 1.

> *Remark* 4.14. One should first notice that classical KFs fail at properly tracking eigenfrequencies: we applied a classical UKF algorithm with the above-described FE model projected on a truncated modal basis made of the first 100 eigenmodes of the cantilevered specimen (in order to be competitive enough in terms of CPU time). Unfortunately, despite all attempts to calibrate covariance matrices properly, the algorithm systematically diverged (negative stiffness parameter estimates). This can be explained by the fact that the model to update is too stiff to properly describe the observed state of the structure (see Tab. 1.5). Note that this is consistent with the inaccurate results provided by total least-squares minimizations in an offline model updating context.
>
> Contrary to classical KFs, mechanical fields are not explicitly integrated in the MDKF as only the mCRE gradient value is exploited in the correction step of the algorithm. This makes MDKF still relevant in cases where classical KFs fail at identifying parameters due to strong model discrepancies, as illustrated in the following.

In order to assess the relevance of the proposed methodology in this context, the MDKF algorithm is carried out on the complete SMART2013 database and post-processing CPU-time inspection shall allow us to conclude on the suitability of the approach for further online applications. Practically:

- ▷ a precalibration test (based on run #6 data) allows to estimate relevant values for mCRE tuning parameters $\alpha = 10^{-2}$ and $z(\omega)$. As for the previous case, covariance error matrices are set to $\boldsymbol{Q}_\theta = 10^{-4}\boldsymbol{I}, \boldsymbol{R} = 10^{-8}$.
- ▷ the measurements of all runs are gathered into a single data block, meaning the campaign from run #6 to #24 is processed at once. The frequency weighting function is updated after each low-PGA input block as new ergodic data is available to compute $z(\omega)$ with data-based H-CMIF as explained in Section 1.4.2.
- ▷ once parameter statistics $\{\widehat{\theta}_k, \boldsymbol{P}_k^\theta\}$ are provided, a low-cost post-processing step consists in propagating parameters uncertainties to relevant QoI, namely the first three(participating) eigenfrequencies. The suitability of MDKF for adaptive control law design can then be judged from eigenfrequencies mean values and associated credible intervals. Of course, the question of the definition of the FE model parametrization is a problem on its own that also directly impacts the performance of the algorithm. This point has already been addressed in Section 1.5.4.

4.5.2 MDKF-based eigenfrequency monitoring in real-time - results and discussion

Data assimilation results obtained after processing the complete SMART2013 database are given in Fig. 4.22 - 4.23 - 4.24. Several remarks can be made regarding:

▷ **MDKF suitability for DDDAS and adaptive control law design**

Using the dedicated strategies for enhanced numerical performance explained in Section 4.3 allows to process data faster than they are assimilated as 0.5 s-overlapped data windows are assimilated in less than 0.3 s on a personal laptop. Here again, the computational burden carried by the numerous calls to mCRE is considerably reduced, and real-time assimilation is achieved as shown in Tab. 4.6.

MDKF step	**CPU time** [s]
Frequency domain preprocessing of loading and measurements	0.028076
Parameter prediction	0.000348
Computing σ-points	0.000497
Propagating σ-points through the state-update	0.002044
Transforming the σ-points through the mCRE observer	0.366661
Computing Kalman gain and a posteriori estimates	0.002682
Total	0.400380

TABLE 4.6: Average CPU time required per iteration by MDKF during the assimilation of SMART2013 run #7 database. About 0.6 s remains for additional post-processing before assimilating new data.

Beyond the possibility to track the evolution of eigenfrequencies in real-time, the **MDKF is able to process strongly nonlinear runs, where *a posteriori* model updating methods are unable to provide any result without data preprocessing** (see the focus on the run #13 in Fig. 4.24). The information provided by MDKF could then be valuable for avoiding unstable experiments in a DDDAS framework, as illustrated in the last chapter of this thesis.

Finally, let us remark that the call for reduced basis when computing the mCRE permits an important computational speed-up, whatever the initial complexity of the FE model to update. This feature suggests that MDKF (and mCRE in general) could be applied to a wide range of online model updating problems.

▷ **The applicability of MDKF to online structural monitoring**

The proposed data assimilation algorithm is able to update the general stiffness parameter of a linear FE model in order to track the structural state of a specimen subjected to complex nonlinear phenomena. The new MDKF algorithm has been able to assimilate data in real-time (regarding CPU-time, according to the above definition) and provided parameter estimates that allow (after post-processing) to observe the eigenfrequency drop that was reported after the experimental campaign [Richard et al. 2016]. In particular, two stages in the test campaign where the modal signature remains globally constant have been well recovered: runs #6 to #12 (phase 1: SMART2008 inputs), and #20 to #24 (phase 3: after-shock analysis).

Besides, the similarities between MDKF estimates and (i) former results from stochastic subspace identification [Charbonnel 2021] and (ii) former mCRE-based model updating confirm the relevance of parameter estimates provided by MDKF in Fig. 4.22-4.23.

Unfortunately for the SMART2013 case, even if a large number of sensors are scattered over the specimen (48 data acquisitions channels), the experimental information they bring is not rich enough to locally quantify the damage state of the specimen, which is a critical issue for SHM perspectives. Although the processed database can be considered rich, the initial gap between the updated model and the highly-noisy ($\delta > 20\%$) data collected from the experimental campaign does not allow us to perform realistic SHM (with

localized damage detection). However, please note that, even when performing offline mCRE-based and least-square-based model updating from the SMART2013 database, we have not been able to identify more than one global stiffness parameter. Therefore, it should be pointed out that the SMART2013 database itself seems hardly exploitable for damage detection problems and SHM, which cannot allow us to draw proper conclusions about the applicability of MDKF for SHM in this specific context.

▷ **The intrinsic quality of the updated model**

Here, contrary to the plane frame problem where $N_\theta = 6$ parameters were updated at once, the FE model has only been parametrized with one global stiffness parameter. Although this simplistic parametrization choice is enough for control prospects, it is certain that the corrections of the FE stiffness matrix proposed herein may lack of relevance for local damage detection purposes. Let us recall that the noise level always exceeds 20% (see Tab. A.1), which makes the identification of stiffness parameters tough. The same issue has been raised in Chapter 1 when performing offline model updating from the SMART2013 database using mCRE and total least-square functionals. If measurements were less noisy and more dense at the bottom of the specimen (which has been shown to be the more sensitive area for stiffness parameters of cantilevered structures), it is likely that more parameters would have been identified, whether in offline or online model updating contexts.

Regarding the SMART2013 FE model itself, the anchorage boundary conditions that fully cantilever the specimen to the shaking table should be questioned. Indeed, an overestimation of the anchorage stiffness (due to the combination of integrated shell elements and volumic elements at the soleplate level) may lead to a globally too rigid FE model.

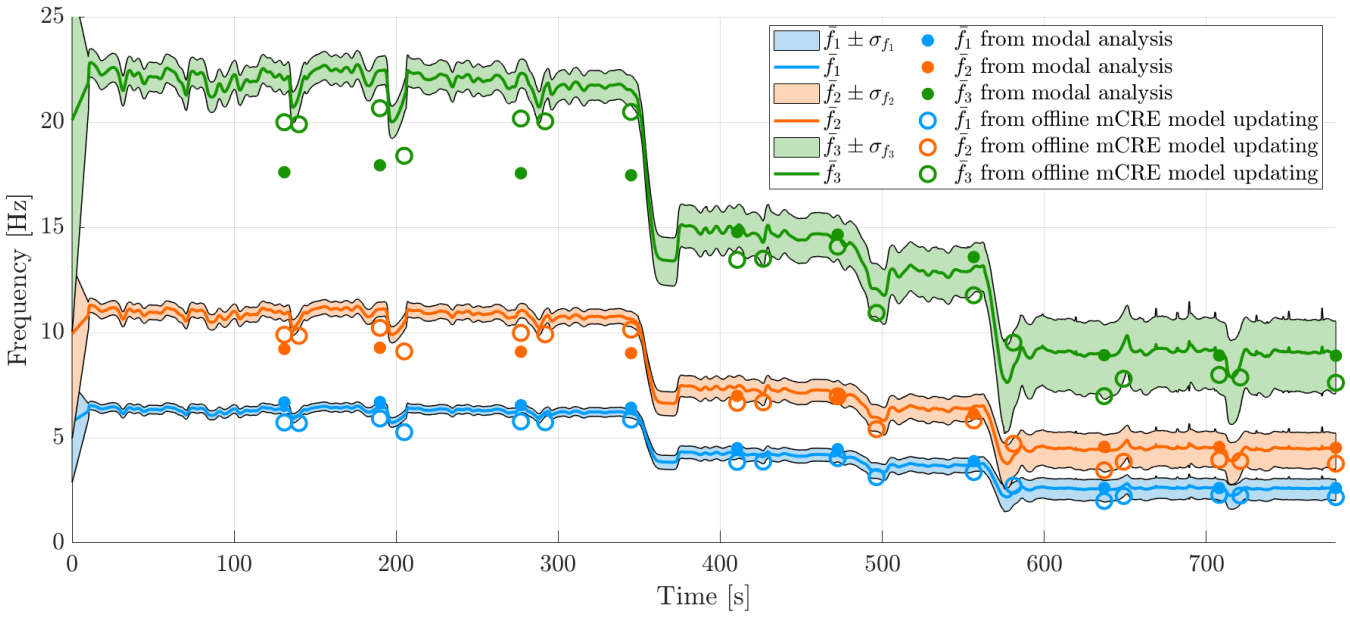

FIGURE 4.22: SMART2013 - Tracking of the three first eigenfrequencies using MDKF. Mean and credible intervals are given, as well as former identification results using SSI techniques (in colored bullets) and offline mCRE-based model updating (in colored circles).

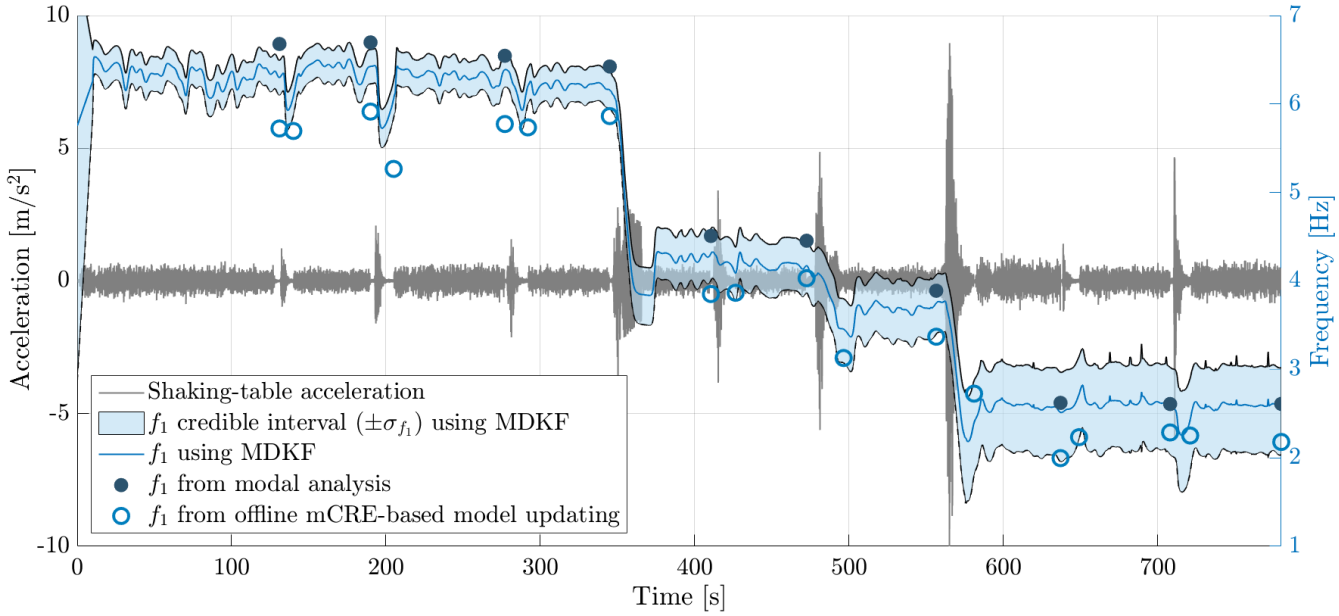

FIGURE 4.23: SMART2013 - Focus on the first eigenfrequency identified by MDKF. The shaking table acceleration recordings in x-direction are given to relate inputs with structural evolution.

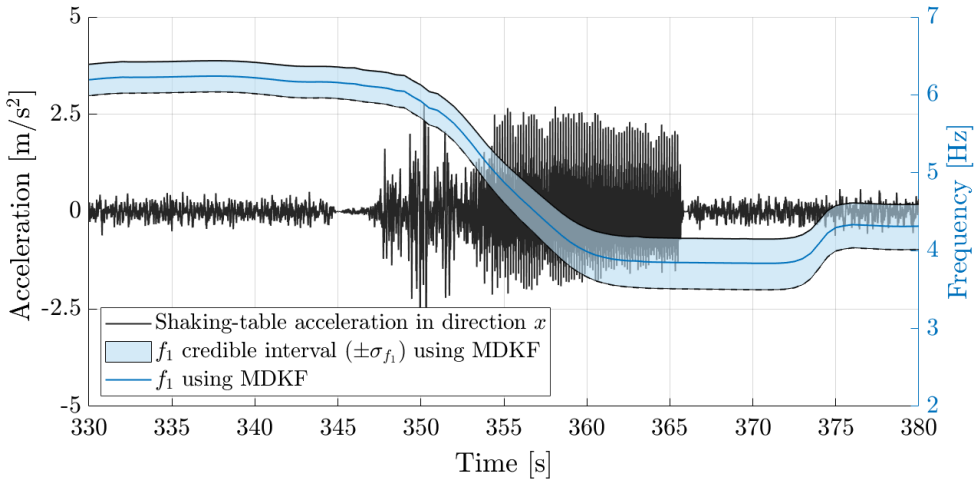

FIGURE 4.24: SMART2013 - Focus on run #13. Although the shaking table device becomes unstable, MDKF still identifies damage occurence and updates eigenfrequencies adequately.

4.6 Conclusion & prospects for future use of MDKF for SHM applications

In this chapter, after a bibliography review of most common data assimilation techniques, a new sequential method, deriving from a KF framework and using the mCRE as an alternative metrics for observations, has been presented with several improvements for its numerical performance. This new online model updating algorithm, called Modified Dual Kalman Filter (MDKF), combines dual KF and mCRE advantages as it proposes a **sequential data assimilation with enhanced robustness with respect to measurement noise**.

Although intuitively constraining at the first sight because of the mCRE definition in the frequency domain, the MDKF has shown **relevant performance from synthetic and actual measurements, both in terms of accuracy and CPU time**. Indeed, the comparison with classical UKF on an academic plane frame example illustrated the relevance of the MDKF which is able to perform accurate and robust identification of stiffness properties in real-time, whatever the complexity of the FE model under study. This academic case study was also the opportunity to

fairly compare possible variants of MDKF according to the KF structure in which the mCRE functional is embedded, with the conclusion that the S3F-based MDKF is the best compromise between computational cost and estimation accuracy. A proof-of-concept for the clustered MDKF extension was also presented, in which a sequential partial state-update was performed according to the model error distribution.

Then, the complete processing of the SMART2013 database highlighted (i) the ability of the MDKF for online eigenfrequency tracking and (ii) the robustness of the algorithm to update a linear FE model from sparse data involving many nonlinear phenomena. General guidelines were also provided regarding the calibration of MDKF internal tuning parameters in order to avoid conditioning the performance of the method to an expert-user's judgment. Even though a full automation of the MDKF algorithm is not obtained yet (and is currently investigated), the positive results obtained herein show the potential of this new sequential data assimilation algorithm. Contrary to the offline mCRE-based model updating case, **the possibility to monitor in real-time the modal signature of the specimen on-the-fly during (nonlinear) seismic tests is a significant improvement compared to the modal analysis tools that are classically deployed in shaking table test campaigns**.

Let us lastly recall that the applicability of MDKF for SHM has not been properly illustrated throughout the SMART2013 example as only one global stiffness parameter has been updated in this application[4]. However, we hope that forthcoming test campaigns at the CEA/TAMARIS facility will allow to validate this statement. Besides, although we will not go into further details regarding the clustered MDKF extension, the latter would be particularly relevant when considering rich/full-field measurements and damage detection problems such as the ones that can occur in SHM applications to achieve real-time monitoring constraints.

In the next chapter, MDKF will be reinvested to perform adaptive model-based control of shaking tables, following the ambition of the thesis work (see Fig. 2).

[4]According to the classical 3 damage detection levels for SHM [Worden et al. 2007], only level 1 "damage detection" has been achieved in this application. Levels 2 "damage localization" and 3 "damage quantification" have not been reached.

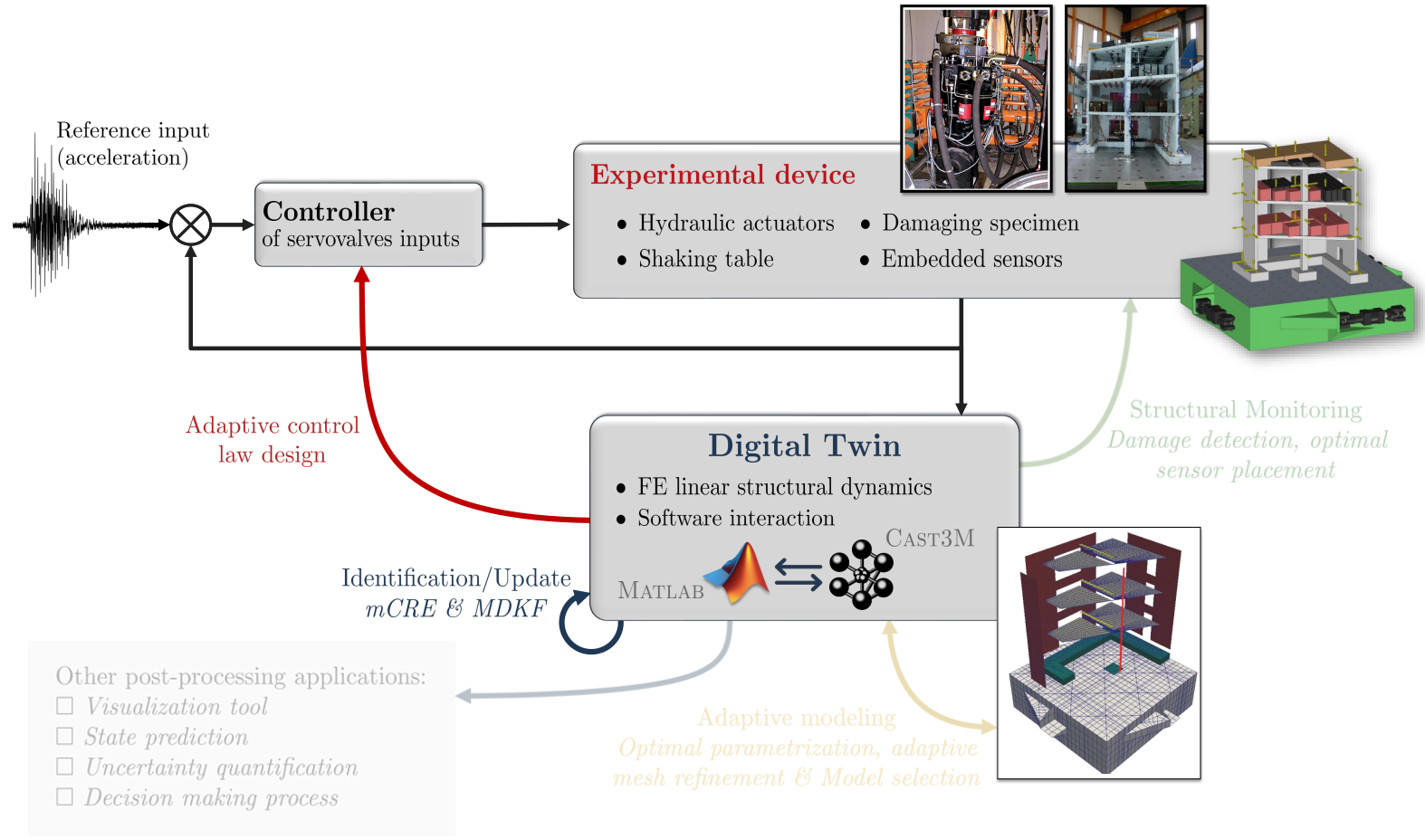

Application to the improvement of shaking table experiments

Who controls the past controls the future.
Who controls the present controls the past.

George Orwell, *1984*

Chapter 5

Towards real-time adaptive control of shaking table experiments

A first proof-of-concept for mCRE-based DDDAS

Shaking table experiments can be performed to assess the response of (damaging) structures subjected to ground motion loading. The performance of such tests is assessed in terms of acceleration (and displacement) replication. However, due to the numerous nonlinearities of the system underlying physics, and due to the fact that the tested specimen properties may vary with time, the control of the hydraulic actuators that are connected to shaking tables may lack of robustness, leading to suddenly unstable experiments.

In this last chapter, the main nonlinearities that disrupt the control of shaking table tests are first presented, alongside with classical control strategies that are commonly used in the field. In light of the recent data assimilation and model updating tools based on the modified Constitutive Relation Error, an exploratory study is performed, in which classical control tools are enhanced using the Modified Dual Kalman Filter, whose formulation and relevance have been previously highlighted. Although no mathematical proof guarantees the stability of such controlled systems, the simulation results that have been obtained on a simple, yet representative, example suggest that the use of a digital twin updated in real-time may contribute to enhance the stability of shaking table experiments, although much work remains to be done before considering an application to actual experimental devices.

Acknowledgements:

A part of this work has been obtained in collaboration with Daniel Martin-Xavier during his M1 research internship at the LMPS under the supervision of Corinne Rouby, Ludovic Chamoin, Pierre-Étienne Charbonnel, and myself. Daniel is deepfully thanked for his work that helped shaping this chapter in its current form.

As I have been quickly introduced to the field of control theory (which was not the main topic of this thesis work), I also particularly thank Alain Le Maoult and Mathieu Grossard for the rich discussions and numerous advices that allowed to set up the proof-of-concept presented in this chapter.

Contents

5.1 Earthquake engineering context

5.1.1 Shaking tables, context of use and limitations

The main objective of a shaking table device is the high-fidelity reproduction of acceleration (and displacement) time histories such as earthquake accelerograms. However, reproducing a dynamic signal is known to remain a difficult task [Hwang et al. 1987]. As emphasized in [Le Maoult et al. 2010; 2012; Charbonnel 2021], the control of the hydraulic actuators that drive shaking tables is still a challenging task, especially because the performance requirements in terms of accuracy are more and more demanding.

Among the inherent difficulties that exist when trying to control hydraulic actuators during shaking table tests, the interaction between the tested specimen and the table is of major importance [Blondet and Esparza 1988]: the modal signature of the tested specimen can suddenly change during experiments due to damage occurence [Charbonnel 2021]. As the modal signature is one of the key feature for control law design, an initially well-calibrated control strategycan become totally inappropriate, leading to unstable experiments[1]. It has been the case during the SMART2013 run #13, which was manually stopped in emergency by operators (see Fig. 5.1).

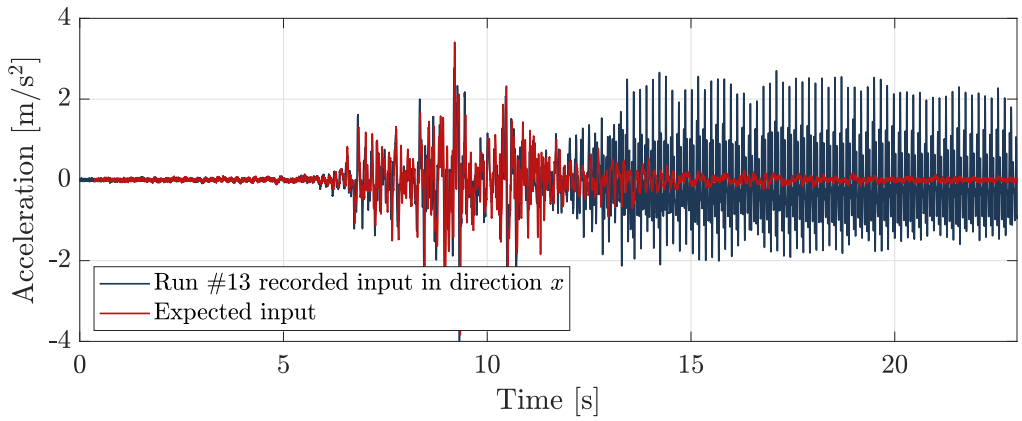

FIGURE 5.1: SMART2013 Run #13 - Shaking table device becoming unstable due to sudden strong damage occurence at the bottom of the specimen.

5.1.2 Objectives and methodology

So far, to take into account the evolving mechanical properties of the specimen, shaking table test campaigns alternate between low-level non damaging random inputs and increasing level seismic inputs (see Fig. 4.23 and A.3). Such a testing approach may pre-damage the healthy specimen before reaching the desired level of loading, even though the random tests permit to incrementally track the modal signature of the specimen using modal analysis tools [Charbonnel 2021]. Besides, although various advanced nonlinear control methods have been proposed for electrohydraulic shaking tables [Plummer 2016; Shen et al. 2016; J. Yao et al. 2016; J. Yao 2018], no clear contribution has been found about on-the-fly adaptive control of shaking table tests taking into account the table/specimen interaction (the specimen is very often considered as a rigid mass). Yet, similar adaptive control algorithms are being developed in the context of real-time hybrid testing [C. E. Silva et al. 2020; Simpson et al. 2020; Abbiati et al. 2021].

The main objective of this work is to explore the possibilities on how MDKF can be advantageously used to enhance shaking table control laws (and as a consequence improve shaking table test campaigns). So far, MDKF has been successfully applied to overall stiffness tracking of structures submitted to random ground motion. The objective of this study thus does not

[1] We refer to the bounded-input/bounded-output (BIBO) stability definition that commonly applies in control theory for linear time-invariant systems.

consist in developing the latest state-of-the-art advanced control design algorithms for shaking tables, but in illustrating **how the information carried by MDKF can be reinvested to design adaptive control laws deemed to improve the stability of shaking table tests**.

Nevertheless, the relevance of the MDKF can only be shown in a representative enough case study. Before considering dedicated control strategies that have been proposed for shaking tables [Merritt 1967; Jelali and Kroll 2003; Plummer 2007], a realistic model of hydraulic actuator is presented. It consists in a linearized state-space model inspired from [Conte and Trombetti 2000], with realistic behavior compared to the one of the CEA/TAMARIS facility. Instabilities due to sudden strong time-varying structural parameters evolutions are highlighted (even with robust control laws), and very similar situations to the ones experimentally observed have been numerically reproduced. Several improvements prospects (of growing intrusiveness) based on the information provided by MDKF are then proposed in order to guarantee (at least) the integrity of the facility by stabilizing shaking table tests in which the specimen undergoes sudden strong damage.

5.2 Modeling of valve-controlled hydraulic systems

If one looks for accurate and predictive models of valve-controlled systems (VCS), an in-depth physics-based description is mandatory in order to include the most relevant dynamic and nonlinear effects that are involved [Merritt 1967; Jelali and Kroll 2003; Plummer 2008; Shen et al. 2011]. To do so, the dynamic behavior of each VCS component must be described. Nonetheless, it is worth mentioning that such complex nonlinear models involve a large number of physical parameters, and some may be unknown or hardly identifiable. Besides, most of models involved in control theory are linearized around the current operating point to exploit the classical Linear Time Invariant control tools that have been developed in the 20$^{\text{th}}$ century. After a brief description of a typical VCS, a linearized model is presented, with all required simplifying assumptions clearly stated. This model will be reinvested in the following sections, and the interested reader is referred to [Jelali and Kroll 2003; Plummer 2008] for extended details.

5.2.1 Description and modeling of hydraulic servo-systems

The main components of a shaking table system are: the table, the hydraulic actuators, the hydraulic power supply (tank, pumps, accumulators) with pipelines, the servo-valves, the control unit and the measurement devices (see Fig. 5.2).

In a nutshell, the (controlled) voltage u_{sv} sent to the servo-valve allows to drive the oil flows (Q_A, Q_B) that are sent to the cylinder chambers. The oil is supplied by a power unit at a constant pressure p_S. The return flow is fed to a tank under the (low) return pressure p_T. The difference of oil flows causes a difference of pressure within the cylinder chambers (p_A, p_B), which thus drives the piston rod motion. It is of paramount importance to notice that a constant servo-valve opening leads to a constant oil flow and differential pressure $p_A - p_B$, which results in a constant velocity imposed for the rod $\dot{x}_t$ (until mechanical stop). This explains the necessity of a pure integrator in the control loop of the rod displacement. The overall shaking table system stands on a reaction mass isolated from the rest of the facility that is recommended to be as stiff as possible to avoid parasitic base motions.

In order to understand the inherent physics of a VCS, the own dynamic behavior of its subcomponents is independently analyzed and modeled [Jelali and Kroll 2003].

Power supply

The behavior of the pump and power supply unit is not critical. Most of the time, the supply pressure is assumed constant. It is a fair assumption in most applications as long as accumulators are placed close to the pumping device and main pipelines to compensate for pressure drops. The pressure supply can be easily controlled in most facilities with dedicated sensors.

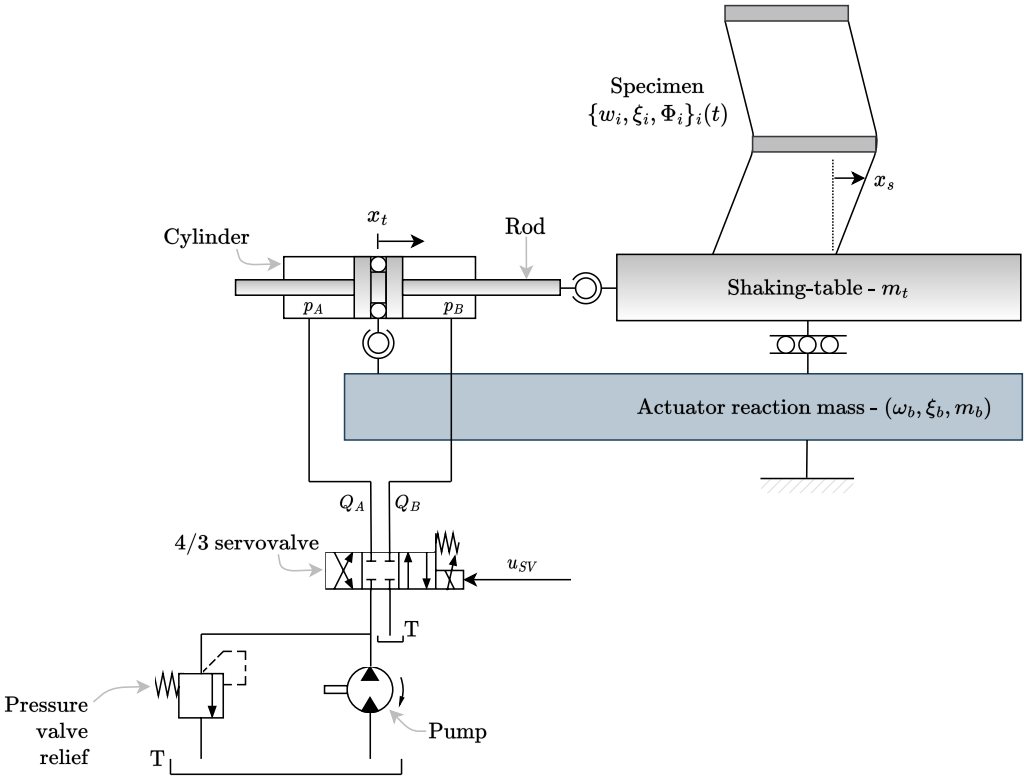

FIGURE 5.2: Uniaxial shaking table powered by a VCS to test a two-story specimen. Control unit and measurement devices are not represented for the sake of clarity. The servo-valve details are also hidden because discussed afterwards.

Pipelines

The main components of a VCS are connected by pipelines. If pipelines are not too long[2], the pipeline volume can be added to the corresponding cylinder chamber, and pipeline dynamics can be neglected. It avoids the modeling of flows using laminar Hagen-Poiseuille equations combined with head losses models as pipes are not fully straight-lined.

Servo-valves

Servo-valves are essential components as they drive the input flows sent to actuators. Unfortunately, their behavior is quite complex to catch accurately, due to several nonlinear phenomena:

- ▷ Dead band related to valve center manufacturing imperfections. The dead band effect occurs around the central position of the spool $x_{sv} = 0$ and its effect depends on the spool geometrical defects (see Fig. 5.3). In the underlapped case, undesirable actuator movements may occur as it is hard to maintain a null differential flow. In the overlapped case, pressure peaks may occur, which may put at risk the integrity of other components. If most commercialized servo-valves are designed to be zero-lapped due to the linear relationship between u_{sv} and the output flow Q, there may remain a residual lapping that disturbs the (assumed linear) valve input-output relationship.
- ▷ The output flow is a square-root function of flow equations spool x_{sv}. For a zero-lapped valves, typical flow-pressure relationships write:

$$Q = c_{sv} x_{sv} \sqrt{\Delta p}\, \mathrm{sign}(\Delta p) \tag{5.1}$$

[2] A rule of thumb involving the effective oil bulk modulus β, the oil density ρ, and the maximal frequency of interest f_{max} allows to estimate the pipeline length l from which flow dynamics cannot be neglected: $l < \frac{1}{10 f_{max}} \sqrt{\frac{\beta}{\rho}}$. With the approximate values for mineral oil properties $\beta = 650$ MPa, $\rho = 850$ kg/m^3 and $f_{max} = 50$ Hz, one has to guarantee that $l < 1.7$ m, which is satisfied at the CEA/TAMARIS facility

where c_{sv}, x_{sv} and Δp respectively refer to the valve constant (also called discharge coefficients), the spool stroke, and the pressure difference between valve orifices.

- ▷ Saturations due to limited spool displacement (mechanical stops) and maximal voltage applicable to the servo-valve.
- ▷ Leakage flow within the valve which impacts the behavior of the latter for small openings.
- ▷ Hysteresis due to friction forces between the spool and the servo-valve body.
- ▷ Flow induced friction forces.

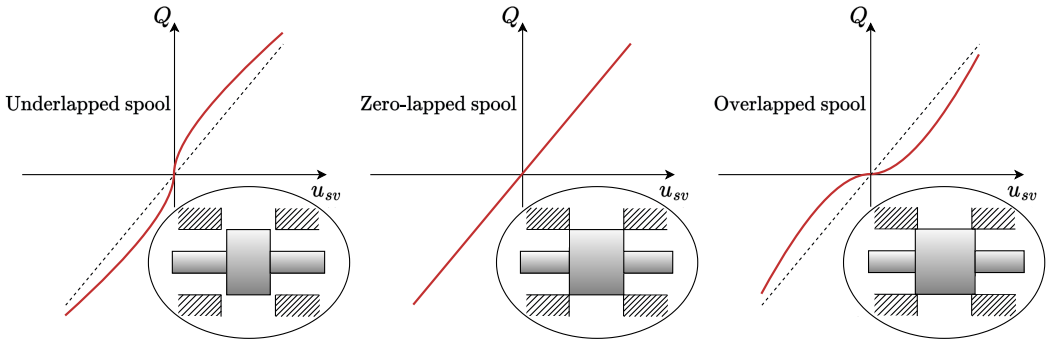

FIGURE 5.3: Dead-band phenomenon and its consequence on the relationship between input voltage and output valve flow.

Moreover, because of their limited flow capacities, multi-stage servo-valves are preferred: they have one or two hydraulic amplification stages that substantially multiply the output flows to drive consequent masses, or to overcome important external forces.

One of the most common servo-valve types used, currently used at the CEA/TAMARIS facility, is the two-stage flapper-nozzle valve (see Fig. 5.4), in which:

(i) the flapper-nozzle system (driven by a low-level voltage) converts the flapper motion into a hydraulically-powered motion of the spool,
(ii) the small spool motions control relatively large oil flows through the spool ports, which acts as an amplifier.

As one can imagine, full physics-based models are too complex to be properly used, particularly because they involve a too important number of uncertain parameters that are hard (or even impossible) to identify. Empirical simplified models can be exploited for control purposes: for instance, single-stage servo-valves are modeled using a 2^{nd} order model whose parameters are provided by manufacturers.

As shown in Fig. 5.4, an inner control loop is present to properly drive the three-stage servo-valve. The main spool displacement is fed back using a LVDT sensor, and a proportional derivative controller allows to stabilize the control of the servo-valve in the frequency range of interest (up to 50 Hz for seismic replication). In practice, the behavior of the inner controlled servo-valve can be drastically simplified: subspace-based identification tests recently performed at the CEA/TAMARIS facility suggest that modeling the controlled servo-valve as a pure gain remains a valid assumption up to about 200 Hz (see Fig. 5.5).

Hydraulic actuator

The actuator is the last component of the servo-system as directly connected to the load. According to [Merritt 1967], an exhaustive mathematical model of hydraulic cylinder must take into account important several effects :

- ▷ The oil compressibility: at the operating temperature, the oil cannot be assumed incompressible, and the fluid inside the chambers acts like a spring, which introduces the so-called *oil column frequency*. The latter drastically limits the perform of hydraulic servo-systems for higher frequencies. Actually, cancelling the undesired effects of the oil column

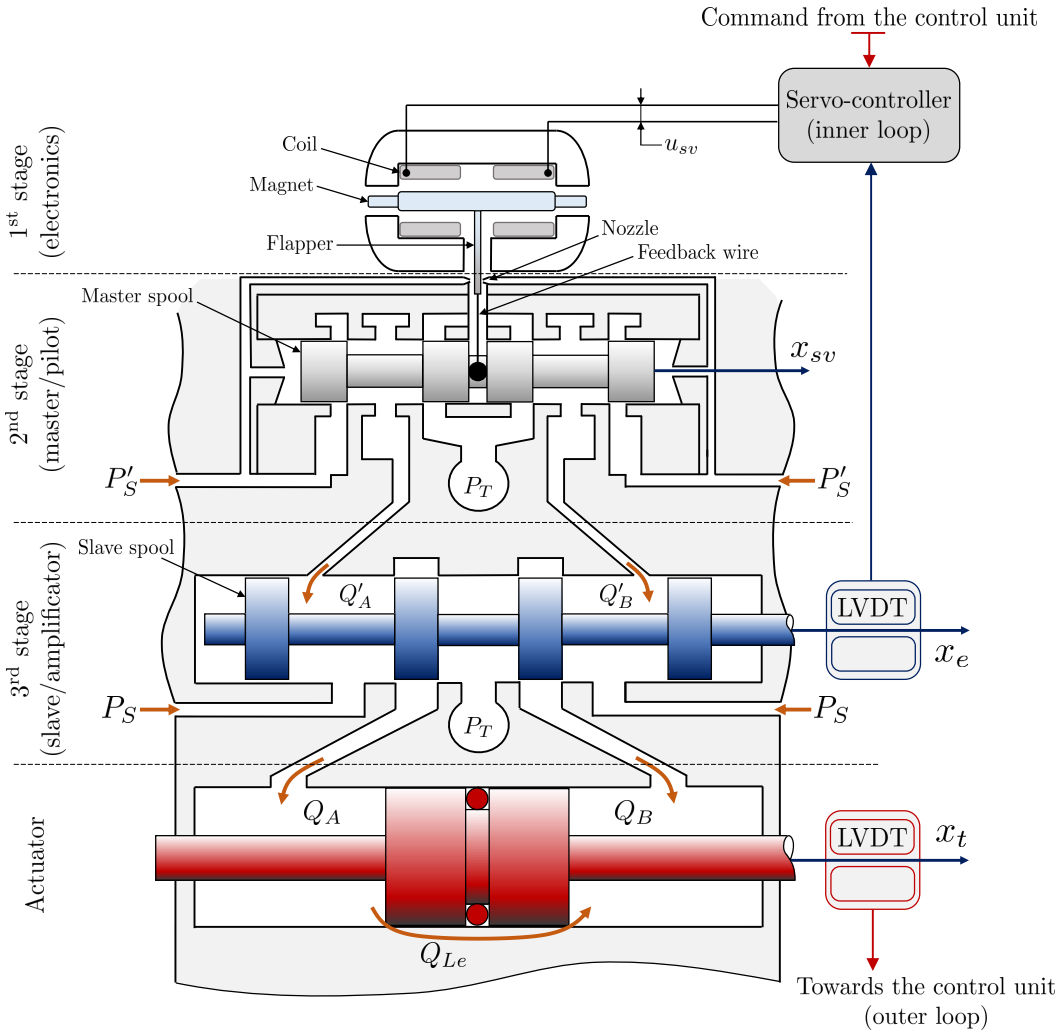

FIGURE 5.4: Scheme of three-stage servo-valve connected to an actuator, with connections to inner and outer control loops.

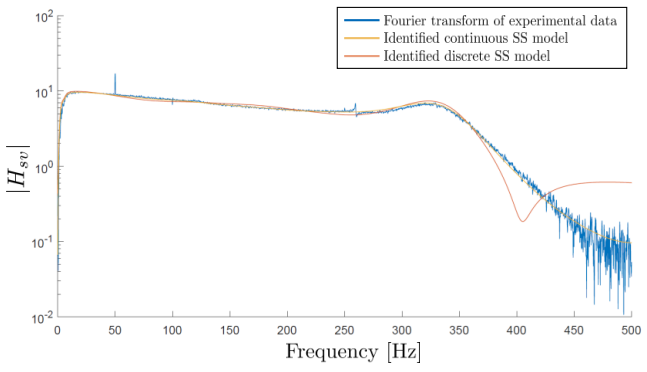

FIGURE 5.5: Identification of the servo-valve inner loop transfer function. A 16th order SS model allows to correctly capture the behavior of the servo-valve up to 350 Hz. A pure gain modeling assumption up to 200 Hz is valid from experimental observations.

frequency is one of the main challenges when designing the outer control loop (see Fig. 5.4) as it occurs within the frequency range of interest for shaking table tests.

- ▷ The dependency of oil bulk modulus and oil density on pressure and temperature.
- ▷ The nonlinear friction forces opposing the piston/rod velocity.

In such a context, the flow continuity leads to the pressure dynamics equations of the cylinder:

$$\begin{cases} Q_A - Q_{Le} = \dot{V}_A + \frac{V_A}{\beta(p_A)}\dot{p}_A \\ Q_B - Q_{Le} = \dot{V}_B + \frac{V_B}{\beta(p_B)}\dot{p}_B \end{cases} \quad \text{with} \quad \begin{cases} V_A = \frac{1}{2}V_0 + x_t A_p \\ V_B = \frac{1}{2}V_0 - x_t A_p \\ Q_{Le} = k_{Le}(p_A - p_B) \end{cases} \tag{5.2}$$

In terms of notations, x_t is the actuator stroke, Q_{Le} the leakage flow between both chambers with k_{Le} the associated leakage coefficient, A_p is the piston section, V_0 is the amount of fluid stacked into the chambers and β the effective oil bulk modulus. As the pressure drives the motion of the piston rod, one can also write the piston motion dynamics equation:

$$m_t\ddot{x}_t + F_f(\dot{x}_t) = (p_A - p_B)A_p - F_{ext} \tag{5.3}$$

where m_t is the sum of the masses from the fluid in the chambers and pipelines, from the piston and from the table. F_{ext} is the reaction force coming from the structure clamped on the table. F_f is the friction model, which is classically defined using the so-called Stribeck friction model:

$$F_f(\dot{x}_t) = \sigma_t\dot{x}_t + \text{ sign}(\dot{x}_t)\left[F_C + F_S\exp\left(-\frac{|\dot{x}_t|}{c_S}\right)\right] \tag{5.4}$$

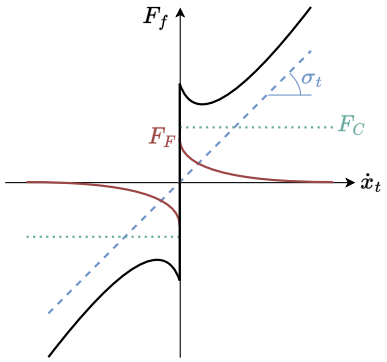

FIGURE 5.6: Stribeck friction force model.

It combines linear viscosity, static and Coulomb friction with dedicated parameters. The typical nonlinear shape of Stribeck friction model is shown in Fig. 5.6. Such strong nonlinearities are ignored in linearized models, but they are responsible for the difficulties to maintain the $(\dot{x}_t = 0)$-command stable: the strong discontinuity makes the cancellation of the steady-state error difficult and causes parasitic motions around a constant piston position [Alleyne and R. Liu 1999; Alleyne and R. Liu 2000; Le Maoult et al. 2010].

5.2.2 Towards a linearized shaking table model

Eventually, the dynamical properties of the valve-controlled system may be significantly changed once the actuator is connected to a compliant structure (which is the case during shaking table tests), as suggested by the F_{ext} term in the piston motion dynamics. Therefore, the (nonlinear) behavior of the specimen that is tested should also be included into the set of governing equations (*i.e.* from the servo-valve input voltage to the structural response). In a very general manner [Geradin and Rixen 2015], the response of a nonlinear structure (in a FE sense) submitted to a ground motion loading reads:

$$\boldsymbol{M}\ddot{x}_s + f_s(\dot{x}_s, x_s) = -\boldsymbol{M}\ddot{x}_t \tag{5.5}$$

where f_s describes the nonlinear internal forces. In the linear case, one has $f_s = \boldsymbol{D}\dot{x}_s + \boldsymbol{K}x_s$.

The nonlinear shaking table device model governed by (5.1) to (5.5) is yet representative of many underlying nonlinear phenomena, but too computationally expensive to be used in for real-time applications, and it is also inadequate in the perspective of being accomodated with classical control strategies, which are mostly based on linear(ized) models. In the following, we propose to derive the linearized shaking table model proposed by [Conte and Trombetti 2000]. The main equations of the model (with assumptions) are briefly recalled below, but one should particularly note that all the control issues due to nonlinear phenomena will not be observable using this linear model. The disturbance rejection capabilities of the model will assess whether the control strategy is able to efficiently cancel the effects of valve lapping and Stribeck friction in the frequency range of interest.

The mandatory assumptions to justify the linear model given by [Conte and Trombetti 2000] are listed below:

- ▷ As the servo-valve can be driven much more accurately than the remainder of the shaking table system (actuator, outer control loop, reaction mass), the effect of the inner control loop is usually neglected in the overall modeling. Therefore, the oil flow rate sent to the actuator can be modeled as a linear function of the servo-valve input voltage.
- ▷ The base (reaction mass) on which stands the shaking table is assumed infinitely stiff.
- ▷ The pipeline dynamics is neglected in the frequency range of interest.
- ▷ The fluid leakage through the actuator seals is assumed proportional to the pressure in the cylinder chambers.
- ▷ The friction forces in the actuator are neglected compared to the other forces at stake (reaction force from the structure in particular).
- ▷ The oil is assumed compressible, and its mass is neglected with respect to the masses of piston, table and structure. Its temperature is assumed constant, and the bulk modulus dependency into pressure and temperature is neglected as well.
- ▷ The specimen response is assumed to remain linear and modeled as a single DoF (SDoF) system with modal properties associated to its first eigenfrequency (strong assumption and inconsistent with damage occurence that will be all).

The associated system of (linear) equations in the time domain reads:

$$\begin{cases} Q_{sv}(t) = k_{sv} u_{sv}(t) \\ Q_{sv}(t) = Q_{Le}(t) + A_p \dot{x}_t + \dfrac{V_0}{4\beta A_p} \dot{F}_a \\ Q_{Le}(t) = k_{Le} \dfrac{F_a(t)}{A_p} \\ F_a(t) = (m_t + m_s)\ddot{x}_t + m_s \ddot{x}_s \\ \ddot{x}_s + 2\xi_s \omega_s \dot{x}_s + \omega^2 x_s(t) = -\ddot{x}_t \end{cases} \tag{5.6}$$

In terms of notations, x_d refers to the desired shaking table displacement, k_{sv} is the servo-valve gain, q_{sv} is the oil flow rate sent from the servo-valve to the actuator, F_a is the actuator force, k_{Le} is the leakage coefficient, and (ω_s, ξ_s) denote the eigenproperties (angular frequency and damping ratio) of the structure seen as a SDoF system[3]. An associated state-space representation is:

$$\dot{x} = \boldsymbol{A}x + \boldsymbol{B}u_{sv}$$
$$\text{with } x = \begin{bmatrix} x_t & \dot{x}_t & F_a & x_s & \dot{x}_s \end{bmatrix}^T$$

$$\boldsymbol{A} = \begin{bmatrix} 0 & 1 & 0 & 0 & 0 \\ 0 & 0 & \frac{1}{m_t} & \omega_s^2 \frac{m_s}{m_t} & 2\xi_s\omega_s \frac{m_s}{m_t} \\ 0 & -\frac{4\beta A_p^2}{V_0} & -\frac{4\beta A_p}{V_0} k_{Le} & 0 & 0 \\ 0 & 0 & 0 & 0 & 1 \\ 0 & 0 & -\frac{1}{m_t} & -\omega_s^2 \left(1 + \frac{m_s}{m_t}\right) & -2\xi_s\omega_s \left(1 + \frac{m_s}{m_t}\right) \end{bmatrix}, \quad \boldsymbol{B} = \begin{bmatrix} 0 \\ 0 \\ \frac{4\beta A_p}{V} k_{sv} \\ 0 \\ 0 \end{bmatrix} \tag{5.7}$$

One can directly notice that $\boldsymbol{A}$ is not a full rank matrix as the first column is null, due to the fact that a hydraulic actuator is flow-based. Therefore, a zero-pole naturally appears in the equivalent transfer function of (5.7) as the actuator stroke is not directly controlled. An equivalent block-scheme written in the Laplace domain of (5.6) is given in Fig. 5.7. The associated frequency response function for the parameter set given in Tab. 5.1 is shown in Fig. 5.8. The influence of the specimen dynamics is emphasized, especially (i) on the impact on the oil column frequency (at around 35 Hz in that case) and (ii) on the effect of low-damping around the specimen eigenfrequency. It thus seems that the outer-loop control law sensitivity with respect to the specimen modal parameters is not neglictible, which can (partially) justify the control issues that appeared with sudden damage occurences.

[3] If the structure is modeled as a multi-DoF system, the last equation becomes a matrix system $\Phi_n^T \boldsymbol{M}_s \Phi_n \ddot{q}_{s,n} + \Phi_n^T \boldsymbol{D}_s \Phi_n \dot{q}_{s,n} + \Phi_n^T \boldsymbol{K}_s \Phi_n q_{s,n} = \Phi_n^T M_s \ddot{x}_t$, with $x_s(t) = \sum_{n=1}^{L} \Phi_n q_n(t)$ for all modes Φ_n stored in $\boldsymbol{\Phi}_L$.

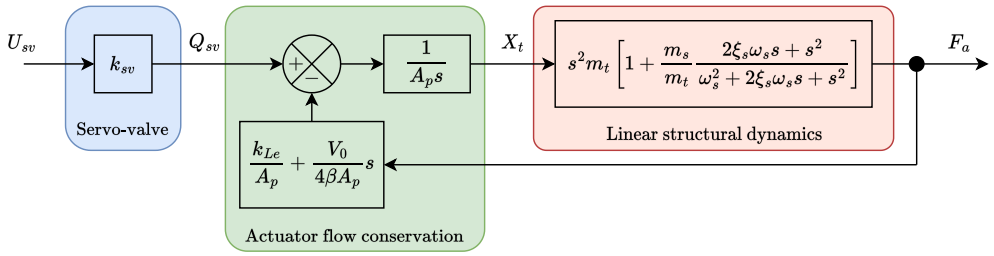

FIGURE 5.7: Block-scheme of the linearized shaking table model, with emphasis on components contributions and couplings (s is the Laplace variable).

Parameters	Reference value		
Servo-valve gain	k_{sv}	=	5400.10^{-6} m^3/V/s
Piston effective section	A_p	=	40.10^{-4} m^2
Volume of oil column in the actuator	V	=	1700.10^{-6} m^3
Oil bulk modulus	β	=	675.10^6 Pa
Valve leakage coefficient	k_{Le}	=	$2.5.10^{-19}$ m^3/Pa/s
Mass of the table	m_t	=	500 kg
Mass of the specimen	m_s	=	1000 kg
Eigenfrequency of the specimen	$\omega_s/(2\pi)$	=	5 Hz
Damping ratio of the specimen	ξ_s	=	0.05 [-]

TABLE 5.1: Reference setting parameters of the shaking table device, considering a SDoF specimen clamped on the table.

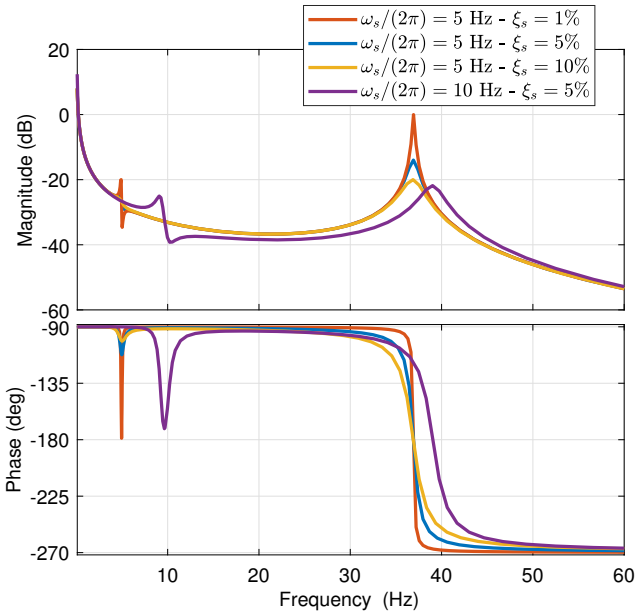

FIGURE 5.8: Bode plot of the shaking table system linearized transfer function (given in Fig. 5.7), with emphasis on the impact of the specimen modal properties on the frequency response X_t/U_{sv}.

Lastly, to remain consistent with practical applications, the full state X is not observed. The measurements Y are the only available knowledge that the user has access to for the design of control strategies in practice. It is a common practice to measure the pression difference between chambers Δp, the position and the acceleration of the piston $(x_t, \ddot{x}_t)$, and the position and the acceleration of the specimen $(x_s, \ddot{x}_s)$.

5.2.3 Concluding remarks on the modeling of shaking table devices

VCSs are complex systems that necessitate advanced knowledge in thermics, structural mechanics, and fluid mechanics to get an exhaustive physics-based description. Because the internal parameters in such complex models are sometimes unknown or hardly identifiable in an accurate manner, more or less complex models have been derived according to the user requirements. In this section, we mentioned many nonlinear phenomena that are influent but that are (fairly) neglected in order to get an appropriate model for control purposes. Therefore, although the VCS model used in the remainder of this study is imperfect, **it is worth having a model built from degraded physics as long as it is exploitable and identifiable**. The knowledge of the model errors can allow the user to select appropriate control laws, in particular ones that can efficiently reject disturbances associated to neglected phenomena. As a remark, having access to an erroneous model (even if not identifiable) can at least be used to evidence sensitivity or inconsistent behavior.

5.3 Review of classical shaking table control strategies

Now that the main phenomena involved in electrohydraulic shaking tables have been described, control strategies can be presented in accordance. The objective of this section is to start from control basics [Mullhaupt 2017; Preumont 2018] before introducing the key ideas hidden behind advanced control strategies such as the ones presented in [J. Yao et al. 2014; Shen et al. 2016; J. Yao et al. 2016]. The reader should keep in mind that the main target here is the control of VCSs, which implies that not all the control strategies of the literature will be mentioned (*e.g.* fuzzy control or control based on Neural Networks that are getting popular for robotics applications).

Although a closed-loop on the actuator rod displacement is the most intuitive approach for shaking tables, **the acceleration transmitted to the table is the main quantity of interest**. Indeed, the resistance of equipments to seism is often quantified in terms of pseudo-spectral acceleration[4], and a correct displacement tracking performance does not guarantee relevant acceleration replication. The main challenges shaking table control laws must address deal with:

- ▷ the compensation of the oil column resonance within the frequency range of interest. It is a hard task due to the low damping and time-varying properties of the specimen. If not taken into account, situations like the one of Fig. 5.1 may happen;
- ▷ the rejection of the servo-system nonlinearities, in particular the Stribeck friction and the valve spool lapping. They are responsible for the so-called stick-slip instabilities at close-to-zero actuator velocity setpoint;
- ▷ the robustness to modeling errors: if the estimator that intends to predict the response of the system is not accurate, associated control laws may be inadequate. This is one major issue when performing inverse model control, as discussed further. A typical example is the spillover instability [Preumont 2018], which appears when the contribution of residual high-frequency modes is not neglictible but not taken into account by the model;
- ▷ the parasitic motions of multi-axis shaking tables when trying to replicate 3D ground motions. A minimal cross-coupling between each actuator must be achieved so as to avoid parasitic interferences [Plummer 2008; 2016]. This is typically the case for the AZALEE shaking table, in which at least 2 actuators are involved per loading direction.

[4]The pseudo-spectral acceleration is constructed by varying the frequency of a 1-DoF oscillator and plotting this frequency on the x-axis and the temporal maximum of the response to a seismic load on the y-axis. This provides a pseudo-acceleration response spectrum for a fixed damping.
They are widely used in earthquake engineering because, at a first approximation, structures can be assimilated to oscillators whose natural frequencies and damping are approximately known.
For example the French authority of nuclear safety norm RFS 2001-1 or the NF EN 60068-2-57 which specifies the pseudo-spectral acceleration error that is accepted when assessing the seismic risk of nuclear power plant equipments.

Of course, these issues must be handled within the physical bounds of the system performance: (i) the piston mechanical stops limit the range of actuator displacement, (ii) the servovalve voltage saturation impacts the oil flow sent to the actuator and thus the maximum piston velocity, (iii) the acceleration of the table is limited by the piston effective area and by the pressure supply.

> *Remark* 5.1. There is no unified manner to control shaking tables because most of them are not designed in the same manner. One can refer to [Gomez and Stoten 2000] for one of the rare attempts to compare European shaking tables. The CEA/TAMARIS shaking table control strategy is presented in [Le Maoult et al. 2012; Moutoussamy 2013] and is quite close to the one of the E-Defense, the world's largest shaking table [Tagawa and Kajiwara 2007].

5.3.1 Feedback control

If either the output or some part of the output is returned to the input side and used as part of the system input, then it is known as feedback, also referred as closed-loop control. Feedback plays an important role to improve the performance of controlled systems as the information collected by sensors is used to drive the system according to given performance requirements (see Fig. 5.9).

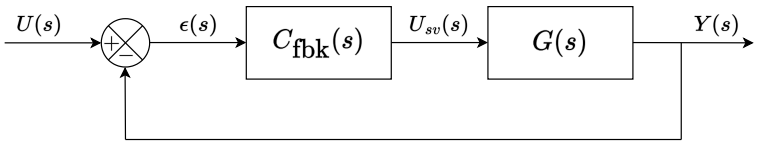

FIGURE 5.9: Feedback control system scheme. s denotes the Laplace variable, G the system transfer function, and C_{fbk} the controller transfer function.

Among the desired features of the closed-loop system are the stability properties, expressed by the gain and phase margins, the transient response characteristics, the frequency bandwidth, the high-frequency attenuation for measurement noise rejection, and the ability to maintain the output at a desired value with minimum static error.

The most standard feedback controller is the *Proportional Integral Derivative controller* (PID) with all its variants (P, PI and PD, lead and lag compensators). In the Laplace domain, the PID transfer function reads:

$$C_{\text{PID}}(s) = K_p + \frac{K_i}{s} + K_d s \tag{5.8}$$

where K_p, K_i, K_d are the three gains that respectively weigh the proportional, integral and derivative actions of the controller. Although neither the most recent nor most complex control approach, PID is still considered for its robustness and simple framework [S. Bhattacharyya 2017]. One of the main challenges when using PID controllers is their calibration: different strategies have been proposed to tune PID gains at best. First tuning approaches were built from empirical observations: the Ziegler and Nichols technique for instance [Ziegler and Nichols 1942]. Since the 1990's, automated tuning techniques have been implemented in commercial softwares[5] [Astrom and Hagglund 1995; Wang and Shao 2000]. More recently, [Kang et al. 2005] even tried to optimize the calibration of PID gains using neural networks.

Another strong limitation lies in the fact that PID are designed for linear time invariant systems, which makes them therefore not well suited for damaging shaking table experiments in which modal properties of the tested specimen may significantly vary with time. An adaptive PID control strategy has been proposed in [Foltin and Sekaj 2006], but it remains an empirical

[5] An example is the `pidtune` function of the MATLAB© control system toolbox.

alternative that can be useful only when it is possible to anticipate for system nonlinearities and associated effects on the control framework.

Regarding the need for both displacement and acceleration tracking performance, note that acceleration feedback can be used alongside displacement feedback, but it cannot be used alone as the displacement of the rod is mechanically constrained. Due to the closeness of pressure and acceleration in actuators dynamics, acceleration feedback is also referred to as pressure feedback in the literature [Jelali and Kroll 2003]. Although theoretically beneficial, it seems there are no clear guidelines given for the calibration of the inner acceleration feedback loop when coupled to displacement feedback.

The interested reader will also find control strategies based on force feedback [Alleyne and R. Liu 1999; Alleyne and R. Liu 2000], which is encouraged by the presence of force sensors in the actuator rod. Force feedback allows to attenuate the structure/actuator interaction by directly providing a measure of the reaction force transmitted by the actuator to the table. Force feedback is often used alongside displacement-based feedback control as multi-axis shaking tables are over-constrained (when having more actuators than kinematic DoFs). Thus, internal force control is used to prevent actuators 'fighting' against each other [Plummer 2008; 2016].

5.3.2 Feedforward control

Feedforward control is classically used in addition to feedback control. It complements the latter and modifies the input signal by anticipation of the open-loop response [Jelali and Kroll 2003]. The major difference with feedback control is that it does not take into account the information carried by measurements. It is thus not subjected to identification delays. In most applications, feedforward controllers integrate an inverse model of the open-loop. Because there is no consideration for the structure response during the test itself and thus no interaction between the system and the feedforward controller, the latter allows (if well calibrated) to control shaking table tests even after the oil column eigenfrequency [Conte and Trombetti 2000; Butterworth et al. 2012]. However, such methods are not robust at all to damage occurence as as they fully ignore the system evolution, which justifies the combined use with feedback control [Le Maoult et al. 2010].

For shaking table experiments, frequency-domain feedforward control is commonly proposed by control industrials (ISTAR, Pulsar ICS,...). A principle scheme is given in Fig. 5.10. The inverse model of the open-loop $\widehat{G}^{-1}$ is computed offline. Several inherent limitations to such control approach must be reported:

- ▷ test campaigns are getting more complex, as it necessitates to update the inverse closed-loop model estimate $\widehat{H}^{-1}$. In particular, it explains why tests campaigns alternate between low level non-damaging tests and seismic tests of increasing intensity [Richard et al. 2016; Charbonnel 2021].
- ▷ The knowledge of the input signal $U(s)$ must be complete before the test has been launched, which is not the case for hybrid experiments [Moutoussamy 2013; Abbiati et al. 2021].
- ▷ The control strategy is more sensitive as any discrepancy between the estimated inverse model with the actual device may turn the controlled device unstable.

Overall, it is worth combining feedback and feedforward control techniques. It is often referred to as 2-DoF control in the literature: a popular example is the 2-DoF PID [Araki and Taguchi 2003], while a generalization of combined feedback and feedforward control is known as three-variable controller (TVC). It encapsulates both acceleration, velocity and displacement feedback, hence its popular use for shaking table control laws [Plummer 2007; Shen et al. 2016]: the fact that TVC explicitely compares measured displacement, velocity and acceleration is appealing for shaking table tests as it may meet both acceleration and displacement requirements. For example, the E-defense shaking table uses a TVC as basic controller [Tagawa and Kajiwara 2007]. The CEA/TAMARIS facility shaking tables are also based on a strategy derived from

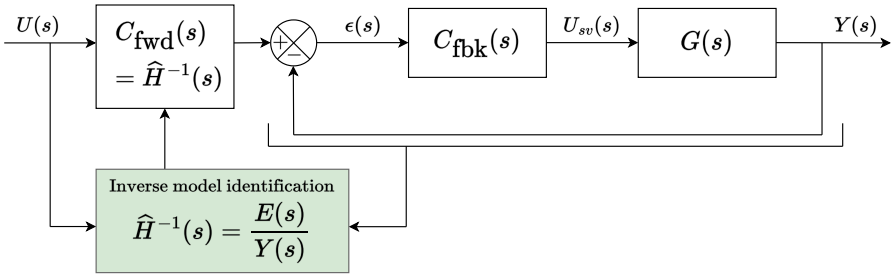

FIGURE 5.10: Feedforward control coupled to feedback control. s denotes the Laplace variable, G the system transfer function, C_{fwd} and C_{fbk} the controller transfer functions.

the TVC [Le Maoult et al. 2012]. A TVC block diagram is shown in Fig. 5.11. It includes a velocity filter, as the latter is very often reconstructed from displacement and acceleration data [Tagawa and Kajiwara 2007]. The reference signal generator block allows to obtain coherent displacement, velocity and acceleration inputs from an initial acceleration input command.

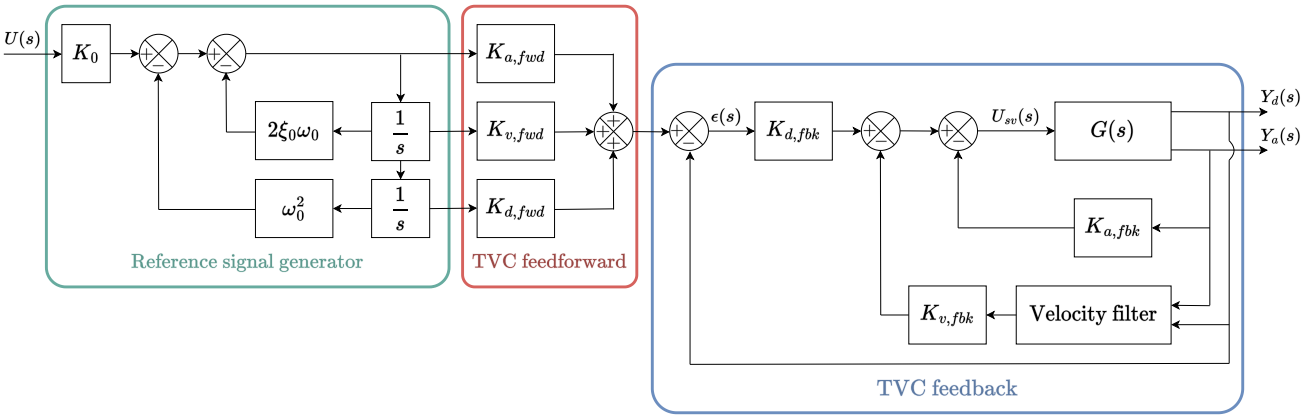

FIGURE 5.11: Three-variable controller - Feedback and feedforward gains are denoted by $\square_{fbk}$ and $\square_{fwd}$, respectively. Measured acceleration Y_a and displacement Y_d are distinguished to fit with practical applications. (K_0, ξ_0, ω_0) are the reference signal generator parameters.

5.3.3 State-space estimation-based control

Since the groundbreaking work of Kalman for state estimation and optimal control, [Kalman 1960; 1964], state-space-based control methods became popular due to (i) their applicability to any problem that can be described by a (linearized) first-order partial differential equation in time, (ii) the natural generalization of transfer function it represents for Multi-Input Multi-Output (MIMO) systems and, (iii) the mathematical proofs associated to the stability and robustness of these methods.

SS-based control aims to position at best the poles of the closed-loop transfer function in the stability area, according to the phase and gain margins that are specified (denoted m_φ and m_δ respectively - see Fig. 5.12). A system remains stable if all its poles are located in the left-half plane of the root locus. Performance requirements are achieved if they are far enough from the $\Re(s) = m_\delta$ border, and inside the cone of angle m_φ that limitates the damping rate of eigenmodes. Another safety margin m_ε is defined: it represents the fact that poles cannot be too strictly chosen to avoid too important demands on the command and saturation phenomena.

There are many control strategies that can be used to obtain the desired pole positions. Among them, Ackermann's formulae [Ackermann 1980] is often used for placing poles at desired locations (as long as the system is controllable) [Y. Xu et al. 2008; Ouyang et al. 2013]. Another very popular approach from the optimal control theory is the *Linear Quadratic* command (LQ), largely discussed in [Preumont 2018] and applied for shaking table tests in [Phillips et al. 2014; Najafi and Spencer 2020] among other contributions. LQ is widely used due to its connec-

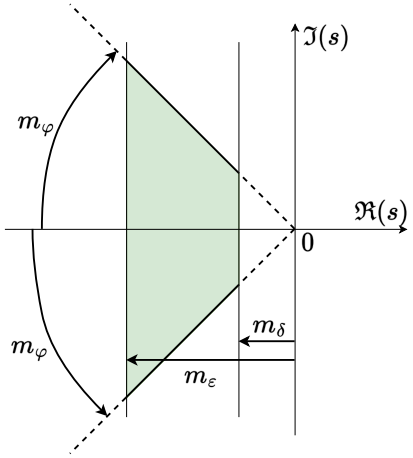

FIGURE 5.12: Emphasis on the *nice stability area* (in green) for pole placement in the root locus. It is defined according to the phase and gain margins denoted m_φ and m_δ.

tions with Kalman filtering [Kalman 1964], and due to the *Linear Quadratic Gaussian* extension (LQG) to take measurement noise and model uncertainty into account.

In cases where the full state vector is not directly accessible (number of measurements lower than the number of state variables), an observer is mandatory for state reconstruction, independently from the control scheme. Ackermann's formula can be reinvested herein to build a *Luenberger* observer. The KF can also be used as it designs an optimal observer in the sense that it minimizes the variance of the state estimate [Kalman 1960]. A comparison between Luenberger observer and EKF has been proposed in [Y. Zhang et al. 2009], with the conclusion that the Luenberger observer is more efficient than EKF for steady-state performance and low speed operation, but lacks of robustness to measurement noise features.

Observability and controllability

All the following mathematical developments and control algorithms are valid only if the system one aims to control is observable and controllable.

Controllability measures the ability of a given actuator configuration to control all the states of the system; conversely, observability measures the ability of a given sensor configuration to supply all the information necessary to estimate all the system states. Classically, control theory offers controllability and observability tests which are based on the rank deficiency of the controllability and observability matrices: the system is controllable if the controllability matrix is full rank, and observable if the observability matrix is full rank.

Considering the linear time invariant system described by the linear SS model of (4.2) with matrices $\boldsymbol{A}$, $\boldsymbol{B}$, $\boldsymbol{C}$, and the state vector x is of size n_x, the controllability matrix $\mathcal{C}$ and the observability matrix $\mathcal{O}$ are defined as:

$$\mathcal{C} = \begin{bmatrix} \boldsymbol{B} & \boldsymbol{AB} & \boldsymbol{A}^2\boldsymbol{B} & \dots & \boldsymbol{A}^{n_x-1}\boldsymbol{B} \end{bmatrix} \; ; \; \mathcal{O} = \begin{bmatrix} \boldsymbol{C}^T & (\boldsymbol{CA})^T & (\boldsymbol{CA}^2)^T & \dots & (\boldsymbol{CA}^{n_x-1})^T \end{bmatrix}^T \tag{5.9}$$

If $\text{rank}(\mathcal{C}) = n_x$, then the pair $(\boldsymbol{A}, \boldsymbol{B})$ is said to be controllable. Similarly, if $\text{rank}(\mathcal{O}) = n_x$, then the pair $(\boldsymbol{A}, \boldsymbol{C})$ is said to be observable. If these conditions are met, then one can write a controlled-observed system under the following form:

$$\begin{cases} \dot{x} = (\boldsymbol{A} - \boldsymbol{BK})x + \boldsymbol{B}u - \boldsymbol{L}(\boldsymbol{C}x - y + v) + w \\ x(t=0) = 0 \end{cases} \tag{5.10}$$

The regulator $\boldsymbol{K}$ directly multiplies the state vector to guarantee the system stability, and the observer $\boldsymbol{L}$ allows to estimate the state from measurements. The dynamics of the system is thus modified by integrating the gap between model predictions and measurements (see Fig. 5.14). Note that the design of the observer and the regulator are mathematically independent (as they are quantified by different pairs of matrices).

Controllability of a 2-DoFs system: a first analytical example to emphasize the table-specimen interaction

To understand how the interaction between the (nonlinear) specimen and the shaking table can disturb the control of the latter, and in order to illustrate the concept of controllability, let us consider a 2-DoFs spring-mass-damper system that represents a shaking table with a structure embedded on it. Its representation and notations are given in Fig. 5.13. As it is the case in practice when actuators apply a force to drive the shaking table, a force is applied to the intermediate mass (which represents the table). A state-space representation of such a problem is given by :

$$\boldsymbol{A} = \begin{bmatrix} 0 & 0 & 1 & 0 \\ 0 & 0 & 0 & 1 \\ -\frac{K_t+K_s}{M_t} & \frac{K_s}{M_t} & -\frac{D_t+D_s}{M_t} & \frac{D_s}{M_t} \\ \frac{K_s}{M_t} & -\frac{K_s}{M_t} & \frac{D_s}{M_t} & -\frac{D_s}{M_t} \end{bmatrix}, \; \boldsymbol{B} = \begin{bmatrix} 0 \\ 0 \\ \frac{1}{M_t} \\ 0 \end{bmatrix}, \; x = \begin{bmatrix} x_t \\ \dot{x}_t \\ x_s \\ \dot{x}_s \end{bmatrix} \tag{5.11}$$

As a reminder, the system is controllable only if the rank of $\mathcal{C}$ is equal to $\dim(X) = 4$. In other words, the controllability of the 2-DoFs spring-mass system can be assessed by calculating the determinant of $\mathcal{C}$. In this particular case, it can be shown that

$$\det \mathcal{C} = -\frac{K_s^2}{M_s^2 M_t^4} \tag{5.12}$$

which illustrates the fact that a sudden drop of the specimen eigenfrequency (that can be directly related to damage or stiffness loss [Cawley and Adams 1979]) can lead to an almost uncontrollable system. Indeed, one can easily imagine that the mass M_s would be harder to control if the stiffness K_s gets closer to 0. Although this simplistic problem fully ignores the inherent difficulties due to the hydraulic actuator and servo-systems nonlinear dynamics, one can already imagine how control laws can become inefficient in case of sudden damage occurrence.

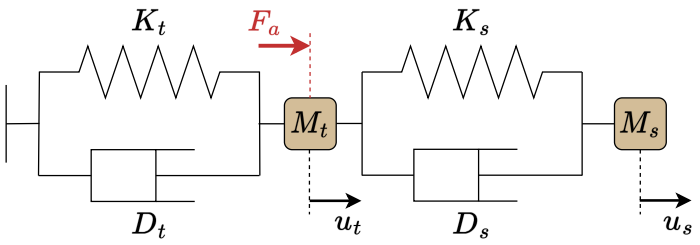

FIGURE 5.13: Two spring-mass system as a first coarse modeling of a specimen embedded on a shaking table.

Regulator design

■ **Direct pole placement by state feedback**

The principle of the state-feedback approach is to synthesize a full state feedback under the form $u = -\boldsymbol{K}\widehat{x}$, where $\widehat{x}$ is the reconstructed estimated state. Owing to the separation principle between observer and regulator, let us first focus on the gain matrix $\boldsymbol{K}$, which is selected to achieve desirable properties of the closed-loop system. Details on the observer design are given afterwards.

Following (5.10), the closed-loop system matrix is $\boldsymbol{A} - \boldsymbol{BK}$. Its eigenvalues are the closed-loop poles; they determine the natural behavior of the closed-loop system and are solutions of the characteristic equation:

$$\det\left[s\boldsymbol{I} - (\boldsymbol{A} - \boldsymbol{BK})\right] = 0 \tag{5.13}$$

A system of the $n_x{}^{\text{th}}$ order involves n_x state variables. Therefore, there are n_x feedback gains $\{k_i\}_{i=1}^{n_x}$ that can be adjusted. The state feedback design task consists in selecting these gains so

that the roots of (5.13) are at desirable locations in the complex plane. If the system is controllable, all poles can be assigned arbitrarily. In other words, (5.13) becomes:

$$\det\left[s\boldsymbol{I}-(\boldsymbol{A}-\boldsymbol{B}\boldsymbol{K})\right]=\prod_{i=1}^{n_x}(s-k_i)=0 \tag{5.14}$$

However, it may not always be practical to assign poles arbitrarily, because the control effort may be too large for the actuators, or the large values of the feedback gains may unduly increase the bandwidth of the control system and lead to noise problems [Preumont 2018]. For shaking table tests, since the value assigned to poles is directly related to the dynamical performance of the closed-loop system, it is recommended to position poles in the complex left half plane with a modulus of a least 50 Hz.

■ Linear Quadratic Regulator design

One effective way to design a full state feedback is the optimal *Linear Quadratic Regulator* (LQR). This approach is common and popular as it carries a strong energy meaning. The objective is to identify the gain matrix K which minimizes the cost-function:

$$\mathcal{J}_{LQ}=\int_0^\infty x^T\boldsymbol{Q}_{LQ}x+u^T\boldsymbol{R}_{LQ}u\,\mathrm{d}t \tag{5.15}$$

where $\boldsymbol{Q}_{LQ}$ is a semi-positive definite matrix and $\boldsymbol{R}_{LQ}$ is a strictly positive definite matrix. The functional $\mathcal{J}_{LQ}$ is made of two contributions, one from the state x and the other from the control command u. Contrary to the direct pole placement technique in which *a priori* intelligence must be put on the choice of the poles, the LQR designer has to calibrate the relative weight of matrices $\boldsymbol{Q}_{LQ}$ and $\boldsymbol{R}_{LQ}$. Very often, one selects $\boldsymbol{Q}_{LQ}=\boldsymbol{C}^T\boldsymbol{C}$ to design the regulator according to the measured states, and $\boldsymbol{R}_{LQ}=\rho^{-1}\boldsymbol{I}$ where $\rho\in\mathbb{R}^+$ is a scalar parameter that defines the trade-off between fast closed-loop poles and control effort. Unfortunately, there is no automated way to choose the parameter ρ except the trial and error empirical method, where the user progressively decreases the value of ρ^{-1} to find the best compromise between command energy and closed-loop performance [Preumont 2018].

Observer design

■ Luenberger observer

In most practical situations, a direct measurement of all the states is not feasible. As discussed earlier, if the system is observable, the states can be reconstructed from a model of the system and the output measurements. If the state estimator does not take into account the output measurements, the obtained estimate $\widehat{x}$ may be totally different from the one of the real system. The SS system (4.2) is thus modified so as to integrate a data-to-model distance:

$$\begin{cases}\dot{\widehat{x}}=\boldsymbol{A}x+\boldsymbol{B}u-\boldsymbol{L}(\boldsymbol{C}x-y+v)+w\\ \widehat{x}(t=0)=0\end{cases} \tag{5.16}$$

The observer $\boldsymbol{L}$ is called a *Luenberger observer* [Luenberger 1971] (see Fig. 5.14). What has been mathematically shown is that, without any errors v and w, the reconstruction error $\epsilon=\widehat{x}-x$ converges towards 0 with a dynamics conditioned by the observer. Such a dynamics is conditioned by the eigenvalues of $(\boldsymbol{A}-\boldsymbol{L}\boldsymbol{C})$ that must be appropriately chosen. If this choice can be theoretically made arbitrarly if the pair $(\boldsymbol{A},\boldsymbol{C})$ is observable, the choice of $\boldsymbol{L}$ must be done with caution because of the existence of model error and measurement noise. A rule of thumb recommends that the eigenvalues of the observer should be at least 5 times faster than the regulator eigenvalues [Preumont 2018]. Once the desired eigenvalue locations are fixed, $\boldsymbol{L}$ can be easily obtained numerically[6]. Note that the pole assignment procedure is identical to that used for the regulator design.

[6] For example, one can use the MATLAB© `place` function.

■ **Kalman Filter**

The KF, also known as Linear Quadratic Estimation, is a sequential stochastic data assimilation method derived from the Bayes theorem, that initially applies to linear dynamical systems under Gaussian assumptions [Kalman 1960; 1964]. Extended details about the KF has been already given in Chapter 4 and Appendix D. For control purposes, it is worth noticing that the KF state correction equation has the same form as the observation equation (5.16), except that the Kalman gain is statistically optimal with respect to a quadratic function of the estimate error.

The calibration of model and measurement errors covariance matrices is crucial to obtain a relevant reconstructed state when using KF. Here again, a trial and error calibration method is often mandatory on the relative weight of $\boldsymbol{Q}$ with respect to $\boldsymbol{R}$, the latter being well-known in practice as it characterizes measurement noise features.

The combination of KF and LQR is called *Linear Quadratic Gaussian* (LQG) control, illustrated in Fig. 5.15. It is a control approach known to be robust: [Luo and Johnson 1993] studied the effects of model bias and measurement noise on the robustness of LQG control for linearized systems, with the proposal of a sufficient condition of stability robustness for the continuous-time LQG regulator subject to system perturbations when assuming they are bounded.

> *Remark* 5.2. LQR and KF formulations are said to be *dual*. In the LQR approach, the regulator design is based on the open-loop transfer function between the input command u and the controlled variable x, while the KF observer design is based on the transfer function between the system noise w and the output y. Actually, the KF and the LQ gain can both be written as the solutions of Ricatti equations, except that matrices $\boldsymbol{A}$, $\boldsymbol{B}$, $\boldsymbol{Q}_{LQ}$, and $\boldsymbol{R}_{LQ}$ are involved for LQR, whereas matrices $\boldsymbol{A}$, $\boldsymbol{C}$, $\boldsymbol{Q}$, and $\boldsymbol{R}$ are involved for the KF. The interested reader will find exhaustive explanations in [Preumont 2018].

Prefilter design

A prefilter on the input signal u allows to cancel steady-state errors [Jelali and Kroll 2003]. Its value can be directly determined from the transfer function of the regulated closed-loop. To ensure that model predictions fit with measurements at $t \to \infty$, a prefilter can be explicitly chosen owing to the final value theorem:

$$\boldsymbol{F} = \left[\boldsymbol{C}^T \left(\boldsymbol{B}\boldsymbol{K}^T - \boldsymbol{A}\right))^{-1}\boldsymbol{B}\right]^{-1} \tag{5.17}$$

5.3.4 Adaptive control of shaking tables

To ensure satisfactory acceleration replication, controller parameters have to be repeatedly redesigned due to the specimen time-varying structural properties. Control laws must then be adaptive in the sense that they must somehow be tuned in accordance to observed changes. Historically, the question is not new; [Leitmann 1979] is probably one of the first papers dealing with state-feedback control deemed to be robust to structural parameters variations. A mathematical framework is proposed to quantify the effect of bounded state-space matrices variations on the stability and robustness of control algorithms.

Many adaptive control techniques have been proposed in the litterature to minimize the effect of nonlinear VCSs behavior on acceleration replication, but **the concept of adaptive control does not always refer to real-time adaptation of controllers**. Among adaptive techniques, let us first mention the concept of *iterative control*: intermediate non-damaging broad-band tests are performed to account for structural changes between seismic tests. A feedforward inverse model is iteratively recalibrated, and the process is repeated with growing-level seismic tests until the reference command signal has been transmitted [Plummer 2007]. This is exactly what is currently done at the CEA/TAMARIS facility. As already discussed, offline adaptive control is not useful when sudden damage occurs during a test, and the need to perform intermediary tests may predamage the tested specimen before reaching the desired excitation level, which

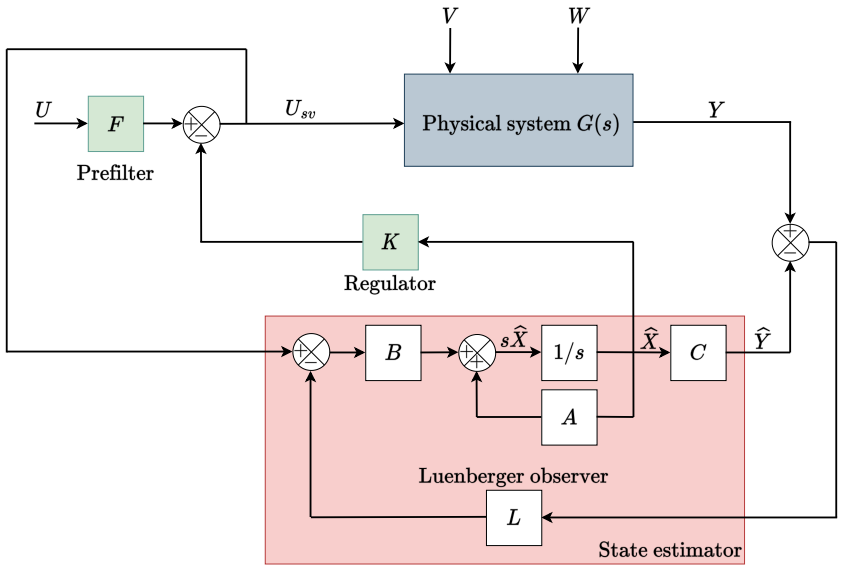

FIGURE 5.14: Control structure (in the Laplace domain) based on a state-feedback estimator and a Luenberger observer (with $\boldsymbol{D} = 0$).

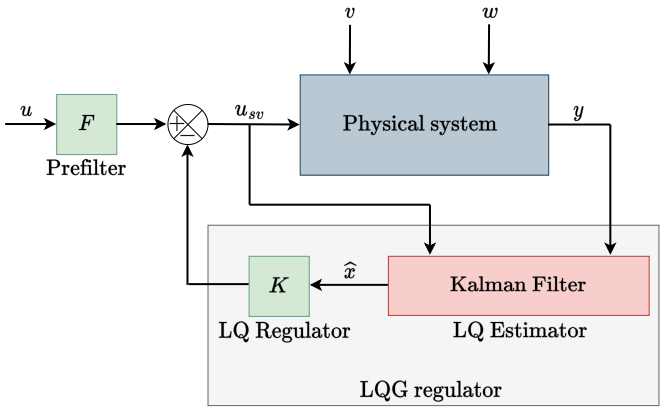

FIGURE 5.15: Control structure based on a Linear Quadratic Gaussian (LQG) regulator.

might disturb the interpretation of test results. This motivation led to the development of the online adaptive controllers that are reviewed in [Shen et al. 2016].

Besides, *adaptive feedforward control* has been proposed for the suppression of the reaction force generated by a specimen [Seki et al. 2009a; b]. The proposed approach includes a Notch filter (also known as band-stop filter) that aims at compensating the reaction force from the specimen. *Adaptive inverse control* is a similar approach except that it uses a finite impulse response command filter [Shen et al. 2011]. The combination of AIC with Least Mean Square (LMS) for state reconstruction is probably the most widely used adaptive algorithm for practical applications such as adaptive noise cancellation, owing to its simplicity, robustness and effectiveness. The filtered-X LMS algorithm is an extension of the LMS algorithm for active noise and vibration control which takes into account the presence of the error path transfer function between the output of an adaptive control filter and the measurements [Bjarnason 1995; Dertimanis et al. 2015].

Another classical approach is the *minimal control synthesis* (MCS) [Stoten and Benchoubane 1993; Stoten and Gomez 2001]. Contrary to PID in which tuning quality is mostly user-dependent, MCS continually adapts to accommodate parameter variations with minimal requirements on the operator expertise. The main advantage that MCS has over alternative adaptive algorithms is that system or disturbance parametrization are required in order to achieve global asymptotic stability of the closed-loop error dynamics [Ahmed et al. 2012]. MCS

has been widely used and reviewed in the literature: it has been extended to nonlinear systems [Bernardo and Stoten 2006] and coupled with adaptive inverse control for shaking table tests [Shen et al. 2011].

Although a wide variety of adaptive control algorithms have been proposed and compared [Butterworth et al. 2012; Shen et al. 2016], there are still lots of open questions associated with VCSs nonlinear control, such as finding a manner to handle heavy parametric uncertainty and uncertain nonlinearities [J. Yao 2018].

Eventually, note that pragmatic control design choices are also made according to the requirements and industrial supplier choices of each shaking table device, which explains the strong discrepancies between European shaking tables reported in [Gomez and Stoten 2000]. Finally, it is worth recalling that this brief review of adaptive control techniques is not intended to be exhaustive but to provide first insights into how to drive shaking tables in a most sophisticated way (see [Plummer 2007; Shen et al. 2016; J. Yao et al. 2016] for complementary explanations).

5.3.5 Model predictive control, a well-suited approach for DDDAS?

Initiated at the end of the 1970s for industrial applications [Richalet et al. 1978], *Model Predictive Control* (MPC) designates a class of time-domain control algorithms that use an explicit process model to compute an optimal future control sequence within a finite time horizon, often referred as *moving horizon control* [Cutler and Ramaker 1980; Richalet 1993]. Linear MPC is now present as a toolbox in several softwares[7]. This control technique is particularly attractive in recent control applications because:

- ▷ it can easily integrate constraints and nonlinearities as no assumption is made regarding the mathematical form of the model. MPC estimates an optimal command that respects actuation restrictions, input and output constraints or imposed states of the system.
- ▷ it is applicable to systems whose linearization is poorly efficient (dead-time, multivariate and unstable processes, non-minimal phase characteristics) that cannot be simplified or neglected in classical control strategies that are based on linearized models [Allgöwer et al. 2004; Rahideh and Hasan Shaheed 2011].
- ▷ it is easier to tune a MPC than a traditional PID, which explains its application in industrial control systems [Richalet and O'Donovan 2009].

However, **MPC requires an accurate model of the controlled system**, which is not always the case in all situations. In particular, regarding the control of shaking table experiments, the models at disposal are not predictive enough to legitimately consider such a model-based approach. Indeed, understanding the behaviour of RC specimen submitted to dynamical 3D loading is still an open research question [Richard et al. 2016], and the models that are available are still too expensive to be used in real-time. For extended information, in particular the mathematical formulation of the MPC problem, the reader is referred to [Qin and Badgwell 2003; Richalet and O'Donovan 2009; Mullhaupt 2017].

5.4 Numerical investigations on shaking table control

Now that control strategies and modeling of shaking table devices have been briefly reviewed, preliminary numerical results are presented from controlled shaking table tests that have been fully simulated in MATLAB©.

> *Remark* 5.3. Compared to what is currently done in the field of control theory, the proposed approaches can be considered simple. However, they still provide a framework in which the relevance of the MDKF can be assessed. As mentionned in the beginning of this report, this study remains exploratory and much work needs to be done before considering practical

[7] See *e.g.* the MATLAB© MPC toolbox or the open-source do-mpc toolbox for Python users.

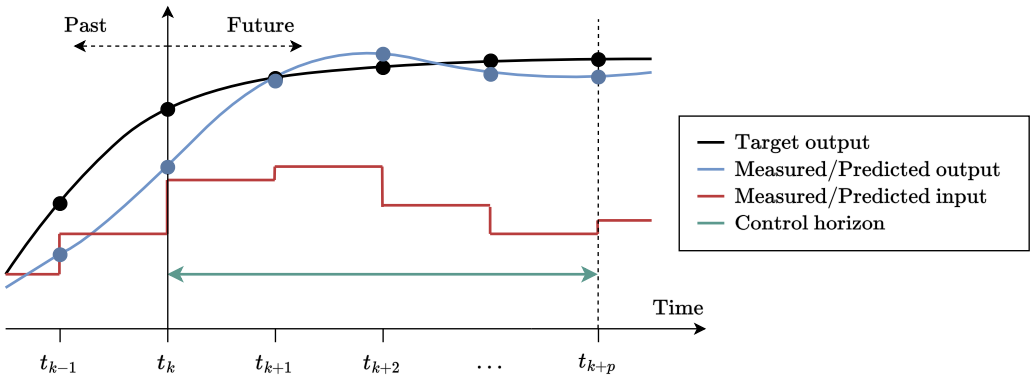

FIGURE 5.16: Model Predictive Control principle scheme.

use of MDKF for DDDAS. The following case study must be considered as a preliminary intention which encourages the investigation of more complex problems.

5.4.1 Control context: model, inputs, performance criteria

Regarding modeling features, the full shaking table system was modelled with the linearized system of equations previously presented in (5.6). An input voltage saturation was added to avoid non-physical meaning fully divergent results. The specimen is considered as a SDoF mass-spring-damper system. All the numerical values of internal parameters used in the forthcoming simulation results are given in Tab. 5.1.

Measurements are collected every $\Delta t = 10^{-3}$ s. In parallel, the time step for the discrete state-space model of the shaking table system evolution is set lower than 10^{-4} s to ensure the convergence of the discrete time integration scheme.

The input sent to the control algorithm is an acceleration signal. It is first processed by a signal generator (2^{nd} order filter - see Fig. 5.11) so as to generate consistent acceleration, velocity and displacement signals that are QoI for state-feedback control.

In this study, the focus is mostly put on pole placement and LQG techniques, as they belong to the class of most popular and standard control approaches. Four normalized accuracy indicators are introduced to assess control performance in terms of time-domain displacement tracking, time-domain acceleration tracking, frequency-domain power spectral density matching, and pseuso-spectral acceleration matching. They are defined as follows:

$$\begin{aligned} \eta_{t,x} &= \frac{\|x_t(t) - x_t^\star(t)\|^2_{L^2([0;T])}}{\|x_t^\star(t)\|^2_{L^2([0;T])}} \; ; \qquad \eta_{t,\ddot{x}} = \frac{\|\ddot{x}_t(t) - \ddot{x}_t^\star(t)\|^2_{L^2([0;T])}}{\|\ddot{x}_t^\star(t)\|^2_{L^2([0;T])}} \\ \eta_{\omega,PSD} &= \frac{\left\|\mathcal{S}_{x_t,x_t}(\omega) - \mathcal{S}_{x_t^\star,x_t^\star}(\omega)\right\|^2_{L^2(D_\omega)}}{\left\|\mathcal{S}_{x_t^\star,x_t^\star}(\omega)\right\|^2_{L^2(D_\omega)}} \; ; \qquad \eta_{\omega,\Gamma_s} = \frac{\|\Gamma_s(\ddot{x}_t) - \Gamma_s(\ddot{x}_t^\star)\|^2_{L^2(D_\omega)}}{\|\Gamma_s(\ddot{x}_t^\star)\|^2_{L^2(D_\omega)}} \end{aligned} \tag{5.18}$$

where $\bullet^\star$ refers to the target of $\bullet$, T refers to the time duration of the test, $D_\omega = [0 \text{ Hz}; 50 \text{ Hz}]$ the frequency range of interest. $\mathcal{S}_{x_t,x_t}$ and $\Gamma_s(x_t)$ respectively denote the PSD and the pseudo-spectral acceleration of the shaking table displacement x_t.

5.4.2 First control simulation results

Now that the control context has been described, let us present some control results obtained using pole placement and LQG. A particular effort has also been put at properly calibrating the controller gains. The relevance of the four criteria previously written for calibration will thus be observed.

Controller by state-feedback, Luenberger observer and pole placement

As explained previously, the calibration of a state-feedback controller by pole placement with Luenberger observer does only restrict to the specification of the desired distance and spreading of regulator poles to the origin of the complex plane.

After a few tests, it appears that the distance of regulator poles to the origin is the most sensitive tuning parameter. Its influence on the control assessment criteria is presented in Fig. 5.17. It shows that for optimal displacement tracking, it is recommended to choose a regulator gain as high as possible. However, it is not the case for acceleration tracking, whose associated criterion starts increasing at around 80 Hz. In practice, the measured displacement spuriously oscillates around the target displacement when the regulator poles distance is overcalibrated, which implies a divergence of measured acceleration compared to the target signal. A very similar trend is also illustrated by the frequency-domain criteria that also present a global minimum below 100 Hz. It thus illustrates that the regulator poles should be carefully chosen for a correct control performance. In addition, we present in Fig. 5.18 and 5.19 the simulation results obtained with a correctly tuned and an overestimated regulator.

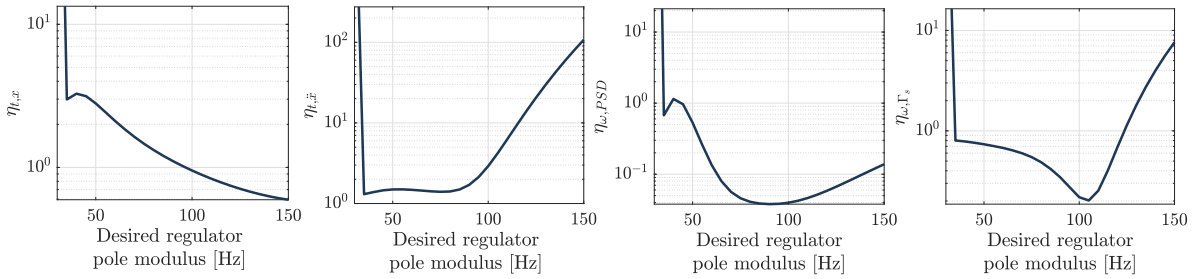

FIGURE 5.17: State-feedback by pole placement - effect of the regulator calibration (user choice whose lower bound fixed by system performance expectations) on the control performance.

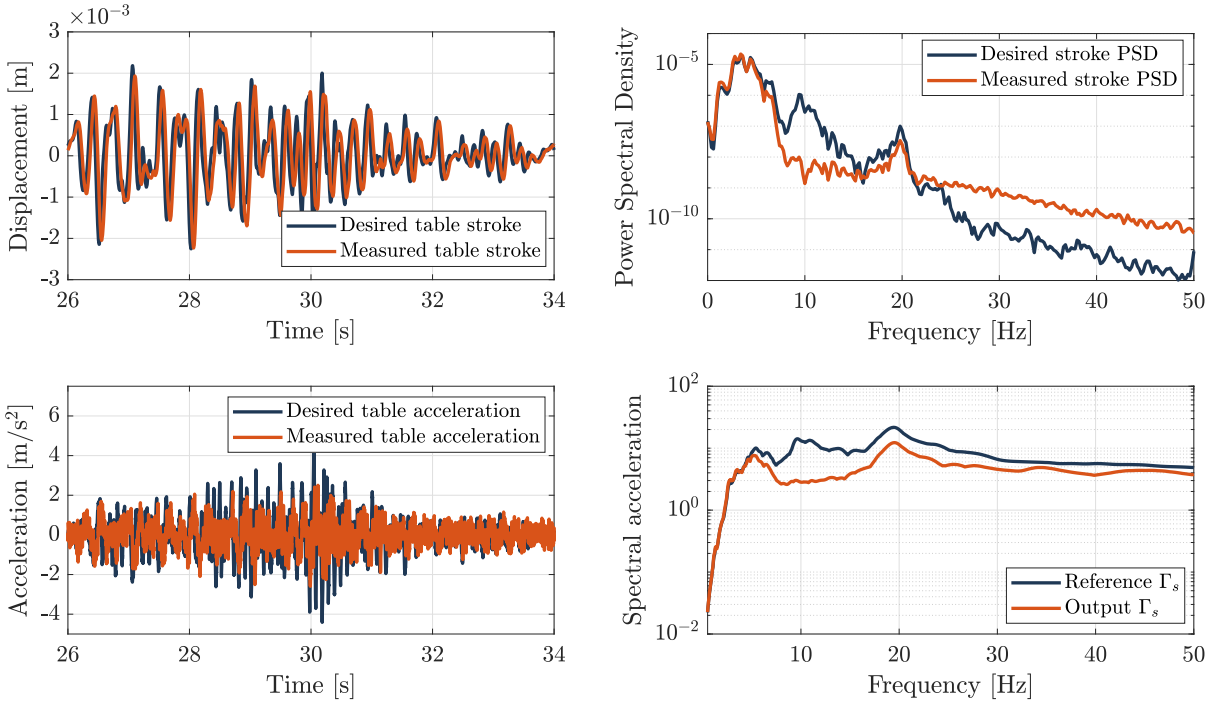

FIGURE 5.18: Controller by state-feedback set by pole placement - example of good compromise between acceleration and displacement requirements, with a regulator pole modulus distance chosen at 100 Hz. The four quantities of interest are plotted (displacement tracking, acceleration tracking, PSDs, and pseudo-spectral acceleration).

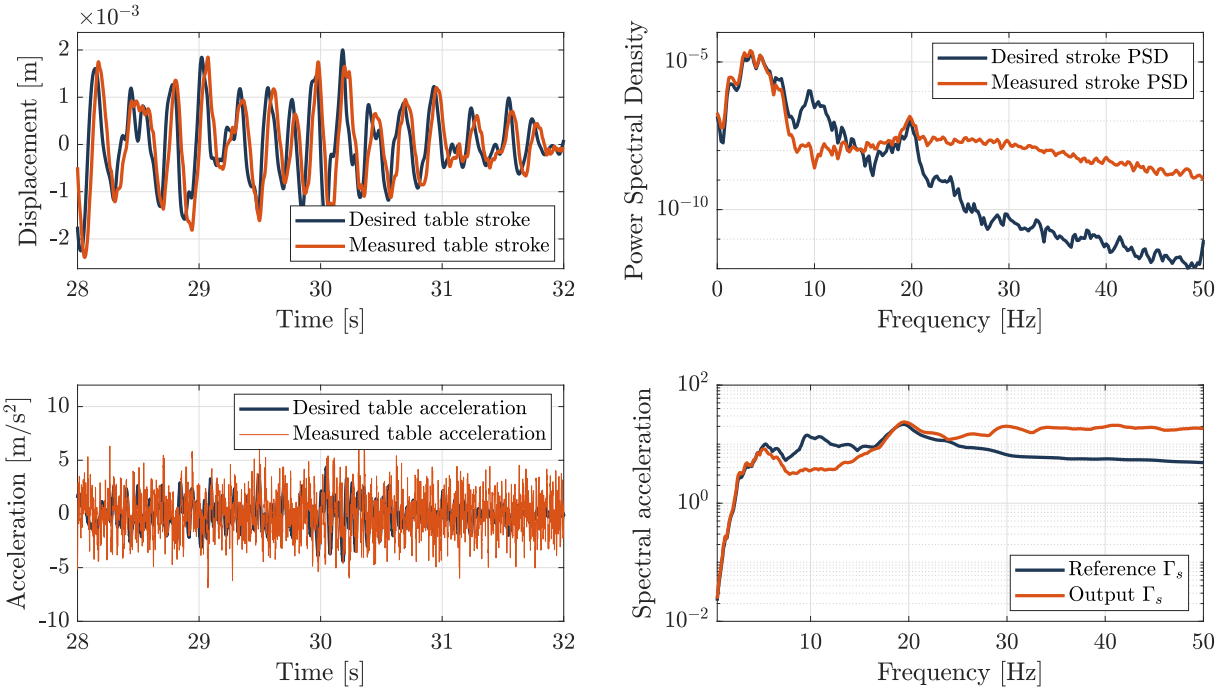

FIGURE 5.19: Controller by state-feedback set by pole placement - example of inappropriate compromise between acceleration and displacement requirements, with a regulator pole modulus distance chosen at 130 Hz. The four quantities of interest are plotted (displacement tracking, acceleration tracking, PSDs, and pseudo-spectral acceleration).

Linear Quadratic Gaussian controller

The calibration of a LQG requires the setting of $\boldsymbol{Q}_{LQ}, \boldsymbol{R}_{LQ}, \boldsymbol{Q}$ and $\boldsymbol{R}$. First, one can restrict the structure of $\boldsymbol{Q}_{LQ}$ to $\boldsymbol{C}^T \text{diag}\,[Q_{x_t}\ Q_{\ddot{x}_t}\ 0\ 0\ 0]\,\boldsymbol{C}$. Doing so, the LQR correcting actions will be devoted to handle at best the system acceleration and displacement table tracking. As only the relative weighting of $\boldsymbol{Q}_{LQ}$ with respect to $\boldsymbol{R}_{LQ}$ matters for LQ, $\boldsymbol{R}_{LQ} = 1$ is fixed and we will only focus on the pair $(Q_{x_t}, Q_{\ddot{x}_t})$.

In Fig. 5.20 is presented the effect of varying Q_{x_t} and $Q_{\ddot{x}_t}$ on the four accuracy indicators of interest after having imposed $R_{LQ} = 1$. One can observe here that all four criteria bring to light that there is a compromise between acceleration and displacement weightings to control the system at best. As the LQ regulator is explicitely optimized both for displacement and acceleration tracking performance, acceleration tracking is better than for pole placement, as observed by comparing the control performance achieved in Fig. 5.18 and 5.21.

Note that the KF covariance matrices $(\boldsymbol{Q}, \boldsymbol{R})$ are fixed once and for all and not modified afterwards, as they are less sensitive compared to LQ internal parameters (for this particular example).

5.4.3 Need for adaptive control

PID controller tuning variability

Although PID controllers are not relevant enough to produce robust control laws (compared to SS-based feedback), the dependency of the PID gains with respect to the specimen state of Fig. 5.22 illustrates the strong need for adaptive control when the specimen evolves during a test. To obtain such a result, the linearized model (5.6) was used and PID gains were tuned using the MATLAB© `pidtune` function. It should be noted that when damage occurs, *i.e.* when eigenfrequency falls, regulator gains can suddenly become overrated if not adapted.

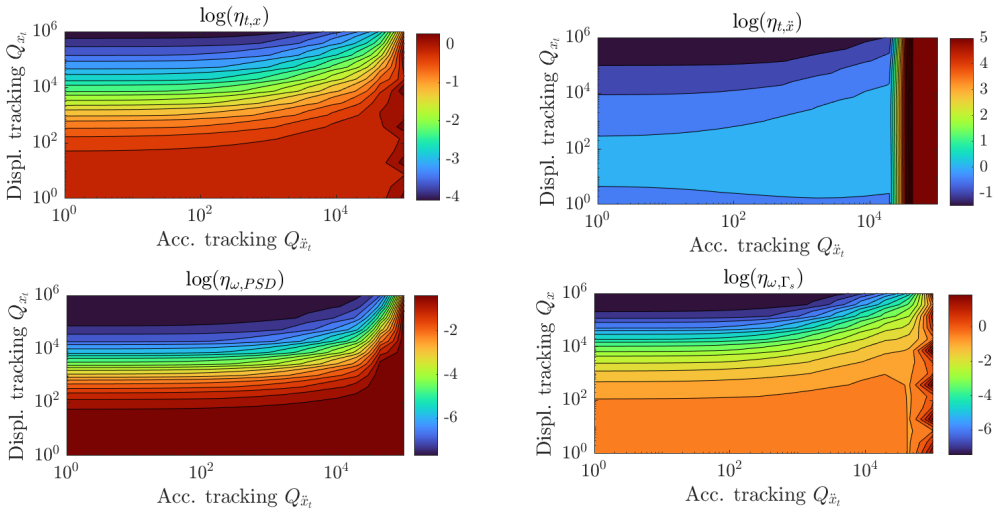

FIGURE 5.20: Calibration of LQG controller - compromise between acceleration and displacement requirements for efficient control. The four quantities of interest (displacement tracking, acceleration tracking, PSDs, and pseudo-spectral acceleration) are plotted in log-scale.

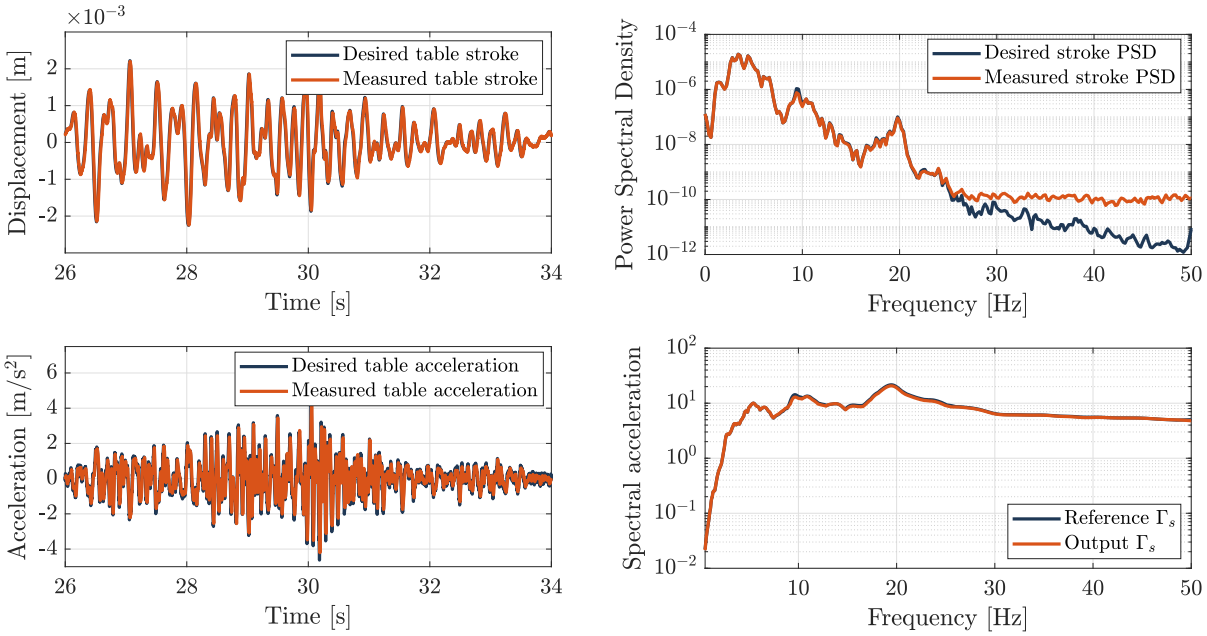

FIGURE 5.21: LQG controller - example of good compromise between acceleration and displacement requirements, with $(Q_{x_t}, Q_{\ddot{x}_t}, R_{LQ}) = (10^5, 10^2, 1)$. The four quantities of interest are plotted (displacement tracking, acceleration tracking, PSDs, and pseudo-spectral acceleration).

Lack of robustness of SS-based feedback control for time-varying systems

If well calibrated, SS-based feedback control laws (pole placement or LQG) are able to correctly replicate displacement and acceleration signals on shaking tables. However, all the simulation results that have been presented before did not consider time-varying properties, such as structural damage. As an illustration of how control laws may lack of robustness, we present in Fig. 5.23 the effect of sudden damage on control laws, becoming inappropriate whereas initially well-calibrated. As a matter of fact, a 100 Hz distance of regulator poles to the complex plan origin was chosen (like in Fig. 5.18) and a 75% damage loss at $t = 30$ s lead to an unstable test ending. This test result can be closely related to what happened during the run #13 of the SMART2013 test campaign, during which a very similar control instability occured after sudden cracking at the bottom of the specimen [Richard et al. 2016].

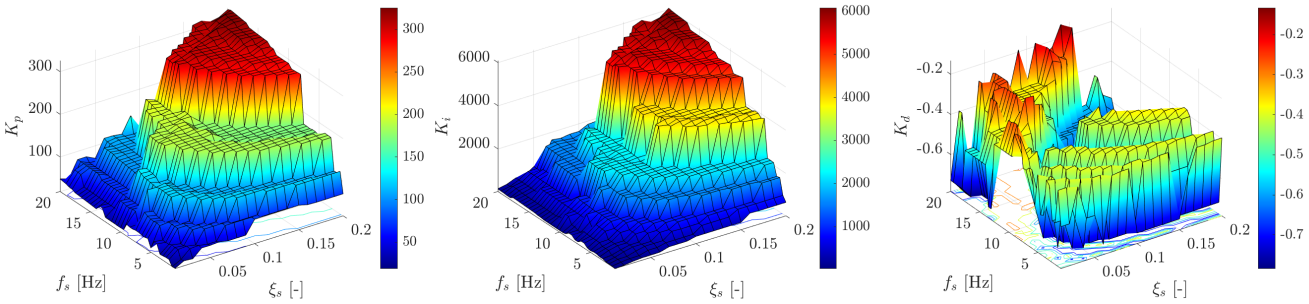

FIGURE 5.22: Significant variability of optimal PID gains (automatically computed with the MATLAB© `pidtune` function) with respect to specimen properties.

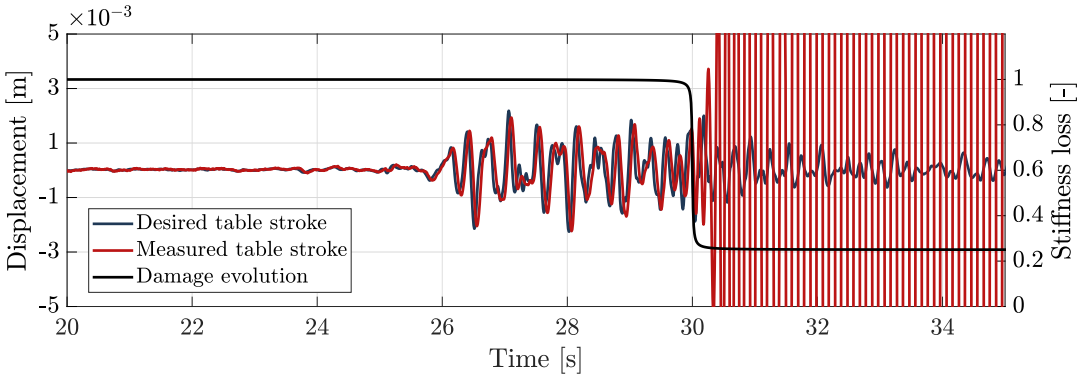

FIGURE 5.23: Shaking table test controlled by pole placement becoming unstable due to sudden damage occurence, although control laws were initially well calibrated.

Note that a sudden loss of accuracy (much less spectacular though because not fully unstable) has been observed with LQG as well.

5.4.4 Towards enhanced control of shaking tables with MDKF

The solution of the mCRE problem is close to the problem of determination of an observer in the sense that one tries to reconstruct the state of a system (here the dynamical response of a mechanical structure) by minimizing the estimation error, *i.e.* the difference between the real state of the structure and its estimate, hence the coupling between mCRE and KFs (see Chapter 4).

Since LQG state estimator is based on a KF as well, it would be interesting to integrate the mCRE within such a control framework. Actually, we owe to [Formosa 2002] the first research work trying to integrate the CRE for active control of smart structures (equipped with piezoelectric actuators). Formosa proposed a "LQ-CRE" control framework in which the state estimation from measurements was performed using the mCRE. On an academic example (vibrating plate with a damage defect), the feasibility of using mCRE for control purposes was illustrated, and LQG control was shown less performant than LQ-CRE control in the high-frequency bandwidth.

The objective here is to propose a novel manner to perform DDDAS by informing the controller of the state evolution, based on the MDKF. In this last study, a new methodology which takes MDKF into consideration within a SS-feedback control strategy is presented.

The time-frequency formulation of the MDKF is the main limitation that prevents the direct use of Formosa's control framework: due to the sliding window technique that allows for progressive data assimilation, parameters are updated at a coarse time scale compared to the data acquisition frequency. Besides, the mechanical fields provided by the mCRE are provided in the frequency domain, but only for a restricted subset of angular frequencies ($\omega \in D_\omega$). Using discrete inverse Fourier transforms would not be accurate enough if one wanted to directly

exploit the mCRE-computed mechanical fields.

The valuable information that can be exploited from MDKF for control laws is the parameter estimates. The MDKF-based adaptive control law perspectives are illustrated in Fig. 5.24. Note that MDKF can infer on the control strategy at different levels of "intrusiveness":

- ▷ If sudden stiffness loss is detected, the prefilter gain can be lowered towards zero. The target signal will no longer be replicated, but additional damage on the structure should not happen, and the safety of the installation will be preserved.
- ▷ The estimator state-space model can be updated so that the control strategy is informed of the specimen evolution.
- ▷ To go even further, the controller gains could be adapted on-the-fly according to MDKF estimates. However, such operations may not be feasible in real-time. An empirical way to do so is to built an *a priori* mapping of controller gains according to damage in state-space matrices [Foltin and Sekaj 2006] and to interpolate within this map during the data assimilation process. The underlying difficulty in that case lies in the fact that controller gains specifications for optimal control are also function of the damage level.

> *Remark* 5.4. Control simulation results must be analyzed with caution when MDKF adapts the SS model and/or the controller gains as no mathematical proof guarantees stability and robustness for time-varying online adaptive control.

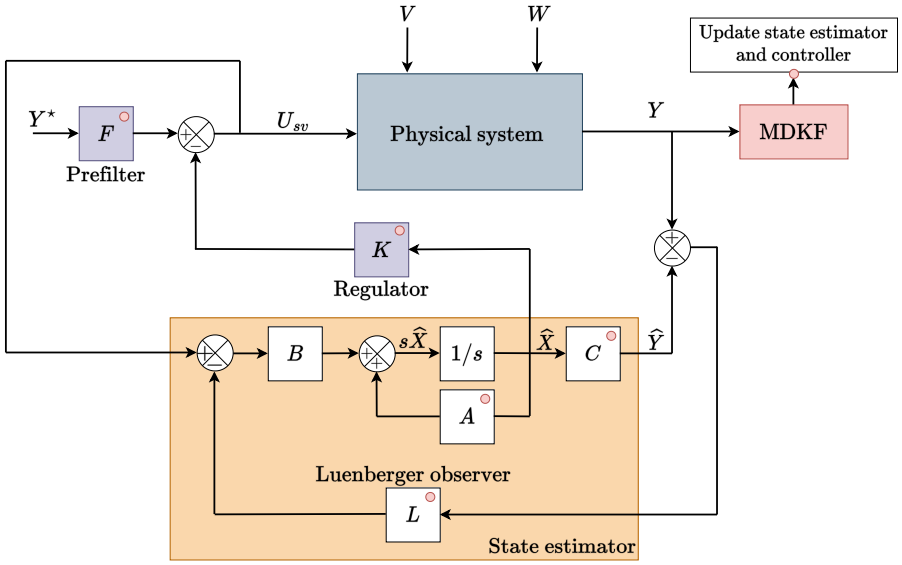

FIGURE 5.24: Perspective of using on-the-fly model updating algorithms to perform adaptive control design on a pole-placement-based state-feedback control framework.

In Fig. 5.25, we present the benefits of adaptive control based on MDKF on a controller based on Luenberger observer and pole placement regulator. Without tuning the controller gains, it is possible to exploit the stiffness tracking provided by MDKF to stabilize the shaking table test once damage occured (in spite of the MDKF identification delay due to the data windowing process). Although the example remains simple in terms of modeling complexity, note that the result of Fig. 5.25 is achieved in real-time! **This can be seen a first proof-of-concept showing the relevance of mCRE-based DDDAS in low-frequency dynamics, for shaking table experiments**. Therefore, this completes the overall goal of this thesis work depicted in Fig. 2.

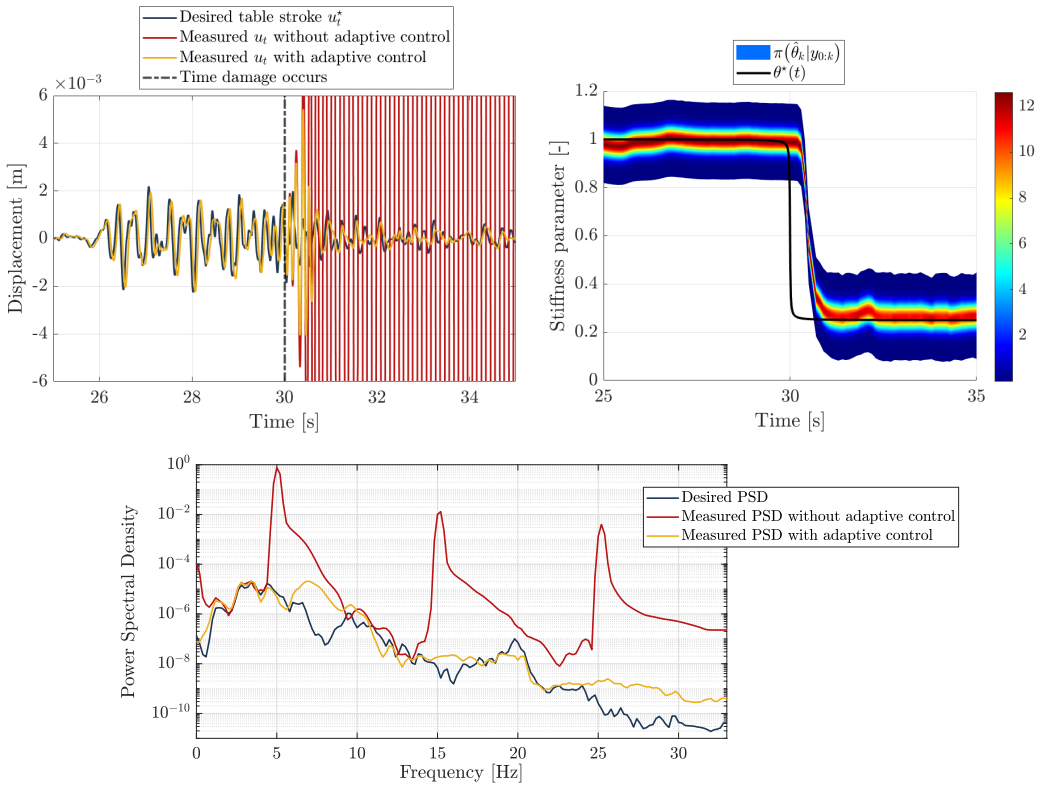

FIGURE 5.25: Control strategy based on Luenberger observer and pole placement regulator - benefits of adapting the state-space matrices with MDKF estimates to enhanced stability.

5.5 Conclusion & prospects for model-based control informed by mCRE

In this chapter, after a description of the difficulties in modeling nonlinearities of valve-controlled systems, a brief review about the wide range of shaking table control strategies was presented. Once having put emphasis on the control instabilities that may happen when the tested specimen gets damaged, we proposed a first full digital twin application for enhanced stability of shaking table experiments. The Modified Dual Kalman Filter algorithm, a data assimilation process based on the modified Constitutive Relation Error functional, is used to track the stiffness loss of a specimen undergoing damaging ground motion experiments. The information provided by MDKF is thus advantageously used to feed and update the state-space model of the controller in accordance. Doing so, **we illustrated on a academic example the feasibility of performing mCRE-based DDDAS**.

Nonetheless, several perspectives must be kept in mind:

- ▷ Using a more realistic shaking table device model fully built from measurements (with input/output identification),
- ▷ Introducing nonlinearities in the specimen response and the actuator behavior,
- ▷ Simulating multi-actuator multi-directional ground motions, which will require to handle the spurious interferences between actuators [Plummer 2008],
- ▷ Going through more complex control strategies than pole placement or LQG, perhaps model predictive control if a ROM from a high-fidelity model is available,
- ▷ Writing a full time-domain mCRE functional projected on a truncated modal basis. Doing so, the LQ-CRE control strategy from [Formosa 2002] may be applicable. It could even be combined with an Augmented Kalman Filter for state-input-parameter estimation when considering output-only measurements [Lourens et al. 2012].

Conclusion and prospects

Main contributions of the thesis

The overall ambition of this thesis work consisted in developing a robust numerical framework to improve the control of shaking tables.

Starting from the offline model updating viewpoint, a fully automated model updating algorithm based on the *modified Constitutive Relation Error* (mCRE) was successfully implemented. Dedicated efforts have been made so as to enhance the robustness of parameter identification when considering low-SNR measurements typical of earthquake engineering experiments and damage detection problems, especially with an averaged formulation of the mCRE functional and a CRE-based parametrization of the problem. In parallel, as the amount of sensors that are embedded on structures may be limited, a novel optimal sensor placement strategy, which introduces the mCRE in the information entropy framework, has been proposed so as to position sensors at best for mCRE-based parameter identification. A complete model updating framework unified around the mCRE concept for SHM is thus achieved.

The offline model updating framework was then extended to sequential data assimilation by integrating the mCRE within a dual Kalman Filter, leading to a new data assimilation framework called *Modified Dual Kalman Filter* (MDKF). The full algorithm was fully detailed, with many variants considered for optimal numerical performance and guidelines based on engineering judgment provided for its easy calibration by non-expert users.

Both offline and online mCRE-based model updating frameworks have been assessed on a wide range of academical examples typical of shaking table experiments and on actual measurements recorded during the SMART2013 test campaign, in which an unstable test occured due to control failure. Although the updated models remained linear and far from being predictive in terms of modal analysis, we have been able to successfully track defects that occured due to complex nonlinear phenomena (constitutive models of steel, concrete, and interfaces, behavior of wall-slab joints, description of damping, damage initiation and propagation) whose modeling is still an open research question.

Lastly, as it was the overall motivation of this work, the challenges regarding the control of shaking tables were considered, and, on a first academical example with a classical control strategy, an adaptive control test based on the information carried by MDKF was performed in real-time. This illustrates the feasibility of achieving mCRE-based DDDAS and one hopes it will lead the path and motivate future investigations.

Prospects

The work presented in this thesis can be extended in several directions stated below:

■ About control and the industrial use of mCRE for DDDAS

As mentioned when dealing with adaptive control, additional tests and investigations must be done regarding a more accurate modeling of shaking table devices. In particular, a black-box model built from actual measurements collected at the CEA/EMSI/TAMARIS facility may allow to fairly compare control strategies and MDKF benefits in a realistic context. For instance, the thesis of Daniel Martin-Xavier, started end 2022, aims at building a robust and stable control algorithm for structures subjected to evolutive damage by means of an updated damage model and a MPC algorithmic structure.

In terms of industrial needs, in addition to the OSP developments, the next step consists in performing real-time data assimilation with MDKF in forthcoming test campaigns, and even adaptive control once a proper control framework based on the mCRE will have been set. In practice, it will require the transfer of all the framework developed in MATLAB© to a real-time controller with low level programming language recently acquired by the CEA/EMSI laboratory. An implementation of the mCRE/MDKF routines in the CEA softwares Cast3M© and Manta [Jamond et al. 2022] may also be considered if needed, following [Oliveira et al. 2022].

■ About the range of applications

The general model updating applications provided in this work were dedicated to an earthquake engineering context but it is perfectly suited for many other applications involving vibratory loadings and low-SNR measurements: vibration-based damage detection, ageing of civil engineering structures, structural health monitoring, fatigue of mechanical components, and more generally systems submitted to vibratory phenomena potentially coupled with thermal evolution. Indeed, once reliable and unreliable quantities of the reference problem have been distinguished by engineering judgement, a mCRE cost-function can be built and minimized following the methodology presented in this thesis. As an example, one can refer to the PhD work of Antoine Roussel which investigates mCRE-based multiphysics model updating for sea wind turbines [Roussel et al. 2022], that are submitted to dynamical excitations due to wind, waves and sea current.

■ About the mCRE formulation and the associated updated model(s)

Regarding the positioning of the mCRE functional among other model updating techniques, only [Waeytens et al. 2016] proposed a fair comparison in quasi-statics for a concrete beam using strain data. Apart from the benchmark described in Chapter 2 and the validation tests showing the relevance of the proposed numerical tools, no experimental or numerical benchmark has been proposed with the intention of positioning the mCRE among other model updating/modal analysis techniques in dynamics. A comparison between time and frequency formulations of the mCRE would also be valuable.

All the models that have been updated in this work are linear, and parameters directly weighted the associated stiffness FE matrices. If this framework is well-suited for the shaking table control problems, such an approach remains insufficient for prognosis purposes, first because linear models cannot correctly predict nonlinear phenomena, and second because the frequency-based formulation of the mCRE is not adequate for inverse Fourier transforms. For more accurate state predictions, either (i) more frequencies must be analyzed by the mCRE, but it leads to much longer reaction delays to parameter changes in an online context, or (ii) a full-time approach must be adopted, and the issues mentioned in [Marchand 2017] arise (time-dependent confidence into measurements, temporal sub-discretization for the computation of admissible mechanical fields, non-homogeneous initial condition at each assimilation time step).

Besides, the question of model complexity and model selection could be addressed. A library of more or less complex models may be all updated in parallel, and one could identify which one is most appropriate regarding a given quantity of interest. A normalized model error map may be used to define which model is most accurate, but one could also imagine considering the best model being such that the uncertainties of the updated parameters remain small. A first study may consist in comparing different "model quality" indicators, and to compare the benefits carried by the CRE compared to other approaches, such as the Bayesian model evidence concept, recently coupled to UKF in [Rosafalco et al. 2021].

Eventually, coupling physics-based models and deep learning techniques for the real-time monitoring of structural damage may be an alternative approach considering the ever-increasing use of machine learning techniques in the last decades. This is the topic of Antoine Benady's thesis, in which a data-driven methodology using neural networks to learn (nonlinear) constitutive laws in the form of thermodynamic potentials is investigated, with the use of mCRE as loss function to facilitate the learning process [Benady et al. 2022].

■ About measurements

In all the examples that have been considered, actual or simulated acceleration data was used for model updating. In practice, the extension to other types of measurements is not a painful task from the mCRE viewpoint (it changes the definition of the model-to-data observation matrix). The integration of strain measurements from gauges or optic fibers would be interesting to perform more accurate model updating in the sense it would facilitate damage detection. The mCRE-based OSP algorithm would easily integrate multiple types of sensors as well [Ercan and Papadimitriou 2021].

Even if it was initially expected to be done with the SMART2013 test campaign, the use of dense measurements from optic fibers or digital image correlation has unfortunately not been possible in the context of this thesis. In such a context, the question of data selection has to be addressed: which data points from DIC or optic fibers should be selected to perform model updating in real-time? What is the optimal path optic fibers should follow for optimal identification? These issues are currently investigated by Sahar Farahbakhsh in her thesis in which mCRE-based damage identification is performed with Rayleigh optic fibers. With such measurement devices, the objective is to exploit measurements in a frugal manner, and to define the model complexity depending on the situation, in order to facilitate data-to-model comparison [Chamoin et al. 2022]. The above-mentioned perspective of model selection, in the sense of model adaptivity also raises herein.

Except from model bias, the blind trust in the location of sensors can be questioned. Indeed, a lack of accurate knowledge on sensor locations propagates an error that can have a significant impact on the identification results. This may be another reason for not having been able to look for defects in the SMART2013 case with a finer spatial resolution. A first study one could perform would consist in quantifying the amount of uncertainty on parameter estimates propagated by uncertain sensor locations.

Appendices

Appendix A

Description of earthquake engineering problems

Several earthquake engineering examples have been involved to assess, compare and validate the contributions presented in the manuscript. For the sake of clarity, this appendix is dedicated to the full description of the most recurrent ones, so that the interested reader can find apart all the necessary details for the implementation.

As a preliminary remark, all models have been built in the CEA FE analysis and simulation software Cast3M© [Cast3M 2020]. Once models have been built, the FE matrices are exported in MATLAB© using the `sormat.eso` function, available since 2012 in the Cast3M© library. The latter has been slightly modified with the export of the internal nodes numbering of the nodes to proceed to the harmonization of the discretized operators. Then, several dedicated routines in MATLAB© functions have been created to extract and correctly read the FE operators of the linear dynamics problems.

A.1 Plane frame submitted to random ground motion

We consider here the plane frame structure of Fig. A.1 whose stiffness distribution is assumed unknown. This structure is clamped to a rigid moving support (*e.g.* a shaking-table). The stiffness reference field (the one to be identified) presents a defect in the wall W10 whereas the initial guess is uniformly underestimating the initial stiffness of the overall structure. According to the considered case studies, the defect in wall W10 suddenly appears during the test or is already present at the beginning of the test. The objective of this academic example is to recover the stiffness distribution based on simulated acceleration measurements with noise of known level δ coming from discrete sensors scattered over the structure (yellow dots in Fig. A.1).

The FE model used to simulate measurements is made of 192 elastic beam elements. The FE model used to perform model updating has half less elements so that a discretization error is systematically present to introduce model bias. Relative time acceleration measurements in both x and y directions are simulated using fast Fourier transforms and the frequency transfer matrix of the direct dynamical problem is formulated in terms of relative displacement X as follows:

$$\boldsymbol{M}\ddot{X} + \boldsymbol{D}\dot{X} + \boldsymbol{K}X = -\boldsymbol{M}\boldsymbol{\Xi}\ddot{U}_d\,, \quad X = U - U_d \tag{A.1}$$

where $\boldsymbol{\Xi}$ is a matrix addressing the bi-axial acceleration ground motion to the associated DoFs and $\ddot{U}_d$ the random ground acceleration input.

In order to assess the robustness of the data assimilation algorithms with respect to measurement noise, a white noise of known standard deviation is added to the synthetic measurements. The noise level δ (in $\%$) is then defined according to the magnitude of the input ground acceleration $\ddot{U}_d$ such that noisy synthetic acceleration data is obtained as follows:

$$\ddot{y}_{noisy}(t) = \ddot{y}(t) + \delta \text{ std}\left(\ddot{U}_d(t)\right)\eta(t) \tag{A.2}$$

where $\eta(t) \sim \mathcal{N}(0,1)$ is a random Gaussian vector of zero mean and unitary standard deviation.

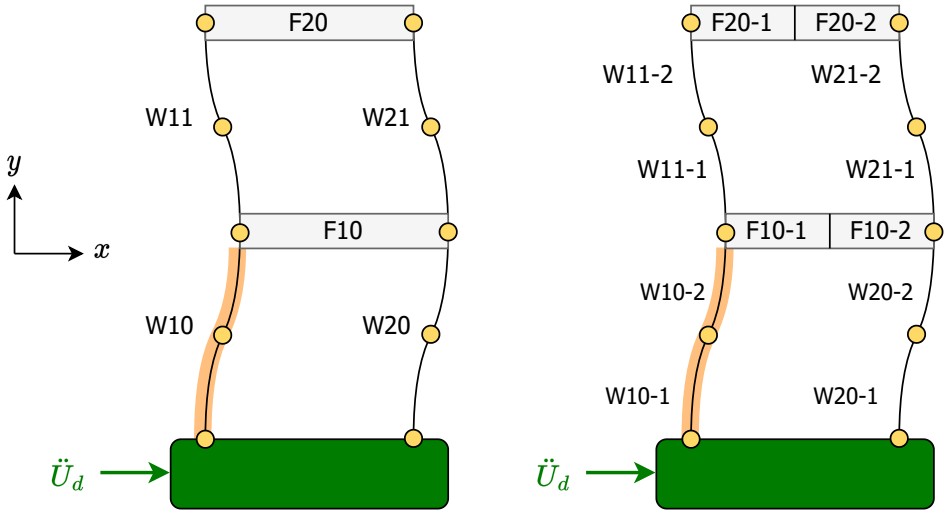

FIGURE A.1: Two-story plane frame submitted to random ground motion. Sensors location (yellow dots) and subdomains labelling (according to the chosen parametrization - $n_\theta = 6$ or 12) are specified. The damaged part of the frame in simulations is highlighted in orange.

A.2 The SMART2013 test campaign

EDF and CEA are deepfully acknowledged for giving access to the SMART2013 database.

In order to assess the vulnerability of RC structures subjected to torsional effects during seismic ground motions, the SEISM Institute led the SMART2013 experimental campaign in the CEA/TAMARIS facility where a three-story trapezoidal RC specimen clamped on the six DoFs AZALEE shaking-table has been subjected to a sequence of seismic tests. Equipped with eight 1000kN maximum capacity hydraulic MTS actuators, the AZALEE shaking-table can reproduce complex seismic loadings on huge specimens. In terms of mass, nearly 34 tons have been added to the 12 tons of the structure to account realistic floor loading and respect Cauchy-Froude's similitude law (see Fig. A.2).

The specimen is instrumented with more than 200 sensors including 64 capacitive accelerometers of ± 10 g range scattered over the RC specimen. 48 out of the 64 accelerometers (pointed on Fig. A.2) have been used as experimental reference for correcting the FE model. Measurements are acquired at a sample frequency of 1000 Hz and filtered with 400 Hz cut-off frequency anti-aliasing filters. A typical ± 0.003 g white noise level was observed on the accelerometers. More precisely, accelerations are recorded on corners of the trapezoid on each story (including soleplate level), while vertical accelerations are measured in-between the masses at floor levels. The displacements and accelerations of the eight hydraulic rods of the AZALEE shaking-table are also measured, providing complete and redundant access to the input imposed on the specimen.

A.2.1 Experimental campaign

A brief recap of the SMART2013 test campaign is given in Tab. A.1. The test sequence consists in an alternation of bi-axial gradually damaging seismic inputs (of increasing level) with random ground motions with low-acceleration level chosen such that the first eigenmodes of the experimental system are excited but without adding further damage to the RC specimen. For illustration purposes, the acceleration table ground motion recordings in the x-direction for the full campaign are also presented in Fig. A.3. Complementary information can be found in [Richard et al. 2016; 2018; Charbonnel 2021] or on the dedicated webpage of the SEISM Institute.

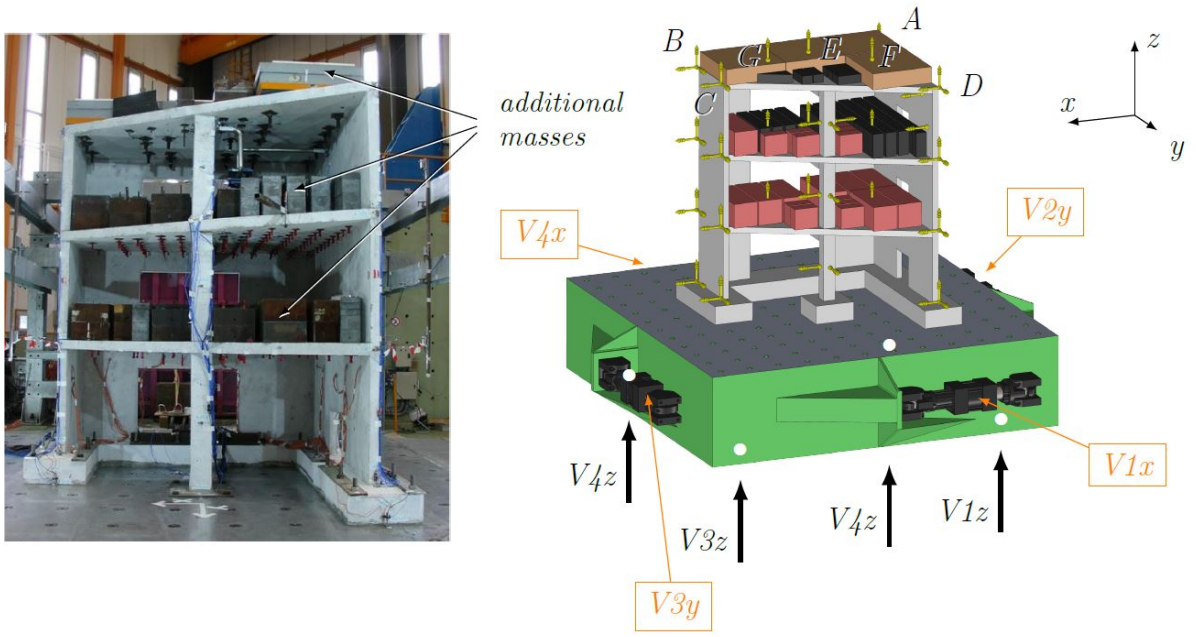

FIGURE A.2: The SMART RC specimen anchored to the AZALEE shaking table with actuators and sensors locations. The yellow arrows indicate the position of the accelerometers that are used for model updating. Only the horizontal actuators ($V_{\#x}$) are represented, the position of the vertical actuators ($V_{\#z}$) underneath the AZALEE table is labeled with white dots and their action marked with black arrows - from [Charbonnel 2021].

Phase 1: SMART2008 inputs - PGA$(x, y) = (0.2g, 0.2g)$		δ [%]
Run #6	Broad-band bi-axial signal $(x+y)$ $0.02g$ RMS	22.6
Run #7	Seismic signal - 50%	-
Run #8	Broad-band bi-axial signal $(x+y)$ $0.02g$ RMS	29.0
Run #9	Seismic signal - 100%	-
Phase 2: Northridge main shock signal - PGA$(x, y) = (1.78g, 0.99g)$		
Run #10	Broad-band bi-axial signal $(x+y)$ $0.02g$ RMS	23.8
Run #11	Seismic signal - 11%	-
Run #12	Broad-band bi-axial signal $(x+y)$ $0.02g$ RMS	31.1
Run #13	Seismic signal - 22%	-
Run #14	Broad-band bi-axial signal $(x+y)$ $0.02g$ RMS	26.1
Run #15	Seismic signal - 22%	-
Run #16	Broad-band bi-axial signal $(x+y)$ $0.02g$ RMS	28.5
Run #17	Seismic signal - 44%	-
Run #18	Broad-band bi-axial signal $(x+y)$ $0.02g$ RMS	28.0
Run #19	Seismic signal - 100%	-
Phase 3: Northridge after-shock signal - PGA$(x, y) = (0.37g, 0.31g)$		
Run #20	Broad-band bi-axial signal $(x+y)$ $0.02g$ RMS	20.1
Run #21	Seismic signal 33%	-
Run #22	Broad-band bi-axial signal $(x+y)$ $0.02g$ RMS	26.0
Run #23	Seismic signal 100%	-
Run #24	Broad-band bi-axial signal $(x+y)$ $0.02g$ RMS	22.5

TABLE A.1: Synthesis of the SMART2013 shaking-table test campaign and computation of noise level δ for the bi-axial random tests.

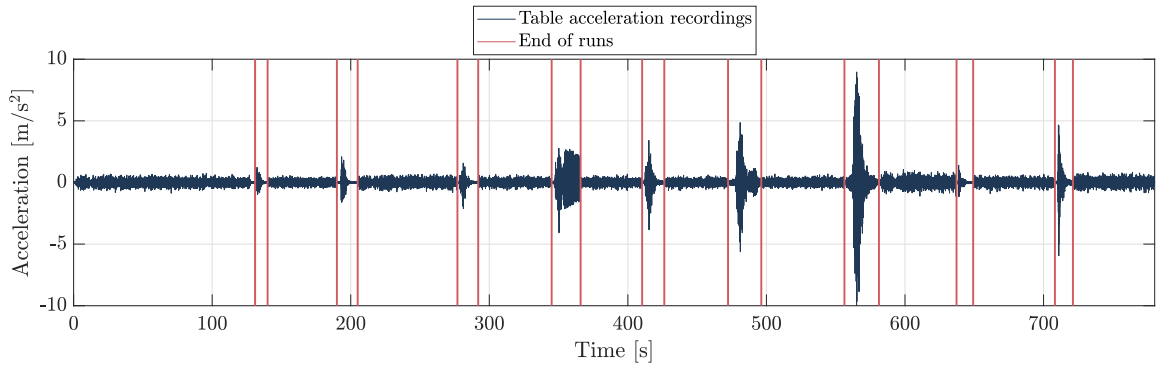

FIGURE A.3: SMART2013 - Recordings from the AZALEE shaking-table acceleration in the x-direction.

A.2.2 FE models at disposal

Two FE models of the SMART2013 specimen, implemented in CAST3M© to process as usual according to engineering practice, are available:

- ▷ **Model 1:** mainly developed by S. Cherubini and B. Richard, the RC specimen has been modeled by an assembly of several finite elements. The shear walls, the slabs and the central beams have been discretized by multi-layered shell finite elements. The foundation has been discretized by volume FE. The column has been represented as a vertical beam made of Timoshenko multi-fiber beam FE. Linear and nonlinear constitutive laws have been given both for concrete (continuum damage mechanics) and steel reinforcing bars (Menegotto-Pinto model) - see [Richard et al. 2016] for additional information. The numerous underlying parameters have been estimated at best from measurements but are most likely subjected to uncertainty or error. The effect of the additionnal masses has been taken into account with additionnal nodal elements on the floors.

- ▷ **Model 2:** developed by N. Ile, the FE mesh is quite similar, except that the entire specimen has been modeled using shell elements. Floor reinforcements are present with additionnal shell elements too. The main consequence is that the FE matrices are of larger size and therefore heavier to handle. The material properties are chosen at best in accordance with the measurements of the test campaign.

> *Remark* A.1. A compatible full shell FE model of the AZALEE shaking-table is also available to be coupled to both models. However, as the model updating procedure will be based on relative measurements, it will not be necessary herein. To the extent that the solicitation inputs are bi-axial and that the shaking-table is considered infinitely more stiff than the specimen, it will be assumed in the following that the soleplate is subjected to 2D rigid body movement. Therefore, the boundary conditions from the hydraulic actuators can be immediately extended at the bottom of the anchorage.

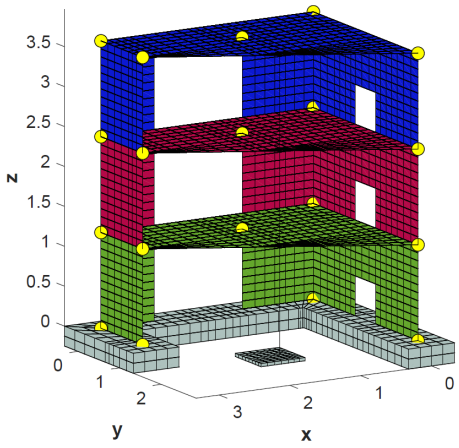

(a) FE mesh of model 1.

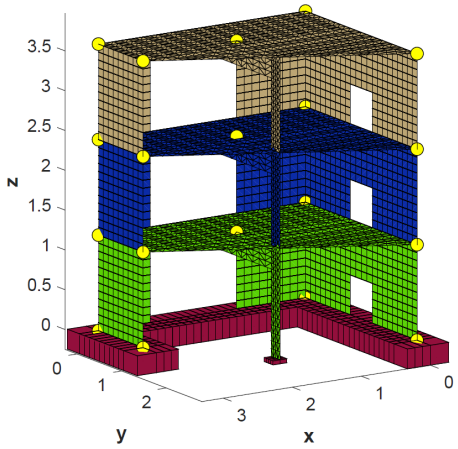

(b) FE mesh of model 2.

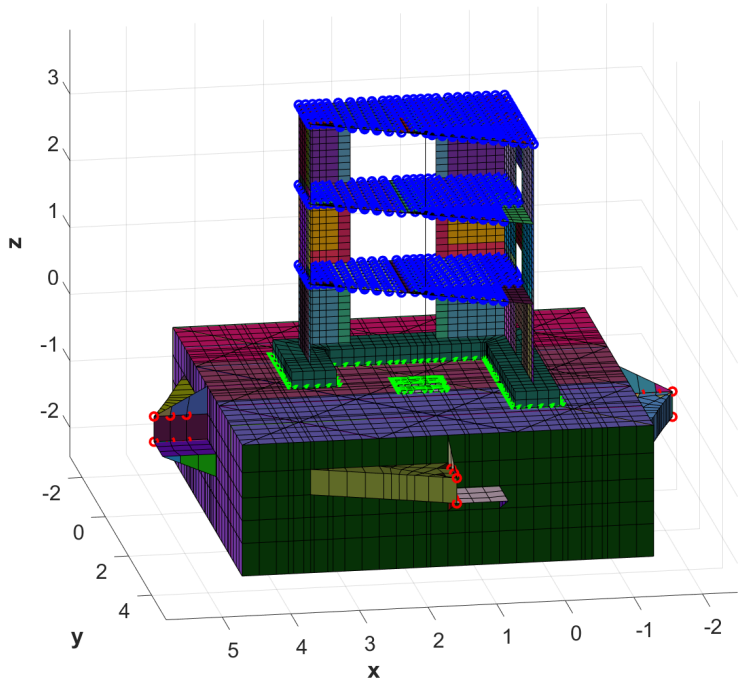

(c) FE mesh of model 1 fixed on the AZALEE shaking-table model (connected dots are in green, additional nodal masses in blue, locked nodes for BCs in red).

FIGURE A.4: Available FE models of the SMART2013 specimen. The yellow circles locate the sensors used for the model updating strategy in subfigures (a-b). Faces colors are random.

Appendix B

Semi-analytical expressions of mCRE derivatives

As a consequence of (1.23) and algorithmic requirements presented in Section 1.2.3, the mCRE-based model updating may become much more efficient in terms of CPU performance if analytical mCRE derivatives were easily computable. Fortunately, it is the case, and this appendix intends to gather all necessary mathematical developments for the proof. For the sake of simplicity, we will restrain the mathematical developments to a single angular frequency ω as the extension to a frequency range D_ω is trivial ($z(\omega)$-weighted integration). Besides, the subscript ω of mechanical fields will be omitted.

B.1 mCRE computation: back to the minimization with respect to mechanical fields

As mentioned above, we denote by $\widehat{s}(\theta;Y) = (\widehat{U},\widehat{V})$ the optimal solution in the mCRE sense for given parameters and measurements. In a FE framework, the constrained minimization problem allowing to determine $\widehat{s}$ is:

$$\widehat{s}(\theta;Y) \;=\; \arg \min_{[-\omega^2\boldsymbol{M}+i\omega\boldsymbol{D}]U+\boldsymbol{K}(\theta)V=F} e_\omega^2(s,\theta;Y) \tag{B.1}$$

Introducing Lagrange multipliers $\widehat{\Lambda}$ and an augmented cost-function, we will show in the remainder of this section that (B.1) is equivalent to the solution of the following linear system:

$$A\left[\begin{array}{c}\widehat{\Lambda}\\ \widehat{U}\end{array}\right] = b \text{ with } \left\{\begin{array}{rcl} \widehat{\Lambda} &=& \widehat{U}-\widehat{V}\\ A &=& \left[\begin{array}{cc}\left[\boldsymbol{K}(\theta)+i\omega\boldsymbol{D}-\omega^2\boldsymbol{M}\right]^H & \alpha\boldsymbol{\Pi}^H\boldsymbol{G}\boldsymbol{\Pi}\\ -\boldsymbol{K}(\theta) & \left[\boldsymbol{K}(\theta)+i\omega\boldsymbol{D}-\omega^2\boldsymbol{M}\right]\end{array}\right]\\ b &=& \left\{\begin{array}{c}\alpha\boldsymbol{\Pi}^H\boldsymbol{G}Y\\ F\end{array}\right\}\end{array}\right. \tag{B.2}$$

As we are dealing with quantities written in the **frequency domain**, derivatives and constraints must be considered with caution: **the real and imaginary parts have to be separated to write consistent mathematical expressions** (in particular Gateaux's derivatives). In the following, $\bullet_r$ and $\bullet_i$ will denote the real and imaginary parts of $\bullet$, respectively.

Let us introduce a set of Lagrange multipliers (Λ_0,Λ_1) to introduce an augmented cost-function that integrates the constraint on $s=(U,V)$:

$$\begin{aligned}\mathcal{L}(U,V,\Lambda_0,\Lambda_1,\theta;Y) \;=\; &\frac{1}{2}\|U-V\|^2_{\boldsymbol{K}(\theta)} \;+\; \frac{\alpha}{2}\|\boldsymbol{\Pi}U-Y\|^2_{\boldsymbol{G}}\\ &+\; \Lambda_0^T\left[[-\omega^2\boldsymbol{M}+i\omega\boldsymbol{D}]U+\boldsymbol{K}(\theta)V-F\right]_r\\ &+\; \Lambda_1^T\left[[-\omega^2\boldsymbol{M}+i\omega\boldsymbol{D}]U+\boldsymbol{K}(\theta)V-F\right]_i\end{aligned} \tag{B.3}$$

After separating real and imaginary parts of mechanical fields and measurements, one gets:

$$\begin{aligned}\mathcal{L}(U_r,U_i,V_r,V_i,\Lambda_0,\Lambda_1,\theta;Y) \;&= \frac{1}{2}\left[U_r-V_r-i(U_i-V_i)\right]^T\boldsymbol{K}(\theta)\left[U_r-V_r+i(U_i-V_i)\right]\\ &+\;\frac{\alpha}{2}\left[\boldsymbol{\Pi}U_r-Y_r-i(\boldsymbol{\Pi}U_i-Y_i)\right]^T\boldsymbol{G}\left[\boldsymbol{\Pi}U_r-Y_r+i(\boldsymbol{\Pi}U_i-Y_i)\right]\\ &+\;\Lambda_0^T\left[\boldsymbol{K}(\theta)V_r-\omega\boldsymbol{D}U_i-\omega^2\boldsymbol{M}U_r-F_r\right]\\ &+\;\Lambda_1^T\left[\boldsymbol{K}(\theta)V_i+\omega\boldsymbol{D}U_r-\omega^2\boldsymbol{M}U_i-F_i\right]\end{aligned} \tag{B.4}$$

As a reminder, the objective is now to find the mechanical fields that are coordinates of the saddle point of $\mathcal{L}$ for a given parameter vector θ. Mathematically, forgetting the $\widehat{\bullet}$ for enhanced readability, this problem reads:

$$\text{Find } (U_r,U_i,V_r,V_i,\Lambda_0,\Lambda_1)\in\mathbb{R}^{n_x}\times\ldots\times\mathbb{R}^{n_x} \text{ such that: } \begin{cases}(U_r^*)^T\,\frac{d\mathcal{L}}{dU_r}=0\;\forall\,U_r^*\in\mathbb{R}^{n_x}\\(U_i^*)^T\,\frac{d\mathcal{L}}{dU_i}=0\;\forall\,U_i^*\in\mathbb{R}^{n_x}\\\quad\vdots\\(\Lambda_1^*)^T\,\frac{d\mathcal{L}}{d\Lambda_1}=0\;\forall\,\Lambda_1^*\in\mathbb{R}^{n_x}\end{cases} \tag{B.5}$$

The six stationarity equations lead to the following system of linear equations:

$$\begin{cases}\boldsymbol{K}(\theta)\left[U_r-V_r\right]+\alpha\boldsymbol{\Pi}^H\boldsymbol{G}\left[\boldsymbol{\Pi}U_r-Y_r\right]-\omega^2\boldsymbol{M}\Lambda_0+\omega\boldsymbol{D}\Lambda_1=0\\ \boldsymbol{K}(\theta)\left[U_i-V_i\right]+\alpha\boldsymbol{\Pi}^H\boldsymbol{G}\left[\boldsymbol{\Pi}U_i-Y_i\right]-\omega\boldsymbol{D}\Lambda_0-\omega^2\boldsymbol{M}\Lambda_1=0\\ -\boldsymbol{K}(\theta)\left[U_r-V_r\right]+\boldsymbol{K}(\theta)\Lambda_0=0\\ -\boldsymbol{K}(\theta)\left[U_i-V_i\right]+\boldsymbol{K}(\theta)\Lambda_1=0\\ \boldsymbol{K}(\theta)V_r-\omega\boldsymbol{D}U_i-\omega^2\boldsymbol{M}U_r=F_r\\ \boldsymbol{K}(\theta)V_i+\omega\boldsymbol{D}U_r-\omega^2\boldsymbol{M}U_i=F_i\end{cases} \tag{B.6}$$

After having identified that $\Lambda_0=U_r-V_r$ and $\Lambda_1=U_i-V_i$ (assuming $\det(\boldsymbol{K}(\theta))\neq 0$), one can simplify this system into a 4-row-block linear system:

$$\underbrace{\begin{bmatrix}\boldsymbol{K}(\theta)-\omega^2\boldsymbol{M} & \alpha\boldsymbol{\Pi}^T\boldsymbol{G}\boldsymbol{\Pi} & \omega\boldsymbol{D} & 0\\ -\boldsymbol{K}(\theta) & \boldsymbol{K}(\theta)-\omega^2\boldsymbol{M} & 0 & -\omega\boldsymbol{D}\\ -\omega\boldsymbol{D} & 0 & \boldsymbol{K}(\theta)-\omega^2\boldsymbol{M} & \alpha\boldsymbol{\Pi}^T\boldsymbol{G}\boldsymbol{\Pi}\\ 0 & \omega\boldsymbol{D} & -\boldsymbol{K}(\theta) & \boldsymbol{K}(\theta)-\omega^2\boldsymbol{M}\end{bmatrix}}_{A_{\text{ext}}(\theta)}\underbrace{\begin{bmatrix}U_r-V_r\\U_r\\U_i-V_i\\U_i\end{bmatrix}}_{X_{\text{ext}}}=\underbrace{\begin{bmatrix}\alpha\boldsymbol{\Pi}^T\boldsymbol{G}Y_r\\F_r\\\alpha\boldsymbol{\Pi}^T\boldsymbol{G}Y_i\\F_i\end{bmatrix}}_{b_{\text{ext}}} \tag{B.7}$$

> *Remark* B.1. This mathematical development is true if $\boldsymbol{\Pi}$ takes its values in $\mathbb{R}$. This is the case for displacement and acceleration measurements in dynamics, but it is not the case for velocity or strain data! One must be a bit more careful if values of $\boldsymbol{\Pi}$ coefficients are in $\mathbb{C}$. However, it should not much change the shape of the matrix system.

The matrix system (B.7) can also be rewritten under the following form in order to fully decouple U from V:

$$\begin{aligned}&\mathcal{A}_{\text{ext}}(\theta)\mathcal{X}_{\text{ext}}=b_{\text{ext}}\text{ with}\\ &\mathcal{A}_{\text{ext}}(\theta)=\begin{bmatrix}\boldsymbol{K}(\theta)-\omega^2\boldsymbol{M}+\alpha\boldsymbol{\Pi}^T\boldsymbol{G}\boldsymbol{\Pi} & -(\boldsymbol{K}(\theta)-\omega^2\boldsymbol{M}) & \omega\boldsymbol{D} & -\omega\boldsymbol{D}\\ -\omega^2\boldsymbol{M} & \boldsymbol{K}(\theta) & -\omega\boldsymbol{D} & 0\\ -\omega\boldsymbol{D} & \omega\boldsymbol{D} & \boldsymbol{K}(\theta)-\omega^2\boldsymbol{M}+\alpha\boldsymbol{\Pi}^T\boldsymbol{G}\boldsymbol{\Pi} & -(\boldsymbol{K}(\theta)-\omega^2\boldsymbol{M})\\ \omega\boldsymbol{D} & 0 & -\omega^2\boldsymbol{M} & \boldsymbol{K}(\theta)\end{bmatrix}\\ &\mathcal{X}_{\text{ext}}^T=\begin{bmatrix}U_r^T & V_r^T & U_i^T & V_i^T\end{bmatrix}\end{aligned} \tag{B.8}$$

Combining the first two rows of (B.7) with the last two ones weighted by i, one can finally recover the system (B.2), which concludes the proof.

B.2 Model updating problem: minimization with respect to stiffness parameters

Now that the mCRE can be computed for any value of θ, its minimization with respect to the latter can be numerically done using unconstrained minimization algorithms such as the gradient steepest descent technique, the BFGS method or the trust-region algorithm[1]. In this section, semi-analytical expressions of the mCRE gradient and Hessian matrix with respect to θ are established for enhanced CPU time and construction of confidence intervals.

B.2.1 Analytical mCRE gradient

Once the mechanicals fields $\widehat{s}$ computed, the expression of the mCRE gradient with respect to the parameters to update can be analytical (only if the link between stiffness and parameters is too). The "tip" is to exploit the augmented cost function $\mathcal{L}$ derivative at the saddle point established above:

$$\left.\frac{\mathrm{d}e_\omega^2}{\mathrm{d}\theta}\right|_{\widehat{s}} \triangleq \left.\frac{\mathrm{d}\mathcal{L}}{\mathrm{d}\theta}\right|_{\widehat{s}} = \frac{\partial e_\omega^2}{\partial\theta} + \underbrace{\frac{\partial\mathcal{L}}{\partial U_r}\frac{\mathrm{d}U_r}{\mathrm{d}\theta} + \frac{\partial\mathcal{L}}{\partial V_r}\frac{\mathrm{d}V_r}{\mathrm{d}\theta} + \frac{\partial\mathcal{L}}{\partial U_i}\frac{\mathrm{d}U_i}{\mathrm{d}\theta} + \frac{\partial\mathcal{L}}{\partial V_i}\frac{\mathrm{d}V_i}{\mathrm{d}\theta}}_{=0 \text{ at the saddle point}} \tag{B.9}$$

As the parameters weight the FE stiffness matrix, a general formulation for the mCRE gradient with respect to parameter $\theta_k, k \in [\![1; n_\theta]\!]$ is:

$$\left.\frac{\mathrm{d}e_\omega^2}{\mathrm{d}\theta_k}\right|_{\widehat{s}} = \frac{1}{2}\left[U_r^T\frac{\partial\boldsymbol{K}}{\partial\theta_k}U_r + U_i^T\frac{\partial\boldsymbol{K}}{\partial\theta_k}U_i - V_r^T\frac{\partial\boldsymbol{K}}{\partial\theta_k}V_r - V_i^T\frac{\partial\boldsymbol{K}}{\partial\theta_k}V_i\right] \tag{B.10}$$

For the stiffness parametrization (1.14), one thus directly gets:

$$\left.\frac{\mathrm{d}e_\omega^2}{\mathrm{d}\theta_k}\right|_{\widehat{s}} = \frac{1}{2}\left[U_r^T\boldsymbol{K}_{0,k}U_r + U_i^T\boldsymbol{K}_{0,k}U_i - V_r^T\boldsymbol{K}_{0,k}V_r - V_i^T\boldsymbol{K}_{0,k}V_i\right] \tag{B.11}$$

The possibility to provide an analytical gradient when minizing the mCRE is thus strongly recommended due to its simplicity of implementation as well as the associated computational speed-up.

B.2.2 Semi-analytical mCRE Hessian matrix

Using the same starting idea, let us compute the mCRE Hessian matrix value at coordinate $j, k \in [\![1; n_\theta]\!]^2$:

$$\begin{aligned}\mathcal{H}_{jk}^\theta = \left.\frac{\mathrm{d}^2e_\omega^2}{\mathrm{d}\theta_j\mathrm{d}\theta_k}\right|_{\widehat{s}} \triangleq \frac{\mathrm{d}^2\mathcal{L}}{\mathrm{d}\theta_j\mathrm{d}\theta_k} = \frac{\partial^2\mathcal{L}}{\partial\theta_j\partial\theta_k} &+ \left[\frac{\mathrm{d}}{\mathrm{d}U_r}\left(\frac{\partial\mathcal{L}}{\partial\theta_k}\right)\right]^T\frac{\mathrm{d}U_r}{\mathrm{d}\theta_j} + \left[\frac{\mathrm{d}}{\mathrm{d}V_r}\left(\frac{\partial\mathcal{L}}{\partial\theta_k}\right)\right]^T\frac{\mathrm{d}V_r}{\mathrm{d}\theta_j} \\ &+ \left[\frac{\mathrm{d}}{\mathrm{d}U_i}\left(\frac{\partial\mathcal{L}}{\partial\theta_k}\right)\right]^T\frac{\mathrm{d}U_i}{\mathrm{d}\theta_j} + \left[\frac{\mathrm{d}}{\mathrm{d}V_i}\left(\frac{\partial\mathcal{L}}{\partial\theta_k}\right)\right]^T\frac{\mathrm{d}V_i}{\mathrm{d}\theta_j}\end{aligned} \tag{B.12}$$

Three terms to develop thus occur:

- The second order partial derivative of the augmented cost-function $\mathcal{L}$ is trivial:

$$\frac{\partial^2\mathcal{L}}{\partial\theta_j\partial\theta_k} = \frac{1}{2}\left[U_r^T\frac{\partial^2\boldsymbol{K}}{\partial\theta_j\partial\theta_k}U_r + U_i^T\frac{\partial^2\boldsymbol{K}}{\partial\theta_j\partial\theta_k}U_i - V_r^T\frac{\partial^2\boldsymbol{K}}{\partial\theta_j\partial\theta_k}V_r - V_i^T\frac{\partial^2\boldsymbol{K}}{\partial\theta_j\partial\theta_k}V_i\right] \tag{B.13}$$

[1] See the MATLAB© optimization toolbox or the `fminunc` documentation for complementary details.

- The crossed derivatives, whose computation is also direct:

$$\begin{cases} \dfrac{\mathrm{d}}{\mathrm{d}U_r}\left(\dfrac{\partial \mathcal{L}}{\partial \theta_k}\right) &= \dfrac{\partial K}{\partial \theta_k} U_r \\ \dfrac{\mathrm{d}}{\mathrm{d}V_r}\left(\dfrac{\partial \mathcal{L}}{\partial \theta_k}\right) &= -\dfrac{\partial K}{\partial \theta_k} V_r \\ \dfrac{\mathrm{d}}{\mathrm{d}U_i}\left(\dfrac{\partial \mathcal{L}}{\partial \theta_k}\right) &= \dfrac{\partial K}{\partial \theta_k} U_i \\ \dfrac{\mathrm{d}}{\mathrm{d}V_i}\left(\dfrac{\partial \mathcal{L}}{\partial \theta_k}\right) &= -\dfrac{\partial K}{\partial \theta_k} V_i \end{cases} \tag{B.14}$$

- The derivatives of $\widehat{s}$ with respect to parameters, whose computation can be obtained by derivation of the system $\mathcal{A}_{\text{ext}}\mathcal{X}_{\text{ext}} = b_{\text{ext}}$:

$$\frac{\mathrm{d}\mathcal{A}_{\text{ext}}}{\mathrm{d}\theta_j}\mathcal{X}_{\text{ext}} + \mathcal{A}_{\text{ext}}\frac{\mathrm{d}\mathcal{X}_{\text{ext}}}{\mathrm{d}\theta_j} = \frac{\mathrm{d}b_{\text{ext}}}{\mathrm{d}\theta_j} \Rightarrow \frac{\mathrm{d}\mathcal{X}_{\text{ext}}}{\mathrm{d}\theta_j} = \mathcal{A}_{\text{ext}}^{-1}\left[\frac{\mathrm{d}b_{\text{ext}}}{\mathrm{d}\theta_j} - \frac{\mathrm{d}\mathcal{A}_{\text{ext}}}{\mathrm{d}\theta_j}\mathcal{X}_{\text{ext}}\right] \tag{B.15}$$

with $\mathcal{A}_{\text{ext}}^{-1}$ that can be already known from the $\mathcal{A}_{\text{ext}}\mathcal{X}_{\text{ext}} = b_{\text{ext}}$ solution to compute the mCRE value (*e.g.* the inverse matrix can be stored) and:

$$\begin{cases} \dfrac{\mathrm{d}b_{\text{ext}}}{\mathrm{d}\theta_j} &= 0 \\ \dfrac{\mathrm{d}\mathcal{A}_{\text{ext}}}{\mathrm{d}\theta_j} &= \begin{bmatrix} \frac{\partial \boldsymbol{K}}{\partial \theta_j} & -\frac{\partial \boldsymbol{K}}{\partial \theta_j} & 0 & 0 \\ 0 & \frac{\partial \boldsymbol{K}}{\partial \theta_j} & 0 & 0 \\ 0 & 0 & \frac{\partial \boldsymbol{K}}{\partial \theta_j} & -\frac{\partial \boldsymbol{K}}{\partial \theta_j} \\ 0 & 0 & 0 & \frac{\partial \boldsymbol{K}}{\partial \theta_j} \end{bmatrix} \end{cases} \tag{B.16}$$

All simplifications done, one has:

$$\frac{\mathrm{d}}{\mathrm{d}\theta_j}\begin{bmatrix} U_r \\ V_r \\ U_i \\ V_i \end{bmatrix} = -\mathcal{A}_{\text{ext}}^{-1}\begin{bmatrix} \dfrac{\partial \boldsymbol{K}}{\partial \theta_j}(U_r - V_r) \\ \dfrac{\partial \boldsymbol{K}}{\partial \theta_j} V_r \\ \dfrac{\partial \boldsymbol{K}}{\partial \theta_j}(U_i - V_i) \\ \dfrac{\partial \boldsymbol{K}}{\partial \theta_j} V_i \end{bmatrix} \tag{B.17}$$

Finally, the general expression of $\mathcal{H}^{\theta}_{jk}$ reads:

$$\begin{aligned} \mathcal{H}^{\theta}_{jk} = \frac{1}{2}\left[U_r^T\frac{\partial^2 \boldsymbol{K}}{\partial\theta_j\partial\theta_k}U_r + U_i^T\frac{\partial^2 \boldsymbol{K}}{\partial\theta_j\partial\theta_k}U_i - V_r^T\frac{\partial^2 \boldsymbol{K}}{\partial\theta_j\partial\theta_k}V_r - V_i^T\frac{\partial^2 \boldsymbol{K}}{\partial\theta_j\partial\theta_k}V_i\right] \\ - \begin{bmatrix} \dfrac{\partial K}{\partial\theta_k}U_r \\ -\dfrac{\partial K}{\partial\theta_k}V_r \\ \dfrac{\partial K}{\partial\theta_k}U_i \\ -\dfrac{\partial K}{\partial\theta_k}V_i \end{bmatrix}^T \mathcal{A}_{\text{ext}}^{-1}\begin{bmatrix} \dfrac{\partial K}{\partial\theta_j}(U_r - V_r) \\ \dfrac{\partial K}{\partial\theta_j}V_r \\ \dfrac{\partial K}{\partial\theta_j}(U_i - V_i) \\ \dfrac{\partial K}{\partial\theta_j}V_i \end{bmatrix} \end{aligned} \tag{B.18}$$

The application of this expression to the stiffness parametrization (1.14) leads to:

$$\mathcal{H}^{\theta}_{jk} = -\begin{bmatrix} K_{0,k}U_r \\ -K_{0,k}V_r \\ K_{0,k}U_i \\ -K_{0,k}V_i \end{bmatrix}^T \mathcal{A}_{\text{ext}}^{-1}\begin{bmatrix} K_{0,j}(U_r - V_r) \\ K_{0,j}V_r \\ K_{0,j}(U_i - V_i) \\ K_{0,j}V_i \end{bmatrix} \tag{B.19}$$

Remark B.2. Due to the fact that the Hessian matrix depends on the inverse of $\mathcal{A}_{\text{ext}}$ whose expression is not analytical (once knowing mechanical fields), the expression of the Hessian can be considered as semi-analytical.

B.2.3 Exploitation for mCRE-based model updating

If the expression of the mCRE gradient with respect to parameters is easily available (according to the stiffness parametrization), **its formulae must be provided to minimization algorithms** in order to get enhanced numerical performances.

The case of the Hessian matrix is a bit different due to the fact that it requires intelligent storage of the inverse matrix of $\mathcal{A}_{\text{ext}}$ for all $\omega \in D_\omega$. In particular, one can note that A is inverted instead of $\mathcal{A}_{\text{ext}}$ due to its reduced size and direct availability from former literature works. Of course, providing the Hessian would also reduce the amount of iterations of nonlinear optimization algorithms but it also carries a storage burden that should be taken into account.

Appendix C

Morozov's discrepancy principle for the mCRE in dynamics

In order to go through technical details without carrying a burden due to notation complexity, please note that the notations used in the following appendices are not necessarily consistent with the ones of the contribution.

C.1 Theorem: Morozov's discrepancy principle

Let us consider an inverse problem $F(x) = y$ with its associated regularized cost-function $\mathcal{J} = \alpha\|F(x) - y_s^\delta\|^2 + R(x)$, R being the regularization function (in Tikhonov's sense). Assuming that a scalar δ_s quantifies measurement noise[1] such that noisy data y satisfies

$$\|F(x) - y\|^2 \leqslant \delta_s^2 \leqslant \|y\|^2 \tag{C.1}$$

and that R is strictly convex, non-negative, weakly coercive and weakly-lower semi-continuous, then, according to [Morozov 1984], there exists an optimal weighting $\widehat{\alpha}(\delta)$ associated to an inverse problem solution $x_{\widehat{\alpha}}^\delta$ such that

$$\|F(x_{\widehat{\alpha}}^{\delta_s}) - y\|^2 = \delta_s^2 \tag{C.2}$$

In other words, it is possible to calibrate the weighting coefficient α according to the noise level quantifier δ_s.

C.2 Adaptation to mCRE-based model updating

As all the conditions on R are met by the modeling error term of the mCRE functional, some attention must be paid to the definition of the upper bound of the data-to-model distance. Let us start from the fact that time-histories can be legitimately modeled such that:

$$y(t) = y_{ex}(t) + \eta(t) \tag{C.3}$$

where $y_{ex}(t)$ is the exact measurement time-series that would have been obtained without any measurement noise and $\eta(t)$ is a white-noise signal, whose value at each acquisition time step follows a standard Gaussian random variable: $\eta(t) \sim \mathcal{N}(0, \delta^2)\ \forall\ t$ with δ the noise amplitude (standard deviation of measurement noise).

Then, the frequency domain pre-processing step requires to take the (discrete) Fourier transform of measurements. Focusing on the frequency range D_ω, and using the linearity property of the Fourier transform, one has:

$$Y_\omega = Y_{ex,\omega} + H_\omega,\ \forall\ \omega \in D_\omega \tag{C.4}$$

[1] The s index allows to clearly distinguish the noise level δ from the bound δ_s of Morozov's theorem (C.2).

where H_ω is the Fourier transform of the random process $\eta(t)$. From here, one can properly introduce the mCRE measurement error by replacing $Y_{ex,\omega}$ with $\mathbf{\Pi}U_\omega$:

$$\|\mathbf{\Pi}U_\omega - Y_\omega\|^2_{\boldsymbol{G}} = \|H_\omega\|^2_{\boldsymbol{G}},\ \forall\ \omega \in D_\omega \tag{C.5}$$

$$\Rightarrow \int_{D_\omega} \frac{z(\omega)}{2}\|\mathbf{\Pi}U_\omega - Y_\omega\|^2_{\boldsymbol{G}}\ \mathrm{d}\omega = \int_{D_\omega} \frac{z(\omega)}{2}\|H_\omega\|^2_{\boldsymbol{G}}\ \mathrm{d}\omega \tag{C.6}$$

If one knows the statistics of the square modulus $\|H_\omega\|^2$ of the discrete Fourier transform of a random process, then the δ scalar of the Morozov discrepancy theorem would be explicitely made available in a formulation dedicated to the mCRE.

C.2.1 Probability distribution function of a random process

H_ω is the amplitude of the discrete Fourier transform of $\{\eta(t_n) = \eta_n\}_{n=0}^{N-1}$ at angular frequency ω. Mathematically, it means that:

$$H_\omega \ \triangleq\ \mathcal{F}\left(\{\eta_n\}_{n=0}^{N-1}, \omega\right) = \sum_{n=0}^{N-1} \eta_n e^{-2i\pi\omega n/N} \tag{C.7}$$

Focusing on the real part of H_ω denoted $\Re(H_\omega)$, one has:

$$\Re(H_\omega) = \sum_{n=0}^{N-1} \eta_n \cos\left(2\pi\omega n/N\right) \tag{C.8}$$

Denoting $y_n = \eta_n \cos\left(2\pi\omega n/N\right)$, it implies that the pdf of y_n satisfies:

$$\pi_{y_n}(y) = \frac{1}{\cos\left(2\pi\omega n/N\right)}\pi_{\eta_n}\left(\frac{y}{\cos\left(2\pi\omega n/N\right)}\right) \tag{C.9}$$

In other words, $y_n \sim \mathcal{N}(0, \delta^2\cos\left(2\pi\omega n/N\right)^2)$. For the sake of conciseness, we will abbreviate $\cos\left(2\pi\omega n/N\right)) \equiv c_{\omega,n}$. With such a notation, one has $y_n \sim \mathcal{N}(0, \delta^2 c^2_{\omega,n})\ \forall\ n \in [\![0; N-1]\!]$.

The pdf of $\Re(H_\omega)$ is the convolution of all the random variables y_n (that have to be summed in the discrete Fourier transform).

$$\pi_{\Re(H_\omega)}(x) = \bigotimes_{n=0}^{N-1} \pi_{y_n}(x) \tag{C.10}$$

Taking the Fourier transform of the last equation allows to simplify the convolutional product:

$$\mathcal{F}\left(\pi_{\Re(H_\omega)}, k\right) = \prod_{n=0}^{N-1} \mathcal{F}\left(\pi_{y_n}, k\right) \tag{C.11}$$

Knowing that the Fourier transform of a Gaussian function of standard deviation σ is also a Gaussian of standard deviation $1/\sigma$, one can write

$$\mathcal{F}\left(\pi_{\Re(H_\omega)}, k\right) \propto \exp\left[-\frac{-k^2\delta^2}{2}\sum_{n=0}^{N-1}\cos\left(2\pi\omega n/N\right)^2\right] = \exp\left[-\frac{-k^2\delta^2 N}{4}\right] \tag{C.12}$$

Therefore, one finally gets that the Fourier transform of $\Re(H_\omega)$ is a random variable following a centered Gaussian pdf of standard deviation $\sqrt{2}/(\delta\sqrt{N})$. One can conclude that $\Re(H_\omega) \sim \mathcal{N}\left(0, \delta^2 N/2\right)$. The same conclusion holds for the imaginary part of H_ω denoted $\Im(H_\omega)$.

We have thus proved that the discrete Fourier transform of a Gaussian random process is also a random variate whose pdf is a multivariate Gaussian law, both its real and imaginary parts taken alone being zero-mean Gaussian random variables of standard deviation $\sigma\sqrt{N/2}$. From this result, it is worth mentioning that:

- the measurement noise level directly impacts the value of H_ω;
- there is no dependency on the considered angular frequency ω, which is consistent with the well-known constant Power Spectral Density (PSD) of a white-noise signal;
- the dependency on the number of sampling points in the time domain N seems intuitively logical as the more data points, the more accurate a Fourier transform of a white noise. This dependency can be cancelled by normalizing the discrete Fourier transform by $1/\sqrt{N}$, which is done numerically in the MATLAB© `fft` function.

C.2.2 Probability distribution function of the squared modulus of a random process

Now that the distribution of H_ω is known, to identify which law follows $\|H_\omega\|^2$, we can exploit the following theorem:

Be $[X_1; \dots; X_d]$ a vector of d random variables such that $X_i \sim \mathcal{N}(0,1)\ \forall i \in [\![1; d]\!]$ and all couples of random variables $(X_i, X_j),\ i \neq j$ are independent. Then the squared norm of vector $[X_1; \dots; X_d]$, denoted Y, follows a chi-squared distribution of degree d. In other words:

$$Y = \sum_{i=0}^{d} X_i^2 \sim \chi^2(d) \text{ with } \pi_Y(y) = \frac{(1/2)^{d/2}}{\Gamma(d/2)} y^{d/2-1} e^{-y/2}$$

where $\Gamma : d \mapsto \int_{\mathbb{R}^+} t^{d-1} e^{-t}\, \mathrm{d}t$ is the Gamma function.

The real and imaginary components of a Fourier transform indeed correspond to the individual Fourier transforms even and odd components of the time domain function. As all functions can be decomposed as a sum of an even and odd function, and since the Fourier transform is a one-to-one mapping between the time and frequency domains, the lack of correlation between even and odd parts in the time domain would imply a lack of correlation in the frequency domain too. As we deal with a zero-mean white-noise time series, the real and imaginary parts of its Fourier transform are thus uncorrelated.

As $\Re(H_\omega)$ and $\Im(H_\omega)$ are both centered Gaussian random variables of standard deviation $\delta\sqrt{N/2}$, one can deduce that the pdf of $2N/\sigma^2\|H_\omega\|^2$ is a noncentered chi-squared distribution of degree 2 with $\lambda = 0$. After variable change, one finally obtains an analytical formulation for the pdf of $\|H_\omega\|^2$:

$$\pi_{\|H_\omega\|^2}(x) = \frac{e^{-x/(\delta^2/N)}}{\delta^2/N} \tag{C.13}$$

As mentioned in the remarks of the previous paragraph, a $1/\sqrt{N}$ normalization of the Fourier transforms allows to take off the dependency into the number of time points N.

Therefore, the squared modulus of a zero-mean random process $\|H_\omega\|^2$ follows a noncentered $\chi^2(2)$ probability distribution conditioned by the measurement noise variance δ^2, whatever the value of ω. In particular, one can note that

$$\mathbb{E}\left(\|H_\omega\|^2\right) = \delta^2 \tag{C.14}$$

where $\mathbb{E}(\square)$ is the mathematical expectation operator. Assuming G is proportional to the identity matrix, *i.e.* $G = G_0 I$, then one recovers (1.43), which is the adaptation of Morozov's discrepancy principle to the mCRE framework (in the frequency domain).

C.2.3 Numerical illustrations

To provide a simple numerical illustration of the property described above, let us use MATLAB© and apply the following steps:

- Monte-Carlo sampling: draw a large number 100000 of 10 s-long random white-noise signals $x(t)$, having a given sampling frequency $f_s = 1000$ Hz and a given standard deviation $\sigma = 1$.

- Extract the $f_0 = 10$ Hz component, denoted X_{ω_0} (arbitrary choice) of the ($1/\sqrt{N}$-normalized) discrete Fourier transform of each signal;
- Use maximum likelihood estimation (MLE) to fit the histogram of $\Re(X_{\omega_0})$, $\Im(X_{\omega_0})$, $|X_{\omega_0}|$ with standard pdfs.

The results are displayed in Fig. C.1, and are in perfect accordance with the previous mathematical developments.

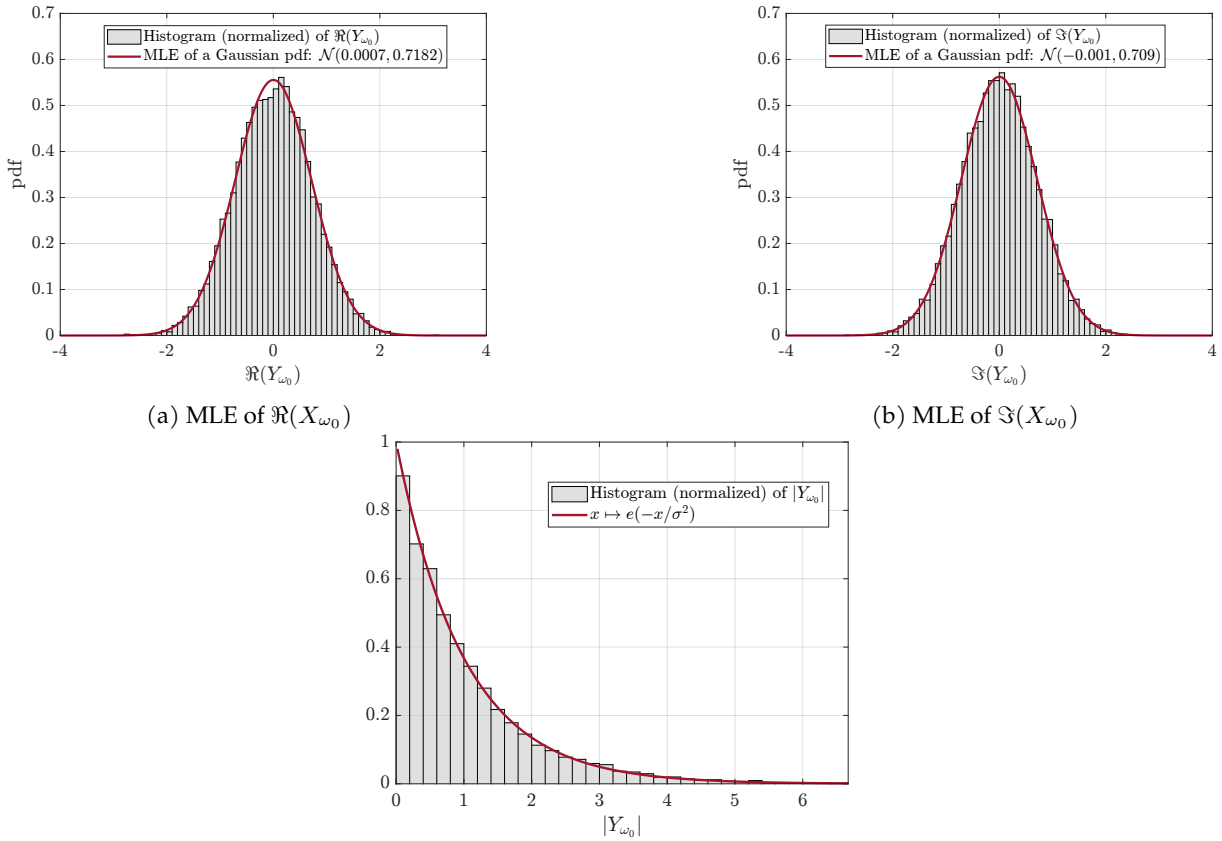

(a) MLE of $\Re(X_{\omega_0})$

(b) MLE of $\Im(X_{\omega_0})$

(c) MLE of $|X_{\omega_0}|$

Figure C.1: Numerical evidence of the probability distribution function followed by the discrete Fourier transform of white-noise signals.

Appendix D

An interpretation of Kalman filtering from Bayesian inference

Starting from the following linear state-space dynamical system:

$$\begin{cases} x_{k+1} &= \boldsymbol{A}x_k + \boldsymbol{B}e_k + w_k \\ y_k &= \boldsymbol{C}x_k + v_k \end{cases} \tag{D.1}$$

with x_k, y_k, w_k, v_k respectively refer to the discretized state vector, measurements, model error noise and measurement noise (all at time step k), let us show that the Kalman filter equations can also be derived from the Bayesian inference framework.

D.1 Bayes theorem, Markov process and Gaussian pdfs

Let us first rewrite Bayes' theorem by considering discrete measurements that have been sequentially obtained:

$$\pi\left(x_k|y_{0:k}\right) \;=\; \frac{\pi\left(y_{0:k}|x_k\right)\pi\left(x_k\right)}{\pi\left(y_{0:k}\right)} \tag{D.2}$$

where $\pi(\square)$ is the pdf associated with the random variable $\square$ and the index $(0:k)$ denotes all values over interval $[t_0, t_k]$.

Then assuming that,

(i) The state vector is a Markov process: $\pi(x_k|x_{0:k-1}) = \pi(x_k|x_{k-1})$,

(ii) Observations are independent from the state history: $\pi(y_k|x_{0:k}) = \pi(y_k|x_k)$,

then one can rewrite Bayes' theorem as follows:

$$\pi\left(x_k|y_{0:k}\right) \;=\; \frac{\pi(x_k, y_k|y_{0:k-1})}{\pi(y_k|y_{0:k-1})} \;=\; \frac{\pi(y_k|x_k, y_{0:k-1})\pi(x_k|y_{0:k-1})}{\pi(y_k|y_{0:k-1})} \;=\; \frac{\pi(y_k|x_k)\pi(x_k|y_{0:k-1})}{\pi(y_k|y_{0:k-1})} \tag{D.3}$$

Therefore, the *posterior* pdf $\pi\left(x_k|y_{0:k}\right)$ only depends on (i) the *prior* pdf $\pi\left(x_k|y_{0:k-1}\right)$ which reflects the model quality and (ii) the likelihood pdf $\pi(y_k|x_k)$ which reflects the measure quality as well as the uncertainty propagation into the model. Note that the normalization term (denominator) does not impact much the *posterior* pdf.

To determine the optimal state x_k, the *Maximum a Posteriori* method can be applied. To do so, one must explicit the likelihood and *prior* pdfs. The Gaussian assumption previously made permits to write those pdfs in the following form:

$$\pi(\square) \propto \exp\left(-\frac{1}{2}\left(\square - \mathbb{E}\left(\square\right)\right)^T)\boldsymbol{P}_{\square}^{-1}\left(\square - \mathbb{E}\left(\square\right)\right)\right) \tag{D.4}$$

In other words, the determination of expected values and covariance matrices of the likelihood and *prior* pdfs is sufficient to obtain the *posterior* pdf.

D.2 Likelihood pdf formulation - mean and covariance

The mean value of the likelihood can be immediately estimated inasmuch as observations are statistically independent of the state:

$$\mathbb{E}\left(y_k|x_k\right) \;=\; \mathbb{E}\left(y_k\right) \;=\; \mathbb{E}\left(\boldsymbol{C}x_k + v_k\right) \;=\; \mathbb{E}\left(\boldsymbol{C}x_k\right) \tag{D.5}$$

as the measurement noise is assumed to be a zero-mean Gaussian variable. Due to the fact that only one trajectory at time point k is considered, one finally gets:

$$\mathbb{E}\left(y_k|x_k\right) \;=\; \boldsymbol{C}x_k \tag{D.6}$$

Regarding the covariance matrix of the likelihood pdf, one can also use the statistical independence between state and observations to directly obtain:

$$\text{cov}[y_k|x_k] \;=\; \text{cov}[y_k] \;=\; \mathbb{E}\left(\left(y_k - \mathbb{E}\left(y_k\right)\right)\left(y_k - \mathbb{E}\left(y_k\right)\right)^T\right) \;=\; \mathbb{E}\left(v_k v_k^T\right) \tag{D.7}$$

Insofar as v_k is a Gaussian random variable having a covariance matrix $\boldsymbol{R}$, one concludes that

$$\text{cov}[y_k|x_k] \;=\; \boldsymbol{R} \tag{D.8}$$

The likelihood pdf therefore reads:

$$\pi(y_k|x_k) \propto \exp\left(-\frac{1}{2}\left(y_k - \boldsymbol{C}x_k\right)^T \boldsymbol{R}^{-1}\left(y_k - \boldsymbol{C}x_k\right)\right) \tag{D.9}$$

D.3 Prior pdf formulation - mean and covariance

Using the statistical independence between current state and former measurements, one has directly a simplified expression of the *prior* pdf mean:

$$\mathbb{E}\left(x_k|y_{0:k-1}\right) \;=\; \mathbb{E}\left(x_k\right) \;=\; \mathbb{E}\left(\boldsymbol{A}x_{k-1} + \boldsymbol{B}e_{k-1} + w_{k-1}\right) \;=\; \mathbb{E}\left(\boldsymbol{A}x_{k-1} + \boldsymbol{B}e_{k-1}\right) \tag{D.10}$$

as the process noise is assumed to be a zero-mean Gaussian variable. Due to the fact that only one trajectory at time point k is considered and denoting $\hat{x}_k^- \;=\; \boldsymbol{A}x_{k-1} + \boldsymbol{B}e_{k-1}$, the *a priori* estimate, one finally gets:

$$\mathbb{E}\left(x_k|y_{0:k-1}\right) \;=\; \mathbb{E}\left(\widehat{x}_k^-\right) \;=\; \widehat{x}_k^- \tag{D.11}$$

Following the same process as for the likelihood pdf, the covariance of the *a priori* pdf reads:

$$\text{cov}[x_k|y_{0:k-1}] \;=\; \text{cov}[x_k] \;=\; \mathbb{E}\left(\left(x_k - \mathbb{E}\left(x_k\right)\right)\left(x_k - \mathbb{E}\left(x_k\right)\right)^T\right) \tag{D.12}$$

One can therefore conclude that

$$\text{cov}[x_k|y_{0:k-1}] \;= \boldsymbol{P}_k^- \tag{D.13}$$

The *prior* pdf therefore reads:

$$\pi(x_k|y_{0:k-1}) \propto \exp\left(-\frac{1}{2}\left(x_k - \widehat{x}_k^-\right)^T \left(\boldsymbol{P}_k^-\right)^{-1}\left(x_k - \widehat{x}_k^-\right)\right) \tag{D.14}$$

D.4 Maximum a Posteriori principle

The substitution of (D.9) and (D.14) into (D.3) enables to rewrite the *posterior* pdf:

$$\pi(x_k|y_{0:k}) \propto \exp\left\{-\frac{1}{2}\left[\left(y_k - \boldsymbol{C}x_k\right)^T \boldsymbol{R}^{-1}\left(y_k - \boldsymbol{C}x_k\right) + \left(x_k - \widehat{x}_k^-\right)^T \left(\boldsymbol{P}_k^-\right)^{-1}\left(x_k - \widehat{x}_k^-\right)\right]\right\} \tag{D.15}$$

In order to recover the *a posteriori* optimal state estimate, one intends to apply a MAP principle to maximize the *posterior* pdf:

$$\left.\frac{\partial \log \pi(x_k|y_{0:k})}{\partial\, x_k}\right|_{x_k=\widehat{x}_k} = 0 \tag{D.16}$$

The use of (D.15) allows to write the expression of the *a posteriori* state estimate based on the *a priori* estimate and current measurements:

$$\widehat{x}_k \;=\; \left(\boldsymbol{C}^T\boldsymbol{R}^{-1}\boldsymbol{C} + (\boldsymbol{P}_k^-)^{-1}\right)^{-1}\left((\boldsymbol{P}_k^-)^{-1}\widehat{x}_k^- + \boldsymbol{C}^T\boldsymbol{R}^{-1}y_k\right) \tag{D.17}$$

This expression can be simplified using the inverse matrix lemma[1]. All simplifications done, one obtains:

$$\widehat{x}_k \;=\; \widehat{x}_k^- + \boldsymbol{K}_k\left(y_k - \boldsymbol{C}\widehat{x}_k^-\right) \tag{D.18}$$

where $\boldsymbol{K}_k$ is the so-called Kalman gain:

$$\boldsymbol{K}_k \;=\; \boldsymbol{P}_k^-\boldsymbol{C}^T(\boldsymbol{C}\boldsymbol{P}_k^-\boldsymbol{C}^T + \boldsymbol{R})^{-1} \tag{D.19}$$

To have a full correction scheme from measurements, an explicit formulation of covariance matrices $\boldsymbol{P}_k^-$ and $\boldsymbol{P}_k$ is required. Using the notations of Section 4.2.1, one can establish that:

$$\boldsymbol{P}_k^- \;=\; \text{cov}[\epsilon_k^-\epsilon_k^{-T}] \text{ with } \epsilon_k^- = x_k - \widehat{x}_k^- \tag{D.20}$$

as the definition of the *a priori* estimate at point k is derived from the *a posteriori* estimate at step $k-1$. From a theoretical point of view, it reads:

$$\begin{aligned}\epsilon_k^- \;&=\; \underbrace{\boldsymbol{A}x_{k-1} + \boldsymbol{B}e_{k-1} + w_{k-1}}_{x_k \text{ from } x_{k-1}} - \underbrace{(\boldsymbol{A}\widehat{x}_{k-1} + \boldsymbol{B}e_{k-1})}_{\widehat{x}_k^- \text{ definition}} \\ &=\; \boldsymbol{A}\epsilon_{k-1} + w_{k-1}\end{aligned} \tag{D.21}$$

As a consequence, an expression of $\boldsymbol{P}_k^-$ from the state and covariance estimates of the previous time step is available:

$$\boldsymbol{P}_k^- \;=\; \boldsymbol{A}\text{cov}\left[\epsilon_{k-1}\epsilon_{k-1}^T\right]\boldsymbol{A}^T + \text{cov}[w_{k-1}w_{k-1}^T] \;=\; \boldsymbol{A}\boldsymbol{P}_{k-1}\boldsymbol{A}^T + \boldsymbol{Q} \tag{D.22}$$

In order to obtain all the KF equations, the correction of the predicted state covariance matrix is still missing. In other words, one needs to formulate the equation giving $\boldsymbol{P}_k$ with respect to $\boldsymbol{P}_k^-$. To do so, it is mandatory to start from the covariance definition of the *a posteriori* error estimate:

$$\begin{aligned}\epsilon_k \;&=\; x_k - \widehat{x}_k = x_k - \widehat{x}_k^- - \boldsymbol{K}_k(y_k - \boldsymbol{C}\widehat{x}_k^-) \\ &=\; \epsilon_k^- - \boldsymbol{K}_k\boldsymbol{C}\epsilon_k^- - \boldsymbol{K}_k v_k \;=\; (\boldsymbol{I} + \boldsymbol{K}_k\boldsymbol{C})\epsilon_k^- - \boldsymbol{K}_k v_k\end{aligned} \tag{D.23}$$

Therefore, the *a posteriori* state covariance matrix reads:

$$\boldsymbol{P}_k \;= (\boldsymbol{I} - \boldsymbol{K}_k\boldsymbol{C})\boldsymbol{P}_k^-(\boldsymbol{I} - \boldsymbol{K}_k\boldsymbol{C})^T + \boldsymbol{K}_k\boldsymbol{R}\boldsymbol{K}_k^T \tag{D.24}$$

Substituting the expression of the Kalman gain (D.19) allows to simplify this expression:

$$\begin{aligned}\boldsymbol{P}_k \;&=\; \boldsymbol{P}_k^- - \boldsymbol{K}_k\boldsymbol{C}\boldsymbol{P}_k^- - \boldsymbol{P}_k^-\boldsymbol{C}^T\boldsymbol{K}_k^T + \boldsymbol{K}_k^T(\boldsymbol{C}\boldsymbol{P}_k^-\boldsymbol{C}^T + \boldsymbol{R})\boldsymbol{K}_k \\ &=\; \boldsymbol{P}_k^- - \boldsymbol{P}_k^-\boldsymbol{C}^T(\boldsymbol{C}\boldsymbol{P}_k^-K_k^T + \boldsymbol{R})^{-1}\boldsymbol{C}\boldsymbol{P}_k^- \\ &=\; (\boldsymbol{I} - \boldsymbol{K}_k\boldsymbol{C})\boldsymbol{P}_k^-\end{aligned} \tag{D.25}$$

All the Kalman filter equations, for both prediction and correction steps have then be recovered from the Bayesian inference framework.

[1] Inverse matrix lemma: $\boldsymbol{A} = \boldsymbol{B}^{-1} + \boldsymbol{C}\boldsymbol{D}^{-1}\boldsymbol{C}^T \Leftrightarrow \boldsymbol{A}^{-1} = \boldsymbol{B} - \boldsymbol{B}\boldsymbol{C}(\boldsymbol{D} + \boldsymbol{C}^T\boldsymbol{B}\boldsymbol{C})^{-1}\boldsymbol{C}^T\boldsymbol{B}$.

Appendix E

Publications and communications

The research work presented in this manuscript has been the subject of publications and communications in conferences that are listed below:

Publications in peer-reviewed journals

M. Diaz, P.-É. Charbonnel, and L. Chamoin [2022c]. "Robust energy-based model updating framework for random processes in dynamics: application to shaking-table experiments". *Computers and Structures* 264.106746, p. 40. DOI: https://doi.org/10.1016/j.compstruc.2022.106746

M. Diaz, P.-É. Charbonnel, and L. Chamoin [2023a]. "A new Kalman filter approach for structural parameter tracking: Application to the monitoring of damaging structures tested on shaking-tables". *Mechanical Systems and Signal Processing* 182, p. 109529. DOI: 10.1016/j.ymssp.2022.109529

M. Diaz, P.-É. Charbonnel, and L. Chamoin [2023d]. "Merging experimental design and structural identification around the concept of modified Constitutive Relation Error in low-frequency dynamics for enhanced structural monitoring". *Mechanical Systems and Signal Processing* (*under review*) - *available in hal* (*03878634*)

M. Diaz, P.-É. Charbonnel, and L. Chamoin [2023c]. "Fully automated model updating framework for damage detection based on the modified Constitutive Relation Error". *Computational Mechanics*. DOI: 10.1007/s00466-023-02382-z

National communications

M. Diaz, P.-É. Charbonnel, and L. Chamoin [2021]. "Towards a fully automated model updating framework for low-frequency dynamics: application to shaking-table testings". *Journée thématique Identification & Validation de la Fédération Francilienne de Mécanique* (*F2M*). ENSAM, Paris

M. Diaz, P.-É. Charbonnel, and L. Chamoin [2022e]. "Vers une stratégie robuste et automatisée pour le recalage de modèles en dynamique vibratoire : application au suivi des structures endommageantes testées sur table vibrante". *15ème Colloque National en Calcul des Structures* (*CSMA 2022*). Giens, France

M. Diaz, P.-É. Charbonnel, and L. Chamoin [2022b]. "Automated physics-guided data assimilation strategy for model updating in dynamics - Application to the monitoring of structures tested on shaking tables". *Journée scientifique de l'Institut SEISM Paris-Saclay* (*GIS SEISM*). Saclay, France

International communications

M. Diaz, P.-É. Charbonnel, and L. Chamoin [2022a]. "A new data assimilation framework using the modified Constitutive Relation Error for online structural monitoring: application to shaking-table experiments". *8th European Congress on Computational Methods in Applied Sciences and Engineering - ECCOMAS Congress 2022*. Oslo, Norway

M. Diaz, P.-É. Charbonnel, and L. Chamoin [2022d]. "Towards an automated physics-regularized model updating strategy applied to the monitoring of civil engineering structures in low-frequency dynamics". *7th European Conference on Structural Control - EACS 2022*. Warsaw, Poland

M. Diaz, P.-É. Charbonnel, and L. Chamoin [2023b]. "A new physics-guided data assimilation framework for online structural monitoring: application to shaking-table tests". *COMPDYN2023 - 9th ECCOMAS Thematic Conference on Computational Methods in Structural Dynamics and Earthquake Engineering*. Athens, Greece

Appendix F

Extended abstract in French

Contexte industriel et problématique

L'analyse et la prédiction de la réponse de systèmes dynamiques nécessitent la mise à disposition de modèles numériques avancés. Ces derniers peuvent être construits directement sur la base de données ou à partir des équations traduisant les phénomènes physiques sous-jacents. Quoi qu'il en soit, il est impératif que le degré de représentativité du modèle soit suffisamment élevé pour son utilisation pratique : ce n'est pas le niveau de complexité du modèle mais le niveau de confiance que l'on peut avoir en ses prédictions qui est déterminant lorsqu'on le confronte à des données expérimentales.

Comme la plupart des systèmes sont désormais instrumentés avec de nombreux capteurs, les modèles numériques sont directement comparés et augmentés par comparaison aux mesures collectées. La validation et l'enrichissement du modèle par les données font partie du paradigme du jumeau numérique, dont les applications sont nombreuses et variées [Chinesta et al. 2018]. Cet aspect est également mis en exergue au sein du paradigme *Dynamic Data Driven Application Systems* - DDDAS [Darema 2004], où l'objectif est d'établir une synergie forte entre le modèle et les données:

(i) Le système réel est piloté grâce aux prédictions du modèle,
(ii) et le modèle est recalé grâce aux mesures assimilées en temps réel.

C'est dans ce cadre que s'inscrivent les travaux de thèse présentés dans ce mémoire, avec une application dédiée aux besoins industriels du CEA pour le génie parasismique.

Le laboratoire EMSI du CEA Saclay est équipé de tables vibrantes permettant de reproduire des chargements sismiques complexes sur des ouvrages de génie civil de taille conséquente. Ces tables sont connectées et pilotées par des vérins hydrauliques de forte puissance. Ces actionneurs sont eux-mêmes contrôlés par l'intermédiaire de servo-valves, composants permettant d'alimenter en débit les vérins à tension électrique donnée.

En pratique, le contrôle de ces actionneurs n'est pas une tâche facile, en raison des nombreux phénomènes non-linéaires présents dans le système. Si des stratégies de contrôle robustes, couplant contrôle par rétroaction et par anticipation telles que le TVC [Tagawa and Kajiwara 2007] peuvent être employées, de nouveaux besoins ont émergé ces dernières années, poussant les techniques de contrôle à leurs limites au détriment parfois de la sécurité de l'installation. Ces nouveaux besoins pour les essais standards sont aujourd'hui d'atteindre précision, rapidité et stabilité sans réaliser d'essai d'identification (pré-test) et sans contrainte de niveau d'essai, de manière à ne pas pré-endommager des structures et d'être capable de simuler un séisme de fort niveau dès le premier essai.

Les lois de commande des vérins hydrauliques qui les pilotent n'intègrent pas directement l'évolution de l'état de santé des structures testées, pouvant pourtant soudainement se dégrader et conduire à des essais instables, menaçant l'intégrité de l'installation expérimentale [Richard et al. 2016]. Les stratégies de contrôle implémentées sont actuellement de type "itératives" : les gains du contrôleur sont réglés essai après essai pour tenir compte de l'endommagement progressif de la structure, jusqu'à atteindre le niveau de sollicitation initialement ciblé [Le Maoult et al. 2010; Gang et al. 2013].

L'objectif de cette thèse est de mettre en place un cadre DDDAS pour faciliter et améliorer le contrôle des tables vibrantes. Pour ce faire, une stratégie d'assimilation de données unifiée autour du concept d'erreur en relation de comportement modifiée (ERCm) est développée, permettant de recaler un modèle numérique de la structure testée pour, *in fine*, régler à la volée les lois de contrôle en temps réel.

L'erreur en relation de comportement modifiée, fonctionnelle robuste pour le recalage de modèle *a posteriori*

L'ERCm est une fonctionnelle d'identification déterministe qui se distingue des fonctionnelles de type "moindres-carrés" par le terme d'erreur en relation de comportement (ERC) [Chouaki et al. 1997]. Cette erreur de modèle au sens mécanique fort complète le terme classique de distance entre les données et le modèle, de sorte à ne plus nécessiter de régularisation au sens de Tikhonov, dont le choix est toujours *a priori* et dépendant de l'utilisateur. Dans le cadre ERCm, on s'affranchit donc du caractère mal-posé du problème inverse par l'intermédiaire d'un indicateur de qualité intrinsèque du modèle. Cela permet de tenir compte simultanément de l'effet de bruit de mesure (dans la distance aux données), et de l'erreur de modèle (dans le terme d'ERC). En pratique, l'ERC est construite en distinguant parmi les équations du problèmes lesquelles sont fiables et lesquelles ne le sont pas. Une fois cette séparation faite, l'ERCm permet de quantifier à quel point une solution mécanique respectant strictement les équations fiables du problème (dans notre cas, conditions aux limites, géométries, équilibre dynamique, position des capteurs) est valable au sens des équations sujettes à caution (dans notre cas, relations de comportement et proximité aux mesures collectées).

Cette fonctionnelle a largement été utilisée ces 30 dernières années dans la littérature, en raison de sa forte convexité et de sa forte robustesse au bruit de mesure [Deraemaeker et al. 2002; Allix et al. 2005; Feissel and Allix 2007; Aquino and Bonnet 2019] avec des applications variées, allant de la détection de défauts dans des structures [Faverjon and Sinou 2009; Charbonnel et al. 2013; T. Silva and Maia 2017; Guo et al. 2018; Oliveira et al. 2021], jusqu'à la reconstruction complète de champs paramétriques en élasto-dynamique (lorsque la densité de points d'acquisition le permet) [Banerjee et al. 2013; Warner et al. 2014; Guchhait and Banerjee 2018], ou l'identification à la volée de comportements non-linéaires [Marchand et al. 2019].

Dans le cadre de ces travaux de thèse, une stratégie d'identification par ERCm a d'abord été mise en œuvre *a posteriori* pour traiter des mesures dans le domaine fréquentiel en basses-fréquences, pour d'abord évaluer la capacité à traiter les données recoltées d'essais achevés. Une stratégie intégralement automatisée a été proposée pour identifier les paramètres de raideur de modèles éléments finis de manière robuste et fiable [M. Diaz et al. 2022c; 2023c]. Une attention particulière a été prêtée pour améliorer le réglage de la fonctionnelle en exploitant le plus possible la richesse d'informations contenue dans les données:

- ▷ La pondération des fréquences de la plage d'analyse est réglée selon le contenu fréquentiel des données à disposition, grâce à un indicateur modal [Allemang and Brown 2006].
- ▷ Un pré-traitement des données par fenêtrage permet d'augmenter la robustesse statistique au bruit de mesure.
- ▷ Une norme de Mahalanobis pour mesurer la distance entre modèles et données est préconisée, intégrant de fait une connaissance de la corrélation des données via la matrice de covariance du bruit de mesure des capteurs utilisés.

- ▷ Le réglage du paramètre de pondération relative de l'ERC par rapport à la distance aux mesures est critique dans l'obtention de résultats d'identification pertinents. Plusieurs stratégies de réglage sont proposées. Un critère de Morozov [Nair et al. 2003] a notamment été formulé explicitement pour l'ERCm. Si des tests de validation sur données simulées ont montré que les valeurs proposées n'étaient pas parfaitement optimales en vue de l'identification de paramètres, les propositions faites dans ce mémoire permettent déjà de trouver un ordre de grandeur cohérent, permettant à l'algorithme de converger. Reste alors à l'utilisateur à faire quelques tests autour de la valeur fournie pour améliorer les tendances observées.

Toutes ces contributions ont été validées par une large gamme de tests de recalage de raideur de modèles de structures soumises à des chargements sismiques en pied, à partir de mesures d'accélération simulées et bruitées.

Pour mettre en évidence la pertinence de la méthode, les mesures acquises lors de la campagne SMART2013 [Richard et al. 2016] ont été utilisées à des fins de recalage dans le but d'améliorer la prédiction des fréquences propres de modèles éléments finis à disposition. Ces premiers résultats concordent avec les résultats d'analyse modale de référence obtenus au CEA [Charbonnel 2021] et sont donc encourageants dans la perspective d'utiliser l'ERCm en temps réel pour suivre la signature modale d'une structure endommageante.

Enfin, toujours dans un cadre de recalage *a posteriori*, une stratégie de placement de capteurs a été proposée dans le but d'améliorer les résultats d'identification par ERCm pour un budget de capteurs donné [M. Diaz et al. 2023d]. Jusqu'alors, les stratégies de placement de capteurs optimales étaient dédiées à des fonctionnelles déterministes quadratiques standards. Ici, on intègre l'ERCm dans le critère de sélection des positions optimales des capteurs. Une entropie de l'information modifiée par rapport à sa formulation classique [Papadimitriou et al. 2000] permet de limiter les incertitudes des paramètres identifiés par ERCm. Un benchmark comparatif pour le placement d'accéléromètres sur une structure 3D de type portique à deux étages a permis de valider la formulation proposée. Des études en perspective ont aussi permis de quantifier l'incertitude (et la sensibilité) sur les paramètres liée à un mauvais positionnement des capteurs.

Vers une stratégie d'assimilation de données intégrant l'ERCm: le filtre de Kalman Dual Modifié

Pour répondre à la problématique globale de la thèse, la stratégie d'identification doit être capable de traiter des données à la volée, d'où la nécessité d'étendre la méthode de recalage *a posteriori* précédemment évoquée à un cadre d'assimilation (séquentielle) de données.

Pour ce faire, l'idée évoquée dans les travaux de Marchand [Marchand 2017] consiste à intégrer l'ERCm au sein d'un filtre de Kalman [Kalman 1960; 1964]. En effet, le filtre de Kalman est le cadre mathématique approprié pour l'assimilation de données: il s'agit d'un estimateur d'état récursif optimal, dérivé du filtrage bayésien pour des processus markoviens et des variables aléatoires toutes supposées gaussiennes. En pratique, un schéma de type prédiction par le modèle - correction par les données s'applique à chaque pas de temps d'assimilation, de sorte à suivre l'état courant du système. Depuis son introduction dans les années 60, le filtre de Kalman n'a eu de cesse d'être étendu à des cas d'applications de plus en plus complexes, avec entre autres:

- ▷ la possibilité d'exploiter des opérateurs non-linéaires par linéarisation locale et utilisation de modèles d'ordre réduit - filtre de Kalman *Extended* [Hoshiya and Saito 1984; González et al. 2017]
- ▷ la possibilité d'utiliser des opérateurs non-linéaires par régularisation statistique avec propagation d'un nombre de particules bien choisies à travers les opérateurs non-linéaires - filtre de Kalman *Unscented* [S. J. Julier and Uhlmann 1997; Wan and Van Der Merwe 2000;

Mariani and Ghisi 2007], filtre particulaire [Chatzi and Smyth 2009], filtre d'ensemble [Evensen 2003], filtre S3F [Papakonstantinou et al. 2022a],

- ▷ l'extension pour l'identification de paramètres de modèle à la volée - filtres de Kalman joint et dual [Mariani and Corigliano 2005; Ebrahimian et al. 2015; Astroza et al. 2019a],
- ▷ l'extension pour l'identification de chargement de le cas où les mesures ne représentent que l'état mécanique du système - filtre de Kalman augmenté [Lourens et al. 2012; Ercan et al. 2023].

L'ERCm n'a été incluse dans un filtre de Kalman que par Marchand avec un changement de la métrique de l'équation d'observation du filtre de Kalman, pour des problèmes en quasi-statique et une formulation temporelle de l'ERCm. Autrement dit, les prédictions du modèle ne sont plus corrigées pour assurer la correspondance entre l'état mécanique prédit et les mesures, mais pour minimiser séquentiellement l'ERCm avec les nouvelles mesures acquises.

Dans le cadre de ces travaux, nous proposons une formulation plus robuste, où au lieu de minimiser la valeur de l'ERCm (qui est dépendante du problème en question, du niveau de bruit de mesure, du modèle considéré etc.), nous garantissons séquentiellement la correction des paramètres vers la condition d'optimalité du problème inverse, c'est-à-dire, vérifier que le gradient de l'ERCm par rapport aux paramètres est bien nul [M. Diaz et al. 2023a]. Ce nouveau formalisme d'assimilation de données, appelé filtre de Kalman Dual Modifié (MDKF) a été validé sur la base de mesures d'accélérations simulées sur un portique à 2 étages où un des murs s'endommage soudainement. Cet exemple académique a permis de mettre en évidence les forces de la méthode, à savoir :

- ▷ la robustesse accrue au bruit de mesure grâce à l'utilisation de l'ERCm,
- ▷ la capacité à assimiler très rapidement les données avec précision, à condition de bien choisir la base de filtre de Kalman implémentée : les filtres *Unscented* et S3F se sont révélés les meilleurs compromis dans les applications envisagées,
- ▷ la possibilité d'effectuer de l'identification partielle en isolant et recalant uniquement les paramètres associés aux zones les plus erronées au sens de l'ERC,
- ▷ la facilité de réglage des matrices de covariance de biais de modèle et de bruit de mesure, souvent délicates à gérer pour des filtres de Kalman traditionnels.

La principale limitation de la méthode est liée à l'utilisation d'une formulation fréquentielle de l'ERCm, qui se heurte à l'assimilation séquentielle des données en temps. Une technique de fenêtre glissante est mise en place pour assurer la précision fréquentielle requise par l'ERCm, au prix d'un inévitable délai à l'identification. Si l'on peut penser que cette subtilité algorithmique pourrait s'avérer limitante dans le cas où l'évolution des paramètres est soudaine, la capacité à traiter avec le MDKF l'ensemble des données d'accélération acquises lors de la campagne expérimentale SMART2013 montre le potentiel de la méthode. En particulier, avoir pu suivre en temps réel l'évolution de la signature modale d'une structure complexe en béton armé à partir d'un modèle linéaire (alors que des phénomènes non-linéaires - endommagement et dissipation entre autres - sont en jeu) souligne la robustesse et l'efficacité de la stratégie proposée.

Application au contrôle adaptatif des tables vibrantes

Pour finalement tenter de répondre à la problématique initiale du sujet de thèse, à savoir l'amélioration du contrôle des tables vibrantes, une ultime étude exploratoire a été menée pour s'informer des stratégies de contrôle actuellement implémentées sur table vibrante, au CEA [Le Maoult et al. 2012] et ailleurs [Shen et al. 2016; Preumont 2018]. En parallèle, une revue des principales non-linéarités rendant le contrôle des tables complexe a été faite : comportement des servo-valves avec boucle de contrôle interne, propriétés du fluide variable avec la température et la pression, frottement de Stribeck au niveau de la tige des vérins, mouvements parasites dans le cas de vérins combinés, couplage à une structure endommageante. Afin de proposer une première approche pour un cadre DDDAS, un modèle linéarisé inspiré des travaux de [Conte

and Trombetti 2000] a été utilisé. En faisant varier la raideur globale de la structure, modélisée dans cet exemple comme un système masse-ressort amorti, on parvient à reproduire, avec une stratégie de contrôle par retour d'état, des essais instables comme ceux observés lors de la campagne SMART2013. Une preuve de concept a montré la pertinence du contrôle adaptatif, où la commande par retour d'état adaptée en temps réel par les résultats d'identification issus du MDKF, a pu stabiliser un essai sismique simulé. Une vraie piste de recherche est donc ouverte où des stratégies de type "gain scheduling" pourraient désormais permettre d'améliorer le pilotage de systèmes complexes à partir de modèles identifiés à la volée. A voir évidemment à quel point les résultats mis en exergue dans cette preuve de concept sont généralisables...

Perspectives d'applications dans le cadre DDDAS et pour le suivi d'état de santé des structures

Un dialogue essais/calculs complet a été proposé autour du concept d'erreur en relation de comportement modifiée, en partant d'une vision *offline* pour aller jusqu'à une proposition de cadre DDDAS pour le contrôle amélioré de tables vibrantes. Ce cadre bénéficie des avantages inhérents à l'ERCm, et des efforts notables ont été réalisés pour permettre à un utilisateur non-initié de l'appréhender plus facilement, avec notamment un intérêt porté aux points sensibles liés à la résolution des problèmes inverses : richesse des données, pertinence du chargement, sensibilité paramétrique à la fonction-coût, placement des capteurs et effet des erreurs de positionnement, prise en compte du biais de modèle. Les résultats d'identification, d'assimilation de données, et la preuve de concept obtenue pour l'amélioration du contrôle des tables suggèrent le bien-fondé de l'approche et ouvrent ainsi la voie à des perspectives de contrôle hybride et à de nouveaux outils pour le suivi de l'état de santé de structures.

Inscrit dans la continuité de ces travaux de thèse, le projet DREAM-ON [Chamoin 2021] vise à instaurer un cadre DDDAS pour le suivi de l'état de santé de parcs éoliens, basé sur un approfondissement des outils développés dans cette thèse, en utilisant (i) des mesures par fibre optique, bien plus riches que celles d'accéléromètres [Chamoin et al. 2022], (ii) des réseaux de neurones informés par la physique (PINNs en anglais) pour apprendre la forme-même du comportement mécanique de la structure sans *a priori* [Benady et al. 2022], (iii) des stratégies de contrôle avancées de type *Model Predictive Control*, plus robustes et permettant d'anticiper à court-terme les évolutions du système [Richalet 1993].

Une autre perspective d'application demeure dans l'utilisation de l'ERCm et du MDKF pour le suivi d'état de santé de structures en conditions opérationnelles. Des études complémentaires doivent être menées, notamment sur les capacités d'identifiabilité de l'endommagement sur des ouvrages de génie civil, en comparaison avec les techniques traditionnelles de *Structural Health Monitoring* [Sohn et al. 2003; Barthorpe and Worden 2020]. Une extension doit aussi être proposée pour tenir compte du fait qu'en conditions opérationnelles, les efforts d'entrée sont méconnus ou non estimables. De premières pistes pour ce problème peuvent se trouver dans des stratégies de type filtre de Kalman augmenté [Lourens et al. 2012; Capalbo et al. 2023], ou par une reformulation de l'ERCm, en séparant différemment les équations selon leur degré de confiance.

Bibliography

Abbiati, G., Bursi, O. S., Caperan, P., Di Sarno, L., Molina, F. J., Paolacci, F., and Pegon, P. (2015). "Hybrid simulation of a multi-span RC viaduct with plain bars and sliding bearings: Hybrid Simulations of a Multi-Span RC Viaduct". *Earthquake Engineering & Structural Dynamics* 44.13, pp. 2221–2240. DOI: 10.1002/eqe.2580.

Abbiati, G., Lanese, I., Eftekhar Azam, S., Bursi, O. S., and Pavese, A. (2021). "A framework for hybrid simulation with online model updating suitable for hard real-time computing". *Structural Control and Health Monitoring* 28.1. DOI: 10.1002/stc.2652.

Ackermann, J. (1980). "Parameter space design of robust control systems". *IEEE Transactions on Automatic Control* 25.6, pp. 1058–1072. DOI: 10.1109/TAC.1980.1102505.

Ahmadian, H., Mottershead, J., and Friswell, M. (1998). "Regularisation methods for finite element model updating". *Mechanical Systems and Signal Processing* 12.1, pp. 47–64. DOI: 10.1006/mssp.1996.0133.

Ahmed, M., Lachhab, N., and Svaricek, F. (2012). "Non-model based adaptive control of electro-hydraulic servo systems using prefilter inversion". *International Multi-Conference on Systems, Signals & Devices*, pp. 1–6. DOI: 10.1109/SSD.2012.6197984.

Aitken, A. C. (1935). "Note on Selection from a Multivariate Normal Population". *Proceedings of the Edinburgh Mathematical Society* 4.2, pp. 106–110. DOI: 10.1017/S0013091500008063.

Alarcon, A., Bodel, C., and Bonnet, M. (2011a). "A coupled Unscented Kalman Filter and modified Error in Constitutive Relation technique for structural dynamics identification", p. 6.

Alarcon, A., Bodel, C., and Bonnet, M. (2011b). "Une méthode d'identification en dynamique des structures basée sur le filtre de Kalman et l'erreur en relation de comportement". *10ème colloque national en calcul des structures*. Giens, p. 9.

Allemang, R. J. and Brown, D. L. (2006). "A Complete Review of the Complex Mode Indicator Function (CMIF) with Applications", p. 38.

Allemang, R. J., Brown, D. L., Phillips, A. W., and Allemang, R. (2010). "Survey of Modal Techniques Applicable to Autonomous/Semi-Autonomous Parameter Identification". *Proceedings of ISMA2010 including USD2010*, pp. 3331–3372.

Alleyne, A. and Liu, R. (2000). "Systematic control of a class of nonlinear systems with application to electrohydraulic cylinder pressure control". *IEEE Transactions on Control Systems Technology* 8.4, pp. 623–634. DOI: 10.1109/87.852908.

Alleyne, A. and Liu, R. (1999). "On the Limitations of Force Tracking Control for Hydraulic Servosystems". *Journal of Dynamic Systems, Measurement, and Control* 121.2, pp. 184–190. DOI: 10.1115/1.2802453.

Allgöwer, F., Findeisen, R., and Nagy, Z. K. (2004). "Nonlinear Model Predictive Control: From Theory to Application". 35.3, p. 18.

Allix, O., Feissel, P., and Nguyen, H. (2005). "Identification strategy in the presence of corrupted measurements". *Engineering Computations* 22.5/6, pp. 487–504. DOI: 10.1108/02644400510602989.

Alvandi, A. and Cremona, C. (2006). "Assessment of vibration-based damage identification techniques". *Journal of Sound and Vibration* 292.1, pp. 179–202. DOI: 10.1016/j.jsv.2005.07.036.

Amir, M., Papakonstantinou, K. G., and Warn, G. P. (2022). "Scaled Spherical Simplex Filter and State-Space Damage-Plasticity Finite-Element Model for Computationally Efficient System Identification". *Journal of Engineering Mechanics* 148.2, p. 04021138. DOI: 10.1061/(ASCE)EM.1943-7889.0001945.

Aquino, W. and Bonnet, M. (2019). "Analysis of the Error in Constitutive Equation Approach for Time-Harmonic Elasticity Imaging". *SIAM Journal on Applied Mathematics* 79.3, pp. 822–849. DOI: 10.1137/18M1231237. eprint: https://doi.org/10.1137/18M1231237.

Araki, M. and Taguchi, H. (2003). "Two-Degree-of-Freedom PID Controllers". *International Journal of Control, Automation, and Systems* 1.4, pp. 401–411.

Argaud, J.-P., Bouriquet, B., Caso, F. de, Gong, H., Maday, Y., and Mula, O. (2018). "Sensor placement in nuclear reactors based on the generalized empirical interpolation method". *Journal of Computational Physics* 363, pp. 354–370. DOI: 10.1016/j.jcp.2018.02.050.

Argaud, J.-P., Bouriquet, B., Gong, H., Maday, Y., and Mula, O. (2017). "Stabilization of (G)EIM in Presence of Measurement Noise: Application to Nuclear Reactor Physics". *Spectral and High Order Methods for Partial Differential Equations ICOSAHOM 2016*. Ed. by M. L. Bittencourt, N. A. Dumont, and J. S. Hesthaven. Lecture Notes in Computational Science and Engineering. Cham: Springer International Publishing, pp. 133–145. DOI: 10.1007/978-3-319-65870-4_8.

Argyris, C., Chowdhury, S., Zabel, V., and Papadimitriou, C. (2018). "Bayesian optimal sensor placement for crack identification in structures using strain measurements". *Structural Control and Health Monitoring* 25.5, e2137. DOI: 10.1002/stc.2137.

Arulampalam, M., Maskell, S., Gordon, N., and Clapp, T. (2002). "A tutorial on particle filters for online nonlinear/non-Gaussian Bayesian tracking". *IEEE Transactions on Signal Processing* 50.2, pp. 174–188. DOI: 10.1109/78.978374.

Asch, M., Bocquet, M., and Nodet, M. (2016). *Data Assimilation: Methods, Algorithms, and Applications*. Philadelphia, PA: Society for Industrial and Applied Mathematics. DOI: 10.1137/1.9781611974546.

Astrom, K. J. and Hagglund, T. (1995). *PID controllers: theory, design and tuning*. Instrument Society of America.

Astroza, R., Alessandri, A., and Conte, J. P. (2019a). "A dual adaptive filtering approach for nonlinear finite element model updating accounting for modeling uncertainty". *Mechanical Systems and Signal Processing* 115, pp. 782–800. DOI: 10.1016/j.ymssp.2018.06.014.

Astroza, R., Ebrahimian, H., and Conte, J. P. (2019b). "Performance comparison of Kalman-based filters for nonlinear structural finite element model updating". *Journal of Sound and Vibration* 438, pp. 520–542. DOI: 10.1016/j.jsv.2018.09.023.

Auroux, D. (2007). "Generalization of the dual variational data assimilation algorithm to a nonlinear layered quasi-geostrophic ocean model". *Inverse Problems* 23.6, p. 2485. DOI: 10.1088/0266-5611/23/6/013.

Avci, O., Abdeljaber, O., Kiranyaz, S., Hussein, M., Gabbouj, M., and Inman, D. J. (2021). "A review of vibration-based damage detection in civil structures: From traditional methods to Machine Learning and Deep Learning applications". *Mechanical Systems and Signal Processing* 147, p. 107077. DOI: 10.1016/j.ymssp.2020.107077.

Azarbayejani, M., El-Osery, A. I., Choi, K. K., and Taha, M. M. R. (2008). "A probabilistic approach for optimal sensor allocation in structural health monitoring". *Smart Materials and Structures* 17.5, p. 055019. DOI: 10.1088/0964-1726/17/5/055019.

Bach, V.-S., Le, T.-C., Nguyen, C.-T., Tran, M.-H., Pham, M.-N., and Ho, D.-D. (2023). "Damage Identification for Steel Frame Structures Using Two-Step Approach Combining Modal Strain Energy Method and Genetic Algorithm". *ICSCEA 2021*. Lecture Notes in Civil Engineering. Singapore: Springer Nature, pp. 767–775. DOI: 10.1007/978-981-19-3303-5_69.

Balasko, B., Abonyi, J., and Feil, B. (2005). "Fuzzy clustering and data analysis toolbox". *Department of Process Engineering, University of Veszprem, Veszprem*.

Balmès, E. (1996). "Parametric families of reduced of reduced finite element models. Theory and applications." *Mechanical Systems and Signal Processing* 10.4, pp. 381–394. DOI: 10.1006/mssp.1996.0027.

Balmès, E. (2000). "Review and Evaluation of Shape Expansion Methods". *Proceedings of SPIE - The International Society for Optical Engineering*, p. 8.

Balmès, E., Martin, G., Vermot Des Roches, G., Chancelier, T., and Thouviot, S. (2022). "Expansion in structural dynamics : a perspective gained from success and errors in test/FEM twin building". *15ème colloque national en calcul des structures*. 83400 Hyères-les-Palmiers, France: Université Polytechnique Hauts-de-France [UPHF].

Banerjee, B., Walsh, T. F., Aquino, W., and Bonnet, M. (2013). "Large scale parameter estimation problems in frequency-domain elastodynamics using an error in constitutive equation functional". *Computer Methods in Applied Mechanics and Engineering* 253, pp. 60–72. DOI: 10.1016/j.cma.2012.08.023.

Bangerth, W. (2008). "A Framework for the Adaptive Finite Element Solution of Large-Scale Inverse Problems". *SIAM Journal on Scientific Computing* 30.6, pp. 2965–2989. DOI: 10.1137/070690560.

Bangerth, W. and Joshi, A. (2008). "Adaptive finite element methods for the solution of inverse problems in optical tomography". *Inverse Problems* 24.3, p. 034011. DOI: 10.1088/0266-5611/24/3/034011.

Barbarella, E., Allix, O., Daghia, F., Lamon, J., and Jollivet, T. (2016). "A new inverse approach for the localization and characterization of defects based on compressive experiments". *Computational Mechanics* 57.6, pp. 1061–1074. DOI: 10.1007/s00466-016-1278-y.

Barthe, D., Deraemaeker, A., Ladevèze, P., and Loch, S. L. (2004). "Validation and Updating of Industrial Models Based on the Constitutive Relation Error". *AIAA Journal* 42.7, pp. 1427–1434. DOI: 10.2514/1.11882.

Barthorpe, R. J. and Worden, K. (2020). "Emerging Trends in Optimal Structural Health Monitoring System Design: From Sensor Placement to System Evaluation". *Journal of Sensor and Actuator Networks* 9.3, p. 31. DOI: 10.3390/jsan9030031.

Batou, A. (2019). "A sensitivity-based one-parameter-at-a-time model updating method". *Mechanical Systems and Signal Processing* 122, pp. 247–255. DOI: 10.1016/j.ymssp.2018.12.025.

Beck, J. L. and Katafygiotis, L. S. (1998). "Updating Models and Their Uncertainties. I: Bayesian Statistical Framework". *Journal of Engineering Mechanics* 124.4, pp. 455–461. DOI: 10.1061/(ASCE)0733-9399(1998)124:4(455).

Becker, R. and Vexler, B. (2005). "Mesh refinement and numerical sensitivity analysis for parameter calibration of partial differential equations". *Journal of Computational Physics* 206.1, pp. 95–110. DOI: 10.1016/j.jcp.2004.12.018.

Ben Azzouna, M., Feissel, P., and Villon, P. (2015). "Robust identification of elastic properties using the Modified Constitutive Relation Error". *Computer Methods in Applied Mechanics and Engineering* 295, pp. 196–218. DOI: 10.1016/j.cma.2015.04.004.

Benady, A., Chamoin, L., and Baranger, E. (2022). "Physics-informed neural networks derived from a mCRE functional for constitutive modelling". *IUTAM Symposium on Data-driven Mechanics*. Paris, France.

Benner, P., Grivet-Talocia, S., Quarteroni, A., Rozza, G., Schilders, W., and Silveira, L. M. (2020). *Model Order Reduction: Snapshot-Based Methods and Algorithms*. Vol. 2. De Gruyter. DOI: 10.1515/9783110671490.

Benning, M. and Burger, M. (2018). "Modern Regularization Methods for Inverse Problems". *arXiv:1801.09922* [*math*].

Bensoussan, A. (1972). "Optimization of sensor's location in a distributed filtering problem." *Stability of stochastic dynamical systems*. Springer, pp. 62–84.

Bernardo, M. di and Stoten, D. P. (2006). "Minimal Control Synthesis Adaptive Control of Nonlinear Systems: Utilizing the Properties of Chaos". *Philosophical Transactions: Mathematical, Physical and Engineering Sciences* 364.1846, pp. 2397–2415.

Bhattacharyya, M. and Feissel, P. (2022). "A bayesian inference of material parameters from DIC data".

Bhattacharyya, S. (2017). "Robust control under parametric uncertainty: An overview and recent results". *Annual Reviews in Control* 44, pp. 45–77. DOI: 10.1016/j.arcontrol.2017.05.001.

Bjarnason, E. (1995). "Analysis of the filtered-X LMS algorithm". *IEEE Transactions on Speech and Audio Processing* 3.6, pp. 504–514. DOI: 10.1109/89.482218.

Blachowski, B. (2019). "Modal Sensitivity Based Sensor Placement for Damage Identification Under Sparsity Constraint". *Periodica Polytechnica Civil Engineering*. DOI: 10.3311/PPci.13888.

Blachowski, B., Ostrowski, M., Tauzowski, P., Swiercz, A., and Jankowski, L. (2020). "Sensor placement for structural damage identification by means of topology optimization". *AIP Conference Proceedings* 2239.1, p. 020002. DOI: 10.1063/5.0007817.

Blondet, M. and Esparza, C. (1988). "Analysis of shaking table-structure interaction effects during seismic simulation tests". *Earthquake Engineering & Structural Dynamics* 16.4, pp. 473–490. DOI: 10.1002/eqe.4290160402.

Bobillot, A. and Balmès, E. (2001). "Solving Minimum Dynamic Residual Expansion and Using Results for Error Localization". *Proc. IMAC XIX*. Kissimee, Florida, p. 7.

Bolzon, G., Fedele, R., and Maier, G. (2002). "Parameter identification of a cohesive crack model by Kalman filter". *Comput. Methods Appl. Mech. Engrg.*, p. 25.

Bonnet, M. and Aquino, W. (2015). "Three-dimensional transient elastodynamic inversion using an error in constitutive relation functional". *Inverse Problems* 31.3, p. 035010. DOI: 10.1088/0266-5611/31/3/035010.

Bonnet, M. and Constantinescu, A. (2005). "Inverse problems in elasticity". *Inverse Problems* 21.2, R1–R50. DOI: 10.1088/0266-5611/21/2/R01.

Bonney, M. S., Angelis, M. de, Dal Borgo, M., Andrade, L., Beregi, S., Jamia, N., and Wagg, D. J. (2022). "Development of a digital twin operational platform using Python Flask". *Data-Centric Engineering* 3, e1. DOI: 10.1017/dce.2022.1.

Bora, D. J. and Gupta, A. K. (2014). "A Comparative study Between Fuzzy Clustering Algorithm and Hard Clustering Algorithm". *International Journal of Computer Trends and Technology* 10.2, pp. 108–113. DOI: 10.14445/22312803/IJCTT-V10P119.

Bouclier, R., Louf, F., and Chamoin, L. (2013). "Real-time validation of mechanical models coupling PGD and constitutive relation error". *Computational Mechanics* 52.4, pp. 861–883. DOI: 10.1007/s00466-013-0850-y.

Brownjohn, J. (2007). "Structural health monitoring of civil infrastructure". *Philosophical Transactions of the Royal Society A: Mathematical, Physical and Engineering Sciences* 365.1851, pp. 589–622. DOI: 10.1098/rsta.2006.1925.

Brownjohn, J., Xia, P.-Q., Hao, H., and Xia, Y. (2001). "Civil structure condition assessment by FE model updating: methodology and case studies". *Finite Elements in Analysis and Design*, p. 15.

Bruggi, M. and Mariani, S. (2013). "Optimization of sensor placement to detect damage in flexible plates". *Engineering Optimization* 45.6, pp. 659–676. DOI: 10.1080/0305215X.2012.690870.

Bui, H. D. and Constantinescu, A. (2000). "Spatial localization of the error of constitutive law for the identification of defects in elastic bodies". *Archives of Mechanics* 52.4-5, pp. 511–522. DOI: 10.24423/aom.23.

Bursi, O. S., Ceravolo, R., Erlicher, S., and Zanotti Fragonara, L. (2012). "Identification of the hysteretic behaviour of a partial-strength steel-concrete moment-resisting frame structure subject to pseudodynamic tests: Nonlinear identification of a steel-concrete frame structure". *Earthquake Engineering & Structural Dynamics* 41.14, pp. 1883–1903. DOI: 10.1002/eqe.2163.

Butterworth, J. A., Pao, L. Y., and Abramovitch, D. Y. (2012). "Analysis and comparison of three discrete-time feedforward model-inverse control techniques for nonminimum-phase systems". *Mechatronics*. Special Issue on Distributed Intelligent MEMS: from hardware to software 22.5, pp. 577–587. DOI: 10.1016/j.mechatronics.2011.12.006.

Cantero-Chinchilla, S., Beck, J. L., Chiachío, M., Chiachío, J., Chronopoulos, D., and Jones, A. (2020). "Optimal sensor and actuator placement for structural health monitoring via an efficient convex cost-benefit optimization". *Mechanical Systems and Signal Processing* 144. DOI: 10.1016/j.ymssp.2020.106901.

Capalbo, C. E., De Gregoriis, D., Tamarozzi, T., Devriendt, H., Naets, F., Carbone, G., and Mundo, D. (2023). "Parameter, input and state estimation for linear structural dynamics using parametric model order reduction and augmented Kalman filtering". *Mechanical Systems and Signal Processing* 185, p. 109799. DOI: 10.1016/j.ymssp.2022.109799.

Carden, E. P. and Brownjohn, J. M. W. (2008). "Fuzzy Clustering of Stability Diagrams for Vibration-Based Structural Health Monitoring". *Computer-Aided Civil and Infrastructure Engineering* 23.5, pp. 360–372. DOI: 10.1111/j.1467-8667.2008.00543.x.

Cast3M (2020). http://www-cast3m.cea.fr.

Cawley, P. and Adams, R. D. (1979). "The location of defects in structures from measurements of natural frequencies". *The Journal of Strain Analysis for Engineering Design* 14.2, pp. 49–57. DOI: 10.1243/03093247V142049.

Chamoin, L. (2021). "Merging advanced sensing techniques and simulation tools for future structural health monitoring technologies". *The Project Repository Journal* 10.1, pp. 124–127. DOI: 10.54050/PRJ10124127.

Chamoin, L., Farahbakhsh, S., and Poncelet, M. (2022). "An educational review on distributed optic fiber sensing based on Rayleigh backscattering for damage tracking and structural health monitoring". *Measurement Science and Technology*.

Chamoin, L., Ladevèze, P., and Waeytens, J. (2014). "Goal-oriented updating of mechanical models using the adjoint framework". *Computational Mechanics* 54.6, pp. 1415–1430. DOI: 10.1007/s00466-014-1066-5.

Charbonnel, P.-É. (2021). "Fuzzy-driven strategy for fully automated modal analysis: Application to the SMART2013 shaking-table test campaign". *Mechanical Systems and Signal Processing* 152, p. 107388. DOI: 10.1016/j.ymssp.2020.107388.

Charbonnel, P.-É., Ladevèze, P., Louf, F., and Le Noac'h, C. (2013). "A robust CRE-based approach for model updating using in situ measurements". *Computers & Structures* 129, pp. 63–73. DOI: 10.1016/j.compstruc.2013.08.002.

Chatzi, E. N., Chatzis, M. N., and Papadimitriou, C., eds. (2020). *Robust Monitoring, Diagnostic Methods and Tools for Engineered Systems*. Frontiers Research Topics. Frontiers Media SA. DOI: 10.3389/978-2-88966-088-9.

Chatzi, E. N. and Smyth, A. W. (2009). "The unscented Kalman filter and particle filter methods for nonlinear structural system identification with non-collocated heterogeneous sensing". *Structural Control and Health Monitoring* 16.1, pp. 99–123. DOI: 10.1002/stc.290.

Chatzis, M. N., Chatzi, E. N., and Triantafyllou, S. P. (2017). "A Discontinuous Extended Kalman Filter for non-smooth dynamic problems". *Mechanical Systems and Signal Processing* 92, pp. 13–29. DOI: 10.1016/j.ymssp.2017.01.021.

Cheng, M. and Becker, T. C. (2021). "Performance of unscented Kalman filter for model updating with experimental data". *Earthquake Engineering & Structural Dynamics* 50.7, pp. 1948–1966. DOI: 10.1002/eqe.3426.

Chinesta, F., Cueto, E., Abisset-Chavanne, E., Duval, J. L., and Khaldi, F. E. (2018). "Virtual, Digital and Hybrid Twins: A New Paradigm in Data-Based Engineering and Engineered Data". *Archives of Computational Methods in Engineering* 27.1, pp. 105–134. DOI: 10.1007/s11831-018-9301-4.

Chinesta, F., Ladevèze, P., and Cueto, E. (2011). "A Short Review on Model Order Reduction Based on Proper Generalized Decomposition". *Archives of Computational Methods in Engineering* 18.4, pp. 395–404. DOI: 10.1007/s11831-011-9064-7.

Chouaki, A., Ladevèze, P., and Proslier, L. (1997). "An Updating Method for Damped Structural Dynamics Models", p. 8.

Chouaki, A., Ladevèze, P., and Proslier, L. (1998). "Updating Structural Dynamic Models with Emphasis on the Damping Properties". *AIAA Journal* 36.6, pp. 1094–1099. DOI: 10.2514/2.486.

Claire, D., Hild, F., and Roux, S. (2004). "A finite element formulation to identify damage fields: the equilibrium gap method". *International Journal for Numerical Methods in Engineering* 61.2, pp. 189–208. DOI: 10.1002/nme.1057.

Cohen, A., Dahmen, W., Mula, O., and Nichols, J. (2022). "Nonlinear Reduced Models for State and Parameter Estimation". *SIAM/ASA Journal on Uncertainty Quantification* 10.1, pp. 227–267. DOI: 10.1137/20M1380818.

Conte, J. P. and Trombetti, T. L. (2000). "Linear dynamic modeling of a uni-axial servo-hydraulic shaking table system". *Earthquake Engineering & Structural Dynamics* 29.9, pp. 1375–1404. DOI: 10.1002/1096-9845(200009)29:9<1375::AID-EQE975>3.0.CO;2-3.

Corigliano, A. and Mariani, S. (2001). "Parameter identification of a time-dependent elastic-damage interface model for the simulation of debonding in composites". *Composites Science and Technology*, p. 13.

Corus, M., Balmès, E., and Nicolas, O. (2006). "Using model reduction and data expansion techniques to improve SDM". *Mechanical Systems and Signal Processing* 20.5, pp. 1067–1089. DOI: 10.1016/j.ymssp.2005.02.012.

Curt, J., Capaldo, M., Hild, F., and Roux, S. (2022). "An algorithm for structural health monitoring by digital image correlation: Proof of concept and case study". *Optics and Lasers in Engineering* 151, p. 106842. DOI: 10.1016/j.optlaseng.2021.106842.

Cutler, C. R. and Ramaker, B. L. (1980). "Dynamic matrix control??A computer control algorithm". *Joint Automatic Control Conference* 17, p. 72. DOI: 10.1109/JACC.1980.4232009.

Darema, F. (2004). "Dynamic Data Driven Applications Systems: A New Paradigm for Application Simulations and Measurements". *Computational Science - ICCS 2004*. Ed. by M. Bubak, G. D. van Albada, P. M. A. Sloot, and J. Dongarra. Lecture Notes in Computer Science. Berlin, Heidelberg: Springer, pp. 662–669. DOI: 10.1007/978-3-540-24688-6_86.

Decouvreur, V., Deraemaeker, A., Ladevèze, P., and Bouillard, P. (2007). "Building a suited reduced modal basis for updating 3D acoustic models with the constitutive law error method". *Computer Methods in Applied Mechanics and Engineering* 196.35-36, pp. 3400–3408. DOI: 10.1016/j.cma.2007.03.006.

Decouvreur, V., Ladevèze, P., and Bouillard, P. (2008). "Updating 3D acoustic models with the constitutive relation error method: A two-stage approach for absorbing material characterization". *Journal of Sound and Vibration* 310.4-5, pp. 985–997. DOI: 10.1016/j.jsv.2007.08.012.

Deraemaeker, A., Ladevèze, P., and Leconte, P. (2002). "Reduced bases for model updating in structural dynamics based on constitutive relation error". *Computer Methods in Applied Mechanics and Engineering* 191.21-22, pp. 2427–2444. DOI: 10.1016/S0045-7825(01)00421-2.

Deraemaeker, A., Ladevèze, P., and Romeuf, T. (2004). "Model validation in the presence of uncertain experimental data". *Engineering Computations* 21.8, pp. 808–833. DOI: 10.1108/02644400410554335.

Deraemaeker, A., Reynders, E., De Roeck, G., and Kullaa, J. (2008). "Vibration-based structural health monitoring using output-only measurements under changing environment". *Mechanical Systems and Signal Processing* 22.1, pp. 34–56. DOI: 10.1016/j.ymssp.2007.07.004.

Dertimanis, V. K., Mouzakis, H. P., and Psycharis, I. N. (2015). "On the acceleration-based adaptive inverse control of shaking tables". *Earthquake Engineering & Structural Dynamics* 44.9, pp. 1329–1350. DOI: https://doi.org/10.1002/eqe.2518. eprint: https://onlinelibrary.wiley.com/doi/pdf/10.1002/eqe.2518.

Diaz, M. I., Aquino, W., and Bonnet, M. (2015). "A modified error in constitutive equation approach for frequency-domain viscoelasticity imaging using interior data". *Computer Methods in Applied Mechanics and Engineering* 296, pp. 129–149. DOI: 10.1016/j.cma.2015.07.025.

Diaz, M., Charbonnel, P.-É., and Chamoin, L. (2021). "Towards a fully automated model updating framework for low-frequency dynamics: application to shaking-table testings". *Journée thématique Identification & Validation de la Fédération Francilienne de Mécanique* (*F2M*). ENSAM, Paris.

Diaz, M., Charbonnel, P.-É., and Chamoin, L. (2022a). "A new data assimilation framework using the modified Constitutive Relation Error for online structural monitoring: application to shaking-table experiments". *8th European Congress on Computational Methods in Applied Sciences and Engineering - ECCOMAS Congress 2022*. Oslo, Norway.

Diaz, M., Charbonnel, P.-É., and Chamoin, L. (2022b). "Automated physics-guided data assimilation strategy for model updating in dynamics - Application to the monitoring of structures tested on shaking tables". *Journée scientifique de l'Institut SEISM Paris-Saclay* (*GIS SEISM*). Saclay, France.

Diaz, M., Charbonnel, P.-É., and Chamoin, L. (2022c). "Robust energy-based model updating framework for random processes in dynamics: application to shaking-table experiments". *Computers and Structures* 264.106746, p. 40. DOI: https://doi.org/10.1016/j.compstruc.2022.106746.

Diaz, M., Charbonnel, P.-É., and Chamoin, L. (2022d). "Towards an automated physics-regularized model updating strategy applied to the monitoring of civil engineering structures in low-frequency dynamics". *7th European Conference on Structural Control - EACS 2022*. Warsaw, Poland.

Diaz, M., Charbonnel, P.-É., and Chamoin, L. (2022e). "Vers une stratégie robuste et automatisée pour le recalage de modèles en dynamique vibratoire : application au suivi des structures endommageantes testées sur table vibrante". *15ème Colloque National en Calcul des Structures* (*CSMA 2022*). Giens, France.

Diaz, M., Charbonnel, P.-É., and Chamoin, L. (2023a). "A new Kalman filter approach for structural parameter tracking: Application to the monitoring of damaging structures tested on shaking-tables". *Mechanical Systems and Signal Processing* 182, p. 109529. DOI: 10.1016/j.ymssp.2022.109529.

Diaz, M., Charbonnel, P.-É., and Chamoin, L. (2023b). "A new physics-guided data assimilation framework for online structural monitoring: application to shaking-table tests". *COMPDYN2023 - 9th ECCOMAS Thematic Conference on Computational Methods in Structural Dynamics and Earthquake Engineering*. Athens, Greece.

Diaz, M., Charbonnel, P.-É., and Chamoin, L. (2023c). "Fully automated model updating framework for damage detection based on the modified Constitutive Relation Error". *Computational Mechanics*. DOI: 10.1007/s00466-023-02382-z.

Diaz, M., Charbonnel, P.-É., and Chamoin, L. (2023d). "Merging experimental design and structural identification around the concept of modified Constitutive Relation Error in low-frequency dynamics for enhanced structural monitoring". *Mechanical Systems and Signal Processing* (*under review*) - *available in hal* (*03878634*).

Djatouti, Z., Waeytens, J., Chamoin, L., and Chatellier, P. (2020). "Coupling a goal-oriented inverse method and proper generalized decomposition for fast and robust prediction of quantities of interest in building thermal problems". *Building Simulation* 13.3, pp. 709–727. DOI: 10.1007/s12273-020-0603-8.

Ebrahimian, H., Astroza, R., and Conte, J. P. (2015). "Extended Kalman filter for material parameter estimation in nonlinear structural finite element models using direct differentiation method". *Earthquake Engineering & Structural Dynamics* 44.10, pp. 1495–1522. DOI: 10.1002/eqe.2532.

Eftekhar Azam, S., Bagherinia, M., and Mariani, S. (2012a). "Stochastic system identification via particle and sigma-point Kalman filtering". *Scientia Iranica* 19.4, pp. 982–991. DOI: 10.1016/j.scient.2012.06.007.

Eftekhar Azam, S. (2014). *Online Damage Detection in Structural Systems*. SpringerBriefs in Applied Sciences and Technology. Cham: Springer International Publishing. DOI: 10.1007/978-3-319-02559-9.

Eftekhar Azam, S., Ghisi, A., and Mariani, S. (2012b). "Parallelized sigma-point Kalman filtering for structural dynamics". *Computers & Structures* 92-93, pp. 193–205. DOI: 10.1016/j.compstruc.2011.11.004.

Eftekhar Azam, S. and Mariani, S. (2013). "Investigation of computational and accuracy issues in POD-based reduced order modeling of dynamic structural systems". *Engineering Structures* 54, pp. 150–167. DOI: 10.1016/j.engstruct.2013.04.004.

Eftekhar Azam, S. and Mariani, S. (2018). "Online damage detection in structural systems via dynamic inverse analysis: A recursive Bayesian approach". *Engineering Structures* 159, pp. 28–45. DOI: 10.1016/j.engstruct.2017.12.031.

Ercan, T. and Papadimitriou, C. (2021). "Optimal Sensor Placement for Reliable Virtual Sensing Using Modal Expansion and Information Theory". *Sensors* 21.10, p. 3400. DOI: 10.3390/s21103400.

Ercan, T., Sedehi, O., Katafygiotis, L. S., and Papadimitriou, C. (2023). "Information theoretic-based optimal sensor placement for virtual sensing using augmented Kalman filtering". *Mechanical Systems and Signal Processing* 188, p. 110031. DOI: 10.1016/j.ymssp.2022.110031.

Evensen, G. (1994). "Sequential data assimilation with a nonlinear quasi-geostrophic model using Monte Carlo methods to forecast error statistics". *Journal of Geophysical Research* 99.C5, p. 10143. DOI: 10.1029/94JC00572.

Evensen, G. (2003). "The Ensemble Kalman Filter: theoretical formulation and practical implementation". *Ocean Dynamics* 53.4, pp. 343–367. DOI: 10.1007/s10236-003-0036-9.

Fan, W. and Qiao, P. (2011). "Vibration-based Damage Identification Methods: A Review and Comparative Study". *Structural Health Monitoring* 10.1, pp. 83–111. DOI: 10.1177/1475921710365419.

Farhat, C. and Hemez, F. M. (1993). "Updating finite element dynamic models using an element-by-element sensitivity methodology". *AIAA Journal* 31.9, pp. 1702–1711. DOI: 10.2514/3.11833.

Faverjon, B., Ladevèze, P., and Louf, F. (2009). "Validation of stochastic linear structural dynamics models". *Computers & Structures* 87.13-14, pp. 829–837. DOI: 10.1016/j.compstruc.2009.02.007.

Faverjon, B. and Sinou, J.-J. (2009). "Identification of an open crack in a beam using an a posteriori error estimator of the frequency response functions with noisy measurements". *European Journal of Mechanics - A/Solids* 28.1, pp. 75–85. DOI: 10.1016/j.euromechsol.2008.02.006.

Feissel, P. and Allix, O. (2007). "Modified constitutive relation error identification strategy for transient dynamics with corrupted data: The elastic case". *Computer Methods in Applied Mechanics and Engineering* 196.13-16, pp. 1968–1983. DOI: 10.1016/j.cma.2006.10.005.

Ferrier, R., Cocchi, A., and Hochard, C. (2021). "Modified constitutive relation error for field identification: Theoretical and experimental assessments on fiber orientation identification in a composite material". *International Journal for Numerical Methods in Engineering*. DOI: 10.1002/nme.6842.

Figueiredo, E. and Brownjohn, J. (2022). "Three decades of statistical pattern recognition paradigm for SHM of bridges". *Structural Health Monitoring*, p. 14759217221075241. DOI: 10.1177/14759217221075241.

Fisher, R. A. (1925). "Theory of Statistical Estimation". *Mathematical Proceedings of the Cambridge Philosophical Society* 22.5, pp. 700–725. DOI: 10.1017/S0305004100009580.

Foltin, M. and Sekaj, I. (2006). "A new Adaptive PID Control Approach Based on Closed-Loop Response Recognition". *Proceedings of the 7th WSEAS International Conference on Automation & Information*. Cavtat, Croatia, pp. 156–160.

Formosa, F. (2002). "Contribution à l'amélioration de la modélisation de structures legères en vue de leur contrôle actif". PhD thesis. ENS de Cachan.

Friswell, M. I. and Mottershead, J. E. (1995). *Finite Element Model Updating in Structural Dynamics*. Ed. by G. M. L. Gladwell. Vol. 38. Solid Mechanics and its Applications. Dordrecht: Springer Netherlands. DOI: 10.1007/978-94-015-8508-8.

Friswell, M. I. (2007). "Damage identification using inverse methods". *Philosophical Transactions of the Royal Society A: Mathematical, Physical and Engineering Sciences* 365.1851, pp. 393–410. DOI: 10.1098/rsta.2006.1930.

Gang, S., Zhen-Cai, Z., Lei, Z., Yu, T., Chi-fu, Y., Jin-song, Z., Guang-da, L., and Jun-Wei, H. (2013). "Adaptive feed-forward compensation for hybrid control with acceleration time waveform replication on electro-hydraulic shaking table". *Control Engineering Practice* 8.21, pp. 1128–1142. DOI: 10.1016/j.conengprac.2013.03.007.

García-Macías, E. and Ubertini, F. (2022). "Integrated SHM Systems: Damage Detection Through Unsupervised Learning and Data Fusion". *Structural Health Monitoring Based on Data Science Techniques*. Ed. by A. Cury, D. Ribeiro, F. Ubertini, and M. D. Todd. Structural Integrity. Cham: Springer International Publishing, pp. 247–268. DOI: 10.1007/978-3-030-81716-9_12.

Gelb, A., ed. (1974). *Applied optimal estimation*. Cambridge, Mass: M.I.T. Press.

Geradin, M. and Rixen, D. J. (2015). *Mechanical Vibrations: theory and applications to structural dynamics*. John Wiley & Sons, Ltd.

Ghosh, S., Zou, Z., Babaniyi, O., Aquino, W., Diaz, M. I., Bayat, M., and Fatemi, M. (2017). "Modified error in constitutive equations (MECE) approach for ultrasound elastography". *The Journal of the Acoustical Society of America* 142.4, pp. 2084–2093. DOI: 10.1121/1.5006911.

Goldberg, D. (2002). *The design of innovation: Lessons from and for competent genetic algorithms*. Springer. Vol. 1.

Gomes, G. F., Mendez, Y. A. D., Silva Lopes Alexandrino, P. da, Cunha, S. S. da, and Ancelotti, A. C. (2019). "A Review of Vibration Based Inverse Methods for Damage Detection and Identification in Mechanical Structures Using Optimization Algorithms and ANN". *Archives of Computational Methods in Engineering* 26.4, pp. 883–897. DOI: 10.1007/s11831-018-9273-4.

Gomez, E. G. and Stoten, D. P. (2000). "A comparative study of the adaptive MCS control algorithm on European shaking-tables". *Proceedings of the 12t World Conference on Earthquake Engineering*. Vol. 2626. Auckland, New-Zealand.

Gong, H., Maday, Y., Mula, O., and Taddei, T. (2019). "PBDW method for state estimation: error analysis for noisy data and nonlinear formulation". *arXiv:1906.00810* [*math*].

González, D., Badías, A., Alfaro, I., Chinesta, F., and Cueto, E. (2017). "Model order reduction for real-time data assimilation through Extended Kalman Filters". *Computer Methods in Applied Mechanics and Engineering* 326, pp. 679–693. DOI: 10.1016/j.cma.2017.08.041.

Gove, J. H. and Hollinger, D. Y. (2006). "Application of a dual unscented Kalman filter for simultaneous state and parameter estimation in problems of surface-atmosphere exchange". *Journal of Geophysical Research* 111.D8, D08S07. DOI: 10.1029/2005JD006021.

Grewal, M. S. and Andrews, A. P. (2008). *Kalman Filtering: Theory and Practice Using MATLAB®*. 1st ed. Wiley. DOI: 10.1002/9780470377819.

Guchhait, S. and Banerjee, B. (2016). "Anisotropic linear elastic parameter estimation using error in the constitutive equation functional". *Proceedings of the Royal Society A: Mathematical, Physical and Engineering Sciences* 472.2192, p. 20160213. DOI: 10.1098/rspa.2016.0213.

Guchhait, S. and Banerjee, B. (2018). "Constitutive error based parameter estimation technique for plate structures using free vibration signatures". *Journal of Sound and Vibration* 419, pp. 302–317. DOI: 10.1016/j.jsv.2018.01.020.

Guillaume, P., Verboven, P., Cauberghe, B., Vanlanduit, S., Parloo, E., and De Sitter, G. (2003). "Frequency-Domain System Identification Techniques for Experimental and Operational Modal Analysis". *IFAC Proceedings Volumes*. 13th IFAC Symposium on System Identification (SYSID 2003), Rotterdam, The Netherlands, 27-29 August, 2003 36.16, pp. 1609–1614. DOI: 10.1016/S1474-6670(17)34990-X.

Guo, J., Wang, L., and Takewaki, I. (2018). "Modal-based structural damage identification by minimum constitutive relation error and sparse regularization". *Structural Control and Health Monitoring* 25.12, e2255. DOI: 10.1002/stc.2255.

Hadj-Sassi, K. (2007). "Une Stratégie d'Estimation Conjointe des Paramètres et de l'Etat de Structures à Comportements Non Linéaires. Assimilation de Données et Erreur en Loi de Comportement". PhD thesis. Paris: Ecole Polytechnique.

Haik, W., Maday, Y., and Chamoin, L. (2023). "A real-time variational data assimilation method with data-driven model enrichment for time-dependent problems". *Computer Methods in Applied Mechanics and Engineering* 405, p. 115868. DOI: 10.1016/j.cma.2022.115868.

Helfrick, M. N., Pingle, P. S., Niezrecki, C., and Avitabile, P. (2009). "Using Full-field Vibration Measurement Techniques for Damage Detection". Vol. 58. Orlando, Florida, USA, pp. 1289–1295.

Hemez, F. and Farhat, C. (1994). "An Energy Based Optimum Sensor Placement Criterion and its Application to Structural Damage Detection".

Hemez, F. M. and Doebling, S. W. (2001). "Review and assessment of model updating for nonlinear, transient dynamics". *Mechanical Systems and Signal Processing* 15.1, pp. 45–74. DOI: 10.1006/mssp.2000.1351.

Heredia-Zavoni, E., Montes-Iturrizaga, R., and Esteva, L. (1999). "Optimal instrumentation of structures on flexible base for system identification". *Earthquake Engineering & Structural Dynamics* 28.12, pp. 1471–1482. DOI: 10.1002/(SICI)1096-9845(199912)28:12<1471::AID-EQE872>3.0.CO;2-M.

Heredia-Zavoni, E. and Esteva, L. (1998). "Optimal instrumentation of uncertain structural systems subject to earthquake ground motions". *Earthquake Engineering & Structural Dynamics* 27.4, pp. 343–362. DOI: 10.1002/(SICI)1096-9845(199804)27:4<343::AID-EQE726>3.0.CO;2-F.

Hommels, A. (2008). "Comparison of the Ensemble Kalman filter with the Unscented Kalman filter: application to the construction of a road embankment", p. 10.

Hoshiya, M. and Saito, E. (1984). "Structural Identification by Extended Kalman Filter". *Journal of Engineering Mechanics* 110.12, pp. 1757–1770. DOI: 10.1061/(ASCE)0733-9399(1984)110:12(1757).

Hu, X., Prabhu, S., Atamturktur, S., and Cogan, S. (2017). "Mechanistically-informed damage detection using dynamic measurements: Extended constitutive relation error". *Mechanical Systems and Signal Processing* 85, pp. 312–328. DOI: 10.1016/j.ymssp.2016.08.013.

Hu, X., Chodora, E., Prabhu, S., and Atamturktur, S. (2019). "Extended constitutive relation error-based approach: The role of mass in damage detection". *Structural Control and Health Monitoring* 26.5, e2318. DOI: 10.1002/stc.2318.

Huang, S., Feissel, P., and Villon, P. (2016). "Modified constitutive relation error: An identification framework dealing with the reliability of information". *Computer Methods in Applied Mechanics and Engineering* 311, pp. 1–17. DOI: 10.1016/j.cma.2016.06.030.

Hwang, J., Chang, K., and Lee, G. (1987). *The system characteristics and performance of a shaking table.* Tech. rep. NCEER Report n°87-0004. State University of New York at Buffalo, NY: National Center for Earthquake Engineering Research, p. 48.

Ibáñez, R., Abisset-Chavanne, E., Ammar, A., González, D., Cueto, E., Huerta, A., Duval, J. L., and Chinesta, F. (2018). "A Multidimensional Data-Driven Sparse Identification Technique: The Sparse Proper Generalized Decomposition". *Complexity* 2018, pp. 1–11. DOI: 10.1155/2018/5608286.

Jamond, O., Lelong, N., Fourmont, A., Bluthé, J., Breuze, M., Bouda, P., Brooking, G., Drui, F., Epalle, A., Fandeur, O., Folzan, G., Helfer, T., Kloss, F., Latu, G., Motte, A., Nahed, C., Picard, A., Prat, R., Ramière, I., Steins, M., and Prabel, B. (2022). "MANTA : un code HPC généraliste pour la simulation de problèmes complexes en mécanique". *CSMA 2022 15ème Colloque National en Calcul des Structures*. Giens, France.

Jelali, M. and Kroll, A. (2003). *Hydraulic Servo-systems*. Ed. by M. J. Grimble and M. A. Johnson. Advances in Industrial Control. London: Springer London. DOI: 10.1007/978-1-4471-0099-7.

Julier, S., Uhlmann, J., and Durrant-Whyte, H. (2000). "A new method for the nonlinear transformation of means and covariances in filters and estimators". *IEEE Transactions on Automatic Control* 45.3, pp. 477–482. DOI: 10.1109/9.847726.

Julier, S. (2002). "The scaled unscented transformation". *Proceedings of the 2002 American Control Conference (IEEE Cat. No.CH37301)*. Anchorage, AK, USA: IEEE, 4555–4559 vol.6. DOI: 10.1109/ACC.2002.1025369.

Julier, S. J. and Uhlmann, J. K. (1997). "A New Extension of the Kalman Filter to Nonlinear Systems", p. 12.

Kaipio, J. and Sommersalo, E. (2005). "Statistical Inversion Theory". *Statistical and Computational Inverse Problems*, pp. 49–114.

Kalman, R. E. (1960). "A New Approach to Linear Filtering and Prediction Problems". *Journal of Basic Engineering* 82.1, pp. 35–45. DOI: 10.1115/1.3662552.

Kalman, R. E. (1964). "When Is a Linear Control System Optimal?" *Journal of Basic Engineering* 86.1, pp. 51–60. DOI: 10.1115/1.3653115.

Kammer, D. C. (1992a). "Effects of Noise on Sensor Placement for On-Orbit Modal Identification of Large Space Structures". *Journal of Dynamic Systems, Measurement, and Control* 114.3, pp. 436–443. DOI: 10.1115/1.2897366.

Kammer, D. C. (1991). "Sensor placement for on-orbit modal identification and correlation of large space structures". *Journal of Guidance, Control, and Dynamics* 14.2, pp. 251–259. DOI: 10.2514/3.20635.

Kammer, D. C. (1992b). "Effect of model error on sensor placement for on-orbit modal identification of large space structures". *Journal of Guidance, Control, and Dynamics* 15.2, pp. 334–341. DOI: 10.2514/3.20841.

Kammer, D. C. and Tinker, M. L. (2004). "Optimal placement of triaxial accelerometers for modal vibration tests". *Mechanical Systems and Signal Processing* 18.1, pp. 29–41. DOI: 10.1016/S0888-3270(03)00017-7.

Kandepu, R., Foss, B., and Imsland, L. (2008). "Applying the unscented Kalman filter for nonlinear state estimation". *Journal of Process Control* 18.7-8, pp. 753–768. DOI: 10.1016/j.jprocont.2007.11.004.

Kang, Y., Chu, M.-H., Liu, Y.-L., Chang, C.-W., and Chien, S.-Y. (2005). "An Adaptive Control Using Multiple Neural Networks for the Position Control in Hydraulic Servo System". *Advances in Natural Computation*. Ed. by L. Wang, K. Chen, and Y. S. Ong. Lecture Notes in Computer Science. Berlin, Heidelberg: Springer, pp. 296–305. DOI: 10.1007/11539117_44.

Kapteyn, M. G., Knezevic, D., Huynh, P., Tran, M., and Willcox, K. (2019). "Data-driven physics-based digital twins via a library of component-based reduced-order models". *International Journal for Numerical Methods in Engineering*.

Katafygiotis, L. S. and Beck, J. L. (1998). "Updating Models and Their Uncertainties. II: Model Identifiability". *Journal of Engineering Mechanics* 124.4, pp. 463–467. DOI: 10.1061/(ASCE)0733-9399(1998)124:4(463).

Kirkegaard, P. and Brincker, R. (1994). "On the optimal location of sensors for parametric identification of linear structural systems". *Mechanical Systems and Signal Processing* 8.6, pp. 639–647. DOI: 10.1006/mssp.1994.1045.

Ladevèze, P. and Leguillon, D. (1983). "Error Estimate Procedure in the Finite Element Method and Applications". *SIAM Journal on Numerical Analysis* 20.3, pp. 485–509. DOI: 10.1137/0720033.

Ladevèze, P., Puel, G., Deraemaeker, A., and Romeuf, T. (2006). "Validation of structural dynamics models containing uncertainties". *Computer Methods in Applied Mechanics and Engineering* 195.4-6, pp. 373–393. DOI: 10.1016/j.cma.2004.10.011.

Ladevèze, P. and Chamoin, L. (2011). "On the verification of model reduction methods based on the proper generalized decomposition". *Computer Methods in Applied Mechanics and Engineering* 200.23, pp. 2032–2047. DOI: 10.1016/j.cma.2011.02.019.

Ladevèze, P. and Chamoin, L. (2016). "The Constitutive Relation Error Method: A General Verification Tool". *Verifying Calculations - Forty Years On*. Ed. by L. Chamoin and P. Díez. Cham: Springer International Publishing, pp. 59–94. DOI: 10.1007/978-3-319-20553-3_4.

Lakshmivarahan, S. and Stensrud, D. J. (2009). "Ensemble Kalman Filter: Application to meteorological data assimilation". *IEEE Control Systems* 29 (3), pp. 34–46. DOI: 10.1109/MCS.2009.932225.

Law, K. J. H., Stuart, A. M., and Zygalakis, K. C. (2015). "Data Assimilation: A Mathematical Introduction". *arXiv:1506.07825* [*math, stat*].

Le, T.-C., Bach, V.-S., Nguyen, C.-T., Tran, M.-H., and Ho, D.-D. (2023). "An Improved Approach for Damage Identification in Plate-Like Structures Based on Modal Assurance Criterion and Modal Strain Energy Method". *ICSCEA 2021*. Ed. by J. N. Reddy, C. M. Wang, V. H. Luong, and A. T. Le. Lecture Notes in Civil Engineering. Singapore: Springer, pp. 737–745. DOI: 10.1007/978-981-19-3303-5_66.

Le Maoult, A., Chaudat, T., and Moutoussamy, L. (2012). "CEA shaking table control strategy". *EACS 2012 – 5th European Conference on Structural Control*. Genoa, Italy, p. 9.

Le Maoult, A., Queval, J.-C., and Bairrao, R. (2010). "Dynamic Interaction Between the Shaking Table and the Specimen During Seismic Tests". *Advances in Performance-Based Earthquake Engineering*. Ed. by M. N. Fardis. Geotechnical, Geological and Earthquake Engineering. Dordrecht: Springer Netherlands, pp. 431–440. DOI: 10.1007/978-90-481-8746-1_40.

Lefebvre, T., Bruyninckx, H., and De Schutter, J. (2004). "Kalman filters for non-linear systems: a comparison of performance". *International Journal of Control* 77.7, pp. 639–653. DOI: 10.1080/00207170410001704998.

Leitmann, G. (1979). "Guaranteed asymptotic stability for a class of uncertain linear dynamical systems". *Journal of Optimization Theory and Applications* 27.1, pp. 99–106. DOI: 10.1007/BF00933328.

Li, D. S., Li, H. N., and Fritzen, C. P. (2007). "The connection between effective independence and modal kinetic energy methods for sensor placement". *Journal of Sound and Vibration* 305.4, pp. 945–955. DOI: 10.1016/j.jsv.2007.05.004.

Li, W., Sun, S., Jia, Y., and Du, J. (2016). "Robust unscented Kalman filter with adaptation of process and measurement noise covariances". *Digital Signal Processing* 48, pp. 93–103. DOI: 10.1016/j.dsp.2015.09.004.

Link, M. and Weiland, M. (2009). "Damage identification by multi-model updating in the modal and in the time domain". *Mechanical Systems and Signal Processing*. Special Issue: Inverse Problems 23.6, pp. 1734–1746. DOI: 10.1016/j.ymssp.2008.11.009.

Liu, X., Escamilla-Ambrosio, P., and Lieven, N. (2009). "Extended Kalman filtering for the detection of damage in linear mechanical structures". *Journal of Sound and Vibration* 325.4-5, pp. 1023–1046. DOI: 10.1016/j.jsv.2009.04.005.

Long, Q., Motamed, M., and Tempone, R. (2015). "Fast Bayesian optimal experimental design for seismic source inversion". *Computer Methods in Applied Mechanics and Engineering* 291, pp. 123–145. DOI: 10.1016/j.cma.2015.03.021.

Louf, F., Enjalbert, P., Ladevèze, P., and Romeuf, T. (2010). "On lack-of-knowledge theory in structural mechanics". *Comptes Rendus Mécanique* 338.7-8, pp. 424–433. DOI: 10.1016/j.crme.2010.07.012.

Lourens, E., Reynders, E., De Roeck, G., Degrande, G., and Lombaert, G. (2012). "An augmented Kalman filter for force identification in structural dynamics". *Mechanical Systems and Signal Processing* 27, pp. 446–460. DOI: 10.1016/j.ymssp.2011.09.025.

Luenberger, D. (1971). "An introduction to observers". *IEEE Transactions on Automatic Control* 16.6, pp. 596–602. DOI: 10.1109/TAC.1971.1099826.

Luo, J. S. and Johnson, A. (1993). "Stability robustness of the continuous-time LQG system under plant perturbation and noise uncertainty". *Automatica* 29.2, pp. 485–489. DOI: 10.1016/0005-1098(93)90143-H.

Luxburg, U. von (2007). "A tutorial on spectral clustering". *Statistics and Computing* 17.4, pp. 395–416. DOI: 10.1007/s11222-007-9033-z.

Maday, Y. and Mula, O. (2013). "A Generalized Empirical Interpolation Method: Application of Reduced Basis Techniques to Data Assimilation". *Analysis and Numerics of Partial Differential Equations*. Ed. by F. Brezzi, P. Colli Franzone, U. Gianazza, and G. Gilardi. Springer INdAM Series. Milano: Springer Milan, pp. 221–235. DOI: 10.1007/978-88-470-2592-9_13.

Maday, Y., Patera, A. T., Penn, J. D., and Yano, M. (2015a). "A parameterized-background data-weak approach to variational data assimilation: formulation, analysis, and application to acoustics". *International Journal for Numerical Methods in Engineering* 102.5, pp. 933–965. DOI: 10.1002/nme.4747.

Maday, Y., T, A., Penn, J. D., and Yano, M. (2015b). "PBDW State Estimation: Noisy Observations; Configuration-Adaptive Background Spaces; Physical Interpretations". *ESAIM: Proceedings and Surveys* 50, pp. 144–168. DOI: 10.1051/proc/201550008.

Maia, N., Reynier, M., and Ladevèze, P. (1994). "Error Localization for Updating Finite Element Models Using Frequency-response-functions". Proceedings of SPIE - The International Society for Optical Engineering.

Mallardo, V. and Aliabadi, M. (2013). "Optimal Sensor Placement for Structural, Damage and Impact Identification: A Review". *Structural Durability & Health Monitoring* 9.4, pp. 287–323. DOI: 10.32604/sdhm.2013.009.287.

Mandel, J. (2009). "A Brief Tutorial on the Ensemble Kalman Filter". *arXiv:0901.3725* [*physics*].

Marchand, B. (2017). "Assimilation de données et recalage rapide de modèles mécaniques complexes". PhD thesis. Cachan: Université Paris-Saclay.

Marchand, B., Chamoin, L., and Rey, C. (2016). "Real-time updating of structural mechanics models using Kalman filtering, modified constitutive relation error, and proper generalized decomposition: Real-time updating of structural mechanics models". *International Journal for Numerical Methods in Engineering* 107.9, pp. 786–810. DOI: 10.1002/nme.5197.

Marchand, B., Chamoin, L., and Rey, C. (2019). "Parameter identification and model updating in the context of nonlinear mechanical behaviors using a unified formulation of the modified Constitutive Relation Error concept". *Computer Methods in Applied Mechanics and Engineering* 345, pp. 1094–1113. DOI: 10.1016/j.cma.2018.09.008.

Mariani, S. and Corigliano, A. (2005). "Impact induced composite delamination: state and parameter identification via joint and dual extended Kalman filters". *Computer Methods in Applied Mechanics and Engineering* 194.50-52, pp. 5242–5272. DOI: 10.1016/j.cma.2005.01.007.

Mariani, S. and Ghisi, A. (2007). "Unscented Kalman filtering for nonlinear structural dynamics". *Nonlinear Dynamics* 49.1-2, pp. 131–150. DOI: 10.1007/s11071-006-9118-9.

Martin, G., Balmès, E., Chancelier, T., Thouviot, S., and Lemaire, R. (2022). "A Structural Dynamics Modification Strategy based on Expanded Squeal Operational Deflection Shapes".

Maybeck, P. S. (1979). *Stochastic models, estimation and control*. Mathematics in science and engineering vol. 141. New York: Academic Press.

McConnell, K. . G. and Varoto, P. S. (1995). *Vibration testing: theory and practice*. John Wiley & Sons.

Merritt, H. E. (1967). *Hydraulic Control Systems*. J. Wiley.

Metallidis, P., Verros, G., Natsiavas, S., and Papadimitriou, C. (2003). "Fault Detection and Optimal Sensor Location in Vehicle Suspensions". *Journal of Vibration and Control* 9.3-4, pp. 337–359. DOI: 10.1177/107754603030755.

Miyamoto, S., Ichihashi, Hidetomo, and Honda, Katsuhiro (2008). *Algorithms for Fuzzy Clustering*. Vol. 229. Studies in Fuzziness and Soft Computing. Berlin, Heidelberg: Springer Berlin Heidelberg. DOI: 10.1007/978-3-540-78737-2.

Moaveni, B., Conte, J. P., and Hemez, F. M. (2009). "Uncertainty and Sensitivity Analysis of Damage Identification Results Obtained Using Finite Element Model Updating". *Computer-Aided Civil and Infrastructure Engineering* 24.5, pp. 320–334. DOI: 10.1111/j.1467-8667.2008.00589.x.

Moireau, P. and Chapelle, D. (2011). "Reduced-order Unscented Kalman Filtering with application to parameter identification in large-dimensional systems". *ESAIM: Control, Optimisation and Calculus of Variations* 17.2, pp. 380–405. DOI: 10.1051/cocv/2010006.

Morozov, V. A. (1968). "The error principle in the solution of operational equations by the regularization method". *USSR Computational Mathematics and Mathematical Physics* 8.2, pp. 63–87. DOI: 10.1016/0041-5553(68)90034-7.

Morozov, V. A. (1984). *Methods for Solving Incorrectly Posed Problems*. New York, NY: Springer New York. DOI: 10.1007/978-1-4612-5280-1.

Mottershead, J. E. and Friswell, M. I. (1993). "Model Updating In Structural Dynamics: A Survey". *Journal of Sound and Vibration* 167.2, pp. 347–375. DOI: 10.1006/jsvi.1993.1340.

Mottershead, J. E. and Foster, C. D. (1991). "On the treatment of ill-conditioning in spatial parameter estimation from measured vibration data". *Mechanical Systems and Signal Processing* 5.2, pp. 139–154. DOI: 10.1016/0888-3270(91)90020-6.

Mottershead, J. E., Link, M., and Friswell, M. I. (2011). "The sensitivity method in finite element model updating: A tutorial". *Mechanical Systems and Signal Processing* 25.7, pp. 2275–2296. DOI: 10.1016/j.ymssp.2010.10.012.

Moutoussamy, L. (2013). "Essais hybrides temps réel sur structure de génie civil". PhD thesis. Cachan: ENS Cachan.

Mula, O. (2022). "Inverse Problems: A Deterministic Approach using Physics-Based Reduced Models". *arXiv:2203.07769* [*cs, math*].

Mullhaupt, P. (2017). *Introduction à l'Analyse et à la Commande des Systèmes Non Linéaires*.

Naets, F., Croes, J., and Desmet, W. (2015a). "An online coupled state/input/parameter estimation approach for structural dynamics". *Computer Methods in Applied Mechanics and Engineering* 283, pp. 1167–1188. DOI: 10.1016/j.cma.2014.08.010.

Naets, F., Cuadrado, J., and Desmet, W. (2015b). "Stable force identification in structural dynamics using Kalman filtering and dummy-measurements". *Mechanical Systems and Signal Processing* 50-51, pp. 235–248. DOI: 10.1016/j.ymssp.2014.05.042.

Nagata, T., Nonomura, T., Nakai, K., Yamada, K., Saito, Y., and Ono, S. (2021). "Data-driven sparse sensor placement based on A-optimal design of experiment with ADMM". *IEEE Sensors Journal* 21.13, pp. 15248–15257. DOI: 10.1109/JSEN.2021.3073978.

Nair, M. T., Schock, E., and Tautenhahn, U. (2003). "Morozov's Discrepancy Principle under General Source Conditions". *Zeitschrift für Analysis und ihre Anwendungen*, pp. 199–214. DOI: 10.4171/ZAA/1140.

Najafi, A. and Spencer, B. F. (2020). "Modified model-based control of shake tables for online acceleration tracking". *Earthquake Engineering & Structural Dynamics* 49.15, pp. 1721–1737. DOI: 10.1002/eqe.3326.

Nasr, D., Dahr, R. E., Assaad, J., and Khatib, J. (2022). "Comparative Analysis between Genetic Algorithm and Simulated Annealing-Based Frameworks for Optimal Sensor Placement and Structural Health Monitoring Purposes". *Buildings* 12.9, p. 1383. DOI: 10.3390/buildings12091383.

Nguyen, H. N., Chamoin, L., and Ha Minh, C. (2022). "mCRE-based parameter identification from full-field measurements: Consistent framework, integrated version, and extension to nonlinear material behaviors". *Computer Methods in Applied Mechanics and Engineering* 400, p. 115461. DOI: https://doi.org/10.1016/j.cma.2022.115461.

Nguyen, H.-M., Allix, O., and Feissel, P. (2008). "A robust identification strategy for rate-dependent models in dynamics". *Inverse Problems* 24.6, p. 065006. DOI: 10.1088/0266-5611/24/6/065006.

Nguyen, N.-H., Cheong Khoo, B., and Willcox, K. (2014). "Model order reduction for Bayesian approach to inverse problems". *Asia Pacific Journal on Computational Engineering* 1.1, p. 2. DOI: 10.1186/2196-1166-1-2.

Oliveira, H., Louf, F., and Gatuingt, F. (2021). "Numerical study based on the Constitutive Relation Error for identifying semi-rigid joint parameters between planar structural elements". *Engineering Structures* 236, p. 112015. DOI: 10.1016/j.engstruct.2021.112015.

Oliveira, H., Louf, F., and Gatuingt, F. (2022). "MCRE-based finite element model updating: Cast3M implementation". *Advances in Engineering Software* 173, p. 103220. DOI: 10.1016/j.advengsoft.2022.103220.

Oliveira, H., Louf, F., Hervé-Secourgeon, E., and Gatuingt, F. (2020). "Wall-slab joint parameter identification of a reinforced concrete structure using possibly corrupted modal data". *International Journal for Numerical and Analytical Methods in Geomechanics* 44.1, pp. 19–39. DOI: 10.1002/nag.2994.

Olivier, A. and Smyth, A. W. (2017). "Particle filtering and marginalization for parameter identification in structural systems". *Structural Control and Health Monitoring* 24.3, e1874. DOI: https://doi.org/10.1002/stc.1874. eprint: https://onlinelibrary.wiley.com/doi/pdf/10.1002/stc.1874.

Onat, A. (2019). "A Novel and Computationally Efficient Joint Unscented Kalman Filtering Scheme for Parameter Estimation of a Class of Nonlinear Systems". *IEEE Access* 7, pp. 31634–31655. DOI: 10.1109/ACCESS.2019.2902368.

Orlande, H. R. B., Colaço, M. J., Dulikravich, G. S., and Vianna, F. L. V. (2011). *Kalman and Particle filters*. Tech. rep., p. 39.

Ostachowicz, W., Soman, R., and Malinowski, P. (2019). "Optimization of sensor placement for structural health monitoring: a review". *Structural Health Monitoring* 18.3, pp. 963–988. DOI: 10.1177/1475921719825601.

Ouyang, H., Richiedei, D., and Trevisani, A. (2013). "Pole assignment for control of flexible link mechanisms". *Journal of Sound and Vibration* 332.12, pp. 2884–2899. DOI: 10.1016/j.jsv.2013.01.004.

Overschee, P. v. and Moor, B. L. d. (1996). *Subspace Identification for Linear Systems: Theory — Implementation — Applications*. Springer New York, NY. DOI: https://doi.org/10.1007/978-1-4613-0465-4.

Papadimitriou, C. (2004). "Optimal sensor placement methodology for parametric identification of structural systems". *Journal of Sound and Vibration* 278.4, pp. 923–947. DOI: 10.1016/j.jsv.2003.10.063.

Papadimitriou, C. (2005). "Pareto optimal sensor locations for structural identification". *Computer Methods in Applied Mechanics and Engineering*. Special Issue on Computational Methods in Stochastic Mechanics and Reliability Analysis 194.12, pp. 1655–1673. DOI: 10.1016/j.cma.2004.06.043.

Papadimitriou, C., Beck, J. L., and Au, S.-K. (2000). "Entropy-Based Optimal Sensor Location for Structural Model Updating". *Journal of Vibration and Control* 6.5, pp. 781–800. DOI: 10.1177/107754630000600508.

Papadimitriou, C. and Lombaert, G. (2012). "The effect of prediction error correlation on optimal sensor placement in structural dynamics". *Mechanical Systems and Signal Processing* 28, pp. 105–127. DOI: 10.1016/j.ymssp.2011.05.019.

Papadimitriou, C. and Papadioti, D.-C. (2013). "Component mode synthesis techniques for finite element model updating". *Computers & Structures* 126, pp. 15–28. DOI: https://doi.org/10.1016/j.compstruc.2012.10.018.

Papakonstantinou, K. G., Amir, M., and Warn, G. P. (2022a). "A Scaled Spherical Simplex Filter (S3F) with a decreased n+2 sigma points set size and equivalent 2n+1 Unscented Kalman Filter (UKF) accuracy". *Mechanical Systems and Signal Processing* 163, p. 107433. DOI: 10.1016/j.ymssp.2020.107433.

Papakonstantinou, K. G., Warn, G. P., and Amir, M. (2022b). "A theoretical and numerical study on the Scaled Spherical Simplex filter with n+2 sigma points and its UKF equivalency for recursive Bayesian estimation". Oslo, Norway, p. 1.

Peeters, B. and De Roeck, G. (2001). "Stochastic System Identification for Operational Modal Analysis: A Review". *Journal of Dynamic Systems, Measurement, and Control* 123.4, pp. 659–667. DOI: 10.1115/1.1410370.

Pereira Álvarez, P., Kerfriden, P., Ryckelynck, D., and Robin, V. (2021). "Real-Time Data Assimilation in Welding Operations Using Thermal Imaging and Accelerated High-Fidelity Digital Twinning". *Mathematics* 9.18, p. 2263. DOI: 10.3390/math9182263.

Phillips, B. M., Wierschem, N. E., and Spencer, B. F. (2014). "Model-based multi-metric control of uniaxial shake tables". *Earthquake Engineering & Structural Dynamics* 43.5, pp. 681–699. DOI: 10.1002/eqe.2366.

Pled, F., Chamoin, L., and Ladevèze, P. (2011). "On the techniques for constructing admissible stress fields in model verification: Performances on engineering examples". *International Journal for Numerical Methods in Engineering* 88.5, pp. 409–441. DOI: 10.1002/nme.3180.

Plummer, A. R. (2007). "Control techniques for structural testing: A review". *Proceedings of the Institution of Mechanical Engineers, Part I: Journal of Systems and Control Engineering* 221.2, pp. 139–169. DOI: 10.1243/09596518JSCE295.

Plummer, A. R. (2008). "A Detailed Dynamic Model of a Six-Axis Shaking Table". *Journal of Earthquake Engineering* 12.4, pp. 631–662. DOI: 10.1080/13632460701457264.

Plummer, A. R. (2016). "Model-based motion control for multi-axis servohydraulic shaking tables". *Control Engineering Practice* 53, pp. 109–122. DOI: 10.1016/j.conengprac.2016.05.004.

Pregnolato, M., Gunner, S., Voyagaki, E., De Risi, R., Carhart, N., Gavriel, G., Tully, P., Tryfonas, T., Macdonald, J., and Taylor, C. (2022). "Towards Civil Engineering 4.0: Concept, workflow and application of Digital Twins for existing infrastructure". *Automation in Construction* 141, p. 104421. DOI: 10.1016/j.autcon.2022.104421.

Preumont, A. (2018). *Vibration Control of Active Structures*. Vol. 246. Solid Mechanics and Its Applications. Cham: Springer International Publishing. DOI: 10.1007/978-3-319-72296-2.

Prudencio, E. E., Bauman, P. T., Williams, S. V., Faghihi, D., Ravi-Chandar, K., and Oden, J. T. (2013). "A Dynamic Data Driven Application System for Real-time Monitoring of Stochastic Damage". *Procedia Computer Science*. 2013 International Conference on Computational Science 18, pp. 2056–2065. DOI: 10.1016/j.procs.2013.05.375.

Puel, G. and Aubry, D. (2011). "Using mesh adaption for the identification of a spatial field of material properties: SPATIAL FIELD IDENTIFICATION USING MESH ADAPTION". *International Journal for Numerical Methods in Engineering* 88.3, pp. 205–227. DOI: 10.1002/nme.3170.

Qin, S. and Badgwell, T. A. (2003). "A survey of industrial model predictive control technology". *Control Engineering Practice* 11.7, pp. 733–764. DOI: 10.1016/S0967-0661(02)00186-7.

Rahideh, A. and Hasan Shaheed, M. (2011). "Stable model predictive control for a nonlinear system". *Journal of the Franklin Institute* 348.8, pp. 1983–2004. DOI: 10.1016/j.jfranklin.2011.05.015.

Rasheed, A., San, O., and Kvamsdal, T. (2020). "Digital Twin: Values, Challenges and Enablers From a Modeling Perspective". *IEEE Access* 8, pp. 21980–22012. DOI: 10.1109/ACCESS.2020.2970143.

Reynders, E. (2012). "System Identification Methods for (Operational) Modal Analysis: Review and Comparison". *Archives of Computational Methods in Engineering* 19.1, pp. 51–124. DOI: 10.1007/s11831-012-9069-x.

Reynders, E., Houbrechts, J., and De Roeck, G. (2012). "Fully automated (operational) modal analysis". *Mechanical Systems and Signal Processing* 29, pp. 228–250. DOI: 10.1016/j.ymssp.2012.01.007.

Reynders, E. and Roeck, G. D. (2008). "Reference-based combined deterministic–stochastic subspace identification for experimental and operational modal analysis". *Mechanical Systems and Signal Processing* 22.3, pp. 617–637. DOI: 10.1016/j.ymssp.2007.09.004.

Reynier, M. and Abou-kandil, H. (1999). "Sensors Location For Updating Problems". *Mechanical Systems and Signal Processing* 13.2, pp. 297–314. DOI: 10.1006/mssp.1998.1213.

Richalet, J. (1993). "Industrial applications of model based predictive control". *Automatica* 29.5, pp. 1251–1274. DOI: 10.1016/0005-1098(93)90049-Y.

Richalet, J., Rault, A., Testud, J. L., and Papon, J. (1978). "Model predictive heuristic control: Applications to industrial processes". *Automatica* 14.5, pp. 413–428. DOI: 10.1016/0005-1098(78)90001-8.

Richalet, J. and O'Donovan, D. (2009). *Predictive Functional Control*. Advances in Industrial Control. London: Springer London. DOI: 10.1007/978-1-84882-493-5.

Richard, B., Cherubini, S., Voldoire, F., Charbonnel, P.-E., Chaudat, T., Abouri, S., and Bonfils, N. (2016). "SMART 2013: Experimental and numerical assessment of the dynamic behavior by shaking table tests of an asymmetrical reinforced concrete structure subjected to high intensity ground motions". *Engineering Structures* 109, pp. 99–116. DOI: 10.1016/j.engstruct.2015.11.029.

Richard, B., Voldoire, F., Fontan, M., Mazars, J., Chaudat, T., Abouri, S., and Bonfils, N. (2018). "SMART 2013: Lessons learned from the international benchmark about the seismic margin assessment of nuclear RC buildings". *Engineering Structures* 161, pp. 207–222.

Ritto, T. and Rochinha, F. (2021). "Digital twin, physics-based model, and machine learning applied to damage detection in structures". *Mechanical Systems and Signal Processing* 155, p. 107614. DOI: 10.1016/j.ymssp.2021.107614.

Rosafalco, L., Eftekhar Azam, S., Manzoni, A., Corigliano, A., and Mariani, S. (2021). "Unscented Kalman Filter Empowered by Bayesian Model Evidence for System Identification in Structural Dynamics". *IOCA 2021*. MDPI, p. 3. DOI: 10.3390/IOCA2021-10896.

Roussel, A., Capaldo, M., Chamoin, L., and Argaud, J.-P. (2022). "Modified Constitutive Relation Error for Multi-Physics Wind Turbine Calibration". *Journal of Physics: Conference Series* 2265.4, p. 042040. DOI: 10.1088/1742-6596/2265/4/042040.

Rozza, G., Huynh, D. B. P., and Patera, A. T. (2008). "Reduced Basis Approximation and a Posteriori Error Estimation for Affinely Parametrized Elliptic Coercive Partial Differential Equations". *Archives of Computational Methods in Engineering* 15.3, p. 229. DOI: 10.1007/s11831-008-9019-9.

Rubio, P.-B., Chamoin, L., and Louf, F. (2021). "Real-time data assimilation and control on mechanical systems under uncertainties". *Advanced Modeling and Simulation in Engineering Sciences* 8.1, p. 4. DOI: 10.1186/s40323-021-00188-3.

Rubio, P.-B., Louf, F., and Chamoin, L. (2018). "Fast model updating coupling Bayesian inference and PGD model reduction". *Computational Mechanics* 62.6, pp. 1485–1509. DOI: 10.1007/s00466-018-1575-8.

Ručevskis, S., Rogala, T., and Katunin, A. (2022). "Optimal Sensor Placement for Modal-Based Health Monitoring of a Composite Structure". *Sensors* 22.10, p. 3867. DOI: 10.3390/s22103867.

Salama, M., Rose, T., and Garba, J. (1987). "Optimal placement of excitations and sensors for verification of large dynamical systems". *28th Structures, Structural Dynamics and Materials*

Conference. American Institute of Aeronautics and Astronautics. DOI: https://doi.org/10.2514/6.1987-782.

Samir, Z., Chamoin, L., and Abbas, M. (2022). "Une approche performante de recalage en dynamique vibratoire par erreur en relation de comportement modifiée et décomposition de domaine".

Seki, K., Iwasaki, M., Kawafuku, M., Hirai, H., and Yasuda, K. (2009a). "Adaptive Compensation for Reaction Force With Frequency Variation in Shaking Table Systems". *IEEE Transactions on Industrial Electronics* 56.10, pp. 3864–3871. DOI: 10.1109/TIE.2009.2022519.

Seki, K., Iwasaki, M., Kawafuku, M., Hirai, H., and Yasuda, K. (2009b). "Adaptive feedforward compensation for reaction force with nonlinear specimen in shaking tables". *2009 IEEE International Conference on Mechatronics*, pp. 1–6. DOI: 10.1109/ICMECH.2009.4957139.

Shah, P. C. and Udwadia, F. E. (1978). "A Methodology for Optimal Sensor Locations for Identification of Dynamic Systems". *Journal of Applied Mechanics* 45.1, pp. 188–196. DOI: 10.1115/1.3424225.

Shen, G., Zheng, S.-T., Ye, Z.-M., Huang, Q.-T., Cong, D.-C., and Han, J.-W. (2011). "Adaptive inverse control of time waveform replication for electrohydraulic shaking table". *Journal of Vibration and Control* 17.11, pp. 1611–1633. DOI: 10.1177/1077546310380431.

Shen, G., Zhu, Z., Li, X., Li, G., Tang, Y., and Liu, S. (2016). "Experimental evaluation of acceleration waveform replication on electrohydraulic shaking tables: A review". *International Journal of Advanced Robotic Systems* 13.5, p. 172988141666253. DOI: 10.1177/1729881416662537.

Shi, Z. Y., Law, S. S., and Zhang, L. M. (2000). "Optimum Sensor Placement for Structural Damage Detection". *Journal of Engineering Mechanics* 126.11, pp. 1173–1179. DOI: 10.1061/(ASCE)0733-9399(2000)126:11(1173).

Silva, C. E., Gomez, D., Maghareh, A., Dyke, S. J., and Spencer, B. F. (2020). "Benchmark control problem for real-time hybrid simulation". *Mechanical Systems and Signal Processing* 135, p. 106381. DOI: https://doi.org/10.1016/j.ymssp.2019.106381.

Silva, T. and Maia, N. (2017). "Detection and localisation of structural damage based on the error in the constitutive relations in dynamics". *Applied Mathematical Modelling* 46, pp. 736–749. DOI: 10.1016/j.apm.2016.07.002.

Simoen, E., De Roeck, G., and Lombaert, G. (2015). "Dealing with uncertainty in model updating for damage assessment: A review". *Mechanical Systems and Signal Processing* 56-57, pp. 123–149. DOI: 10.1016/j.ymssp.2014.11.001.

Simpson, T., Dertimanis, V. K., and Chatzi, E. N. (2020). "Towards Data-Driven Real-Time Hybrid Simulation: Adaptive Modeling of Control Plants". *Frontiers in Built Environment* 6. DOI: 10.3389/fbuil.2020.570947.

Sohn, H., Farrar, C. R., Hemez, F., and Czarnecki, J. (2003). "A Review of Structural Health Monitoring Literature: 1996-2001". *Los Alamos National Laboratory*.

Song, M., Astroza, R., Ebrahimian, H., Moaveni, B., and Papadimitriou, C. (2020). "Adaptive Kalman filters for nonlinear finite element model updating". *Mechanical Systems and Signal Processing* 143, p. 106837. DOI: 10.1016/j.ymssp.2020.106837.

Sorenson, H. W. (1970). "Least-squares estimation: from Gauss to Kalman". *IEEE Spectrum* 7.7, pp. 63–68. DOI: 10.1109/MSPEC.1970.5213471.

Stoica, P. and Moses, R. L. (2005). *Spectral analysis of signals*. Upper Saddle River, N.J: Pearson/Prentice Hall.

Stoten, D. P. and Benchoubane, H. (1993). "The minimal control synthesis identification algorithm". *International Journal of Control* 58.3, pp. 685–696. DOI: 10.1080/00207179308923022.

Stoten, D. P. and Gomez, E. G. (2001). "Adaptive control of shaking tables using the minimal control synthesis algorithm". *Philosophical Transactions of the Royal Society of London. Series A: Mathematical, Physical and Engineering Sciences* 359.1786, pp. 1697–1723. DOI: 10.1098/rsta.2001.0862.

Stuart, A. M. (2010). "Inverse problems: A Bayesian perspective". *Acta Numerica* 19, pp. 451–559. DOI: 10.1017/S0962492910000061.

Tagawa, Y. and Kajiwara, K. (2007). "Controller development for the E-Defense shaking table". *Proceedings of the Institution of Mechanical Engineers, Part I: Journal of Systems and Control Engineering* 221.2, pp. 171–181. DOI: 10.1243/09596518JSCE331.

Taher, S. A., Li, J., and Fang, H. (2023). "Simultaneous seismic input and state estimation with optimal sensor placement for building structures using incomplete acceleration measurements". *Mechanical Systems and Signal Processing* 188, p. 110047. DOI: 10.1016/j.ymssp.2022.110047.

Tarantola, A. (2005). *Inverse Problem Theory and Methods for Model Parameter Estimation*. Society for Industrial and Applied Mathematics. DOI: 10.1137/1.9780898717921.

Tatsis, K., Agathos, K., Chatzi, E., and Dertimanis, V. (2022). "A hierarchical output-only Bayesian approach for online vibration-based crack detection using parametric reduced-order models". *Mechanical Systems and Signal Processing* 167, p. 108558. DOI: https://doi.org/10.1016/j.ymssp.2021.108558.

Terejanu, G. A. (2008). *Extended Kalman Filter Tutorial*.

Terejanu, G. A. (2011). *Unscented Kalman Filter Tutorial*.

Teughels, A. and De Roeck, G. (2005). "Damage detection and parameter identification by finite element model updating". *Archives of Computational Methods in Engineering* 12.2, pp. 123–164. DOI: 10.1007/BF03044517.

Tikhonov, A. N. and Arsenin, V. Y. (1977). *Solution of ill posed problems*. Wiley. New York, pp. 521–524.

Titurus, B. and Friswell, M. I. (2008). "Regularization in model updating". *International Journal for Numerical Methods in Engineering* 75.4, pp. 440–478. DOI: 10.1002/nme.2257.

Udwadia, F. E. (1994). "Methodology for Optimum Sensor Locations for Parameter Identification in Dynamic Systems". *Journal of Engineering Mechanics* 120.2, pp. 368–390. DOI: 10.1061/(ASCE)0733-9399(1994)120:2(368).

Van Biesbroeck, A., Gauchy, C., Feau, C., and Garnier, J. (2023). *Reference prior for Bayesian estimation of seismic fragility curves*. DOI: 10.48550/ARXIV.2302.06935.

Van Der Merwe, R. and Wan, E. (2004). *Sigma-Point Kalman Filters for Probabilistic Inference in Dynamic State-Space Models*. Oregon Health & Science University.

Waeytens, J., Rosić, B., Charbonnel, P.-E., Merliot, E., Siegert, D., Chapeleau, X., Vidal, R., Corvec, V. le, and Cottineau, L.-M. (2016). "Model updating techniques for damage detection in concrete beam using optical fiber strain measurement device". *Engineering Structures* 129, pp. 2–10. DOI: 10.1016/j.engstruct.2016.08.004.

Wagg, D. J., Worden, K., Barthorpe, R. J., and Gardner, P. (2020). "Digital Twins: State-of-the-Art and Future Directions for Modeling and Simulation in Engineering Dynamics Appli-

cations". *ASCE-ASME J Risk and Uncert in Engrg Sys Part B Mech Engrg* 6.3, p. 030901. DOI: 10.1115/1.4046739.

Wan, E. and Van Der Merwe, R. (2000). "The unscented Kalman filter for nonlinear estimation". *Proceedings of the IEEE 2000 Adaptive Systems for Signal Processing, Communications, and Control Symposium (Cat. No.00EX373)*. Lake Louise, Alta., Canada: IEEE, pp. 153–158. DOI: 10.1109/ASSPCC.2000.882463.

Wang, Y.-G. and Shao, H.-H. (2000). "Optimal tuning for PI controller". *Automatica* 36.1, pp. 147–152. DOI: 10.1016/S0005-1098(99)00130-2.

Warner, J. E., Diaz, M. I., Aquino, W., and Bonnet, M. (2014). "Inverse material identification in coupled acoustic-structure interaction using a modified error in constitutive equation functional". *Computational Mechanics* 54.3, pp. 645–659. DOI: 10.1007/s00466-014-1018-0.

Weber, B., Paultre, P., and Proulx, J. (2007). "Structural damage detection using nonlinear parameter identification with Tikhonov regularization". *Structural Control and Health Monitoring* 14.3, pp. 406–427. DOI: 10.1002/stc.164.

Weber, B., Paultre, P., and Proulx, J. (2009). "Consistent regularization of nonlinear model updating for damage identification". *Mechanical Systems and Signal Processing*. Special Issue: Inverse Problems 23.6, pp. 1965–1985. DOI: 10.1016/j.ymssp.2008.04.011.

Welch, G. and Bishop, G. (2006). "An Introduction to the Kalman Filter", p. 16.

Williams, M. S. and Blakeborough, A. (2001). "Laboratory testing of structures under dynamic loads: an introductory review". *Philosophical Transactions of the Royal Society of London. Series A: Mathematical, Physical and Engineering Sciences* 359.1786, pp. 1651–1669. DOI: 10.1098/rsta.2001.0860.

Worden, K. and Burrows, A. P. (2001). "Optimal sensor placement for fault detection". *Engineering Structures* 23.8, pp. 885–901. DOI: 10.1016/S0141-0296(00)00118-8.

Worden, K., Farrar, C. R., Manson, G., and Park, G. (2007). "The fundamental axioms of structural health monitoring". *Proceedings of the Royal Society A: Mathematical, Physical and Engineering Sciences* 463.2082, pp. 1639–1664. DOI: 10.1098/rspa.2007.1834.

Wu, M. and Smyth, A. W. (2007). "Application of the unscented Kalman filter for real-time nonlinear structural system identification". *Structural Control and Health Monitoring* 14.7, pp. 971–990. DOI: 10.1002/stc.186.

Xu, Y., Hua, H., and Han, J. (2008). "Modeling and controller design of a shaking table in an active structural control system". *Mechanical Systems and Signal Processing* 22.8, pp. 1917–1923. DOI: 10.1016/j.ymssp.2008.02.003.

Yang, C. (2022). "A novel non-probabilistic sensor placement method for structural health monitoring using an iterative multi-objective optimization algorithm". *IEEE Sensors Journal*, pp. 1–1. DOI: 10.1109/JSEN.2022.3217669.

Yao, J., Dietz, M., Xiao, R., Yu, H., Wang, T., and Yue, D. (2016). "An overview of control schemes for hydraulic shaking tables". *Journal of Vibration and Control* 22.12, pp. 2807–2823. DOI: 10.1177/1077546314549589.

Yao, J. (2018). "Model-based nonlinear control of hydraulic servo systems: Challenges, developments and perspectives". *Frontiers of Mechanical Engineering* 13.2, pp. 179–210. DOI: 10.1007/s11465-018-0464-3.

Yao, J., Jiao, Z., and Ma, D. (2014). "Extended-State-Observer-Based Output Feedback Nonlinear Robust Control of Hydraulic Systems With Backstepping". *IEEE Transactions on Industrial Electronics* 61.11, pp. 6285–6293. DOI: 10.1109/TIE.2014.2304912.

Yao, L., Sethares, W. A., and Kammer, D. C. (1993). "Sensor placement for on-orbit modal identification via a genetic algorithm". *AIAA Journal* 31.10, pp. 1922–1928. DOI: 10.2514/3.11868.

Yi, T.-H. and Li, H.-N. (2012). "Methodology Developments in Sensor Placement for Health Monitoring of Civil Infrastructures". *International Journal of Distributed Sensor Networks* 8.8, p. 612726. DOI: 10.1155/2012/612726.

Yin, T., Yuen, K.-V., Lam, H.-F., and Zhu, H.-p. (2017). "Entropy-Based Optimal Sensor Placement for Model Identification of Periodic Structures Endowed with Bolted Joints". *Computer-Aided Civil and Infrastructure Engineering* 32.12, pp. 1007–1024. DOI: 10.1111/mice.12309.

Yu, T. K. and Seinfled, J. H. (1973). "Observability and optimal measurement location in linear distributed parameter systems". *International Journal of Control* 18.4, pp. 785–799. DOI: 10.1080/00207177308932556.

Yuen, K.-V., Katafygiotis, L. S., Papadimitriou, C., and Mickleborough, N. C. (2001). "Optimal Sensor Placement Methodology for Identification with Unmeasured Excitation". *Journal of Dynamic Systems, Measurement, and Control* 123.4, pp. 677–686. DOI: 10.1115/1.1410929.

Zhang, C. D. and Xu, Y. L. (2016). "Comparative studies on damage identification with Tikhonov regularization and sparse regularization: Damage Detection with Tikhonov Regularization and Sparse Regularization". *Structural Control and Health Monitoring* 23.3, pp. 560–579. DOI: 10.1002/stc.1785.

Zhang, Y., Zhao, Z., Lu, T., Yuan, L., Xu, W., and Zhu, J. (2009). "A comparative study of Luenberger observer, sliding mode observer and extended Kalman filter for sensorless vector control of induction motor drives". *2009 IEEE Energy Conversion Congress and Exposition*, pp. 2466–2473. DOI: 10.1109/ECCE.2009.5316508.

Zhou, K., Wu, Z., Yi, X., Zhu, D., Narayan, R., and Zhao, J. (2017). "Generic Framework of Sensor Placement Optimization for Structural Health Modeling". *Journal of Computing in Civil Engineering* 31, p. 04017018. DOI: 10.1061/(ASCE)CP.1943-5487.0000662.

Ziegler, J. G. and Nichols, N. B. (1942). "Optimum Settings for Automatic Controllers". *Transactions of the ASME* 64.11. DOI: 10.1115/1.2899060.